Application of smoothed point interpolation methods to numerical modelling of saturated and unsaturated porous media

Author:
Ghaffaripour, Omid

Publication Date:
2018

DOI:
https://doi.org/10.26190/unsworks/3604

APPLICATION OF SMOOTHED POINT INTERPOLATION METHODS TO NUMERICAL MODELLING OF SATURATED AND UNSATURATED POROUS MEDIA

OMID GHAFFARIPOUR, BSc, MSc

A thesis submitted in fulfilment of the requirements for the degree of

DOCTOR OF PHILOSOPHY

School of Civil and Environmental Engineering

UNSW Sydney

AUSTRALIA

December 2018

THE UNIVERSITY OF NEW SOUTH WALES
Thesis/Dissertation Sheet

Surname/Family Name	:	**Ghaffaripour**
Given Name/s	:	**Omid**
Abbreviation for degree as give in the University calendar	:	**PhD**
Faculty	:	**Engineering**
School	:	**Civil and Environmental Engineering**
Thesis Title	:	**Application of smoothed point interpolation methods to numerical modelling of saturated and unsaturated porous media**

Abstract 350 words maximum:

This study aims to develop an efficient computational framework for a rigorous coupled flow and deformation analysis of saturated and unsaturated porous media. The governing equations are derived based on equations of equilibrium, and conservation equations of mass and momentum for each phase. For numerical solution of the governing equations, the edge-based smoothed point interpolation method (ESPIM) is employed due to its numerous advantages over the classical techniques. The ESPIM was originally introduced for problems in single phase media. The extension of the technique to multiphase media is not trivial, and therefore as the first development step, ESPIM is extended for the solution of the coupled hydro-mechanical problems in saturated porous media through a novel approach for evaluation of the coupling matrix. Verification of the proposed ESPIM formulation is performed using several benchmark numerical examples. Subsequently, the method of manufactured solutions (MMS) is introduced, for the first time in geomechanics, for a systematic and more rigorous verification of the computational scheme.
The proposed numerical framework is then extended to include material nonlinearity. For this purpose, a non-associative Mohr-Coulomb constitutive model is adopted and an algorithm is developed based on the modified Newton-Raphson technique to address the nonlinearities arisen from the elasto-plastic constitutive model. Stress integration is performed using the substepping method. The computational framework is then further extended to include the problems in unsaturated soil mechanics, taking account of coupling among different phases, and the hydraulic hysteresis observed in the behaviour of unsaturated soils. A framework based on the effective stress principle is followed in the formulation and a hysteretic water retention model is taken into account which includes the evolution of water retention curve (WRC) with changes of void ratio. An elasto-plastic constitutive model is employed within the context of bounding surface plasticity theory for predicting the nonlinear behaviour of soil skeleton in saturated and unsaturated porous media. The model is validated by comparing the numerical predictions with experimental or numerical data from the literature for fully and partially saturated soils. The results demonstrate the capability of the proposed numerical framework to predict essential characteristics of variably saturated soils.

COPYRIGHT STATEMENT

'I hereby grant the University of New South Wales or its agents the right to archive and to make available my thesis or dissertation in whole or part in the University libraries in all forms of media, now or here after known, subject to the provisions of the Copyright Act 1968. I retain all proprietary rights, such as patent rights. I also retain the right to use in future works (such as articles or books) all or part of this thesis or dissertation.

I also authorise University Microfilms to use the 350 word abstract of my thesis in Dissertation Abstract International (this is applicable to doctoral theses only).

I have either used no substantial portions of copyright material in my thesis or I have obtained permission to use copyright material; where permission has not been granted I have applied/will apply for a partial restriction of the digital copy of my thesis or dissertation.'

Signed …………………………………………..........................

Date …………………………………………..........................

AUTHENTICITY STATEMENT

'I certify that the Library deposit digital copy is a direct equivalent of the final officially approved version of my thesis. No emendation of content has occurred and if there are any minor variations in formatting, they are the result of the conversion to digital format.'

Signed …………………………………………..........................

Date …………………………………………..........................

ORIGINALITY STATEMENT

‘I hereby declare that this submission is my own work and to the best of my knowledge it contains no materials previously published or written by another person, or substantial proportions of material which have been accepted for the award of any other degree or diploma at UNSW or any other educational institution, except where due acknowledgement is made in the thesis. Any contribution made to the research by others, with whom I have worked at UNSW or elsewhere, is explicitly acknowledged in the thesis. I also declare that the intellectual content of this thesis is the product of my own work, except to the extent that assistance from others in the project's design and conception or in style, presentation and linguistic expression is acknowledged.’

Signed ……………………………………………...........................

Date ……………………………………………...........................

INCLUSION OF PUBLICATIONS STATEMENT

UNSW is supportive of candidates publishing their research results during their candidature as detailed in the UNSW Thesis Examination Procedure.

Publications can be used in their thesis in lieu of a Chapter if:

- The student contributed greater than 50% of the content in the publication and is the "primary author", ie. the student was responsible primarily for the planning, execution and preparation of the work for publication
- The student has approval to include the publication in their thesis in lieu of a Chapter from their supervisor and Postgraduate Coordinator.
- The publication is not subject to any obligations or contractual agreements with a third party that would constrain its inclusion in the thesis

Please indicate whether this thesis contains published material or not.

☐ *This thesis contains no publications, either published or submitted for publication (if this box is checked, you may delete all the material on page 2)*

☐ *Some of the work described in this thesis has been published and it has been documented in the relevant Chapters with acknowledgement (if this box is checked, you may delete all the material on page 2)*

☒ *This thesis has publications (either published or submitted for publication) incorporated into it in lieu of a chapter and the details are presented below*

CANDIDATE'S DECLARATION

I declare that:

- I have complied with the Thesis Examination Procedure
- where I have used a publication in lieu of a Chapter, the listed publication(s) below meet(s) the requirements to be included in the thesis.

Name	Signature	Date (dd/mm/yy)
Omid Ghaffaripour		16/08/2018

Postgraduate Coordinator's Declaration (to be filled in where publications are used in lieu of Chapters)

I declare that:

- the information below is accurate
- where listed publication(s) have been used in lieu of Chapter(s), their use complies with the Thesis Examination Procedure
- the minimum requirements for the format of the thesis have been met.

PGC's Name	PGC's Signature	Date (dd/mm/yy)
Hamid Valipour		**17/08/2018**

For each publication incorporated into the thesis in lieu of a Chapter, provide all of the requested details and signatures required

<table>
<tr><td colspan="7">Details of publication #1:
Full title: An edge-based smoothed point interpolation method for elasto-plastic coupled hydro-mechanical analysis of saturated porous media
Authors: Omid Ghaffaripour, Arman Khoshghalb, Nasser Khalili
Journal or book name: Computers and Geotechncis
Volume/page numbers: 82/99-109
Date accepted/ published:4 Oct 2016/ Feb 2017</td></tr>
<tr><td>Status</td><td>Published</td><td>X</td><td>Accepted and In press</td><td></td><td>In progress (submitted)</td><td></td></tr>
<tr><td colspan="7">The Candidate's Contribution to the Work
The candidate developed the numerical formulation and the computer code, prepared the numerical examples, performed the numerical analyses and wrote the manuscript.</td></tr>
<tr><td colspan="7">Location of the work in the thesis and/or how the work is incorporated in the thesis:
The publication is used in lieu of Chapter 5 of this thesis.</td></tr>
<tr><td colspan="7">Primary Supervisor's Declaration
I declare that:
• the information above is accurate
• this has been discussed with the PGC and it is agreed that this publication can be included in this thesis in lieu of a Chapter
• All of the co-authors of the publication have reviewed the above information and have agreed to its veracity by signing a 'Co-Author Authorisation' form.</td></tr>
</table>

Supervisor's name	**Supervisor's signature**	**Date (dd/mm/yy)**
Arman Khoshghalb		**16/08/18**

ABSTRACT

The objective of this study is to develop an efficient computational framework for a rigorous coupled flow and deformation analysis of saturated and unsaturated porous media. The governing equations are derived based on equations of equilibrium, and conservation equations of mass and momentum for each phase of the porous media. For numerical solution of the governing equations, the edge-based smoothed point interpolation method (ESPIM) is employed due to its numerous advantages over the classical techniques. The ESPIM was originally introduced for problems in single phase media. The extension of the technique to multiphase media is not trivial, and therefore as the first development step, ESPIM is extended for the solution of the coupled flow and deformation problems in saturated porous media through a novel approach for evaluation of the coupling matrix of the system. Verification of the proposed ESPIM formulation is carried out using several benchmark numerical examples. Subsequently, the method of manufactured solutions (MMS) is introduced, for the first time in geomechanics, for a systematic and more rigorous verification of the computational scheme.

The proposed numerical framework is then extended to include material nonlinearity. For this purpose, a non-associative Mohr-Coulomb constitutive model is adopted and an algorithm is developed based on the modified Newton-Raphson technique to address the nonlinearities arisen from the elasto-plastic constitutive model. Stress integration is performed using the substepping method. The computational framework is then further extended to include the problems in unsaturated soil mechanics, taking account of coupling among different phases, and the hydraulic hysteresis observed in the behaviour of unsaturated soils. A framework based on the effective stress principle is followed in the formulation and a hysteretic water retention model is taken into account which includes the evolution of water retention curve (WRC) with changes of void ratio. An elasto-plastic constitutive model is employed within the context of bounding surface plasticity theory for predicting the nonlinear behaviour of soil skeleton in saturated and unsaturated porous media. The model is validated by comparing the numerical predictions with experimental or numerical data from the literature for fully and partially saturated soils. The results demonstrate the capability of the proposed numerical framework to predict essential characteristics of variably saturated soils.

ACKNOWLEDGEMENTS

First and foremost, I would like to express my sincere gratitude and appreciation to Dr Arman Khoshghalb, whom I am deeply indebted to for his unconditional support and indispensable guidance during the course of my studies. I could not have asked for a more decent, friendly, and understanding person as my supervisor. My deepest appreciation also goes to my co-supervisor, Professor Nasser Khalili for his encouragement, technical guidance, and provision of financial support during my candidature. The financial assistance received through the receipt of a Tuition Fee Scholarship is also gratefully acknowledged.

Heartfelt love and gratitude goes to my mother, father, and brother Ehsan. I have always felt the warmth of their love and support despite the long geographical distance between us.

Thanks are also extended to my friends and colleagues in the geotechnical group at UNSW each of whom was a great help to me, especially Arash for his support and invaluable technical consultation, and Golnaz for her help with the plasticity model used in Chapter 6. I would also like to show my appreciation to Dr Mohammad Vahab and Dr Babak Shahbodaghkhan for the time they gave me and for the discussions we had.

I am also indebted to Dr Majidreza Nazem for the helpful communication and assistance.

Lastly, thankyou to Armity for always being there for me.

LIST OF PUBLICATIONS

This thesis is submitted in fulfilment of the requirements for the Doctor of Philosophy at the University of New South Wales, Sydney. The work described in the thesis was carried out by the candidate during the years 2014 to 2018. Some of the work described in this thesis has been submitted or published in journals or presented at conferences as follows:

- Ghaffaripour, O., Khoshghalb, A. & Khalili, N. 2017. An edge-based smoothed point interpolation method for elasto-plastic coupled hydro-mechanical analysis of saturated porous media. *Computers and Geotechnics,* 82(99-109).
- Ghaffaripour, O., Khoshghalb, A. “An efficient meshfree method for consolidation analysis of elastoplastic porous media”, 6th Biot Conference on Poromechanics, 9-13 July 2017, Paris, France.
- Ghaffaripour, O., Khoshghalb, A. “A smoothed finite element method for elastoplastic flow and deformation analysis of porous media”, 3rd Australian Conference on Computational Mechanics, 12-14 February 2018, Geelong, Australia.
- Ghaffaripour, O., Khoshghalb, A. “A robust numerical technique for analysis of coupled problems in elasto-plastic porous media”, 9th European Conference on Numerical Methods in Geotechnical Engineering, 25-27 June 2018, Porto, Portugal.
- Ghaffaripour, O., Khoshghalb, A., Esgandani, G., A. “Fully coupled elastoplastic hydro-mechanical analysis of unsaturated porous media using a meshfree method”, Submitted to *International Journal for Numerical and Analytical Methods in Geomechanics*.

Table of Contents

List of Figures

List of Tables

List of Acronyms

BBM	Basic Barcelona Model
BSM	Bounding Surface Model
CCP	Code Comparison Principle
CFD	Computational Fluid Dynamics
CPT	Cone Penetration Test
CSFEM	Cell-based Smoothed Finite Element Method
CSL	Critical State Line
CSPIM	Cell-based Smoothed Point Interpolation Method
DEM	Discrete Element Method
DSM	Direct Stiffness Method
EFG	Element Free Galerkin
EFGM	Element Free Galerkin Method
ESFEM	Edge-based Smoothed Finite Element Method
ESPIM	Edge-based Smoothed Point Interpolation Method
FDM	Finite Difference Method
FE	Finite Element
FEM	Finite Element Method
FPM	Finite Point-set Method
FSI	Fluid-Structure Interaction
GS-Galerkin	Gradient Smoothed Galerkin
LICL	Limiting Isotropic Compression Line
MEM	Maximum-Entropy Meshless
MLPG	Meshless Local Petrov-Galerkin
MLS	Moving Least Square

MM	Meshfree Method
MMS	Method of Manufactured Solutions
MPM	Material Point Method
MQ	Multi Quadrics
MS	Manufactured Solution
NSFEM	Node-based Smoothed Finite Element Method
NSPIM	Node-based Smoothed Point Interpolation Method
PDE	Partial Differential Equation
PFEM	Particle Finite Element Method
PIM	Point Interpolation Method
PPIM	Polynomial Point Interpolation Method
PSC	Plain Strain Compression
PVP	Parametric Variational Principle
RBF	Radial Basis Function
RKPM	Reproducing Kernel Particle Method
RPIM	Radial Point Interpolation Method
SFEM	Smoothed Finite Element Method
SFG	Sheng-Fredlund-Gens
SPH	Smoothed Particle Hydrodynamics
SPIM	Smoothed Point Interpolation Method
TL	Total Lagrangian
TPS	Thin Plate Spline
T-Schemes	Supporting node selection schemes using the Triangular elements
UL	Updated Lagrangian
V&V	Verification and Validation
W^2	Weakened Weak
WRC	Water Retention Curve

List of Symbols

1. Latin Letters

a_{11}, a_{22}	Apparent compressibilities of water and air phases
a_{12}, a_{21}	Coupling terms relating the pore water and pore air volumetric deformations due to change in matric suction
a_{f}	Apparent compressibility of fluid phase
a_i, b_i	Components of $\mathbf{a}$ and $\mathbf{b}$
A	A material constant in the BSM
A_{c}	Cross section area of specimen normal to the direction of flow
A_k^{SD}	Area of the k th smoothing domain
A_i^{tr}	Area of the sub-triangle hosting the i th Gauss point
A, B, C	Coefficients used in the three- point time discretisation scheme
b_{i_j}	Components of $\widehat{\mathbf{B}}_1$, $\widehat{\mathbf{B}}_2$, $\widehat{\mathbf{B}}_3$
c	Drained compressibility of the solid skeleton
c'	Drained cohesion
c_{u}	Undrained cohesion
c_{s}	Solid grains coefficient of compressibility
c_{f}	Fluid phase coefficient of compressibility
c_{w}	Coefficient of compressibility of water
c_{a}	Coefficient of compressibility of air
d	Plastic dilatancy
d_{c}	Local average nodal spacing
e	Void ratio

e_c	A shape parameter for obtaining different RBFs
eps	A small positive number for controlling the error in Newton-Raphson iterations
E'	Effective Young's modulus
E_u	Undrained Young's modulus
E_{ij}^{L}	Discretisation error at i th spatial discretisation and j th time discretisation
f	Random function / Field variable
F	Yield surface in Chapter 5 / Bounding surface in Chapter 6
g	Gravitational acceleration
G	Plastic potential
$G_{j,i}$	Components of $\mathbf{G}$
h	Normalized spatial discretisation size in Chapter 4 / Hardening parameter in Chapters 5 and 6
h_b	Hardening modulus at the bounding surface in the BSM
h_f	Additive hardening modulus at the loading surface in the BSM
H	Thickness of soil layer
J_3	Third stress invariant of deviatoric stress tensor
k	Intrinsic permeability
k_f	Coefficient permeability of fluid phase
k_{rw}	Relative permeability of water
k_{ra}	Relative permeability of air
$k_{w_{sat}}$	Water permeability coefficient in saturated state
$k_{a_{dry}}$	Air permeability coefficient in dry state
k_m	A material constant in the BSM
l	Number of monomials used in polynomial basis functions
L_m^k	Length of the m th segment of the k th smoothing domain

L_2	Second norm
L_∞	Infinity norm
M	Average molecular mass of air
M_{cs}	Slope of the CSL in $q' - p$ plane
$M_{\max}$	Slope of the CSL in $q' - p$ plane for triaxial compression
$M_{\min}$	Slope of the CSL in $q' - p$ plane for triaxial extension
n	Porosity
n_{w}	Porosity of the water phase
n_{a}	Porosity of the air phase
n_1, n_2	Components of the unit outward normal
n_{e}	Number of triangular elements
n_{n}	Number of nodes
n'_{n}	Total number of field nodes on which no essential boundary condition is applied
n_{SD}	Number of smoothing domains
n_{seg}	Number of line segments of the boundary of a smoothing domain
n_{G}	Number of Gauss points on each segment of the boundary of a smoothing domain
N	Specific volume at the reference mean effective stress of $p' = 1\mathrm{kPa}$
O	Higher order error term in spatial and temporal discretisations
p	Number of supporting nodes for a point of interest
p_{f}	Pore fluid pressure
p_{w}	Pore water pressure
p_{a}	Pore air pressure
p_0	A variable controlling the size of the plastic potential in the BSM
p_{atm}	Atmospheric air pressure

p' Mean effective stress

p'_{c} Preconsolidation (yield) stress

p'_{cs} Mean effective stress at the critical state

P_{a} Absolute air pressure

P_i Polynomial basis functions

q Total number of supporting nodes of all the Gauss points on the boundaries of a smoothing domain in Chapter 3 / Deviatoric stress in Chapters 5 and 6

q_{c} A shape parameter for obtaining different RBFs

q_{f} Imposed fluid flux across the boundary

Q Surface surcharge

r_{h} Observed order of accuracy for spatial discretisation

r_i Distance between the point of interest and the node of interest

R Ratio between element sizes of two consecutive meshes in Chapter 4 / Universal air constant in Chapter 6 / A parameter of the BSM in Chapter 6

R_i Radial basis functions

s Matric suction

s_{e} Air entry / Air expulsion suctions at the transition between saturated and unsaturated states

s_{ae} Air entry value

s_{ex} Air expulsion value

s_{rd} Point of suction reversal on the main drying curve

s_{rw} Point of suction reversal on the main drying curve

s_{x} , s_{y} , s_{z} Subtraction of the mean effective stress from the normal stresses

S_{r} Degree of saturation

S_{eff} Effective degree of saturation

S_{res} Residual degree of saturation

t	Time
t_{D}	Dimensionless time
$\tilde{t}$	A parameter which determines the direction of plastic flow in the BSM
T	Absolute temperature
u_1, u_2	Components of displacement vector in x and y directions
u_{ult}	Ultimate surface settlement
U_{z}	Degree of consolidation
V	Total volume
V_{v}	Volume of void
V_{w}	Volume of water phase
V_{a}	Volume of air phase
V_{ch}	Volume of chamber in 1D hydraulic pulse test
w_{G}	Gauss integration weight
w_i^{a}	Components of $\mathbf{w}^{\mathrm{a}}$
w_i^{n}	Components of $\mathbf{w}^{\mathrm{n}}$
W	Domain width
x, y	Space coordinates

2. Greek Letters

α	Time step growth factor / A parameter used in the BSM in Chapter 6
α_{c}	Shape parameter for obtaining different RBFs
β_{h}, β_{t}	Coefficients of spatial and temporal discretisations
γ	Soil unit weight
γ_{f}	Fluid unit weight

Γ	Intercept of the CSL at the reference mean effective stress of $p' = 1\text{kPa}$
Γ_k^{SD}	Boundary of the k th smoothing domain
δ_1, δ_2	Parameters for obtaining relative permeabilities
ε_{v}	Volumetric strain
$\varepsilon_{\mathrm{q}}^{\mathrm{p}}$	Deviatoric plastic strain
$\varepsilon_{\mathrm{v}}^{\mathrm{p}}$	Volumetric plastic strain
ζ	Slope of the scanning curve in $\ln\chi - \ln s$ plane
η	Biot's constant
η_{p}	Slope of the peak strength in the $q' - p$ plane
θ	Lode angle
Θ	A parameter used for obtaining the dimensionless time in 1D hydraulic pulse test
κ	Slope of the unloading-reloading line in the $\upsilon - p'$ plane
λ	Slope of the CSL in the $\upsilon - p'$ plane
λ_{p}	Pore size distribution index
λ_{pd}	Slope of main drying curve in $\ln S_{\mathrm{eff}} - \ln s$ plane
λ_{pw}	Slope of main wetting curve in $\ln S_{\mathrm{eff}} - \ln s$ plane
λ_{psu}	Pore size distribution index at the transition point from saturated to unsaturated state
μ_{a}	Dynamic viscosity of air
μ_{f}	Dynamic viscosity of fluid phase
μ_{w}	Dynamic viscosity of water
ν'	Effective Poisson's ratio
ν_{u}	Undrained Poisson's ratio
ξ	Slope of the scanning curve in $\ln S_{\mathrm{eff}} - \ln s$ plane
ρ	Average density of the mixture

ρ_{a}	Density of air
ρ_{f}	Density of fluid phase
ρ_{s}	Density of solid phase
ρ_{w}	Density of water
σ'_{x}, σ'_{y}, σ'_{y}	Components of effective normal stress
ς	Integration variable
τ	Normalized temporal discretisation size
τ_{xy}, τ_{yz}, τ_{zx}	Components of shear stress
υ	Specific volume
υ_{cs}	Critical state specific volume
υ_{LICL}	Specific volume on the LICL
φ_i	Components of $\mathbf{\Phi}^{\mathrm{u}}$ and $\mathbf{\Phi}^{\mathrm{p}}$
ϕ'	Drained friction angle
ϕ'_{cs}	Constant volume effective friction angle
ϕ_{u}	Undrained friction angle
χ	Effective stress parameter
ψ	Incremental effective stress parameter
ψ'	Drained dilation angle
Ψ	Suction hardening function
ω	Loading rate
Ω	Total problem domain / Material parameter for obtaining the effective stress parameter in Chapter 6
Ω_k^{SD}	Domain of the k th smoothing domain
$\boxed{\Omega}_k^{\mathrm{SD}}$	Representation of a closed smoothing domain

3. Matrices and Vectors

$\mathbf{a}$, $\mathbf{b}$	Coefficient vectors for obtaining the polynomial and radial PIM shape functions
$\mathbf{B}$	Vector of body force per unit mass
$\hat{\mathbf{B}}$	Strain-displacement matrix
$\widehat{\mathbf{B}}_1$, $\widehat{\mathbf{B}}_2$, $\widehat{\mathbf{B}}_3$	Smoothed strain-displacement matrices
$\mathbf{D}^{\mathrm{e}}$	Elastic constitutive matrix
$\mathbf{D}^{\mathrm{ep}}$	Elasto-plastic constitutive matrix
$\mathbf{f}$	Vector storing the values of field function
$\mathbf{F}$	Vector of body forces per unit volume
$\mathbf{F}_{\mathrm{a}}$	Vector of nodal air fluxes
$\mathbf{F}_{\mathrm{f}}$	Vector of nodal fluid fluxes
$\mathbf{F}_{\mathrm{u}}$	Vector of nodal forces
$\mathbf{F}_{\mathrm{w}}$	Vector of nodal water fluxes
$\mathbf{g}$	Gravity acceleration vector
$\mathbf{G}$	Moment matrix
$\mathbf{H}$	Fluid permeability matrix
$\mathbf{H}_{\mathrm{w}}$	Water permeability matrix
$\mathbf{H}_{\mathrm{a}}$	Air permeability matrix
$\mathbf{I}$	Identity matrix
$\mathbf{J}$	Jacobian matrix
$\mathbf{k}$	Intrinsic permeability matrix
$\mathbf{K}$	Stiffness matrix
$\mathbf{K}_{\mathrm{T}}$	Tangent stiffness matrix
$\mathbf{L}_{\mathrm{d}}$	Differential operator matrix
$\mathbf{L}_{\mathrm{n}}$	Matrix of unit outward normal
$\mathbf{m}$	Unit vector normal to the plastic potential

$\mathbf{n}$	Unit vector normal to the yield surface and
$\mathbf{P}$	Vector of polynomial basis functions
$\mathbf{P}_a$	Vector of the nodal pore air pressures
$\mathbf{P}_f$	Vector of the nodal pore fluid pressures
$\mathbf{P}_w$	Vector of the nodal pore water pressures
$\mathbf{Q}$	Coupling matrix
$\mathbf{R}$	Vector of radial basis functions
$\mathbf{R}_0$	RBFs moment matrix
$\mathbf{S}$	Compressibility matrix
$\mathbf{T}$	Vector of boundary tractions
$\mathbf{u}$	Displacement vector of solid phase
$\mathbf{u}_a$	Displacement vector of air phase
$\mathbf{u}_f$	Displacement vector of fluid phase
$\mathbf{u}_w$	Displacement vector of water phase
$\hat{\mathbf{u}}$	Compatible displacement vector
$\mathbf{v}_a$	Absolute velocity of air phase
$\mathbf{v}_{as}$	Relative velocity vector for the air phase with respect to a moving solid
$\mathbf{v}_f$	Absolute velocity of fluid phase
$\mathbf{v}_{fs}$	Relative velocity vector for the fluid phase with respect to a moving solid
$\mathbf{v}_s$	Absolute velocity of solid phase
$\mathbf{v}_w$	Absolute velocity of water phase
$\mathbf{v}_{ws}$	Relative velocity vector for the water phase with respect to a moving solid
$\mathbf{w}^a$	Vector of analytical solution for the state variable of interest
$\mathbf{w}^n$	Vector of numerical solution for the state variable of interest
$\tilde{\mathbf{W}}$	Diagonal matrix of smoothing functions

$\mathbf{x}$	Vector of space coordinates
$\mathbf{X}$	Vector of nodal displacement and pore pressures
$\boldsymbol{\delta}$	Identity vector
$\boldsymbol{\varepsilon}$	Strain vector
$\widehat{\boldsymbol{\varepsilon}}_k$	Smoothed strain vector over the k th smoothing domain
$\hat{\boldsymbol{\varepsilon}}$	Compatible strain vector
$\boldsymbol{\varepsilon}^{\mathrm{a}}$	Vector of strains obtained from analytical solution
$\boldsymbol{\varepsilon}^{\mathrm{n}}$	Vector of strains obtained from numerical solution
$\boldsymbol{\sigma}$	Total stress vector
$\boldsymbol{\sigma}'$	Effective stress vector
$\boldsymbol{\sigma}_{\mathrm{net}}$	Net stress vector
$\boldsymbol{\Phi}^{\mathrm{u}}$	Shape function matrix for displacement phase
$\boldsymbol{\Phi}^{\mathrm{p}}$	Shape function vector for fluid phase
$\boldsymbol{\Psi}_{\mathrm{u}}$, $\boldsymbol{\Psi}_{\mathrm{f}}$, $\boldsymbol{\Psi}_{\mathrm{w}}$, $\boldsymbol{\Psi}_{\mathrm{a}}$	Residual vectors
∇	Gradient operator vector

Chapter 1

1. Introduction

1.1. Background

Predicting the response of porous media under various mechanical, hydraulic or thermal loading conditions has been a major interest in geotechnical engineering, as well as in many other strands such as material science, petroleum industry, and chemical and biomedical engineering. Geotechnical problems, however, can be very complicated in nature. One of these complexities is the effect of one or multiple fluids flowing through porous bodies which necessitates consideration of the interaction between solid and fluid phases. Another complication is the nonlinear response of geomaterials, called material nonlinearity. A great number of nonlinear constitutive models, from the simple elastic perfectly plastic Mohr-Coulomb model to very advanced models have been introduced and evolved through time for various types of geomaterials.

Following the assumptions of continuum mechanics concept, the hydro-mechanical behaviour of variably saturated porous media can be evaluated through the theory of mixtures, in which the porous medium is considered as a uniformly distributed combination of different constituents in a representative porous volume: Solid skeleton, and saturating fluids which are naturally observed as water, air, different types of gases, and oil products. The coupled effect of solid deformation and fluids flow is captured through applying the axioms of mechanics and thermodynamics to different mixture components. The modern concept of theory of mixtures was established by Fillunger (1936) who formulated the balance of mass and momentum for a volume fraction as the fundamental of porous media theory. The mixture theory was further developed by Biot (1956) for two-phase porous media for quasi-static and dynamic analyses. Following the same approach, and applying essential behavioural assumptions depending on the fluid components, the theory of mixtures can be generalised to flow and deformation behaviour of multi-phase porous media. Firstly, the deformation of the solid phase is expressed using the condition of equilibrium on a representative porous volume, which is stated by the linear momentum balance equation for the stated volume. Secondly, the fluid flow in porous media is modelled using a combination of the equation of linear momentum balance for the fluid phase with the mass balance equation of the fluid.

The governing equations for the problems of interest derived from the theory of mixtures are often complicated. Due to this complexity and also various sources of nonlinearity, it is very difficult, if not impossible, to generate exact solutions for these equations unless in simple cases. Basically, there are two approaches available to solve the governing equations: first, making simplifying assumptions and solve the equations analytically and second, providing approximations adopting a proper numerical technique. Since the introduction of the finite difference method (FDM) in 1600's, this direct method paved the way for numerical simulation of problems with simple geometries. From the mid years of the past century, the widely used finite element method (FEM) has been the major tool for tackling engineering problems numerically, among them is the coupled flow and deformation analysis of porous media. Despite its popularity and excellent performance in many problems, the FEM suffers from inherent shortcomings some of which are as follow: Overly stiff behaviour; strong reliance on the quality of the mesh; poor performance when triangular elements are in application; poor stress solutions on element interfaces; difficulties when dealing with large deformation, material breakage, and crack propagation; volumetric locking; and difficulties in adaptive analysis.

With the aim of addressing the shortcomings of the FEM, meshfree methods (MMs) were developed as early as 1970’s and particularly over that past three decades, and have achieved remarkable progress due to their advantages over the classical FEM. MMs are mesh independent (or less mesh dependent in some MMs) and therefore more flexible, and also more capable of handling changing geometries. Numerous MMs have been so far proposed, the first of which being the smoothed particle hydrodynamics (SPH) introduced in 1970’s by Lucy (1977) and Gingold and Monaghan (1977). SPH was followed by many other MMs including (to name a few) the element-free Galerkin methods (EFGM) (Belytschko et al., 1994), reproducing kernel particle methods (RKPM) (Liu et al., 1995), the meshless local Petrov-Galerkin (MLPG) (Atluri and Zhu, 1998), the polynomial point interpolation method (PPIM) (Liu and Gu, 2001) and the Radial point interpolation method (RPIM) (Wang and Liu, 2002b), and more recently the smoothed point interpolation methods (SPIMs) (Liu et al., 2005; Liu and Zhang, 2008; Liu and Zhang, 2009).

The first study on the application of MMs to coupled flow and deformation of saturated porous media was performed by Modaressi and Aubert (1995) through a combination of the EFGM and the FEM. Since then, numerous other studies have been conducted in attempts to benefit from the superior properties of MMs in different geotechnical problems such as two-dimensional contaminant transport through saturated porous media (Kumar and Dodagoudar, 2008), prediction of subsidence over compacting reservoirs (Zhuang et al., 2012), bearing capacity of strip and circular footings (Kardani et al., 2017), consolidation analysis in saturated porous media (Samimi and Pak, 2012; Nazem et al., 2016), soil collapse and erosion processes in excavations (Bui et al., 2006), and analysis of slope stability and discontinuities (Bui et al., 2011).

However, many of the employed MMs suffer from different shortcomings. MMs often employ non-polynomial functions (Dolbow and Belytschko, 1999a). Moreover, the imposition of essential boundary conditions in MMs may be complicated by the difficulties that arise from the lack of Kronecker delta properties (in EFGM and MLPG), which leads to the significant level of computation in MMs (Liu, 2010a). PPIM was proposed to circumvent this problem; however, the non-singularity associated with the creation of polynomial interpolation functions is not guaranteed in this method. Moreover, in PPIM and RPIM, the approximation functions violate continuity across a problem field. A penalty method was used to induce a continuous approximation instead of the discontinuous approximation produced by PPIM and RPIM, but the increase in computational costs are preventive due to the enlarged bandwidth of the attained algebraic system (Liu, 2010a).

SPIMs are the evolved forms of PPIM and RPIM based on the concept of weakened weak (W^2) formulation in which a generalised smoothing gradient operation is performed to form a smoothed and constant strain over parts of the domain, called smoothing domains. Smoothing domains can be constructed based on either nodes, cells, or edges of a background mesh yielding three different SPIM formulations known as NSPIM, CSPIM, and ESPIM, respectively. In SPIMs, background mesh is still in need for performing the numerical integrations. However, unlike the FEM, the numerical solution is not heavily dependent on the quality of the background mesh, and a simple triangular mesh is often sufficient to ensure accuracy of the numerical solutions. SPIMs have some excellent properties such as ultra-accuracy and super convergence, and no mapping is required in their formulation while performing the numerical implementations, circumventing many of the problems involved with other MMs. SPIMs were originally proposed for applications in solid mechanics and were later applied in other disciplines.

1.2. Problem Statement

Despite the outstanding performance of SPIMs, their applications in geotechnical engineering problems have, so far, been very limited. A few coupled formulations which are proposed in this regard suffer from mathematical inaccuracies. The majority of the works available in the literature in applying SPIMs in coupled flow and deformation analysis of porous media are due to Delfim Soares Jr and his co-workers (Schönewald et al., 2012; Soares Jr, 2013b; Soares Jr et al., 2014). Nonetheless, the approach they have adopted in developing their numerical framework is not mathematically rigorous. This is because they adopted an approximation technique for calculation of the coupling matrix of the discretised system of equations in the sense that they used Gauss points located on the boundary on the smoothing domains, rather than conventional Gauss points, for the calculation of the area integrations over the smoothing domains. This approach introduces errors in the calculations, which can be controlled only by refining the background mesh, because adopting more Gauss points for the area integrations is not practical in their approach. It is essential to come up with a better solution for employing SPIMs in coupled problems.

Once a computational scheme is developed, it has to be validated and verified. Validation provides credibility for the correctness of the solution to the chosen system of equations, whereas verification refers to a procedure for making sure that the right equations are targeted to be solved. Validation and verification are each of great importance and should be performed independently for any numerical model developed; however, these two are often mixed up in geotechnical engineering.

The most powerful code verification criterion is the order of accuracy test which examines the convergence rate of the numerical solution, together with the reduction rate of discretisation error as mesh size decreases. This rate is compared with the so-called formal order of accuracy which is a property of the numerical model of interest. There are different approaches to perform the order of accuracy test, the most popular one being benchmarking a code against a few examples with analytical solutions. However, there are not many problems whose analytical solutions are available, and in many cases, the analytical solutions are proposed for simplified versions of problems. This problem necessitates the introduction of a more general verification procedure to be used in problems associated with multi-phase porous media.

SPIMs have been rarely exploited in problems with material nonlinearity. A few works in this field include application of NSPIM to elastoplastic analysis of two-dimensional single-phase materials with gradient-dependent plasticity by Zhang et al. (2015), and studies on nonlinear dynamic analysis of solids and saturated porous media by Soares Jr (Soares Jr, 2013a; Soares Jr, 2013b). The former is presented for single-phase media, and the latter works, contain inaccuracies in implementation of the SPIMs as mentioned earlier. It is, therefore, desirable to develop SPIM formulation for the flow and deformation analysis of elasto-plastic saturated porous media to exploit their full potentials in improving currently available numerical methods.

Despite their outstanding properties, there have been very limited applications of MMs, and no application of SPIMs in particular, in modelling of unsaturated porous media. Furthermore, in many cases, inaccurate formulations have been assumed for flow and deformation analysis of unsaturated soils (Lewis et al., 1998; Sheng et al., 2003a; Tang et al., 2017). The source of inaccuracies include (but not limited to) overlooking the effective stress principle which governs the hydromechanics of unsaturated porous media (Khalili et al., 2004), assumption of linear elasticity, overlooking the effect of hydraulic hysteresis, and over-simplification in modelling the water retention curve (WRC). The current literature is short of an all-inclusive robust formulation for coupled flow and deformation analysis of unsaturated porous media using an efficient MM.

1.3. Thesis Structure

To address the above mentioned shortcomings in the literature, this thesis is prepared in seven Chapters with the following structure:

Chapter 2 contains a comprehensive overview of the available literature on MMs and specifically SPIMs and their applications in geomechanics, followed by a study on the available literature on numerical modelling of unsaturated porous media, and finally a review of the current research on validation and verification techniques and their applications in geomechanics

In Chapter 3, an ESPIM formulation is proposed for coupled flow and deformation analysis of saturated porous media which evaluates the coupling and compressibility matrices very accurately compared to the previous research in this area.

In Chapter 4, the method of manufactured solutions (MMS) which is routinely applied in computational fluid dynamics (CFD), is used for verifying the developed coupled SPIM code in Fortran. This is then followed by a comprehensive order of accuracy test.

A nonlinear framework is proposed in Chapter 5 for elastoplastic modelling of coupled flow and deformation in saturated porous media. The modified Newton-Raphson and sub-stepping stress integration scheme are used in the numerical algorithm.

In Chapter 6, the developed nonlinear SPIM algorithm is further evolved to capture the coupled hydro-mechanical behaviour of unsaturated porous media. A framework based on the effective stress principle is followed in the formulation and a hysteretic water retention model is taken into account which enables the evolution of the WRC and other soil parameters with changes in void ratio. A bounding surface constitutive model is also adopted in the model which enables more realistic numerical simulations.

Chapter 7 provides a summary and conclusions, along with recommendations for further research.

Chapter 2

2. Literature Review

2.1. Introduction

In this chapter, the existing literature relating to the meshfree methods and smoothed point interpolation methods (SPIMs) in particular, and their applications in modelling the coupled hydro-mechanical linear and nonlinear behaviour of saturated and unsaturated porous media will be reviewed. A brief introduction will be presented on mechanics of unsaturated soils, with a review of the most recent numerical studies in this field. Furthermore, an overview of the common methods for validation and verification purposes in code development will be discussed, and the available literature on the application of the method of manufactured solutions (MMS) will be presented.

2.2. An overview of the meshfree methods

Numerical methods have been extensively in use since the advent of computer technology in the past century in order to solve rather complex engineering problems by solving the relevant partial differential equations. There are generally three classical families of numerical techniques: The finite difference method (FDM) which is one of the first numerical approaches to solve partial differential equations, followed by finite volume method and consequently the much more efficient finite element method (FEM). These families are common in employing a mesh and also in using local approximations by polynomials (Babuška et al., 2003). Among these three, FEM, which is developed based on the direct stiffness method (DSM) proposed by Turner (1959), is the most extensively developed numerical tool which has been used widely in the past fifty years to solve miscellaneous problems in engineering, including problems related to hydromechanics of porous media (Lewis et al., 1998; Lewis and Schrefler, 1999; Potts and Zdravkovic, 2001; Sheng et al., 2003a; Khosrojerdi and Pak, 2015). Although FEM is an efficient technique in the majority of the applications, there are some limited yet important problems which are not well-suited to FEM. Some of the limitations of FEM are as follows (Liu, 2010a; Zeng and Liu, 2016):

- The underlying structure of FEM makes it strongly reliant on a quality mesh whose generation is computationally expensive. Usually, the triangular meshes that are readily generated are not of enough quality, especially in problems with complex or time-dependent geometries.
- The FEM shows an overly stiff behaviour, leading to a lower bound to the exact solution of the engineering problems.
- FEM lacks accuracy when triangular and tetrahedral elements are in use in 2D or 3D settings, respectively. This is mainly due to the overly stiff behaviour resulted from fully compatible Galerkin weak form.
- In problems containing extremely large deformations, FEM is difficult to implement and often involves accuracy degradation. FEM is not able to deal with mesh distortions easily.
- FEM involves poor stress solutions on element interfaces.

- It is difficult to simulate crack propagation using FEM because of the discontinuities that do not usually coincide with the original element interfaces. Besides, it is very costly to design re-meshing approaches in FEM to overcome this difficulty, especially in 3D problems in which FEM becomes almost unusable for crack propagation problems.
- The original FEM suffers from volumetric locking phenomenon which reduces the accuracy of solutions significantly when dealing with incompressible materials, i.e. when Poisson's ratio approaches 0.5.

Meshfree methods (MMs) were introduced in 1970's to overcome at least part of these drawbacks by eliminating part of FEM structure and constructing the approximations entirely based on nodes (Belytschko et al., 1996). MMs have been used increasingly in the past two decades and have undergone remarkable progress due to their distinct features. Unlike in FEM, defining the problem domain in MMs can be independent of any predefined mesh, and a set of arbitrarily distributed field nodes which are scattered within the problem domain along with a set of field nodes located on the boundaries of the domain can represent the problem domain. The field variables at any node inside the problem domain is approximated using the shape functions of the field nodes within a local support domain, relating the value of field variables at any point of interest to the value of the variable at the field nodes. Following this philosophy, a large quantity of MMs have been developed since the starting point in 1970's. Although MMs are generally slower than FEM in terms of computational speed, they have some superiorities over FEM such as better adaptability and accuracy, and more flexibility in handling changes in geometry.

The first MM which is referred to as the smoothed particle hydrodynamics (SPH) was introduced in 1970's by Lucy (1977) and Gingold and Monaghan (1977) to solve boundaryless problems in astrophysics and astrodynamics, such as exploding stars and dust clouds. Later, Libersky et al. (1993) exploited SPH for the first time in solid mechanics to demonstrate the application of the method in this field. Although SPH attracted very limited attentions for years, this early technique was later followed by a number of MMs in 1990's. Nayroles et al. (1992) were the first researchers to use moving least square (MLS) approximations in a Galerkin method named the diffuse element method (DEM). DEM was later received modifications by Belytschko et al. (1994), resulting in the introduction of the element-free Galerkin methods (EFGM). These MMs were followed by the reproducing kernel particle methods (RKPM) proposed by Liu et al. (1995), although the two type of MMs share striking similarities. EFGM is one of the first and most popular MMs which have been used to model coupled problems in saturated porous media. In EFGM, the nodal shape functions are constructed based on the MLS technique which makes satisfying the essential boundary conditions difficult due to lack of the Kronecker delta criterion. Furthermore, the MLS approximation involves complicated algorithms for computing shape functions which lead to high computational cost. Another MM which has been used recently in different engineering application is the Maximum-Entropy Meshless (MEM) method. This MM borrows the concept of entropy from information theory as a measure of uncertainty to form non-unique shape functions (Sukumar, 2004).

MMs can be adapted on local weak forms and formulated on overlapping subdomains rather than global weak forms. The meshless local Petrov-Galerkin (MLPG) is one of the well-suited local MMs (Atluri and Zhu, 1998) in which the numerical integration is performed on overlapping subdomains resulting in a truly "meshfree" method because no background mesh is required to perform numerical integration. In MLPG, implementation procedure is quite simple and comparable to numerical methods based on strong form, and also no shape function compatibility is required. However, the method is less computationally efficient than the global weak form MMs and also FEM because of numerous parameters and asymmetric stiffness matrix (Liu and Gu, 2005).

Most MMs require a background mesh to perform numerical integrations. Performing numerical integration in MMs often necessitates assigning more quadrature points, compared to FEM, to produce solutions with adequate accuracy since MMs often employ non-polynomial functions (Dolbow and Belytschko, 1999a).

The imposition of essential boundary conditions in MMs is complicated when the Kronecker delta property is lacking in the shape functions, resulting in a significant level of computation in MMs (Liu, 2010a). To address this difficulty, the point interpolation methods (PIM), Polynomial PIM (PPIM) and radial PIM (RPIM), were formulated by Liu and Gu (2001) and Wang and Liu (2002b), respectively. In the PPIM, the basis functions which are used to approximate unknowns at the field nodes are constructed using polynomials resulting in shape functions that possess delta function property. Therefore, the essential boundary conditions can be easily implemented in this MM. Besides, the complexity in obtaining the shape functions, which is one of EFGM's difficulties, is eliminated using the PPIM. Wang and Liu (2002b) developed the RPIM in which radial basis functions (RBFs) with dimensionless shape parameters are used to construct the shape functions. The main purpose of introducing the RPIM was to overcome the singularity problem of the PPIM method. However, the rigorousness of the both methods is questionable because the compatibility of the approximation function in the whole domain of the problem is violated when PPIM or RPIM shape functions are used (Liu et al., 2004). Moreover, in PPIM and RPIM, the approximation functions violate continuity across a problem field. A penalty method has been suggested to induce a continuous approximation instead of the discontinuous approximation produced by PPIM and RPIM, but the increase in computational costs are preventive due to the enlarged bandwidth of the attained algebraic system (Liu, 2010a).

2.3. Smoothed point interpolation methods

In order to circumvent the problems associated with the PIMs, a novel category of MMs were proposed by Liu and his co-workers (Liu et al., 2005; Liu and Zhang, 2013a; Liu, 2010b; Liu and Zhang, 2008). This new approach is based on the G space theory (Liu and Zhang, 2013a) in which both continuous and discontinuous functions are included, and the generalized gradient smoothing technique (Liu and Zhang, 2013a) is applied to the PPIM and the RPIM, resulting in a new class of MMs known as the smoothed point interpolation methods (SPIMs). In SPIMs, the problem associated with the incompatibility of the displacement field is avoided by adopting a constructed, rather than a compatible, strain field and therefore removing the need for calculation of the derivation of the shape functions. SPIMs can be thought as a combination of MMs and FEM, combining the specific strengths of both methods. In SPIMs, background mesh is still needed for performing the numerical integration; however, unlike the FEM, the numerical solution is not heavily dependent on the quality of the background mesh, and a simple triangular mesh is often sufficient to ensure accuracy of the numerical solutions. The stability and convergence of the proposed methods were mathematically proven by the rigorous properties established by the G space theory (Liu, 2009; Liu and Zhang, 2013b) . Depending on the procedure through which the integration domains, or the so-called smoothing domains, are constructed within the problem domain, SPIMs are divided into three different categories: Edge-based SPIM (ESPIM) (Liu and Zhang, 2008), cell-based SPIM (CSPIM) (Liu and Zhang, 2009), and finally node-based SPIM (NSPIM) (Liu et al., 2005).

Unlike the overly-stiff FEM, SPIMs have properly softened stiffness which gives them a series of excellent properties including possibility of yielding upper bound energy solution, super convergence, accuracy of stress solutions, freedom from volumetric locking, and insensitivity to the quality of the background mesh (Zhang et al., 2007). To date, they have been employed in several fields of engineering such as solid mechanics (Liu et al., 2005; Liu et al., 2009a; Tang et al., 2012), heat transfer (Wu et al., 2010), and mechanics of porous media (Tootoonchi et al., 2016; Soares Jr et al., 2014) in recent years.

The strain smoothing technique has been also applied to the conventional FEM by Liu et al. (2007a) and Liu et al. (2007b), which was originally proposed by Chen et al. (2001), to eliminate spatial instability in nodal integration due to vanishing derivatives of shape functions. This is viewed as a robust way to address the difficulties associated with the conventional FEM. Applying the smoothing gradient technique to FEM results in smoothed FEM (SFEM), which yields a softened stiffness matrix compared to the original FEM, removing the occurrence of volumetric locking and other adverse consequences of overly-stiff behaviour of the conventional FEM such as under-estimation of displacements. SFEMs can be considered as special reduced versions of SPIMs, and in a similar fashion, have various forms, including the cell-based smoothed finite element method (CSFEM) (Liu et al., 2007a), the edge-based smoothed finite element method (ESFEM) (Liu et al., 2009a) and the node-based smoothed finite element method (NSFEM) (Liu et al., 2009b). Various theoretical aspects of SFEMs have been discussed in (Liu et al., 2007b; Nguyen-Xuan et al., 2008). Similar to SPIMs, the non-local information that is brought in from the neighbouring elements leads to more supporting nodes being involved in the creation of the shape functions in SFEMs, resulting in a larger bandwidth of the ensuing stiffness matrix in SFEMs compared to that of the original FEM. The capability of SFEMs in various fields has been demonstrated by applying them to several numerical problems in (Cui et al., 2008; Nguyen-Thoi et al., 2009; Nguyen-Xuan and Nguyen-Thoi, 2009; Nguyen-Xuan et al., 2008).

2.4. Applications of meshfree methods in geomechanics

This section is dedicated to reviewing the existing literature on meshfree numerical modelling in the field of geotechnical engineering, with emphasis on hydromechanics of porous media.

MMs have been used numerously for hydro-mechanical analysis of porous media. The first efforts to investigate the application of MMs in analysing the multiphase problems was made by Modaressi and Aubert (1995) by solving the consolidation problem in saturated soils using the EFGM. The nodal shape functions were constructed based on the MLS technique which makes satisfying the essential boundary conditions difficult due to lack of the Kronecker delta property. Later, to simulate the coupled hydro-mechanical behaviour of multiphase porous media, Modaressi and Aubert (1998) proposed a numerical approach in which displacement of the solid skeleton was approximated by the standard FEM and the fluid pore pressures were modelled using EFGM. Another similar study was performed by Murakami et al. (2000) in which the EFGM was employed for flow-deformation analysis of saturated porous media. Oliaei and Pak (2009) proposed a coupled Element Free Galerkin (EFG) formulation to simulate the consolidation process in saturated porous media, and also performed a study investigating the numerical issues related to utilisation of EFGM in conjunction with the hydro-mechanical analyses (Oliaei et al., 2009). Samimi and Pak (2012) later extended the formulation to three dimensions for analysis of saturated porous media, using the penalty method for imposition of essential boundary conditions and a fully implicit scheme for time discretisation. They evaluated the performance of their model by comparing its results with analytical solutions, and then analysed different consolidation problems in two and three dimensional settings with various loading and drainage conditions to demonstrate the applicability of their presented technique to practical problems. They later extended their three-dimensional formulation for analysis of two immiscible fluids flow through porous materials (Samimi and Pak, 2014). Oliaei et al. (2014) proposed a fully-coupled EFG formulation for the simulation of induced fractures in saturated porous media. This was followed by an improved form of EFGM, proposed by Samimi and Pak (2016). However, the numerical solutions obtained in the presence of discontinuities exhibited slight oscillations, as previously reported for solid mechanics applications (Dolbow and Belytschko, 1999a; Dolbow and Belytschko, 1999b). An enriched EFG formulation that incorporated weak discontinuities was proposed for both saturated and unsaturated porous media by Goudarzi and Mohammadi (2014) in order to restore the accuracy of the numerical solutions. The study was then extended, by Goudarzi and Mohammadi (2015), to simulate a strong discontinuity due to a jump in the primary variable (displacement) and to compute its proportional cohesive forces, inspired by the formulation proposed by in Rethore et al. (2007).

Wang et al. (2001) and Wang et al. (2002) showed the application of PPIM and RPIM to coupled flow-deformation analysis of saturated porous media, using the implicit and the Crank-Nicolson temporal discretization schemes. They showed that spurious ripple effect is observed in the numerical results when time step increments exceed a threshold in Crank-Nicolson temporal discretization scheme. They demonstrated that this effect is not observable when a fully implicit scheme is used in which much larger time steps can be chosen, compared to the acceptable time step range in Crank-Nicolson scheme. However, the fully implicit scheme possesses only first-order accuracy which makes the results less accurate. Wang et al. (2007) tried to alleviate the instability observed in their simulations using an unequal order RPIM; however, some of the numerical results they obtained were unreliable. For instance, the generated pore fluid pressure due to loading in a one dimensional consolidation problem was obtained greater than the applied load which is theoretically impossible.

To address this problem, Khoshghalb et al. (2011) proposed a novel three-point time discretization technique with variable time steps for the time marching of parabolic partial differential equations. This technique has second order accuracy and is oscillation free irrespective of the time step adopted, unlike the conventional Crank-Nicolson method. Khoshghalb and Khalili (2010) used this technique coupled with the RPIM to solve the Biot's formulation capturing the coupled flow-deformation behaviour of saturated porous media. They verified the accuracy of the results obtained using their proposed method by comparing them with analytical or semi-analytical solutions. It was shown that the spurious ripple effect associated with the Crank-Nicolson technique is completely removed when the three-point time discretisation technique is adopted in a MM framework. Khoshghalb and Khalili (2013) extended their previous work to develop a numerical solution for fully coupled flow-deformation problems in unsaturated porous media. They proposed their model using the three-point time discretization technique with growing time steps, Galerkin approach for spatial discretization, and the RPIM. The focus of their study was on determination of constitutive coefficients and effective stress parameters of the medium considering hydraulic hysteresis. Their model worked well in capturing the volume change and suction dependency of the model parameters as well as the coupled behaviour of unsaturated porous media subject to hydraulic hysteresis. Khoshghalb and Khalili (2015) also presented a large deformation formulation for coupled flow and deformation analysis of saturated porous media using the Updated Lagrangian (UL) approach, except that spatial derivations are defined with respect to the configuration of the medium at the last time step, rather than that at the last iteration. This approach facilitates the calculations eliminating the need for dealing with the second Piola-Kirchhoff stress tensor, and can speed up the calculations in some problems as derivative calculation is not required in each iteration. Moreover, a two-dimensional RPIM formulation of contaminant transport in saturated porous media was proposed by Kumar and Dodagoudar (2008) and was validated and verified using experimental, analytical, and FEM results.

The soil properties obtained from the laboratory results were verified through the adaptation of the MLPG method in a set of numerical simulation in studies presented by Sheu (2007). A modified MLPG was also adopted for dynamic analysis of saturated porous media (Soares et al., 2012), followed by an unequal MLPG formulation to supress the pressure oscillation that arises from the imposition of volumetric constraint (Soares Jr, 2010).

Soares Jr et al. (2014) employed ESPIM for dynamic **u**-*p* analysis of porous media using the generalized Newmark method for the time discretization. They constructed the triangular background mesh through a Delaunay triangulation, and took into account two different node selection schemes known as Tr3 and Tr6. They proposed a new approach to construct the mass, coupling, and compressibility matrices, considering the Gauss points on the boundaries of the edge-based smoothing domains. Although this approach may yield acceptable results in problems associated with coupled flow-deformation analysis, it is not rigorous as it approximates the numerical integrations by considering unconventional Gauss points. Soares Jr (2013b) also used the same formulation considering the Tr6 node selection scheme for poro-dynamic models adopting the Newton-Raphson technique, and also an iterative model in which each phase of the coupled problem is dealt with separately.

Tootoonchi et al. (2016) presented a group of CSPIMs based on the generalised gradient smoothing technique for numerical modelling of saturated porous media employing two different automatic node selection schemes, Tr4 and Tr2L, to prevent the singularity of the moment matrix. They proposed a novel approach to evaluate the coupling and compressibility matrices in the discretised system of equations, through which conventional Gauss points within the background cells are used in combination with the Gauss points on the edges of the background cells originally proposed in CSPIM. Moreover, for temporal discretisation they utilised the three-point time marching technique with variable time steps. When applying the SPIMs to axisymmetric problems, the Gauss points located on the axis of symmetry cause singularity problems and hence, the original SPIMs are not directly applicable in axisymmetric settings. Tootoonchi et al. (2018) presented a simple yet innovative approach which makes the application of SPIMs, and in particular CSPIM, to axisymmetric problems possible. They decomposed the strain-displacement matrix into two separate matrices: a smoothed strain-displacement matrix the same as the conventional SPIMs, and a strain displacement matrix containing the terms which cause the singularity problem. The first matrix is dealt with using the boundary integration approach, while the integrations of second matrix are performed over the integration domains and not along their boundaries. This novel work facilitates the application of SPIMs to many engineering problems which are axisymmetric in nature.

Another group of MMs that has been widely applied to a variety of disciplines, including geotechnical engineering, is the material point method (MPM) which was originally formulated in the early 1990's by Sulsky et al. (1994) for problems in solid dynamics. In MPM, the material points are sufficiently small Lagrangian elements to present the problem field of interest, while the gradient of the primary variables is calculated using a stationary background mesh. A vast amount of numerical studies have been conducted using MPM in geotechnical and structural engineering. Coetzee et al. (2005) studied the interaction between anchors and soil using MPM. Jassim et al. (2013) adopted MPM for coupled dynamic flow-deformation analysis. Bandara and Soga (2015) investigated the soil behaviour arising from the coupling interaction of solid grains and fluid flow. The large deformation induced by the mass movements in landslides was studied numerically using MPM by Soga et al. (2015). Bhandari et al. (2016) performed a seismic study of slope failure using MPM. MPM was also used in the study of cone penetration test with different drainage boundary conditions by Ceccato et al. (2016). Abe et al. (2017) adopted MPM in a dynamic analysis of the slope failure that includes weak layers. Cortis et al. (2018) recently contributed in resolving a fundamental disadvantage of MPM by developing a method which allows arbitrary essential boundary conditions to be imposed in MPM. Another disadvantage of MPM is in satisfying the mass conservation law as each particle has its own mass and therefore the number of particles has to be kept constant (Idelsohn et al., 2018). On the other hand, locking behaviour is observed in MPM due to lack of a pressure equation.

Coombs et al. (2018) proposed a method to overcome the problem of volumetric locking in MPM in nearly incompressible materials in solid mechanics.

Originally proposed by Cundall and Strack (1979), the discrete element method (DEM) is a class of numerical methods which is often categorised as a MM. The main idea behind DEM is to characterise the rotational movements of particles by including the distinguishable degrees of freedom, which appropriately captures the contact states of solid particles in granular media. DEM has been utilised in a number of geotechnical engineering applications, including analysis of a shallow foundation lain on a slope by Gabrieli et al. (2009). Jiang and Yin (2012) studied the effect of tunnel lining on the distribution of the soil pressure within the earth using DEM. A two-dimensional analysis of granular media was extended to three-dimensional simulations in a DEM context by Lim and Andrade (2014). Despite the capability of the DEM in modelling soils and rocks as granular materials, this method is computationally demanding and this is why it has not been widely adopted in computational engineering. Furthermore, modelling non-spherical particles with idealised spheres is a common concern in DEM.

The finite point-set method (FPM) is another example of particle MMs that is extensively applied in fluid dynamics; however, several applications of the FPM in geotechnical engineering can also be found in the literature. In FPM, a series of background nodes to which local properties, such as temperature, density and velocity are assigned represent the continuum problem domain. The important feature of FPM is that it possesses the flexibility to express the problem of interest in Lagrangian, Eulerian or mixed Lagrangian-Eulerian discerption with ease of implementation which enables the nodes to be either moved or fixed in space. The influence of a vehicle travelling through body of water was studied by adopting a FPM by Jefferies et al. (2015). Other examples of adopting FPM in soil mechanics problems include a work by Kuhnert and Ostermann (2014) to show the application of FPM to simulating standard laboratory tests, and avalanche simulation by Michel et al. (2017). Like other particle methods, FPM has a high computational cost and requires small time steps to be adopted to obtain reasonable results.

SPH has also been applied to many problems in geotechnical engineering. Blanc and Pastor (2009) applied a two dimensional SPH model to simulate debris flows. Bui and Fukagawa (2013) developed an enhanced SPH model to capture the possible failure modes of embankments taking into account the coupling of flow and deformation in porous media. This work was then extended for large deformation analyses to evaluate the post-peak behaviour of segmental retaining walls (Bui et al., 2015). The use of SPH in large deformation analyses of geomaterials was also investigated by Peng et al. (2015) using a hypo-plastic constitutive model. Holmes et al. (2016) studied the coupling of fluid flow with soil particles in reservoirs through SPH numerical simulations. Hu et al. (2015) carried out three-dimensional analyses to simulate the flow-like behaviour of soil particles in landslides. The flow-like behaviour was also investigated by a combined technique referred to as the depth-integrated SPH, proposed by Blanc and Pastor (2009). Komoróczi et al. (2013) proposed a novel technique by combining SPH and DEM to simulate the brittle-viscous deformation in practical problems, such as hydro-fracturing. Das et al. (2014) applied SPH to model rock fracturing stemming from magma intrusion. Despite all these applications, SPH is known to have stability, accuracy and convergence problems, especially when non-uniform particle distribution patterns are considered. Moreover, due to the particle nature of SPH, application of techniques which are developed for grid-based methods is not straightforward (Liu and Liu, 2003).

The particle finite element method (PFEM) refers to a MM that utilises FEM to discretise the physical domain and to integrate the discretised partial differential equations (PDEs), while in contrast to FEM, the corresponding nodes are free to move according to the motion equation in a Lagrangian sense and can even separate from the main analysis domain (Oñate et al., 2004). The balanced forces along with all the associative physical properties are transferred with the moving nodes as if they are particles. Idelsohn et al. (2004) used PFEM to solve continuous fluid mechanics problems. Idelsohn et al. (2006) later studied fluid-structure interaction (FSI) using PFEM. Although mainly used for applications in FSI, this unique feature has contributed to solving a number of complex geotechnical problems. Carbonell et al. (2009) adopted PFEM for modelling ground excavation. The application of PFEM to coupled problems in engineering was studied by Oñate et al. (2011). Carbonell et al. (2013) presented the influence of the tunnelling including the wear of the cutting tools, and Salazar et al. (2016) exploited PFEM for numerical simulation of a landslide in Lituya Bay in Alaska. The problem with mass conservation mentioned for MPM is overcome in PFEM. However, the main disadvantage of PFEM is that a mesh generation stage has to be performed in almost all time steps which costs a lot of time and memory (Idelsohn et al., 2018).

Several other MMs have also been applied to geotechnical engineering problems. The soft particle method was developed by Chen (2015) to simulate granular media. The method was then used by Schneider-Muntau et al. (2017) for the simulation of shear bands in granular materials under shear. Another approach adapted for numerical simulation of geotechnical engineering problems is the Maximum-Entropy MM (MEM). MEM method was introduced for modelling incompressible and nearly incompressible elastic solids, and two-dimensional Stokes flow (Ortiz et al., 2010; Ortiz et al., 2011). An adaptive FE-EFG method was also proposed by Ullah et al. (2013) for nonlinear problems including material and geometrical nonlinearities. The first applications of MEM method in coupled problems, however, were presented by Zakrzewski et al. (2016) and Nazem et al. (2016). Kardani et al. (2017) later used this MEM model for simulations of small strain geotechnical problems including material nonlinearity, where the Newton-Raphson technique and a dynamic relaxation method were used to solve the governing equations. The material nonlinearity was also considered in a meshless natural neighbour method developed by Zhu et al. (2006). More sophisticated constitutive models were adopted in a study by Obermayr et al. (2013) to simulate cemented sand incorporating a bonded-particle method, and in a work by Schenkengel and Vrettos (2011) to capture the lateral spreading due to the liquefaction phenomenon using the Lattice Boltzman method. A Lagrangian MM was also proposed by Wu et al. (2001) which allows nodal movement in geotechnical problems. A novel DEM-SPH method was formulated by Komoróczi et al. (2013) to simulate induced fractures pressurised by a fluid. In this method, the displacement variable was represented by DEM while SPH adopted to simulate the fluid phase.

2.5. Elastoplastic modelling using SPIMs

Multiple works have been carried out to solve nonlinear elastoplastic problems using MMs (Pamin et al., 2003; Gu, 2008; Wang and Sun, 2011; Hu et al., 2013). However, SPIMs have not, so far, been widely applied to problems related to hydromechanics of elastoplastic porous media. In the following, the few works regarding the elastoplastic analysis adopting SPIMs are discussed.

Zhang et al. (2015) applied NSPIM to elastoplastic analysis of two-dimensional materials with gradient-dependent plasticity and demonstrated the robustness of the model in elastoplastic analyses, albeit for single phase material only. Their formulation was based on parametric variational principle (PVP) and the gradient dependent plasticity. The NSPIM eliminates the inherent overly-stiff problem associated with FEM which leads to problems including locking behaviour and inaccuracy in stress calculations. They showed that due to the softened stiffness yielded by NSPIM, the model is suitable for simulating the material softening behaviour.

Soares Jr (2013a) conducted a study on the application of NSPIM, CSPIM, and ESPIM in elastoplastic dynamic analysis of elastoplastic solids. He considered an alternative approach consistent with the way stiffness matrix is calculated in SPIMs for evaluating the mass matrix and the external load vector. To this end, he employed smoothing domains identical to those considered in the original SPIMs to make use of the already calculated data. Although this method helps with increasing the speed of the computations and boosting up the computational efficiency, it is not computationally rigorous as will be explained later in Chapter 3 of this thesis. Later on, Soares Jr (2013b) adopted a similar approach to solve the time-domain nonlinear coupled system of equations.

2.6. Numerical simulations in unsaturated porous media

Reviewing the literature on numerical simulations of unsaturated porous media warrants at least a short discussion on the approaches available for modelling unsaturated soils. Such a discussion is presented first, followed by the literature on numerical analysis of unsaturated soils.

Investigations on the behaviour of unsaturated soils date back to 1950’s (Bishop, 1959; Bishop et al., 1960). These works were followed by a series of research on applicability of the effective stress principle to unsaturated soils, including the results of a series of oedometer tests published by Jennings and Burland (1962), stating the incapability of the effective stress principle in addressing the collapse phenomena in expansive soils, questioning Terzaghi's statement that any volume change in soil is due exclusively to a change in effective stress. Bishop and Blight (1963) demonstrated the validity of effective stress principle by showing that the shear strength and volume change remain constant in certain stress paths when the individual components of the effective stress are changed in a way that the effective stress remains unchanged. However, many researchers later confirmed the argument stated by Jennings and Burland (1962), raising doubt on the validity of the effective stress principle in addressing the volume change behaviours of unsaturated soils (Aitchison, 1965; Matyas and Radhakrishna, 1968; Brackley, 1971; Fredlund and Morgenstern, 1977; Gens et al., 1995). Consequently, Fredlund and Morgenstern (1977) proposed a new approach as an alternative to the effective stress approach, introducing two independent stress variables to describe the constitutive behaviour of unsaturated soils. This approach was soon adopted by many researchers (Alonso et al., 1990; Wheeler, 1996; Alonso et al., 1999; Wheeler et al., 2002; Chiu and Ng, 2003) and that has led to introduction of several constitutive models to the literature, including the famous Basic Barcelona Model (BBM) by Alonso et al. (1990).

However, over the last 20 years, the effective stress principle has proven to be valid even in unsaturated soils if the effective stress parameter is defined appropriately. A simple and effective relationship for quantification of the effective stress parameter in unsaturated soils was proposed by Khalili and Khabbaz (1998). Loret and Khalili (2000) and Loret and Khalili (2002) discussed the reasons behind difficulties in previous investigations using effective stress principle. They showed that the plastic collapse upon wetting, which for years had been an indication of the failure of the effective stress principle in unsaturated soils mechanics, can be justified adopting a proper elastoplastic constitutive model predicting the hardening effects due to change in suction. Khalili et al. (2004) also showed the uniqueness of the critical state line for both saturated and unsaturated soils. Using the experimental data from the literature, they showed the effective state principle can provide rigorous and accurate predictions for the shear strength and volume change behaviour of unsaturated soils. These studies paved the way for the researchers to propose constitutive models for unsaturated soil based on the concept of the effective stress (Bolzon et al., 1996; Lewis et al., 1998; Gallipoli et al., 2003; Laloui et al., 2003; Sheng et al., 2003a; Sun et al., 2003; Wheeler et al., 2003; Tamagnini, 2004; Georgiadis et al., 2005; Santagiuliana and Schrefler, 2006; Sun et al., 2007a; Sun et al., 2007b; Muraleetharan et al., 2009; Tsiampousi et al., 2013b), rather than the unnecessarily complicated approach proposed earlier by Fredlund and Morgenstern (1977).

Biot (1941) formulated the coupled flow and deformation behaviour of saturated porous media in quasi-static condition and later extended the formulation to dynamic conditions (Biot, 1956). Fredlund and Hasan (1979) presented theory for one-dimensional consolidation of unsaturated soils in which they used the independent stress state variables and an uncoupled flow and deformation formulation. Another study to simulate multiphase flow through porous media was performed by Morel-Seytoux and Billica (1985), although no deformation is assumed in the solid phase which is known to often yield unrealistic results (Narasimhan and Witherspoon, 1978). The same approach was applied in the work by Wu and Forsyth (2001) assuming rigid solid phase.

The Biot’s fundamental formulation was later extended to unsaturated porous media by Lewis and Schrefler (1982), Li et al. (1989), Zienkiewicz et al. (1990) and Xikui and

Zienkiewicz (1992), leading to an extensive array of numerical investigations to capture the coupled flow and deformation behaviour of unsaturated porous media using both two stress state approach and effective stress approach. In the following, some of these works are overviewed with focus on the most recent ones.

Lewis et al. (1998) presented a fully coupled formulation for multiphase flow through saturated and unsaturated porous media and proposed a three-phase model based on the WRC model proposed by Brooks and Corey (1966). They assumed elastic response for the solid skeleton and subsequently incorporated their proposed nonlinear saturation and permeability functions into a finite element (FE) model to simulate multiphase flow in porous media to solve problems of groundwater contamination.

Sheng et al. (2003a) proposed a FE formulation for geotechnical problems involving both saturated and unsaturated soils. They defined a constitutive stress tensor, rather than an effective stress tensor and employed it in a constitutive model similar to the BBM (Alonso et al., 1990). In their formulation, suction is treated as a strain variable instead of a stress variable to simulate suction hardening. In a separate work, Sheng et al. (2003b) showed that the plastic collapse upon wetting can be simulated by this model by adjusting one constitutive equation and one or two material parameter in the BBM model.

Sheng et al. (2008b) overviewed different approaches available for numerical solution of boundary value problems associated with unsaturated media in a FE framework. In this work, they mainly compared the Sheng-Fredlund-Gens (SFG) model (Sheng et al., 2008a) to a few other models, including the BBM. The SFG is formulated based on independent stress state variables and is shown to perform well in many cases. This model, however, involves several parameters that are difficult to identify using routine tests, rendering the model difficult for practical applications.

Khoei and Mohammadnejad (2011) investigated the flow of two immiscible fluid phases through a deformable porous media adopting a fully coupled hydro-mechanical analysis within a FE framework. They used the Pastor-Zienkiewicz generalised constitutive model and examined the validity of their formulation in modelling the liquefaction of San Fernando dam. However, they made several simplifying assumptions in their formulations, including neglecting the effect of hydraulic hysteresis.

A fully coupled formulation for analysis of unsaturated porous media was developed by Khoshghalb and Khalili (2013) in which RPIM was adopted to numerically solve the governing equations. The model is based on the effective stress principle and a WRC model which is an extension of the model originally proposed by Brooks and Corey (1964) to include hydraulic hysteresis (Khalili et al., 2008). All the model parameters including the coefficients of permeability and constitutive coefficients are continuously updated during the analysis through an iterative procedure. The dependency of the degree of saturation on void ratio and suction is taken into account through an extended form of the work by Mašín (2010) to include hydraulic hysteresis effects. While the model was a great step forward towards a more realistic simulation of flow and deformation in unsaturated porous media, it was based on assuming isotropic elastic behaviour for solid skeleton which is often inaccurate for geomaterials.

Another meshfree formulation based on the EFGM for simulation of two-phase flow in porous media was proposed by Samimi and Pak (2014). They utilised Van Genuchten (1980) model for predicting the permeability variations for wetting and non-wetting phases and also degree of saturation in their simulations. Their model, however, lacks a firm theoretical background like the effective stress approach and therefore, cannot accurately simulate the hydro-mechanical behaviour of unsaturated porous media.

A FE model was developed by Shahbodagh-Khan et al. (2015) in which they employed the effective stress based model used earlier by Khoshghalb and Khalili (2013). They took account of the effect of hydraulic hysteresis, but assumed void ratio independent WRC parameters in the analyses. Also investigated in this work are the effects of large deformation, and nonlinear shear modulus.

Tang et al. (2016) utilised the effective stress approach in a FE formulation to compute bearing capacity of shallow foundations, adopting a Mohr-Coulomb model. In their study, they illustrated how suction and hydraulic hysteresis can impact the bearing capacity of shallow foundations. In another study, Tang et al. (2017) used the same formulation to study consolidation problems in unsaturated porous media.

Ghorbani et al. (2016) proposed a comprehensive FE model for coupled analysis of multi-phase flow through unsaturated porous media, under both static and dynamic loading conditions. They, however, adopted an extended Modified Cam-Clay model in their analysis which has several limitations including the unrealistic results in modelling overall behaviour of over-consolidated soils when the yield surface is reached. Ghorbani et al. (2018b) later implemented an objective stress integration scheme into their formulation to deal with large deformations. In another work, Ghorbani et al. (2018a) studied the dependency of WRC on volume changes considering the effect of hydraulic hysteresis on elasto-plastic response of unsaturated porous media.

2.7. Validation and Verification

Due to high cost of physical modelling, computer codes are being developed constantly to approximate the physics of various problems. However, the outcomes of these codes may not always be worthy of trust and confidence. To evaluate the fidelity of modelling and simulation aspects of scientific computing, verification and validation (V&V) must be considered as an unavoidable step in code development. Verification simply refers to a procedure for making sure that the right equations are targeted to be solved, whereas validation provides credibility for the correctness of the solution to the chosen system of equations. Blottner (1990) best described the difference between validation and verification stating that code validation in "solving right governing equations", while code verification is "solving governing equations right".

Validation is referred to as the procedure to check whether the right physical and continuum mathematical models are solved through a code that is developed. In fact, the code itself is not validated, but the model on which the code is based and the assumptions behind the model are (Roache, 2004). Therefore, validation is a responsibility of the scientific community and the ongoing research and is out of the scope of this study.

There are a series of criteria for performing code verification: expert judgement, error quantification, consistency/convergence, and order of accuracy, in order of increasing reliability (Roy, 2005). The most powerful code verification criterion is the order of accuracy test which examines the convergence rate of the numerical solution, along with the rate of discretisation error reduction as mesh size decreases. This rate is compared with the so-called formal order of accuracy which can be obtained by performing a truncation error test. Performing a truncation error test may be difficult in practice. Hence, alternative approaches including the residual method, the statistical method, and the downscaling method can be employed for order verification purposes (Oberkampf and Roy, 2010). Burg and Murali (2006) proved that the exact solution to the mathematical model does not exactly satisfy the discrete equations, and it can be shown that for linear problems, the residual approximates the truncation error. The residual method is easy to implement and has a very low computational cost compared to other approaches mentioned. It is, therefore, adopted in this study for obtaining the formal order of accuracy when performing an order of accuracy test. In the following, a brief overview is provided on different order of accuracy tests.

The fundamental and most rigorous method for obtaining the numerical order of accuracy is comparing the numerical results to analytical solutions of the PDEs governing the physics of the problem. This method is called method of exact solutions. Only a limited number of problems with exact solutions are, however, available in geomechanics, e.g. Terzaghi’s one-dimensional consolidation problem (Terzaghi, 1925), two-dimensional consolidation in poro-elasticity (Schiffman et al., 1969), and one dimensional consolidation of elastic perfectly-plastic material (Small et al., 1976; Carter et al., 1979). Furthermore, the exact solutions invariably involve several simplifying assumptions which result in simple solutions that are often not capable of verifying all aspects of a code.

Another verification approach commonly adopted in geomechanics is to compare the numerical solutions with benchmark experimental data. However, this approach cannot be considered as a reliable verification technique because it cannot distinguish among verification, validation, and experimental errors, and therefore may not identify subtle coding errors. The least reliable verification approach is code comparison principle

(CCP) where results from two codes are compared with each other (Oberkampf et al., 2003). This method can be erroneous and improper when there is no scientific credible evidence that the reference code is an appropriate benchmark code.

The method of manufactured solutions (MMS), which is also referred to as “Man Made Solution”, “Prescribed Forcing Method”, and “Method of Nearby Solution” (ASME, 2009), is a very powerful approach for verifying the open source and in-house computer codes. The basic idea of MMS is to simply manufacture exact continuum solutions to the PDEs of interest (Roache, 2002). To this end, one first assumes an analytic solution to the PDEs according to the available guidelines. Next, the selected manufactured solution is substituted into the PDEs to calculate the source terms which guarantee that the selected manufactured solutions are indeed exact solutions to the governing PDEs. The source terms are distributed terms which should be applied in the code at each cell or node of interest, depending on the nature of the numerical method in hand. Therefore, the source code must be available to modifications so that such an implementation can be made while dealing with MMS. The only purpose of manufacture solutions is determining the order of accuracy of computer codes in solving the corresponding PDEs. Hence, manufactured solutions are not required to be physically realistic as long as they do not yield ill-conditioned insoluble discretised equations (Knupp and Salari, 2002). The initial and boundary conditions are imposed in this method by simply substituting the initial time and boundary coordinates into the analytic expressions. In the following, a brief overview of the existing literature on the application of MMS as a verification method, which is available mainly in the CFD field, is presented.

Oberkampf and Blottner (1998) were the first to mention the term “manufactured solution”, however, the very first articles on MMS were published by Shih (1985) for identifying coding mistakes, and by Steinberg and Roache (1985) where they used a symbolic manipulation approach for verifying a solution to three-dimensional elliptic PDEs. Roache et al. (1990) later extended the MMS concept to groundwater flow. Salari and Knupp (2000) employed MMS in a blind study for a series of examples in computational fluid dynamics and discussed the coding mistake types that MMS is and is not able to reveal. To do so, they altered a previously verified CFD code by deliberately introducing errors to the code and then they tested it using MMS. They showed that any mistake that prevented the governing equations from being solved correctly could be detected by MMS, while none of the mistakes which were not managed to be detected prevented the equations from being solved correctly. In a review article, Roache (2002) studied three MMS examples, including a one-dimensional transient solution to the nonlinear Burger's equation. He illustrated that the same exact answer can be used to verify two different codes with different governing PDEs. Through another example he also showed that making a realistic solution assumption is not necessary.

The application of MMS to the Euler and Navier-Stokes equations was investigated by Roy et al. (2004) using two different finite volume codes. Eça et al. (2007b) presented manufactured solutions for some famous eddy-viscosity turbulence models. A convergence study on two-dimensional, steady, wall-bounded, incompressible turbulent flow was done by Eça et al. (2007a) using MMS. Eça and Hoekstra (2009) focused on three different issues on error evaluation using MMS: The estimation of the iterative error; the influence of the iterative error on the estimation of the discretisation error; and the overall effect of the iterative and discretisation errors on numerical error. Their results show that the magnitude of the iterative error must be two to three times smaller than the discretisation error in order for negligible influence of the iterative error.

Étienne et al. (2012) presented manufactured solutions for verification of a fluid-structure interaction (FSI) code which solves uncoupled Navier-Stokes equation for fluid flow and large deformation equation considering St.Venant-Kirchhoff material in a total Lagrangian (TL) framework. Leng et al. (2013) constructed manufactured solutions for three-dimensional, isothermal, nonlinear Stokes model for flow in glaciers and ice-sheets, and employed their manufactured solution to verify a 3D FE code. Veeraragavan et al. (2016) demonstrated the use of MMS to verify the implementation of coupled heat transfer for fluid-solid solvers. Unlike conventional applications of MMS, they tested the interface implementation using MMS by choosing manufactured solutions which satisfy the physical conditions on the boundaries.

The only published study on the application of MMS in earth sciences is the numerical simulations of seismo-elastic wave propagation in heterogeneous earth models by Petersson and Sjögreen (2018). However, to the best of the author's knowledge, there is not any published peer reviewed study in the realm of fully coupled computational geomechanics which integrated advanced techniques like MMS to verify codes.

If the source code is not accessible, MMS cannot be considered as an option for code verification. Alternatively, black box testing which only requires access to input and output files can be substituted for MMS. Black box testing, which is also called functional testing, can be performed by any code user without the need for any knowledge about the details of the code. The only purpose of the black box testing is checking the accuracy of the outputs rather than any specific element of the code. Black box testing is in fact comparing the code outputs with highly accurate solutions (Oberkampf et al., 2004), e.g. analytical solutions. Finally, if access to the source code, analytical solutions and another reliable high resolution solver are not available, the

Richardson extrapolation can be used for verification study (Roache and Knupp, 1993). An example of using the Richardson extrapolation for error estimation is presented by Roy and Blottner (2003) for hypersonic flows. Baliga and Lokhmanets (2016) presented an overview of the efforts for utilising the Richardson extrapolation in numerical predictions of fluid flow and heat transfer.

2.8. Conclusion

Most common MMs were introduced in a chronological order and typical shortcomings accompanying each method were briefly discussed. SPIMs were introduced as a rather new class of MMs which are very accurate and super convergent and are able to overcome many of the drawbacks in other MMs. A thorough overview on the application of MMs in geomechanics was undertaken stating weaknesses, strengths, and the contributions of each study to the application of MMs in geomechancis, highlighting the need for a robust meshfree algorithm for coupled problems in multiphase porous media. The limited applications of SPIMs in modelling nonlinear material response were reviewed and the deficiencies of each study were highlighted. A thorough literature review was then performed on numerical modelling of the behaviour of unsaturated porous media, beginning with a brief introduction on the historical developments of the mechanics of unsaturated soils. It was pointed out that the effective stress principle has had a crucial role in modern numerical approaches to problems in unsaturated porous media. Finally, the importance of validation and verification in developing numerical models was highlighted, and different verification approaches were discussed. In particular, the order of accuracy study along with the method of manufactured solutions was highlighted and the available literature on the application of this verification method was overviewed.

Chapter 3

3. Coupled flow and deformation analysis of saturated porous media

3.1. Introduction

In this chapter, an edge-based smoothed point interpolation method based on weakened weak (W^2) formulation is developed for numerical analysis of Biot's formulation. Point interpolation method (PPIM or RPIM) in conjunction with four different node selection schemes for defining the support domain at each point of interest is used for construction of the shape functions for both solid and fluid phases. Problem domain is discretised using triangular background elements. Edge-based smoothing domains are then created on top of the background mesh using the edges of the background cells. Strains construction is carried out through a smoothing operation leading to constant smoothed strains over the edge-based smoothing domains. A novel approach for evaluation of the coupling matrix of the porous media is developed. Temporal discretisation is performed using a three-point approximation technique with variable time steps to avoid temporal instabilities. Numerical examples are studied and the results are compared with analytical and semi-analytical solutions to evaluate the performance of the proposed model.

3.2. Sign convention

Compact matrix-vector notation is used throughout the dissertation. Two-dimensional plain strain condition is assumed. Tensors and vectors are identified by boldface letters, and an over-dot represents a time derivative. $\mathbf{L}_\mathrm{d}$ stands for the differential operator matrix as

$$\mathbf{L}_\mathrm{d} = \begin{bmatrix} \dfrac{\partial}{\partial x} & 0 \\ 0 & \dfrac{\partial}{\partial y} \\ \dfrac{\partial}{\partial y} & \dfrac{\partial}{\partial x} \end{bmatrix} \tag{3.1}$$

with x and y being space coordinates. ∇ is the gradient operator vector defined as $\nabla = \mathbf{L}_\mathrm{d}^\mathrm{T}\boldsymbol{\delta}$, with $\boldsymbol{\delta} = \begin{bmatrix}1 & 1 & 0\end{bmatrix}^\mathrm{T}$, and $\mathrm{div}(\cdot) = \nabla \cdot (\cdot)$ is the divergence operator. It should be noted that the sign convention of continuum mechanics is adopted throughout: Compression is taken as negative, and tension is taken as positive. However, the volumetric strain in defined as $\varepsilon_\mathrm{v} = -tr(\boldsymbol{\varepsilon})$ which is positive in compression, where tr is the trace operator. On the other hand, pore fluid pressures are taken as positive in compression following soil mechanics convention.

3.3. Governing equation

According to the theory of mixtures, a saturated porous medium consists of two continuous interacting continuum phases, solid skeleton (or solid matrix) and pore fluid. The framework in this work is presented based on two separate, yet coupled models: a deformation model which takes account of the interaction between the internal total stresses and the external applied forces, and a flow model considering the flow of the fluid phase through the porous medium. The coupling effect of the two models is established utilising the effective stress concept together with the volumetric compatibility relationships for the different phases.

3.3.1. Deformation model

Neglecting inertial effects and assuming homogeneity, differential equation for the general equilibrium in the medium is expressed as

$$\mathbf{L}_{\mathrm{d}}^{\mathrm{T}}\boldsymbol{\sigma} + \mathbf{F} = \mathbf{0} \tag{3.2}$$

where $\boldsymbol{\sigma}$ is the total stress tensor, $\mathbf{F} = \rho\mathbf{B}$ is the vector of body forces per unit volume, $\mathbf{B}$ is the vector of body force per unit mass, and ρ is the average density of the mixture as

$$\rho = n\rho_{\mathrm{f}} + (1-n)\rho_{\mathrm{s}} \tag{3.3}$$

where n is the total porosity of the porous media, and ρ_{f} and ρ_{s} are densities of fluid and solid phases, respectively.

In order to elaborate the total stress vector in equation (3.2), Terzaghi's effective stress principle must be taken into account as follows

$$\boldsymbol{\sigma} = \boldsymbol{\sigma}' - \eta p_{\mathrm{f}}\boldsymbol{\delta} \tag{3.4}$$

in which $\eta = 1 - c_{\mathrm{s}}/c$ is the Biot's constant, where c_{s} and c are the compressibility of the solid grains and drained compressibility of the solid skeleton, respectively.

The effective stress vector $\boldsymbol{\sigma}'$ is related to the strain vector through the elastic constitutive matrix $\mathbf{D}^{\mathrm{e}}$, assuming elastic response of the solid skeleton

$$\boldsymbol{\sigma}' = \mathbf{D}^{\mathrm{e}}\boldsymbol{\varepsilon} \tag{3.5}$$

and the strain vector is obtained from the displacement vector as below

$$\boldsymbol{\varepsilon} = \mathbf{L}_{\mathrm{d}}\mathbf{u} \tag{3.6}$$

where $\mathbf{u}$ is the solid phase displacement vector.

3.3.2. Flow model

For establishing the flow model we first consider the equation of linear momentum balance for fluid phase as

$$\mathbf{v}_{\mathrm{fs}} = -\frac{\mathbf{k}}{\mu_{\mathrm{f}}}(\nabla p_{\mathrm{f}} + \rho_{\mathrm{f}}\mathbf{g}) \tag{3.7}$$

$\mathbf{k}$ indicates the intrinsic permeability matrix defined as $\mathbf{k} = k\mathbf{I}$, where k is the intrinsic permeability assuming isotropic material (i.e., $k_{\mathrm{x}} = k_{\mathrm{y}} = k$), and $\mathbf{I}$ is the 2×2 identity matrix; μ_{f} is the dynamic viscosity of fluid phase; $\mathbf{g} = [0 \quad g]^{\mathrm{T}}$ is the gravity acceleration vector, with g being the gravitational acceleration; and $\mathbf{v}_{\mathrm{fs}}$ is the relative velocity vector for the fluid phase with respect to a moving solid i.e.

$$\mathbf{v}_{\mathrm{fs}} = n(\mathbf{v}_{\mathrm{f}} - \mathbf{v}_{s}) \tag{3.8}$$

where $\mathbf{v}_{\mathrm{f}} = \dot{\mathbf{u}}_{\mathrm{f}}$ and $\mathbf{v}_{\mathrm{s}} = \dot{\mathbf{u}}$ are absolute velocities of fluid phase and the solid phase, respectively, and $\mathbf{u}_{\mathrm{f}}$ is the displacement vector for the fluid.

The mass balance equation for the fluid phase is given by

$$\frac{\partial}{\partial t}(n\rho_{\mathrm{f}})+\mathrm{div}(n\rho_{\mathrm{f}}\mathbf{v}_{\mathrm{f}})=0 \tag{3.9}$$

Substituting equation (3.8) into (3.9) we have

$$-\mathrm{div}(\rho_{\mathrm{f}}\mathbf{v}_{\mathrm{fs}})=\frac{\partial}{\partial t}(n\rho_{\mathrm{f}})+\mathrm{div}(\mathrm{n}\rho_{\mathrm{f}}\mathbf{v}_{\mathrm{s}}) \tag{3.10}$$

Now, introducing the Lagrangian total derivatives concept with respect to moving solid, $\mathrm{d}(\cdot)/\mathrm{d}t=\partial(\cdot)/\partial t+\nabla(\cdot)\cdot\mathbf{v}_{\mathrm{s}}$, and noting that $\mathrm{div}\left[(\cdot)\mathbf{v}_{\alpha}\right]=(\cdot)\,\mathrm{div}(\mathbf{v}_{\alpha})+\nabla(\cdot)\cdot\mathbf{v}_{\alpha}$, equation (3.10) is rearranged to

$$-\mathrm{div}(\rho_{\mathrm{f}}\mathbf{v}_{\mathrm{fs}})=n\frac{\mathrm{d}\rho_{\mathrm{f}}}{\mathrm{d}t}+\rho_{\mathrm{f}}\frac{\mathrm{d}n}{\mathrm{d}t}+n\rho_{\mathrm{f}}\,\mathrm{div}(\mathbf{v}_{\mathrm{s}}) \tag{3.11}$$

Considering the definition of compressibility of barometric fluids, we have

$$\frac{\mathrm{d}\rho_{\mathrm{f}}}{\mathrm{d}t}=\rho_{\mathrm{f}}\mathrm{c}_{\mathrm{f}}\frac{\mathrm{d}p_{\mathrm{f}}}{\mathrm{d}t} \tag{3.12}$$

in which c_{f} is the coefficient of compressibility for the fluid phase. Knowing the definition of porosity, the rate of porosity can be derived as

$$\frac{\mathrm{d}n}{\mathrm{d}t}=\frac{1}{V}\left(\frac{\mathrm{d}V_{\mathrm{v}}}{\mathrm{d}t}-n\frac{\mathrm{d}V}{\mathrm{d}t}\right) \tag{3.13}$$

where V_{v} is the void volume. Substituting equations (3.7), (3.12) and (3.13) into equation (3.11), and noting that $\left(\mathrm{d}V/\mathrm{d}t\right)/V=\mathrm{div}(\mathbf{v}_{\mathrm{s}})$, yields the following equation for the fluid flow in saturated porous media

$$\frac{1}{\rho_{\mathrm{f}}}\mathrm{div}\left[\rho_{\mathrm{f}}\frac{\mathbf{k}}{\mu_{\mathrm{f}}}\left(\nabla p_{\mathrm{f}}+\rho_{\mathrm{f}}\mathbf{g}\right)\right]-nc_{\mathrm{f}}\frac{\mathrm{d}p_{\mathrm{f}}}{\mathrm{d}t}-\frac{1}{V}\frac{\mathrm{d}V_{\mathrm{v}}}{\mathrm{d}t}=0 \tag{3.14}$$

Considering a representative volume V of saturated porous material subjected to external isotropic stress increment of $\mathrm{d}\sigma$, the following equations can be expressed to establish a constitutive link between the volumetric changes and the primary field variables (Khalili and Valliappan, 1996)

$$\frac{\mathrm{d}V}{V} = -\varepsilon_{\mathrm{v}} = c\,\mathrm{d}\sigma + (c - c_{\mathrm{s}})\mathrm{d}p_{\mathrm{f}} \tag{3.15}$$

$$\frac{\mathrm{d}V_{\mathrm{v}}}{V} = (c - c_{\mathrm{s}})\,\mathrm{d}\sigma + \left(c - (1+n)c_{\mathrm{s}}\right)\mathrm{d}p_{\mathrm{f}} \tag{3.16}$$

Now, combining equations (3.15) and (3.16) yields

$$\frac{\mathrm{d}V_{\mathrm{v}}}{V} = -(1 - \frac{c_{\mathrm{s}}}{c})\varepsilon_{\mathrm{v}} + \frac{c_{\mathrm{s}}}{c}\left(c(1-n) - c_{\mathrm{s}}\right)\mathrm{d}p_{\mathrm{f}} \tag{3.17}$$

Noting that $\varepsilon_{\mathrm{v}} = -tr(\boldsymbol{\varepsilon}) = -\mathrm{div}(\mathbf{u})$, the ultimate equation governing the fluid flow in saturated porous media is obtained by substituting equation (3.17) into equation (3.14) as follows

$$\frac{1}{\rho_{\mathrm{f}}}\mathrm{div}\left[\rho_{\mathrm{f}}\,\frac{\mathbf{k}}{\mu_{\mathrm{f}}}\left(\nabla p_{\mathrm{f}} + \rho_{\mathrm{f}}\mathbf{g}\right)\right] = a_{\mathrm{f}}\,\dot{p}_{\mathrm{f}} + \eta\,\mathrm{div}(\dot{\mathbf{u}}) \tag{3.18}$$

with the apparent compressibility coefficient of the fluid phase defined as

$$a_{\mathrm{f}} = n(c_{\mathrm{f}} - c_{\mathrm{s}}) + \eta c_{\mathrm{s}} \tag{3.19}$$

3.3.3. Initial and boundary conditions

The displacement of the solid skeleton and the pore fluid pressure ($\mathbf{u}(\mathbf{x},t)$ and $p_{\mathrm{f}}(\mathbf{x},t)$, respectively, where $\mathbf{x} = \begin{bmatrix} x & y \end{bmatrix}$ stands for coordinate and t stands for time) are the main variables in the governing equations (3.2) and (3.18). The required initial conditions for solving the equations are

$$\mathbf{u}(\mathbf{x},0)=\bar{\mathbf{u}}_0(\mathbf{x}) \tag{3.20}$$

$$p_{\mathrm{f}}(\mathbf{x},0)=\bar{p}_{\mathrm{f0}}(\mathbf{x}) \tag{3.21}$$

where $\bar{\mathbf{u}}_0(\mathbf{x})$ and $\bar{p}_{\mathrm{f0}}(\mathbf{x})$ are prescribed initial displacement vector and pore fluid pressure, respectively.

The boundary conditions are imposed as external displacement and traction as

$$\mathbf{u}(\mathbf{x},t)=\bar{\mathbf{u}}(t) \qquad on\ \Gamma_{\mathrm{u}} \tag{3.22}$$

$$\mathbf{L}_{\mathrm{n}}^{\mathrm{T}}\boldsymbol{\sigma}'(\mathbf{x},t)=\bar{\mathbf{t}}(t) \qquad on\ \Gamma_{\mathrm{t}} \tag{3.23}$$

in which $\bar{\mathbf{u}}(t)$ and $\bar{\mathbf{t}}(t)$ are the prescribed displacement and traction on the corresponding boundaries of Γ_{u} and Γ_{t}, where $\Gamma_{\mathrm{u}}\cup\Gamma_{\mathrm{t}}=\Gamma$ and Γ is the total boundary. The boundary conditions are also imposed as external fluid pressure or flux in the normal direction to the boundary of the pressure field as follows,

$$p_{\mathrm{f}}(\mathbf{x},t)=\bar{p}_{\mathrm{f}}(t) \qquad on\ \Gamma_{\mathrm{p}} \tag{3.24}$$

$$\mathbf{L}_{\mathrm{n}}^{\mathrm{T}}\mathbf{v}_{\mathrm{fs}}(\mathbf{x},t)=\bar{q}_{\mathrm{f}}(t) \qquad on\ \Gamma_{\mathrm{q}} \tag{3.25}$$

where $\bar{p}_{\mathrm{f}}(t)$ and $\bar{q}_{\mathrm{f}}(t)$ are the prescribed pore fluid pressure and fluid flux on the corresponding boundaries of Γ_{p} and Γ_{q}, where $\Gamma_{\mathrm{p}}\cup\Gamma_{\mathrm{q}}=\Gamma$. $\mathbf{L}_{\mathrm{n}}$ is the matrix of unit outward normal, defined as

$$\mathbf{L}_{\mathrm{n}} = \begin{bmatrix} n_1 & 0 \\ 0 & n_2 \\ n_2 & n_1 \end{bmatrix} \tag{3.26}$$

where n_1 and n_2 are the components of the unit outward normal to the domain boundary.

3.4. Edge-based smoothed point interpolation method

3.4.1. Function approximation

In this work, point interpolation methods (PPIM and RPIM) (Liu and Gu, 2001; Wang and Liu, 2002b) are considered for determination of the nodal shape functions. The first group of shape functions applied in the ESPIM are the polynomial point interpolation shape functions in which polynomials are used as the basis functions. A field function f is approximated at the point of interest $\mathbf{x}$ as

$$f(\mathbf{x}) = \sum_{i=1}^{p} P_i(\mathbf{x}) a_i = \mathbf{P}^{\mathrm{T}}(\mathbf{x})\mathbf{a} \tag{3.27}$$

where $P_i(\mathbf{x})$ are the polynomial basis functions obtained from the Pascal's triangle of monomials for 2D problems as shown in Figure 3-1, and $\mathbf{a}$ is a coefficient vector with yet unknown entries as follows

$$\mathbf{P}^{\mathrm{T}}(\mathbf{x}) = \begin{bmatrix} 1 & x & y & x^2 & xy & y^2 & \ldots \end{bmatrix} \tag{3.28}$$

$$\mathbf{a}^{\mathrm{T}} = \begin{bmatrix} a_1 & a_2 & \ldots & a_p \end{bmatrix} \tag{3.29}$$

where p is the number of supporting nodes for the point of interest.

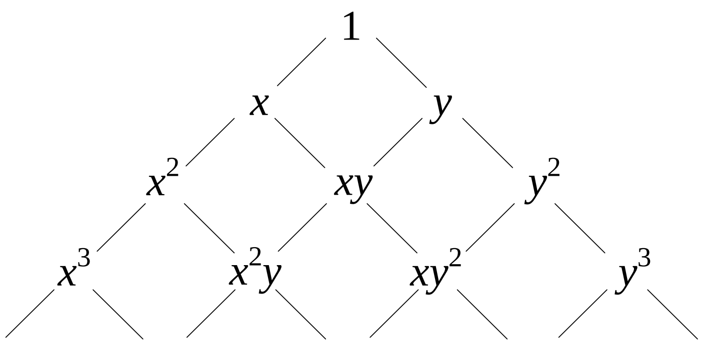

Figure 3-1- Pascal triangle of monomials for 2D domains

The radial point interpolation shape functions based on RBFs are used in the ESRPIM. The approximated field function based on RPIM interpolation enriched with polynomials can be written as

$$f(\mathbf{x}) = \sum_{i=1}^{p} R_i(\mathbf{x}) b_i + \sum_{j=1}^{l} P_j(\mathbf{x}) a_j = \mathbf{R}^{\mathrm{T}}(\mathbf{x})\mathbf{b} + \mathbf{P}^{\mathrm{T}}(\mathbf{x})\mathbf{a} \tag{3.30}$$

where $R_i(\mathbf{x})$ and $P_j(\mathbf{x})$ are radial and polynomial basis functions, respectively, and l is the number of monomials used in the polynomial basis functions. It should be noted that a minimum of three monomials are required to ensure linear consistency (i.e., $l \geq 3$). Adding polynomials to the RPIM shape functions generally improves the accuracy of the results and interpolation stability of the nodal shape functions (Liu and Gu, 2005).

There are various types of RBFs available in the literature (Zhang, 2007; Franke and Schaback, 1998; Kansa, 1990; Sharan et al., 1997). Four of these RBFs are more frequently used which are listed in Table 3-1.

Table 3-1- Typical RBFs available in the literature.

Name	Expression	Shape Parameters
Multi-quadrics (MQ)	$R_i(\mathbf{x}) = (r_i^2 + (\alpha_c d_c)^2)^{q_c}$	$\alpha_c \geq 0, q_c$
Gaussian (EXP)	$R_i(\mathbf{x}) = \exp\left(-\alpha_c \left(\frac{r_i}{d_c}\right)^2\right)$	α_c
Thin Plate Spline (TPS)	$R_i(\mathbf{x}) = r_i^{e_c}$	e_c
Logarithmic	$R_i(\mathbf{x}) = r_i^{e_c} \log r_i$	e_c

In Table 3-1, r_i is the distance between the point of interest $\mathbf{x}$ and the node at $\mathbf{x}_i$, and d_c is the local average nodal spacing. In the current study, the MQ RBFs are chosen due to their simplicity and stability, and the shape parameters α_c and q_c are taken as 4.0 and 1.03 respectively, following the recommendations in (Wang and Liu, 2002a; Liu and Zhang, 2013a).

The coefficients a_i and b_i in equation (3.30) are obtained by satisfying the field approximation function at all supporting nodes, resulting in p equations of the following form

$$f_h = f(\mathbf{x}_h) = \sum_{i=1}^{p} R_i(\mathbf{x}_h) b_i + \sum_{j=1}^{l} P_j(\mathbf{x}_h) a_j , \quad h = 1, 2, ..., p \tag{3.31}$$

where f_h represents the nodal value of the independent variable at the hth node in the support domain. To guarantee a unique solution for $\mathbf{b}$ and $\mathbf{a}$, l extra requirements have to be defined. The following requirements are often enforced,

$$\sum_{i=1}^{p} P_i(\mathbf{x}_i) b_j = \mathbf{0} , \quad j = 1, 2, ..., l \tag{3.32}$$

The combination of equations (3.31) and (3.32) can be presented in matrix form as follows

$$\begin{Bmatrix} \mathbf{f} \\ 0 \end{Bmatrix} = \begin{bmatrix} \mathbf{R}_0 & \mathbf{P} \\ \mathbf{P}^{\mathrm{T}} & \mathbf{0} \end{bmatrix} \begin{Bmatrix} \mathbf{b} \\ \mathbf{a} \end{Bmatrix} = \mathbf{G} \begin{Bmatrix} \mathbf{b} \\ \mathbf{a} \end{Bmatrix} \tag{3.33}$$

where

$$\mathbf{G} = \begin{bmatrix} \mathbf{R}_0 & \mathbf{P} \\ \mathbf{P}^{\mathrm{T}} & \mathbf{0} \end{bmatrix} \tag{3.34}$$

$\mathbf{R}_0$ is the moment matrix of the RBFs,

$$\mathbf{R}_0 = \begin{bmatrix} R_1(r_1) & R_2(r_1) & \cdots & R_p(r_1) \\ R_1(r_2) & R_2(r_2) & \cdots & R_p(r_2) \\ \vdots & \vdots & \ddots & \vdots \\ R_1(r_p) & R_2(r_p) & \cdots & R_p(r_p) \end{bmatrix}_{p\times p} \tag{3.35}$$

$\mathbf{P}$ is the polynomial moment matrix,

$$\mathbf{P} = \begin{bmatrix} P_1(\mathbf{x}_1) & P_2(\mathbf{x}_1) & \cdots & P_l(\mathbf{x}_1) \\ P_1(\mathbf{x}_2) & P_2(\mathbf{x}_2) & \cdots & P_l(\mathbf{x}_2) \\ \vdots & \vdots & \ddots & \vdots \\ P_1(\mathbf{x}_p) & P_2(\mathbf{x}_p) & \cdots & P_l(\mathbf{x}_p) \end{bmatrix}_{p\times l} = \begin{bmatrix} 1 & x_1 & y_1 & \cdots & P_l(\mathbf{x}_1) \\ 1 & x_2 & y_2 & \cdots & P_l(\mathbf{x}_2) \\ \vdots & \vdots & \vdots & \ddots & \vdots \\ 1 & x_p & y_p & \cdots & P_l(\mathbf{x}_p) \end{bmatrix}_{p\times l} \tag{3.36}$$

and $\mathbf{f}$ is the vector storing the values of the field function. Using equation (3.33), the following expression for the field approximation function is obtained,

$$f(\mathbf{x}) = \mathbf{R}^{\mathrm{T}}(\mathbf{x})\mathbf{b} + \mathbf{P}^{\mathrm{T}}(\mathbf{x})\mathbf{a} = \begin{bmatrix} \mathbf{R}^{\mathrm{T}}(\mathbf{x}) & \mathbf{P}^{\mathrm{T}}(\mathbf{x}) \end{bmatrix} \begin{Bmatrix} \mathbf{b} \\ \mathbf{a} \end{Bmatrix} = \begin{bmatrix} \mathbf{R}^{\mathrm{T}}(\mathbf{x}) & \mathbf{P}^{\mathrm{T}}(\mathbf{x}) \end{bmatrix} \mathbf{G}^{-1} \begin{Bmatrix} \mathbf{f} \\ \mathbf{0} \end{Bmatrix} \tag{3.37}$$

The RPIM shape functions can then be extracted from equation (3.37) as

$$\varphi_i(\mathbf{x}) = \sum_{j=1}^{p} R_j(\mathbf{x}) G_{j,i}^{-1} + \sum_{j=1}^{l} P_j(\mathbf{x}) G_{j+p,i}^{-1} \tag{3.38}$$

where $G_{j,i}^{-1}$ shows the entries of matrix $\mathbf{G}^{-1}$. Non-singularity of matrix $\mathbf{G}$ is secured adopting the node selection schemes elaborated in section 3.4.3 , and also by imposing $l < p$ (Liu and Zhang, 2013a).

PPIM and RPIM shape functions benefit from the Kronecker delta function property which facilitates the imposition of the Dirichlet boundary conditions. Furthermore, these shape functions satisfy the partition of unity condition at each point of interest $\mathbf{x}$, i.e., $\sum_{i=1}^{p} \varphi_i(\mathbf{x}) = 1$.

Having calculated the shape functions, the field approximation functions, which are the displacement and fluid pressure functions in this study, can be calculated at any point of interest $\mathbf{x}$ as

$$\mathbf{u}(\mathbf{x}) = \mathbf{\Phi}^{\mathrm{u}}(\mathbf{x})\bar{\mathbf{u}} = \sum_{i=1}^{p} \begin{bmatrix} \varphi_i(\mathbf{x}) & 0 \\ 0 & \varphi_i(\mathbf{x}) \end{bmatrix} \begin{Bmatrix} u_{1_i} \\ u_{2_i} \end{Bmatrix} \tag{3.39}$$

$$p_{\mathrm{f}}(\mathbf{x}) = \mathbf{\Phi}^{\mathrm{p}}(\mathbf{x})\bar{\mathbf{p}}_{\mathrm{f}} = \sum_{i=1}^{p} \varphi_i(\mathbf{x}) p_{\mathrm{f}_i} \tag{3.40}$$

where $\mathbf{u}(\mathbf{x})$ and $p_{\mathrm{f}}(\mathbf{x})$ are the displacement vector and pore fluid pressure at the point of interest $\mathbf{x}$, respectively, u_{1_i} and u_{2_i} are the components of nodal displacements, p_{f_i} is the pore fluid pressure at node i, and $\varphi_i(\mathbf{x})$ are the PPIM or RPIM shape functions associated with node i. $\mathbf{\Phi}^{\mathrm{u}}(\mathbf{x})$ is the shape function matrix for displacement defined as

$$\mathbf{\Phi}^{\mathrm{u}}(\mathbf{x}) = \begin{bmatrix} \varphi_1(\mathbf{x}) & 0 & \varphi_2(\mathbf{x}) & 0 & \cdots & \varphi_p(\mathbf{x}) & 0 \\ 0 & \varphi_1(\mathbf{x}) & 0 & \varphi_2(\mathbf{x}) & & 0 & \varphi_p(\mathbf{x}) \end{bmatrix}_{2\times 2p} \tag{3.41}$$

$\mathbf{\Phi}^{\mathrm{p}}(\mathbf{x})$ is the shape function matrix for pore fluid pressure defined as

$$\mathbf{\Phi}^{\mathrm{p}}(\mathbf{x}) = \begin{bmatrix} \varphi_1(\mathbf{x}) & \varphi_2(\mathbf{x}) & \cdots & \varphi_p(\mathbf{x}) \end{bmatrix}_{1\times p} \tag{3.42}$$

$\bar{\mathbf{p}}_{\mathrm{f}}$ is the vector storing the nodal pore fluid pressures as

$$\bar{\mathbf{p}}_{\mathrm{f}} = \begin{bmatrix} p_{\mathrm{f}_1} & p_{\mathrm{f}_2} & \cdots & p_{\mathrm{f}_p} \end{bmatrix}^{\mathrm{T}} \tag{3.43}$$

and $\bar{\mathbf{u}}$ is the vector storing the nodal displacements as follows

$$\bar{\mathbf{u}} = \begin{bmatrix} u_{1_1} & u_{2_1} & u_{1_2} & u_{2_2} & \cdots & u_{1_p} & u_{2_p} \end{bmatrix}^{\mathrm{T}} \tag{3.44}$$

3.4.2. Construction of smoothing domains

The compatibility condition is not necessarily satisfied in the global domain when PPIM and RPIM shape functions are used (Liu and Gu, 2005). Therefore, the generalised smoothed Galerkin (GS-Galerkin) weak formulation, which accommodates both compatible and incompatible displacement fields is employed to discretise the system of equations in the current smoothed meshfree model. In the GS-Galerkin weak formulation, instead of using a compatible strain field similar to those used in the FEM, a strain field is constructed using the generalized smoothed gradient over smoothing domains. In the present method, a mesh of cells is required which can be created in the same manner as in the standard FEM. A mesh of n_{e} triangular elements with n_{n} number of nodes is considered. For construction of the smoothing domains, on top of the background cells, the problem domain is divided into n_{SD} number of smoothing domains in a non-overlapping and no-gap fashion, so that the total problem domain Ω is defined as follows

$$\Omega = \bigcup_{i=1}^{n_{\mathrm{SD}}} \Omega_i^{\mathrm{SD}} \tag{3.45}$$

and

$$\Omega_i^{\mathrm{SD}} \cap \Omega_j^{\mathrm{SD}} = \varnothing , \quad \forall i \neq j \tag{3.46}$$

where Ω_i^{SD} represents the ith smoothing domain. A constant smoothed strain is assigned to each smoothing domain. The smoothing domains can be constructed in different ways; however, a valid construction must satisfy certain conditions detailed in (Liu and Zhang, 2013a). In the edge-based smoothed point interpolation method, the smoothing domains are associated with edges of the background cells is such a way that the smoothing domain Ω_k^{SD} associated with kth edge is created by connecting the nodes at the ends of this edge to the two centroids of the two adjacent triangular cells sharing edge k, as shown in Figure 3-2. Such a set of smoothing domains satisfies the necessary requirements mentioned above. These set of smoothing domains are also used for performing numerical integrations. Therefore, the domain integrations become simple summation over the smoothing domains.

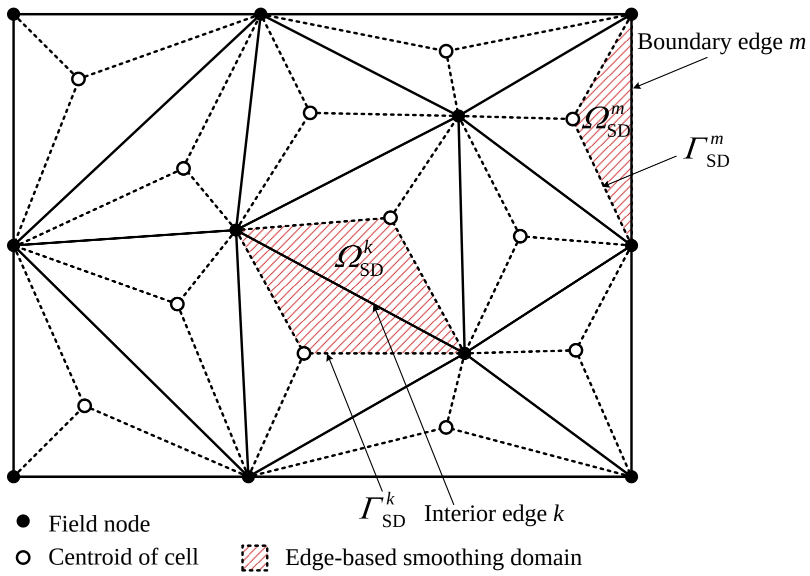

Figure 3-2- The schematic representation of triangularisation of the problem domain and edge based smoothing domains

3.4.3. Node selection schemes

For a point of interest located inside the problem domain, there are different schemes available for selection of supporting nodes using the triangular cells (T-schemes). A brief discretion of the several T-schemes adopted in this study is given below. These schemes are selected as they create shape functions which allow the use of edge based smoothing domains explained earlier. In other words, these T-schemes result in an approximated displacement field which may be discontinuous along the boundary of the smoothing domain only in a finite number of points. The manners in which supporting nodes are adopted in T-schemes are illustrated in Figure 3-3. It should be noted that when the point of interest is on the boundary of the problem domain, only linear interpolation using the two adjacent nodes on the boundary is used. This rule is required to ensure that the ES-PIM method passes the standard patch test (Liu and Zhang, 2013a).

In the definitions to follow, the cell which hosts the point of interest is called home cell which in turn can be a boundary home cell if it has at least one edge on the boundary of the problem domain, or an interior home cell if it has no edge on the boundary of the problem domain. Cells that share an edge with the home cell are called its neighbouring cells.

3.4.3.1. Tr3 Scheme

This is the simplest node selection scheme in which we simply select the three nodes of the home cell of the point of the interest. This scheme is used only for creating PPIM shape functions with polynomial basis and avoids the singularity problem associated with the moment matrix. Therefore, the shape functions can always be constructed using this scheme. The shape functions created are linear and are the same as those in the FEM using linear triangular elements. Tr3 node selection scheme in conjunction with PPIM shape functions results in ESPIM-Tr3 model

3.4.3.2. Tr6/3 scheme

In this scheme, for an interior home cell, six nodes are selected for shape function creation: the three nodes of the home cell and the three remote nodes of the three neighbouring cells. For a boundary home cell, only three nodes of the home cell are selected. This scheme can either be used for creating high-order PIM shape functions or RPIM shape functions. In any case, the problem of singularity of the moment matrix is always avoided and therefore shape functions can always be created. In this study, Tr6/3 scheme is used for creating PPIM shape functions only, resulting into ESPIM-Tr6/3 model.

3.4.3.3. Tr6 scheme

This scheme is the same as Tr6/3 scheme for interior home cells, however it uses six nodes also for boundary cells: the three nodes of the boundary cell, the two remote nodes of the neighbouring cells and one other field node which is nearest to the centroid of the home cell excluding the five nodes which are already selected. Similar to the Tr6/3 scheme, it can be used for creating high-order PPIM or RPIM shape functions with no singularity problem associated with the moment matrix as long as some specific known shape parameters are avoided. Application of Tr6 scheme in construction of RPIM shape functions in this study yields the ESRPIM-Tr6 model.

3.4.3.4. Tr2L scheme

In this scheme, two layers of nodes around the home cell are selected. The first layer includes the three nodes of the home cell and the second layer includes those nodes which are directly connected to the three nodes of the home cell. This scheme selects more nodes compared to the previously mentioned schemes and is mainly used to create RPIM shape functions, avoiding the singularity of the moment matrix. The MM generated based from this node selection scheme is denoted by ESRPIM-Tr2L.

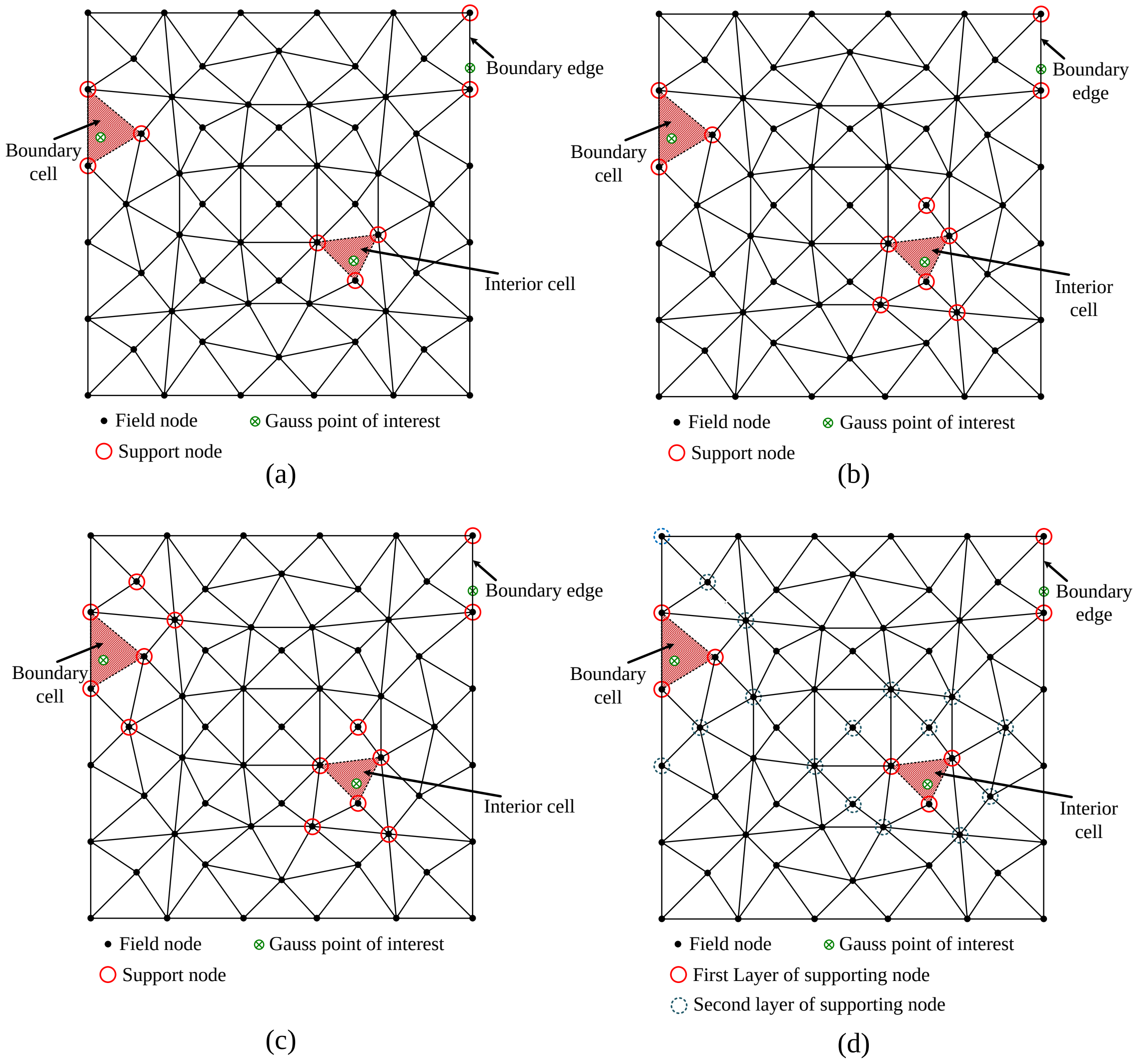

Figure 3-3- Elaboration of various node selection schemes: (a) Tr3 scheme, (b) Tr6/3 scheme (c) Tr6 scheme, (d) Tr2L scheme.

3.4.4. Edge-based smoothing operation

In the FEM, after construction of the displacement field, compatible strain can be calculated using the strain-displacement relationship which is a direct result of differentiation of the shape functions. This results in a compatible displacement field, and the strain field over the entire problem domain. The compatible strain field $\hat{\boldsymbol{\varepsilon}}(\mathbf{x})$ which is obtained from the displacement field $\hat{\mathbf{u}}(\mathbf{x})$ can be shown as

$$\hat{\boldsymbol{\varepsilon}}(\mathbf{x}) = \mathbf{L}_{\mathrm{d}}\hat{\mathbf{u}}(\mathbf{x}) = \sum_{i=1}^{n_{\mathrm{n}}} \mathbf{L}_{\mathrm{d}}\boldsymbol{\Phi}_i^{\mathrm{u}}(\mathbf{x})\hat{\mathbf{u}}_i = \sum_{i=1}^{n_{\mathrm{n}}} \hat{\mathbf{B}}_i(\mathbf{x})\hat{\mathbf{u}}_i = \hat{\mathbf{B}}(\mathbf{x})\hat{\mathbf{u}} \tag{3.47}$$

where

$$\hat{\mathbf{B}}_i(\mathbf{x}) = \begin{bmatrix} \dfrac{\partial \varphi_i}{\partial x_1} & 0 \\ 0 & \dfrac{\partial \varphi_i}{\partial x_2} \\ \dfrac{\partial \varphi_i}{\partial x_2} & \dfrac{\partial \varphi_i}{\partial x_1} \end{bmatrix} \tag{3.48}$$

and $\hat{\mathbf{u}}_i$ and $\boldsymbol{\Phi}_i^{\mathrm{u}}(\mathbf{x})$ are the compatible displacement vector and the shape function matrix of the ith node, $\mathbf{L}_{\mathrm{d}}$ is the differentiation matrix obtained as shown in equation (3.1), and $\hat{\mathbf{u}}$ is the nodal compatible displacement vector.

In the SPIM, the constructed strain $\hat{\boldsymbol{\varepsilon}}_k$ which is constant over each smoothing domain Ω_k^{SD} is approximated by an integral representation as follows

$$\hat{\boldsymbol{\varepsilon}}_k = \int_{\Omega_k^{\mathrm{SD}}} \mathbf{L}_{\mathrm{d}}\mathbf{u}(\varsigma)\tilde{\mathbf{W}}(\mathbf{x}-\varsigma)\mathrm{d}\Omega \tag{3.49}$$

in which $\tilde{\mathbf{W}}$ is a diagonal matrix of smoothing functions associated with $\mathbf{x}$, ζ is the integration variable, and $\mathbf{L}_{\mathrm{d}}\mathbf{u}$ denotes the gradient of the displacement field, or the compatible strain field. $\mathbf{u}$ is the displacement vector and assumed to be square integrable in Ω_k^{SD} in the sense of Lebesgue integration that allows occasional discontinuity at finite points within the smoothing domain. In this work, the simple Heaviside smoothing function of the following form is used

$$\tilde{\mathbf{W}}(\mathbf{x}-\varsigma)=\begin{cases}\dfrac{1}{A_k^{\mathrm{SD}}} & \varsigma\in\boxed{\Omega}_k^{\mathrm{SD}}\\ 0 & \varsigma\notin\boxed{\Omega}_k^{\mathrm{SD}}\end{cases}\tag{3.50}$$

where $A_k^{\mathrm{SD}}=\int_{\Omega_k^{\mathrm{SD}}}\mathrm{d}\Omega$ is the area of the k th smoothing domain and the frame for smoothing domain Ω_k^{SD} represents the closed domain as: $\boxed{\Omega}_k^{\mathrm{SD}}=\Omega_k^{\mathrm{SD}}\bigcup\Gamma_k^{\mathrm{SD}}$, which encompasses the area and the boundary of the smoothing domain. Utilising the Divergence theorem, the integration of the gradient of the field function over the smoothing domains is transformed into the integration of the field function itself over the boundary of the smoothing domains (Liu and Zhang, 2008). Therefore, derivation of an incompatible displacement field resulting from PIM shape functions is avoided in the formulation. This leads to the definition of the smoothed strain over the smoothing domains. The smoothed strain can be defined for both compatible and incompatible displacement fields as follows

$$\widehat{\boldsymbol{\varepsilon}}_k=\frac{1}{A_k^{\mathrm{SD}}}\int_{\Gamma_k^{\mathrm{SD}}}\mathbf{L}_{\mathrm{n}}\mathbf{u}(\mathbf{x})\mathrm{d}\Gamma\tag{3.51}$$

where $\widehat{\boldsymbol{\varepsilon}}_k$ is the constant smoothed strain over the k th smoothing domain (Ω_k^{SD}), with the boundary Γ_k^{SD} $(k=1,2,...,n_{\mathrm{SD}})$, and $\mathbf{L}_{\mathrm{n}}$ is the matrix of unit outward normal defined in equation (3.26).

Substituting equation (3.39) into equation (3.51), the smoothed strain for the k th smoothing domain is obtained as

$$\widehat{\boldsymbol{\varepsilon}}_k=\left(\frac{1}{A_k^{\mathrm{SD}}}\int_{\Gamma_k^{\mathrm{SD}}}\mathbf{L}_{\mathrm{n}}\mathbf{\Phi}^{\mathrm{u}q}(\mathbf{x})\mathrm{d}\Gamma\right)\bar{\mathbf{u}}_q=\sum_{i=1}^{q}\begin{bmatrix}\widehat{b}_{1_i} & 0\\ 0 & \widehat{b}_{2_i}\\ \widehat{b}_{2_i} & \widehat{b}_{1_i}\end{bmatrix}\begin{Bmatrix}u_{1_i}\\ u_{2_i}\end{Bmatrix}=\widehat{\mathbf{B}}_1\bar{\mathbf{u}}_q\tag{3.52}$$

with

$$\mathbf{\Phi}^{\mathrm{u}q}(\mathbf{x}) = \begin{bmatrix} \varphi_1(\mathbf{x}) & 0 & \varphi_2(\mathbf{x}) & 0 & \cdots & \varphi_q(\mathbf{x}) & 0 \\ 0 & \varphi_1(\mathbf{x}) & 0 & \varphi_2(\mathbf{x}) & & 0 & \varphi_q(\mathbf{x}) \end{bmatrix}_{2\times 2q} \tag{3.53}$$

$$\widehat{\mathbf{B}}_1 = \begin{bmatrix} \widehat{b}_{1_1} & 0 & \widehat{b}_{2_1} & 0 & & \widehat{b}_{q_1} & 0 \\ 0 & \widehat{b}_{1_2} & 0 & \widehat{b}_{2_2} & \cdots & 0 & \widehat{b}_{q_2} \\ \widehat{b}_{1_2} & \widehat{b}_{1_1} & \widehat{b}_{2_2} & \widehat{b}_{2_1} & & \widehat{b}_{q_2} & \widehat{b}_{q_1} \end{bmatrix}_{3\times 2q} \tag{3.54}$$

$$\bar{\mathbf{u}}_q = \begin{bmatrix} u_{1_1} & u_{2_1} & u_{1_2} & u_{2_2} & \cdots & u_{1_q} & u_{2_q} \end{bmatrix}^{\mathrm{T}} \tag{3.55}$$

and

$$\widehat{b}_{i_l} = \frac{1}{A_k^{\mathrm{SD}}} \int_{\Gamma_k^{\mathrm{SD}}} \varphi_i(\mathbf{x}) n_l(\mathbf{x}) \mathrm{d}\Gamma, \quad l = 1, 2 \tag{3.56}$$

where q is the total number of supporting nodes of all the Gauss points on the boundaries of the kth smoothing domain ($q \geq p$). Employing the Gauss integration scheme, the integration in equation (3.56) can be further simplified in a summation form considering the linear segments of the smoothing domain boundaries,

$$\widehat{b}_{i_l} = \frac{1}{2A_k^{\mathrm{SD}}} \sum_{m=1}^{n_{\mathrm{seg}}} \left(L_m^k \sum_{n=1}^{n_{\mathrm{G}}} w_{\mathrm{G}}^n \varphi_i(\mathbf{x}_{\mathrm{G}}^{n,m}) n_l^m \right), \quad l = 1, 2 \tag{3.57}$$

where n_{seg} is the number of line segments of the boundary Γ_k^{SD}, n_l^m is the lth component of the unit outward normal vector to the mth segment of Γ_k^{SD}, n_{G} is the number of Gauss points on each segment of Γ_k^{SD}, $\mathbf{x}_{\mathrm{G}}^{n,m}$ is coordinate of the nth Gauss point on the mth segment of Γ_k^{SD}, L_m^k is the length of the mth segment of Γ_k^{SD}, and w_{G}^n is the corresponding Gauss integration weight. $\varphi_i(\mathbf{x}_{\mathrm{G}}^{n,m})$ is the shape function value at node i at the Gauss point of interest $\mathbf{x}_{\mathrm{G}}^{n,m}$. If node i is not among the supporting nodes of the current point of interest, then $\varphi_i(\mathbf{x}_{\mathrm{G}}^{n,m}) = 0$.

It can be observed that unlike the compatible strain field, there is no need for derivation of the shape functions in calculation of the smoothed strains. Hence, the discontinuity of the approximation function does not pose any problem. This further weakens the consistency requirement to shape functions and that is why the formulation is called weakened weak (W^2) formulation, as opposed to the weak formulation used in many numerical techniques such as the FEM (Liu and Zhang, 2008).

3.5. Numerical algorithm

3.5.1. Discretised system of equations

Applying the GS-Galerkin approach to the flow and deformation coupled equations (3.2) and (3.18), and neglecting the effect of the self-weight of the pore fluid in the total head at any point, the general discretised form of the governing equations is defined as

$$\mathbf{KU} - \eta\mathbf{QP}_{\mathrm{f}} = \mathbf{F}_{\mathrm{u}} \tag{3.58}$$

$$-\eta\mathbf{Q}^{\mathrm{T}}\dot{\mathbf{U}} - \mathbf{HP}_{\mathrm{f}} - a_{\mathrm{f}}\mathbf{S}\dot{\mathbf{P}}_{\mathrm{f}} = \mathbf{F}_{\mathrm{f}} \tag{3.59}$$

where $\mathbf{U}$ is the vector of nodal displacements, $\mathbf{P}_{\mathrm{f}}$ is the vector of the nodal pore fluid pressures, $\mathbf{F}_{\mathrm{u}}$ is the vector of nodal forces, $\mathbf{F}_{\mathrm{f}}$ is the vector of nodal fluxes, and $\mathbf{Q}$, $\mathbf{S}$ and $\mathbf{H}$ are the global property matrices of the system. These matrices are evaluated by assembling the corresponding local property matrices associated with each smoothing domain.

Employing the smoothing operation, the global stiffness matrix is obtained as

$$\mathbf{K} = \sum_{k=1}^{n_{\mathrm{SD}}} \mathbf{K}_k^{\mathrm{SD}} = \sum_{k=1}^{n_{\mathrm{SD}}} \left(\int_{\Omega_k^{\mathrm{SD}}} \widehat{\mathbf{B}}_1^{\mathrm{T}} \mathbf{D}^{\mathrm{e}} \widehat{\mathbf{B}}_1 \mathrm{d}\Omega \right) \tag{3.60}$$

where the summation shows the assembly process, $\mathbf{K}_k^{\mathrm{SD}}$ is the local stiffness matrix of the kth smoothing domain, and $\mathbf{D}^{\mathrm{e}}$ is the linear elastic constitutive matrix for plane strain setting as

$$\mathbf{D}^{\mathrm{e}} = \frac{E}{(1+\nu)(1-2\nu)} \begin{bmatrix} 1-\nu & \nu & 0 \\ \nu & 1-\nu & 0 \\ 0 & 0 & \dfrac{1-2\nu}{2} \end{bmatrix} \tag{3.61}$$

with E and ν being the Young's modulus and the Poisson's ratio, respectively. The smoothed strain operator $\widehat{\mathbf{B}}_1$ can be taken out of the integration because it is constant over each smoothing domain. The tangent constitutive matrix $\mathbf{D}^{\mathrm{e}}$ is also taken as constant over each smoothing domain, and as a result, equation (3.60) can be written in the simplified form of

$$\mathbf{K} = \sum_{k=1}^{n_{\mathrm{SD}}} A_k^{\mathrm{SD}} \widehat{\mathbf{B}}_1^{\mathrm{T}} \mathbf{D}^{\mathrm{e}} \widehat{\mathbf{B}}_1 \tag{3.62}$$

The permeability matrix is evaluated through a similar procedure as follows (Ghaffaripour et al., 2017)

$$\mathbf{H} = \sum_{k=1}^{n_{\mathrm{SD}}} \mathbf{H}_k^{\mathrm{SD}} = \sum_{k=1}^{n_{\mathrm{SD}}} \left(\int_{\Omega_k^{\mathrm{SD}}} \widehat{\mathbf{B}}_2^{\mathrm{T}} \frac{\mathbf{k}}{\mu_{\mathrm{f}}} \widehat{\mathbf{B}}_2 \mathrm{d}\Omega \right) = \sum_{k=1}^{n_{\mathrm{SD}}} \frac{A_k^{\mathrm{SD}}}{\mu_{\mathrm{f}}} \widehat{\mathbf{B}}_2^{\mathrm{T}} \mathbf{k} \widehat{\mathbf{B}}_2 \tag{3.63}$$

where $\widehat{\mathbf{B}}_2$ is defined as

$$\widehat{\mathbf{B}}_2 = \begin{bmatrix} \widehat{b}_{1_1} & \widehat{b}_{1_2} & \cdots & \widehat{b}_{1_q} \\ \widehat{b}_{2_1} & \widehat{b}_{2_2} & & \widehat{b}_{2_q} \end{bmatrix}_{2\times q} \tag{3.64}$$

The major challenge in the application of the ESPIM/ESRPIM to coupled problems is evaluating the coupling matrix. To this end, the conventional Gauss points in the triangles composing the smoothing domains, in addition to the Gauss points located on the edges of the smoothing domains, are used to obtain the coupling matrix. Different Gauss points used in the calculation of the coupling matrix in RPIM-Tr6 and RPIM-Tr2L are illustrated in Figure 3-4 for a generic smoothing domain.

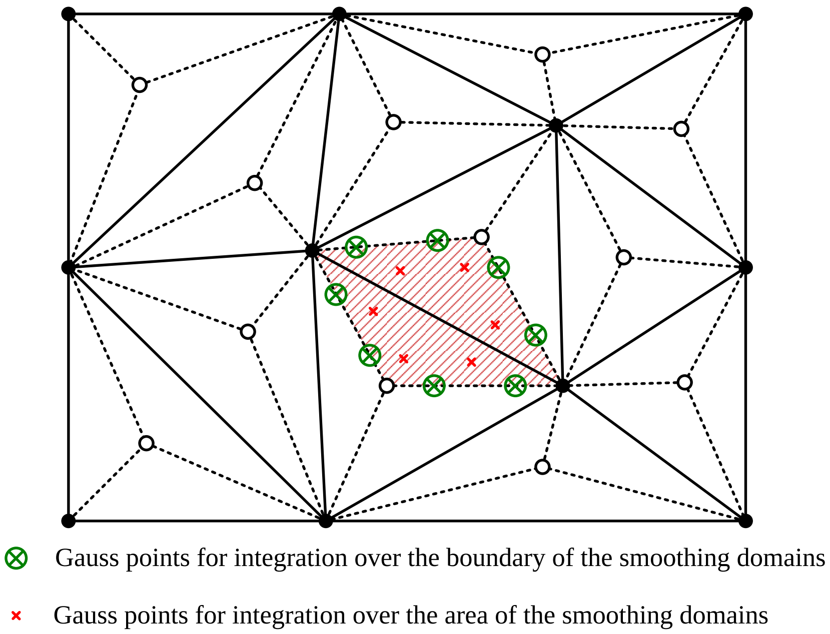

Figure 3-4- Schematic illustration of the Gauss points used for numerical integrations in RPIM-Tr6 and RPIM-Tr2L for an interior smoothing domain.

To evaluate the coupling matrix $\mathbf{Q}$, again the assembly process for all the smoothing domains along with the smoothing operation is required as follows

$$\mathbf{Q} = \sum_{k=1}^{n_{\mathrm{SD}}} \mathbf{Q}_k^{\mathrm{SD}} = \sum_{k=1}^{n_{\mathrm{SD}}} \left(\widehat{\mathbf{B}}_3^{\mathrm{T}} \int_{\Omega_k^{\mathrm{SD}}} \mathbf{\Phi}^{\mathrm{p}q} \mathrm{d}\Omega \right) \tag{3.65}$$

in which $\mathbf{\Phi}^{\mathrm{p}q}$ is the shape function matrix for the pore fluid pressure at each Gauss point of interest, which includes all the supporting nodes of the Gauss points along the boundary of the smoothing domain of interest, as follows

$$\mathbf{\Phi}^{\mathrm{p}q} = \begin{bmatrix} \varphi_1 & \varphi_2 & \cdots & \varphi_q \end{bmatrix}_{1\times q} \tag{3.66}$$

and $\widehat{\mathbf{B}}_3$ is

$$\widehat{\mathbf{B}}_3 = \begin{bmatrix} \widehat{b}_{1_1} & \widehat{b}_{2_1} & \widehat{b}_{1_2} & \widehat{b}_{2_2} & \cdots & \widehat{b}_{1_q} & \widehat{b}_{2_q} \end{bmatrix}_{1\times 2q} \tag{3.67}$$

It is worth mentioning that although the above procedure is simple and the natural extension of the conventional Gauss integration for calculation of the coupling matrix in SPIMs, it had never been used in the literature before this study. Schönewald et al. (2012) adopted an approximation technique for the calculation of the coupling matrix of the discretised system of equations in which they used Gauss points located on the boundary of the smoothing domains, rather than the conventional Gauss points, for the calculation of the area integrations over the smoothing domains. In this approach, the numerical errors can only be controlled by refining the background mesh, because adopting more Gauss points for the area integrations is not practical. The same approach was also used in the studies by Soares Jr (2013b) and Soares Jr et al. (2014).

The term $\int_{\Omega_k^{\mathrm{SD}}} \mathbf{\Phi}^{\mathrm{p}q} \mathrm{d}\Omega$ in equation (3.65) has to be evaluated over each smoothing domain. This is done by dividing each interior smoothing domain into two triangles and using the standard Gauss integration method for the triangular areas. The division is not required for the boundary smoothing domains. In case of PPIM-Tr3 and PPIM-Tr6/3 shape functions, one Gauss point per triangle is sufficient because the shape functions are linear; however, if the shape functions are nonlinear, more Gauss points in each triangle can be adopted. In this study, three Gauss points per triangle are adopted for the numerical integrations when RPIM-Tr6 and RPIM-Tr2L shape functions are used, as shown in Figure 3-4. If the total number of such Gauss points over each triangle is denoted by n_{gtr} (which is either 1 or 3 in this study) and the number of triangles constituting each smoothing domain is denoted by n_{tr} (which is 2 for interior smoothing domains and 1 for boundary smoothing domains), then the coupling matrix can be obtained as follows,

$$\mathbf{Q}=\sum_{k=1}^{n_{\mathrm{SD}}}\left(2\widehat{\mathbf{B}}_3^{\mathrm{T}}\sum_{i=1}^{n_{\mathrm{tr}}}A_i^{\mathrm{tr}}\left(\sum_{j=1}^{n_{\mathrm{gtr}}}w_{\mathrm{G}_j}\mathbf{\Phi}_j^{\mathrm{p}q}\right)\right) \tag{3.68}$$

where A_i^{tr} is the area of the triangle hosting the Gauss point of interest, and w_{G_j} is the weight corresponding to the Gauss point. $\mathbf{\Phi}_j^{\mathrm{p}q}$ is the fluid shape function matrix calculated at the Gauss point of interest.

Those global matrices that do not involve differentiation of the shape functions are calculated without using the smoothing operation. In such cases, the local matrices are calculated over the internal Gauss points of the smoothing domains, and are assembled into the global matrices following the standard approach. We therefore have

$$\mathbf{S}=\sum_{k=1}^{n_{\mathrm{SD}}}\int_{\Omega_k^{\mathrm{SD}}}\mathbf{\Phi}^{\mathrm{p}q\mathrm{T}}\mathbf{\Phi}^{\mathrm{p}q}\mathrm{d}\Omega \tag{3.69}$$

$$\mathbf{F}_{\mathrm{f}}=\sum_{k=1}^{n_{\mathrm{SD}}}\int_{\Gamma_k^{\mathrm{SD}}}\mathbf{\Phi}^{\mathrm{p}q\mathrm{T}}q_{\mathrm{f}}\mathrm{d}\Omega \tag{3.70}$$

where q_{f} is the imposed fluid flux across the boundary. The force vector can also be defined as

$$\mathbf{F}_{\mathrm{u}} = \sum_{k=1}^{n_{\mathrm{SD}}} \left(\int_{\Omega_k^{\mathrm{SD}}} \mathbf{\Phi}^{\mathrm{u}q\mathrm{T}} \mathbf{F} \mathrm{d}\Omega + \int_{\Gamma_k^{\mathrm{SD}}} \mathbf{\Phi}^{\mathrm{u}q\mathrm{T}} \mathbf{T} \mathrm{d}\Gamma \right) \tag{3.71}$$

in which $\mathbf{T}$ is the boundary tractions.

3.5.2. Time discretisation

The system of equations has to be also discretised in time domain. A number of time discretisation schemes are available including forward difference, Crank Nicholson, Galerkin and backward difference method. In the current work, except for the first time step in which a standard backward difference scheme is used, temporal discretisation of the equations is performed using a three-point time discretisation approach with variable time steps (Khoshghalb et al., 2011). In this algorithm, the time derivative of an arbitrary function f at time $t+\alpha\Delta t$ is estimated using the function values at times $t-\Delta t$, t and $t+\alpha\Delta t$ as

$$\dot{f}^{t+\alpha\Delta t} = \frac{Af^{t+\alpha\Delta t} - Bf^{t} + Cf^{t-\Delta t}}{\Delta t} \tag{3.72}$$

$$A = \frac{2\alpha+1}{\alpha(\alpha+1)}, \; B = \frac{\alpha+1}{\alpha}, \; \frac{\alpha}{\alpha+1} \tag{3.73}$$

where α is a constant time step growth factor, which enlarges the time interval in each step and consequently, speeds up the computations. For stability reasons, $1 \le \alpha < 1+\sqrt{2}$ should be satisfied (Khoshghalb et al., 2011).

By introduction of equations (3.72) and (3.73) into equations (3.58) and (3.59), the fully discretised governing equations are obtained in the form of

$$\mathbf{KU}^{t+\alpha\Delta t} - \eta\mathbf{QP}_{\mathrm{f}}^{t+\alpha\Delta t} = \mathbf{F}_{\mathrm{u}}^{t+\alpha\Delta t} \tag{3.74}$$

$$-\eta\mathbf{Q}^{\mathrm{T}}\left(A\mathbf{U}^{t+\alpha\Delta t}-B\mathbf{U}^{t}+C\mathbf{U}^{t-\Delta t}\right)-\Delta t\mathbf{H}\mathbf{P}_{\mathrm{f}}^{t+\alpha\Delta t}-a_{\mathrm{f}}\mathbf{S}\left(A\mathbf{P}_{\mathrm{f}}^{t+\alpha\Delta t}-B\mathbf{P}_{\mathrm{f}}^{t}+C\mathbf{P}_{\mathrm{f}}^{t-\Delta t}\right)=\Delta t\mathbf{F}_{\mathrm{f}}^{t+\alpha\Delta t} \tag{3.75}$$

The overall matrix form of equation is therefore stated as

$$\mathbf{E}\mathbf{W}=\mathbf{Y} \tag{3.76}$$

in which

$$\mathbf{E}=\begin{bmatrix} A\mathbf{K} & -\eta\mathbf{Q} \\ -A\eta\mathbf{Q}^{\mathrm{T}} & -(\Delta t\mathbf{H}+Aa_{\mathrm{f}}\mathbf{S}) \end{bmatrix}_{3n_{\mathrm{n}}\times 3n_{\mathrm{n}}} \tag{3.77}$$

$$\mathbf{W}=\begin{Bmatrix} \mathbf{U}^{t+\alpha\Delta t} \\ \mathbf{P}_{\mathrm{f}}^{t+\alpha\Delta t} \end{Bmatrix}_{3n_{\mathrm{n}}\times 1} \tag{3.78}$$

$$\mathbf{Y}=\begin{bmatrix} A\mathbf{F}_{\mathrm{u}}^{t+\alpha\Delta t} \\ \Delta t\mathbf{F}_{\mathrm{f}}^{t+\alpha\Delta t}-B\eta\mathbf{Q}^{\mathrm{T}}\mathbf{U}^{t}+C\eta\mathbf{Q}^{\mathrm{T}}\mathbf{U}^{t-\Delta t}-Ba_{\mathrm{f}}\mathbf{M}\mathbf{P}_{\mathrm{f}}^{t}+Ca_{\mathrm{f}}\mathbf{M}\mathbf{P}_{\mathrm{f}}^{t-\Delta t} \end{bmatrix}_{3n_{\mathrm{n}}\times 1} \tag{3.79}$$

where n_n is the total number of nodes.

Equation (3.76) should be solved in each time step. However, it is not possible in the first time step to use the three point temporal discretisation scheme. Therefore, the backward difference method is adopted for the first time step and therefore the discretised equations will be as follows,

$$\mathbf{K}\mathbf{U}^{t_0+\alpha\Delta t_0}-\eta\mathbf{Q}\mathbf{P}_{\mathrm{f}}^{t_0+\alpha\Delta t_0}=\mathbf{F}_{\mathrm{u}}^{t_0+\alpha\Delta t_0} \tag{3.80}$$

$$-\eta\mathbf{Q}^{\mathrm{T}}\left(\mathbf{U}^{t_0+\alpha\Delta t_0}-\mathbf{U}^{t_0}\right)-\alpha\Delta t\mathbf{H}\mathbf{P}_{\mathrm{f}}^{t_0+\alpha\Delta t_0}-a_{\mathrm{f}}\mathbf{S}\left(\mathbf{P}_{\mathrm{f}}^{t_0+\alpha\Delta t_0}-\mathbf{P}_{\mathrm{f}}^{t_0}\right)=\alpha\Delta t\mathbf{F}_{\mathrm{f}}^{t_0+\alpha\Delta t_0} \tag{3.81}$$

which leads to the following form of the matrix equation for the first time step

$$\begin{bmatrix} \mathbf{K} & -\eta\mathbf{Q} \\ -\eta\mathbf{Q}^{\mathrm{T}} & -(\alpha\Delta t\mathbf{H}+a_{\mathrm{f}}\mathbf{S}) \end{bmatrix} \begin{Bmatrix} \mathbf{U}^{t_0+\alpha\Delta t_0} \\ \mathbf{P}_{\mathrm{f}}^{t_0+\alpha\Delta t_0} \end{Bmatrix} = \begin{bmatrix} A\mathbf{F}_{\mathrm{u}}^{t_0+\alpha\Delta t_0} \\ \alpha\Delta t\mathbf{F}_{\mathrm{f}}^{t_0} - \eta\mathbf{Q}^{\mathrm{T}}\mathbf{U}^{t_0} - a_{\mathrm{f}}\mathbf{S}\mathbf{P}_{\mathrm{f}}^{t_0} \end{bmatrix} \tag{3.82}$$

where t_0 is the starting time and Δt_0 is the initial time increment.

3.6. Numerical examples

A number of numerical examples are to be evaluated to show the applicability, accuracy and stability of the proposed fully coupled hydro-mechanical meshfree model. Firstly, the model is examined through a one-dimensional consolidation problem and the numerical results are compared to those of analytical solution proposed by Terzaghi (1925). Secondly, a two-dimensional problem is investigated and robustness of the numerical model is demonstrated by comparing the results to the analytical results of Schiffman et al. (1969). Finally, a hydraulic pulse test is modelled and compared to semi-analytical solutions proposed by Selvadurai and Carnaffan (1997) and Selvadurai (2009).

3.6.1. One-dimensional consolidation

The first example studied here is the Terzaghi's one dimensional consolidation problem, as illustrated in Figure 3-5. Single side drainage from the top surface is assumed. The left and right sides and the bottom are all fixed for horizontal displacements, while vertical displacement is allowed on the side boundaries. The thickness of the soil layer is taken as $H = 16\,\mathrm{m}$ and the intensity of the surface surcharge is $Q = 10.0\ \mathrm{kPa}$. Linear elastic drained parameters of soil are assumed as $E' = 30,000\,\mathrm{kPa}$ and $\nu' = 0.3$. The intrinsic coefficient of permeability and dynamic viscosity of water are assumed as $k = 10^{-12}\,\mathrm{m}^2$ and $\mu_{\mathrm{f}} = 10^{-6}\,\mathrm{kPa.s}$, respectively. Analytical solution for this problem is available in Das (2013).

The problem is studied using the four ESPIM models introduced earlier in this chapter. The problem domain is discretised using the same background mesh for all models as illustrated in Figure 3-5, which comprises of 149 nodes and 256 triangular elements. The initial dimensionless time increment is taken as $\Delta t_{\mathrm{D}} = 0.01$, where the dimensionless time is defined as $t_{\mathrm{D}} = E' k \left(1-\nu'\right) t \big/ \left(\mu_{\mathrm{f}} \left(1+\nu'\right)\left(1-2\nu'\right) H^2\right)$. The dimensionless time increment Δt_{D} grows gradually through the analysis with the growth factor $\alpha = 1.1$.

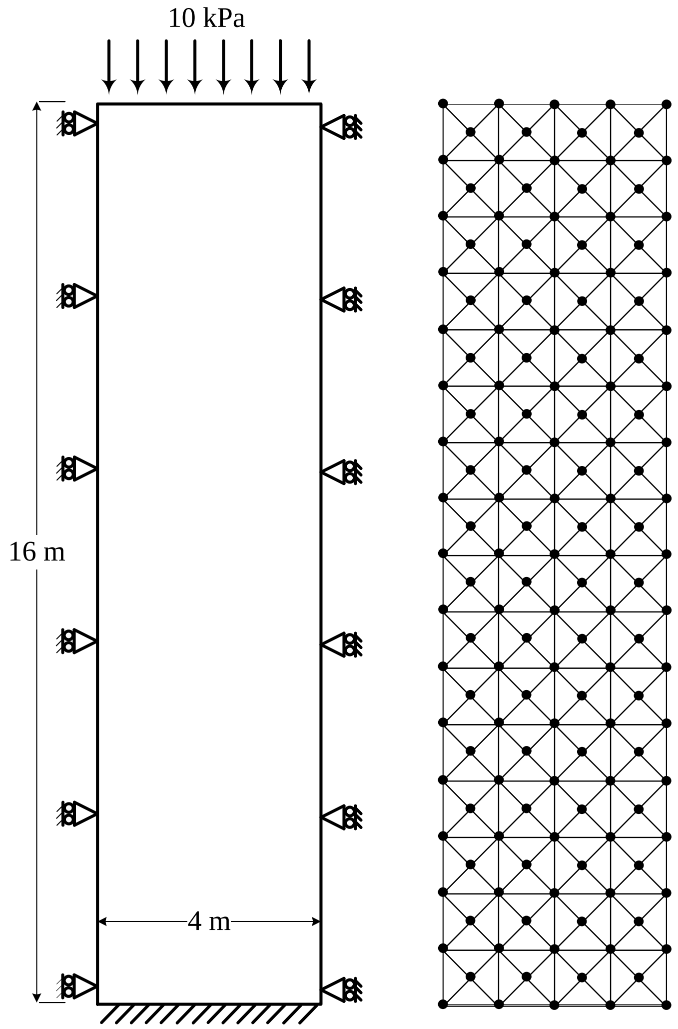

Figure 3-5- Schematic representation of the soil column in 1D consolidation problem and the background mesh associated with it.

The numerical results of different solutions in terms of dimensionless surface settlement u/u_{ult}, in which u_{ult} is the ultimate surface settlement, versus dimensionless time t_{D} are presented in Figure 3-6. One-dimensional consolidation isochrones for this single-drainage soil layer at different dimensionless times are shown in Figure 3-7. In this figure, the numerically obtained degrees of consolidation, $U_{\mathrm{z}} = 1 - p_{\mathrm{f}}/Q$, at dimensionless times equal to $t_{\mathrm{D}} = 0.095$, 0.405 and 0.983 are plotted along the dimensionless depth z/H for different meshfree models used in this study. Also included in Figure 3-6 and Figure 3-7 are the analytical solutions to the problem (Terzaghi, 1925). It can be observed that for this simple 1D consolidation problem, all the numerical results are in perfect agreement with the analytical solution and the different numerical models do not show any advantage over each other.

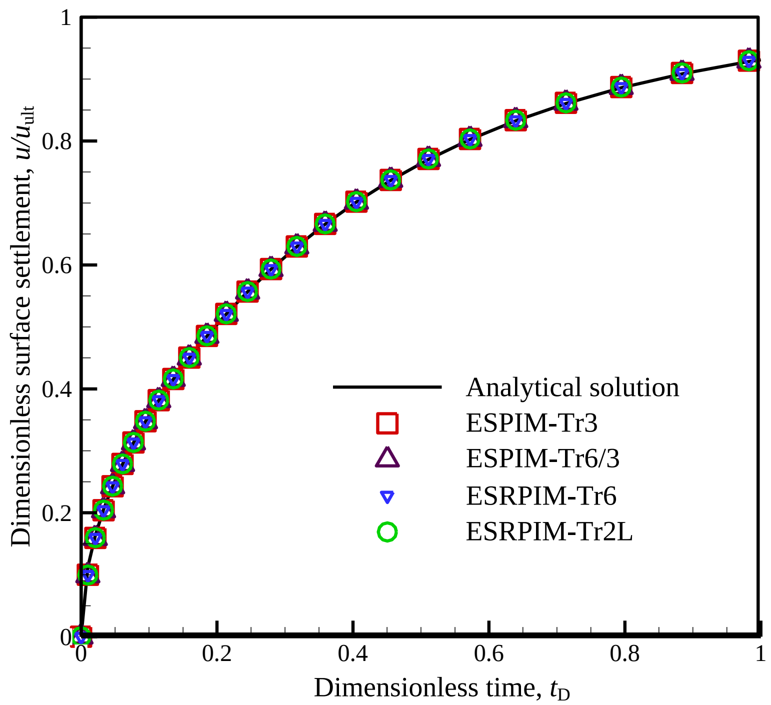

Figure 3-6- Dimensionless surface settlement versus dimensionless time for different ESPIM and ESRPIM models.

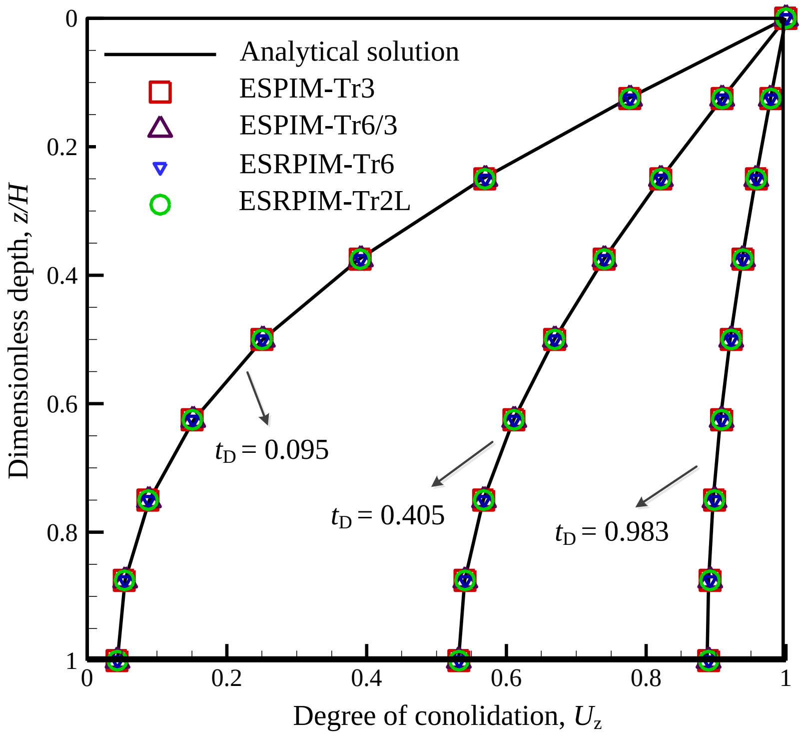

Figure 3-7- One-dimensional consolidation isochrones for a single-drainage soil layer at different dimensionless times

3.6.2. Two-dimensional consolidation

The problem of two-dimensional consolidation of a saturated soil layer under plane strain condition and subjected to a strip loading is studied here. The intensity of the strip loading is $Q = 10.0$ kPa . The top surface is fully drained and the rest of the boundaries are all assumed to be impervious. Horizontal displacement is fixed along vertical boundaries and all displacements are fixed along the bottom of the domain. The lateral extent of the soil layer from the centre of the strip load is assumed to be $6a$ and the depth of the soil layer is taken as $9a$, in which a is the half-width of the strip loaded area. A schematic model of the problem, along with the adopted background mesh, which consists of 925 nodes and 1725 triangular elements, are shown in Figure 3-8. It should be mentioned that only one-half of the medium is simulated because of symmetry.

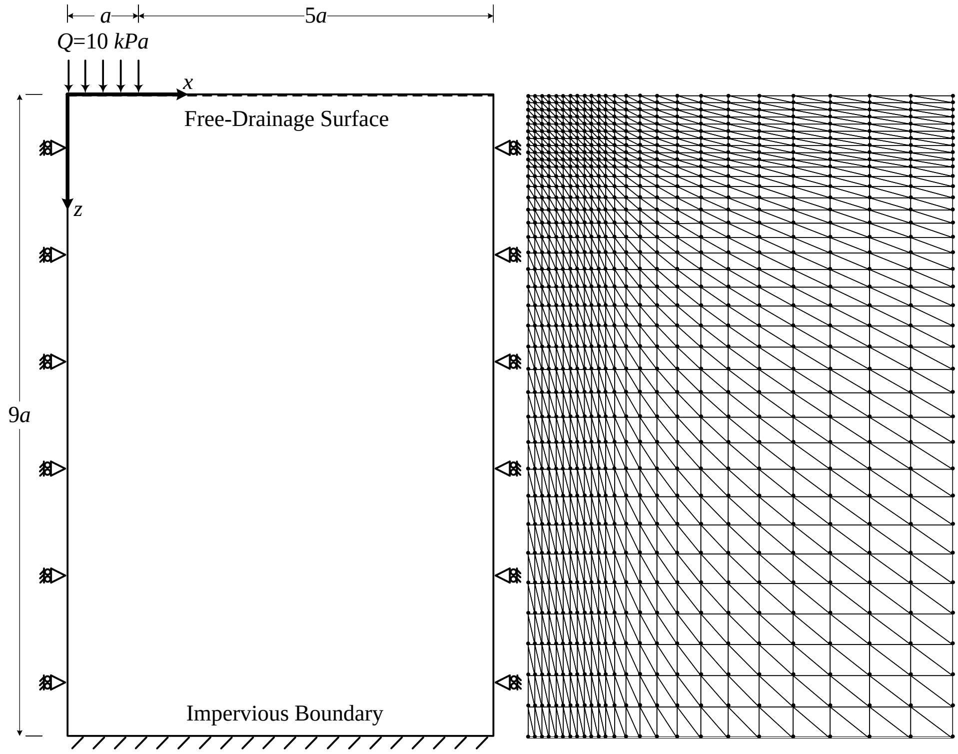

Figure 3-8- Representation of a two-dimensional consolidation problem and the background mesh used in the numerical analysis.

The material properties adopted for the analysis are as follows: $\mu_{\mathrm{f}} = 10^{-6}\,\mathrm{kPa.s}$, $k = 10^{-15}\,\mathrm{m}^2$, $E' = 30{,}000\,\mathrm{kPa}$, $\nu' = 0$ and $a = 1\mathrm{m}$. The initial dimensionless time step is taken $\Delta t_{\mathrm{D}} = 0.01$, where the dimensionless time for this problem is defined as $t_{\mathrm{D}} = E'kt \big/ \left(\mu_{\mathrm{f}}\left(1+\nu'\right)a^2\right)$. The time step growth factor is again taken as $\alpha = 1.1$.

Analytical solution for the variations of the normalised excess pore pressure, p_{f} / Q, with depth ratio, z / a, along the axis of symmetry at dimensionless time $t_{\mathrm{D}} = 0.1$ is available for this problem (Schiffman et al., 1969), and used here for the evaluation of the performance of the different SPIMs developed. The numerical results obtained from different numerical models are plotted along with the analytical solution in Figure 3-9. As shown in this figure, there is a good correspondence between the numerical and analytical results for all the ESPIMs. Nevertheless, the ESPIM-Tr6/3 yields less accurate pore pressures compared to the other three models. It is worth noting that the analytical solution is originally proposed for a semi-infinite domain, as opposed to the limited domain assumed in the numerical solution. Hence, the deviation of the numerical dimensionless pore pressure from the analytical solution as the impervious boundary is approached is because of the truncated boundary effect in the numerical models. This effect is also reported in other meshfree and FEM simulations (Khalili et al., 1999; Tootoonchi et al., 2016; Khoshghalb and Khalili, 2010).

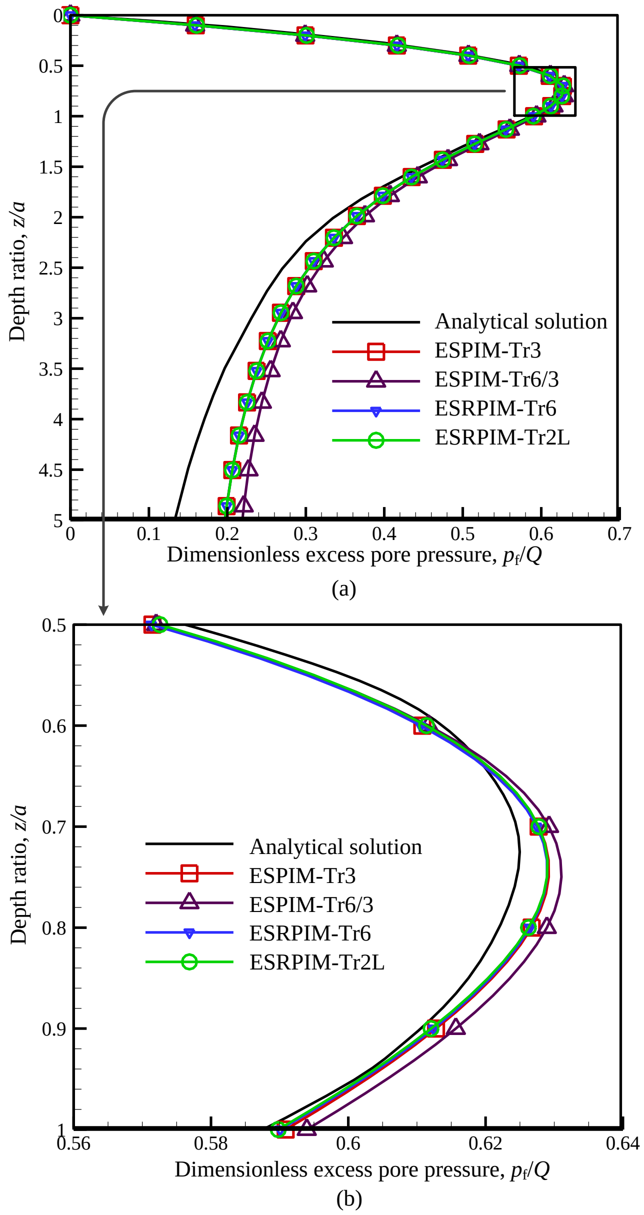

Figure 3-9- Dimensionless excess pore pressure versus depth ratio along the axis of symmetry at $t_D = 0.1$.

3.6.3. Hydraulic pulse test

The last example to verify the ESPIM/ESRPIM models is the one-dimensional hydraulic pulse test. This test involves a pressurizing rigid water chamber attached to a sample (Selvadurai and Carnaffan, 1997; Selvadurai, 2009) and is used to define the hydraulic properties of low-permeability porous material making use of the time dependent pore pressure variations within a specimen when a hydraulic pulse is applied at the boundary of the domain.. The geometry and domain representation of the problem is illustrated in Figure 3-10, where a long porous medium, $10\,\mathrm{mm}$ in diameter and $10\,\mathrm{m}$ in length, is assumed which is attached to a $4\,\mathrm{mm}$ wide rigid water chamber. A very large length to diameter ratio is adopted in this example in order to best simulate the semi-infinite domain assumed in the semi-analytical solution to this problem as detailed in Selvadurai (2009) and Khoshghalb et al. (2011)

A significantly low intrinsic permeability of $k = 10^{-19}\,\mathrm{m}^2$ is assumed in this example. The dynamic viscosity of water is $\mu_\mathrm{f} = 10^{-6}\,\mathrm{kPa.s}$, and the coefficient of compressibility of water is taken as $c_\mathrm{f} = 4.54\times10^{-7}\ \mathrm{kPa}^{-1}$. The drained Young's modulus and the Poisson's ratio are assumed as $E' = 10,000\,\mathrm{kPa}$ and $\nu' = 0.3$, respectively. The initial water pressure in the chamber is $p_{\mathrm{f}0} = 100\,\mathrm{kPa}$.

The essential boundary condition on nodes located on the boundary between the sample and the water chamber ($x = 0$) has to be updated at each time step as follows (Selvadurai, 2009)

$$p_\mathrm{f}^{t+\alpha\Delta t} = p_\mathrm{f}^{t} + \alpha\Delta t\left(\frac{q_{\mathrm{f}_i}}{V_\mathrm{ch} c_\mathrm{f}}\right)^{t} \tag{3.83}$$

where V_{ch} is the volume of the chamber and q_i is the water flux for the boundary nodes.

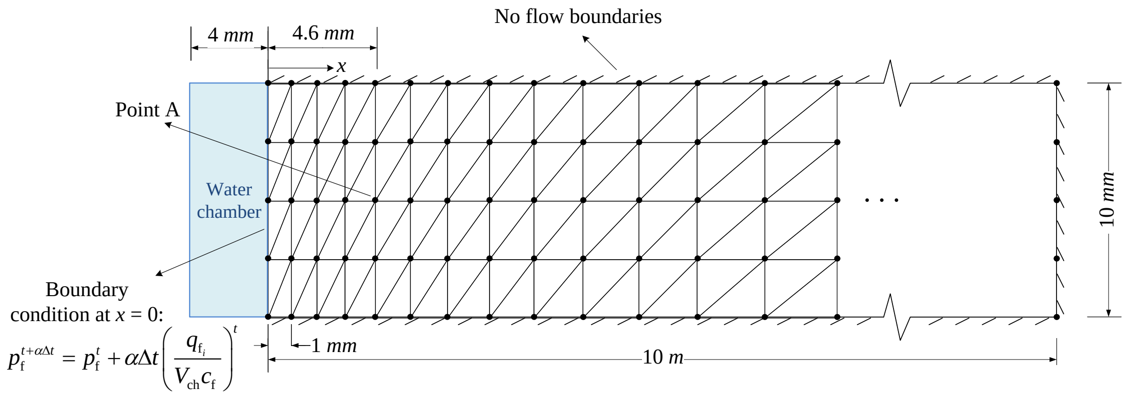

Figure 3-10- Geometry and background mesh assumed in one-dimensional hydraulic pulse test problem (not to scale).

The results of the analyses using the four meshfree models developed in this study are presented in Figure 3-11. It should be noted that the results are only presented in terms of pore water pressure as all field nodes are restrained by zero vertical and horizontal displacements. The dimensionless time factor is defined as $t_{\mathrm{D}} = \Theta^2 t$, where $\Theta^2 = k a_{\mathrm{f}} A_{\mathrm{c}}^{\,2} \Big/ \left(\mu_{\mathrm{f}} \left(V_{\mathrm{ch}} c_{\mathrm{f}}\right)^2\right)$ in which A_{c} is the cross section area of the specimen normal to the direction of flow. The vertical axis in Figure 3-11 denotes the dimensionless pore pressure $p_{\mathrm{f}} / p_{\mathrm{f0}}$ at node A, located $4.6\,\mathrm{mm}$ horizontally away from the left side of the specimen, as shown in Figure 3-10. To obtain the presented results, an initial time step of $\Delta t_0 = 1\,\mathrm{s}$ (equivalent to the dimensionless time step of $\Delta t_{\mathrm{D}_0} = 2.33\times10^{-3}$) is employed which increases in subsequent time steps using a time step growth factor of $\alpha = 1.1$.

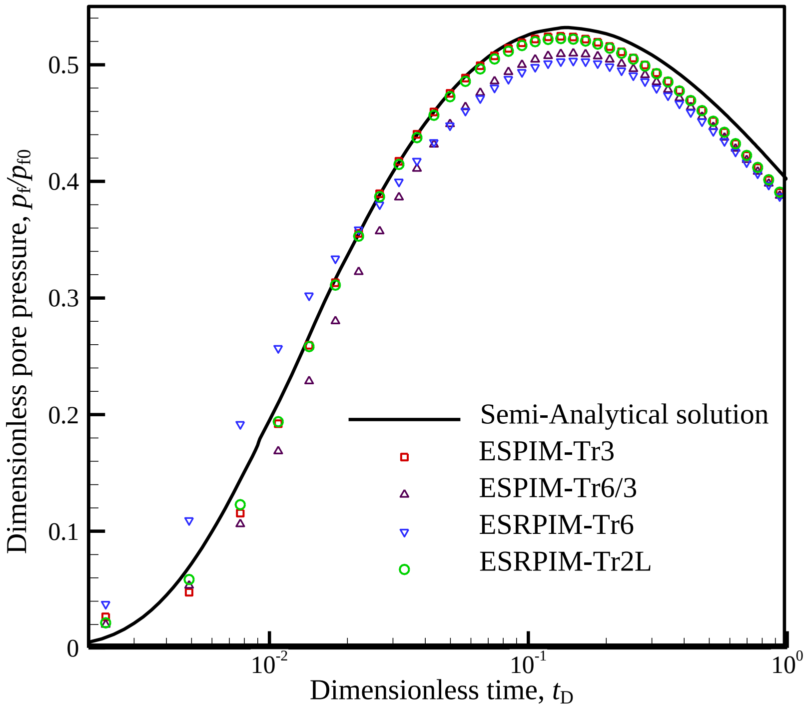

Figure 3-11- Pore pressure variations with time at x=4.6 mm in one-dimensional hydraulic pulse test.

Comparing the numerical and semi-analytical results, it is observed that ESPIM-Tr3 and ESRPIM-Tr2L models are clearly superior to the other two, yielding more accurate results in terms of pore pressure.

3.7. Conclusion

A new approach to apply the edge-based smoothed point interpolation method to fully coupled flow and deformation problems was introduced in this chapter. The displacement and pore fluid pressure fields were both approximated using either PPIM or RPIM shape functions. A strain smoothing technique was performed to assign constant strains to each edge-based smoothing domain. Temporal discretisation was carried out using a three-point time discretisation technique. The coupling matrix of the porous media was evaluated through a combination of the smoothing operation technique and the conventional Gauss integration scheme. Four different node selection schemes were used resulting in four ESPIM/ESRPIM models. The models developed were applied in simulation of three benchmark examples in poro-elasticity. Good agreement between the numerical results and analytical and semi-analytical results were obtained. ESPIM-Tr3 and ESRPIM-Tr2L yielded more accurate results, especially in terms of pore fluid pressures, than ESPIM-Tr6/3 and ESRPIM-Tr6. More in-depth verification of the models and their quantitative comparisons will be presented in the following chapter.

Chapter **4**

4. Code verification using the Method of Manufactured Solutions (MMS)

4.1. Introduction

This chapter is dedicated to application of the order of accuracy study along with the method of manufactured solutions (MMS) for verification of the in-house code developed in this study. The code is developed using Fortran programming language for fully coupled flow and deformation analysis of poro-elastic geomaterials using the ESPIM explained earlier in Chapter 3. To the best of the author's knowledge, order of accuracy study along with MMS has not been utilised in coupled problems in geomechanics to date and therefore this chapter focuses on examining the applicability of this method to geotechnical engineering problems. An overview of code verification techniques are presented first. The essence of an order of accuracy study is then presented in details along with discussions on numerical and formal order of accuracies, followed by an introduction to the MMS. The application of the MMS and order of accuracy study in coupled problems of geomechanics is then presented through verification of the developed in-house code using two manufactured solutions.

4.2. An over view of code verification techniques

Although considered synonymous in common usage, validation and verification (V&V) are two indispensable yet independent steps in evaluating the fidelity of computational codes. To put it simply, according to Blottner (1990) code validation is "solving right governing equations", while code verification is "solving governing equations right". Validation is basically performed by comparing the numerical results with the data obtained from laboratory tests and experiments. Validation is not the focus of this chapter, and it is not discussed further here.

There are different criteria for scientific code verification. The least reliable code verification approach is to seek an expert opinion on the outputs of a code, and this judgement may even be performed by the developer of the code (Roy, 2005). There are also a series of simple tests which may be exploited as part of the verification process while developing a code, but they are not an acceptable replacements for code verification (Oberkampf and Roy, 2010). Symmetry test can be used in problems with symmetrical geometries and boundary conditions. Conservation test is basically checking whether or not conservation of different variables such as mass and energy, according to the physics of the tackled problem, is satisfied. Finally, Galilean invariance test involves changing the inertial reference frames by moving it linearly with a constant speed or by simply exchanging the direction of the coordinate axes, and examining the objectivity of the solutions.

The next common verification approach is code-to-code comparison in which the results of two codes with the same mathematical and physical basis are compared to each other. This approach is valid only if the reference code is already evaluated through a rigorous verification process. In Chapter 7 of this dissertation, a code-to-code comparison is undertaken as part of the verification process for the ESPIM developed for unsaturated porous media.

The criteria discussed so far cannot be used as a substitute for rigorous verification assessments (Oberkampf and Roy, 2010). Discretisation error evaluation is another criterion in which the numerical results obtained from a discrete model using a single spatial and/or time discretisation are compared to an exact or benchmark solution (Oberkampf and Roy, 2010). This type of verification should always be accompanied with a discussion stating whether the discretisation error is small enough or not.

Convergence test, which is also referred to as consistency test, is the assessment of the rate in which the discretisation error is reduced as the mesh size decreases, without evaluating the magnitude of the error. A more comprehensive version of this verification test is called order of accuracy study. An order of accuracy study not only concerns studying the error reduction rate, but also compares this rate with the theoretical order of accuracy, which may also be called the formal order of accuracy. This approach, which is the most reliable code verification technique, is adopted in this study and will discussed in more details in the remainder of this chapter.

4.3. Order of accuracy study

The order of accuracy test is a rigorous code verification test, which examines whether or not the discretisation error of the numerical solution is reduced at the expected rate (Roy, 2005). In the order of accuracy test, the order of accuracy for the numerical scheme is obtained as the mesh and the time step are systematically refined by evaluating the reduction rate of various norms of the solution discretisation error over the domain. The error norms that are often used are L_2 and L_∞. For any state variable w (u_1, u_2 or p_f), these error norms are defined in this study as follows,

$$L_\infty = \left\| \mathbf{w}^{\mathrm{a}} - \mathbf{w}^{\mathrm{n}} \right\| = \max_{i=1}^{n'_{\mathrm{n}}} \left| w_i^{\mathrm{a}} - w_i^{\mathrm{n}} \right| \tag{4.1}$$

$$L_2 = \sqrt{\frac{1}{n'_{\mathrm{n}}} \sum_{i=1}^{n'_{\mathrm{n}}} \left(w_i^{\mathrm{a}} - w_i^{\mathrm{n}} \right)^2} \tag{4.2}$$

where L_∞ is the infinity norm and L_2 is the second norm. $\mathbf{w}^{\mathrm{a}}$ and $\mathbf{w}^{\mathrm{n}}$ are the analytical and numerical solution vectors for the state variable of interest, respectively, where w_i^{a} and w_i^{n} are the entries of these vectors for each node of interest. The variable n'_{n} is the total number of field nodes on which no essential boundary condition is applied.

The numerical order of accuracy is then compared with the formal order of accuracy, obtained or estimated from a truncation error analysis of the discrete equations or interpolation theory, depending on the numerical solution scheme adopted (Roy, 2005; Choudhary et al., 2016). If the discretisation error of the numerical solution does not reduce monotonically, or if the order of accuracy obtained from the numerical solutions fails to match the formal order of accuracy, these could be indications of a probable coding mistake or algorithm inconsistency. It is worth mentioning that there is no iterative procedure involved in the problems studied in this chapter. It is also assumed that the round-off error is negligible compared to the overall discretisation error of the solutions.

4.3.1. Numerical order of accuracy

Oberkampf and Roy (2010) proposed an approach to obtain the spatial order of accuracy in transient problems. To this end, neglecting the higher order terms, the discretisation error of the equations presented at i th spatial discretisation and j th temporal discretisation can be written in the following form

$$E_{ij}^{L} = \beta_{\mathrm{h}} h_i^{r_{\mathrm{h}}} + \beta_{\mathrm{t}} \tau_j^{r_{\tau}} + O\left(h_i^{r_{\mathrm{h}}+1}\right) + O\left(\tau_j^{r_{\tau}+1}\right) \tag{4.3}$$

where r_{h} and r_{τ} are the orders of accuracy in space and time, respectively, obtained from the numerical analysis, β_{h} and β_{t} are the coefficients of spatial and temporal terms, respectively, h_i and τ_j are normalized spatial and temporal discretisation sizes corresponding to the ith spatial discretisation and jth temporal discretisation, respectively, and L is the error norm used for order of accuracy study $(L = L_2$ or $L_{\infty})$. The higher order terms, $O\left(h_i^{r_{\mathrm{h}}+1}\right)$ and $O\left(\tau_j^{r_{\tau}+1}\right)$, can be neglected if the spatial and temporal discretisations adopted are in the asymptotic convergence range. The asymptotic range is defined as the range of discretisation sizes where the lowest-order terms in the truncation error dominate. For the developments to follow, it is assumed that the solution is in asymptotic range; however, it is noted that the identification of the asymptotic range may be challenging for complex scientific computing applications (Oberkampf and Roy, 2010).

To obtain the spatial order of accuracy of the code, a constant time step is selected $(j = \mathrm{c})$ rendering the temporal discretisation error term in equation (4.3) a constant. Spatial discretisation errors are then found through systematic mesh refinements. For three spatial discretisations $(i = 1$ to $i = 3)$, we have

$$E_{1\mathrm{c}}^{L} = \beta_{\mathrm{h}} h_1^{r_{\mathrm{h}}} + \beta_{\mathrm{t}} \tau_{\mathrm{c}}^{r_{\tau}};\ E_{2c}^{L} = \beta_{\mathrm{h}} h_2^{r_{\mathrm{h}}} + \beta_{\mathrm{t}} \tau_{\mathrm{c}}^{r_{\tau}};\ E_{3\mathrm{c}}^{L} = \beta_{\mathrm{h}} h_3^{r_{\mathrm{h}}} + \beta_{\mathrm{t}} \tau_{\mathrm{c}}^{r_{\tau}} \tag{4.4}$$

Exploiting the constancy of the temporal discretisation error term, we then have

$$E_{1\mathrm{c}}^{L} - E_{2\mathrm{c}}^{L} = \beta_{\mathrm{h}} \left(h_1^{r_{\mathrm{h}}} - h_2^{r_{\mathrm{h}}}\right) \text{ and } E_{2\mathrm{c}}^{L} - E_{3\mathrm{c}}^{L} = \beta_{\mathrm{h}} \left(h_2^{r_{\mathrm{h}}} - h_3^{r_{\mathrm{h}}}\right) \tag{4.5}$$

If the exact solution is known, the errors can be evaluated for each numerical solution. Thus, we have

$$\frac{E_{1c}^{L}-E_{2c}^{L}}{E_{2c}^{L}-E_{3c}^{L}}=\frac{h_1^{r_h}-h_2^{r_h}}{h_2^{r_h}-h_3^{r_h}}=\frac{\left(\dfrac{h_1}{h_2}\right)^{r_h}-1}{1-\left(\dfrac{h_3}{h_2}\right)^{r_h}} \tag{4.6}$$

Now, introducing the spatial discretisation refinement factor $R=h_2/h_1=h_3/h_2$ (i.e., the ratio between element sizes of two consecutive meshes in the mesh refinement study), the observed order of accuracy for spatial discretisation, r_h, can be obtained from equation (4.4) as follows

$$r_h=\frac{1}{\ln R}\ln\left(\frac{E_{2c}^{L}-E_{3c}^{L}}{E_{1c}^{L}-E_{2c}^{L}}\right) \tag{4.7}$$

As can be seen, the exact solution to the governing equations, which is often unavailable, is required in this procedure. A method to address this difficulty is discussed later in this chapter.

It is worth noting that the temporal order of accuracy can also be obtained in a similar fashion based on several analyses using same spatial discretisations, but different temporal discretisations), although it is not discussed in this study.

4.3.2. Formal order of accuracy

The formal order of accuracy is the theoretical rate of convergence of the discrete solution to the exact solution to the mathematical model. For simple mathematical models and simple solution/discretisation methods, this can be obtained using truncation error analysis of the discrete equations or interpolation theory. For example, when FDM is used for the solution of a parabolic equation, the formal spatial order of accuracy can be obtained using a truncation error analysis (e.g., (Roy, 2005)).

In this study, the ESPIM along with a three point time discretisation technique is applied to coupled flow and deformation problems in two phase saturated porous media. Due to the complexity of the governing equations and the numerical solution technique adopted in this study, determination of the spatial formal order of accuracy directly from the governing equations is difficult, if not impossible. Hence, another approach, called the residual method, is adopted for estimation of the spatial formal order of accuracy. In this approach, the exact solution to the mathematical model is substituted into the discrete governing equations. The exact solution to the mathematical model does not satisfy the discrete equations, and it can be shown that for linear problems, the remainder (referred to as discrete residual) approximates the spatial truncation error (Oberkampf and Roy, 2010). Therefore, by performing a systematic mesh refinement (with a constant time discretisation), and evaluating the discrete residual in each case, the reduction rate of the spatial truncation error can be estimated, which is the spatial formal order of accuracy of the numerical scheme.

4.3.3. Method of Manufactured Solutions

As explained earlier, exact solutions to the governing equations are required in an order of accuracy study to obtain the numerical orders of accuracy. However, exact solutions are often not available for real geotechnical engineering problems with complex initial and boundary conditions and there are only a limited number of exact solutions for complex problems involving the coupled flow and deformation response of geomaterials. Even when exact solutions are found for such complex problems, they are often resulted from significant simplifications assumed in the problems.

Given the weakness of classical methods in solving complex PDEs, the Method of Manufactured Solutions (MMS) can be utilised as an alternative which provides a straightforward and general procedure for generating analytical solution of complex system of PDEs for code verifications. As far as the adopted manufactured solutions (MS) are not mathematically problematic, their physical meaning is of no importance in conducting an order of accuracy test (Roy, 2005). The MMS is, however, code intrusive and cannot be performed on commercial codes, unless the source code can be accessed.

The basic idea behind MMS is to simply manufacture exact continuum solutions to the PDEs of interest (Roache, 2002). To this end, analytic solution to the PDEs are first assumed and next, the selected manufactured solution is substituted into the PDEs to calculate the source terms which guarantee that the selected manufactured solutions are indeed exact solutions to the governing PDEs. The source terms are distributed terms which should be applied in the code at each node of interest, according to the nature of the ESPIM code in hand. Therefore, the source code must be available and open to modifications so that such an implementation can be made while dealing with MMS.

4.4. Numerical examples

Two numerical examples based on two different MSs are discussed in this section to illustrate the application of the proposed verification technique for typical problems in geomechanics. In both examples, a $2\mathrm{m}\times 2\mathrm{m}$ weightless isotropic saturated porous medium is considered in a plane strain setting, in which $-1\,\mathrm{m}\le x\le 1\,\mathrm{m}$ and $0\le y\le 2\,\mathrm{m}$. The state variables u_1, u_2 and p_f are assumed known on the domain boundaries where the essential boundary conditions are imposed. Linear elasticity is assumed for the mechanical behaviour of the solid phase. The material parameters adopted in the numerical analyses are given in Table 4-1.

Table 4-1- Material and physical properties considered in the numerical analyses.

Parameter	Symbol	Value	Unit
Young's Modulus	E	$10,000$	kPa
Poisson's Ratio	ν	0.3	
Porosity	n	0.5	
Coefficient of permeability of fluid	k_{f}	9.81×10^{-4}	m/s
Density of fluid	ρ_{f}	1.0	$\mathrm{t/m^3}$
Dynamic viscosity of fluid	μ_{f}	10^{-6}	kPa.s
Compressibility of fluid	c_{f}	4.54×10^{-7}	kPa^{-1}
Compressibility of solid grains	c_{s}	0	
Gravitational acceleration	g	9.81	$\mathrm{m/s^2}$

Time step increment of $\Delta t = 0.1\,\mathrm{s}$ and a time step growth factor of $\alpha = 1.0$ are assumed for the numerical analyses to obtain spatial order of convergence. Five different models using different background meshes are used for evaluating the solution errors, which are detailed in Table 4-2. The background mesh sizes in Table 4-2 are obtained from $h = \sqrt{A}/\left(\sqrt{n_{\mathrm{n}}} - 1\right)$ (Liu and Zhang, 2013a), where A is the area of the domain and n_{n} is the total number of nodes.

Table 4-2- The properties of different mesh configurations for the numerical examples.

Mesh number	Number of nodes	Number of cells	Mesh size (m)
1	41	64	0.370
2	145	256	0.181
3	545	1024	0.090
4	2113	4096	0.044
5	8321	16384	0.022

The coarsest discretisation with 41 nodes is shown schematically in Figure 4-1 as an example. All refinements are performed systematically by halving the horizontal and vertical nodal distances of the coarser discretisation. This results in a refinement factor of approximately 2.0 which means the background mesh size is also halved through each refinement from the coarsest discretisation (with 41 nodes) to the finest discretisation (with 8321 nodes).

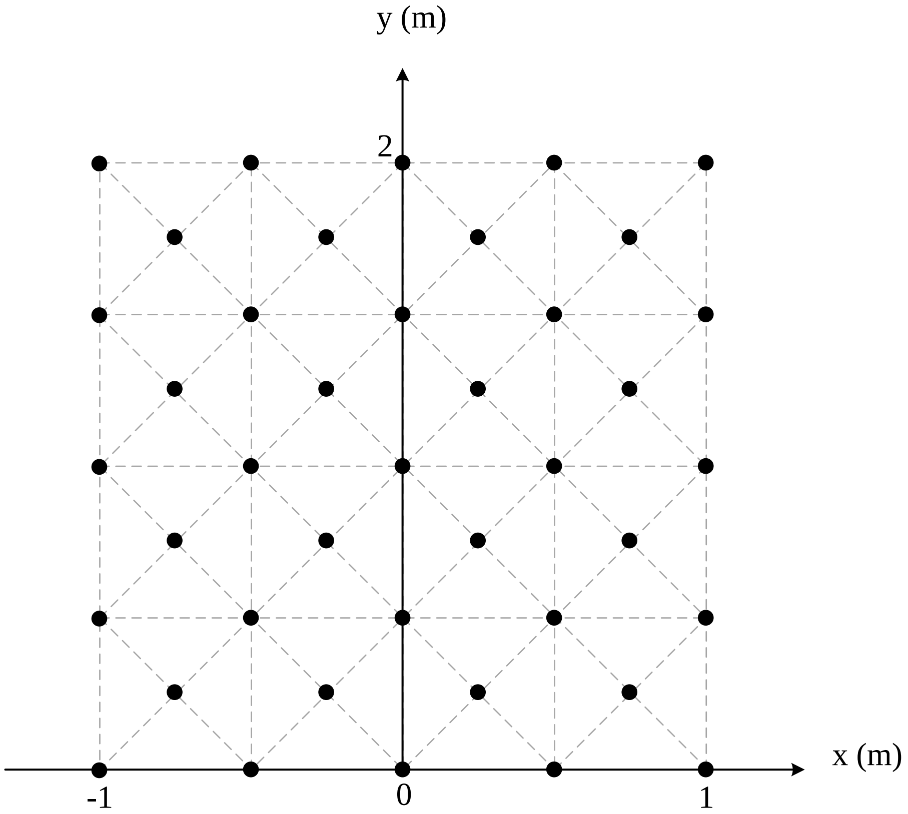

Figure 4-1- The problem domain with 41 nodes.

Now, a solution with analytical functions must be “manufactured” for this problem. The MS does not necessarily need to be physically realistic and can involve general analytical functions. For the governing equations of interest in this study, the selected MS must be smooth analytical functions of both space and time, with derivatives that do not vanish up to the second order in space and first order in time. Also, the solution should have enough complexity without any single term that dominates the other terms to ensure that all terms in the governing equations are exercised during the verification (Pelletier and Roache, 2000; Pelletier, 2010).

In this chapter, two sets of MSs are exercised. The first set is fairly simple and is used to clearly demonstrate the steps needed to perform the order of accuracy study. The second set contains more complexities and is in the form that are often recommended for generation of a comprehensive MS (e.g., (Roy, 2005)).

4.4.1. Example 1

The following arbitrary pore fluid pressure field is first assumed inside the problem domain as a function of space and time,

$$p_{\mathrm{f}}(x,y,t)=t\left(x^2+xy+y^2\right) \tag{4.8}$$

This selection ensures that all the discretised terms of the governing equations are exercised. Substituting equation (4.8) into equation (3.18), possible solutions for the vertical and horizontal displacement fields can be expressed as

$$u_1(x,y,t)=\frac{a_{\mathrm{f}}t}{2}\left(\frac{x^3}{3}+\frac{x^2y}{2}+xy^2\right)-\frac{k_{\mathrm{f}}xt^2}{\rho_{\mathrm{f}}g} \tag{4.9}$$

$$u_2(x,y,t)=\frac{a_{\mathrm{f}}t}{2}\left(\frac{y^3}{3}+\frac{y^2x}{2}+yx^2\right)-\frac{k_{\mathrm{f}}yt^2}{\rho_{\mathrm{f}}g} \tag{4.10}$$

The assumed pore fluid pressure and the resultant displacement fields are shown within the problem domain at $t=10\,\mathrm{s}$ in Figure 4-2.

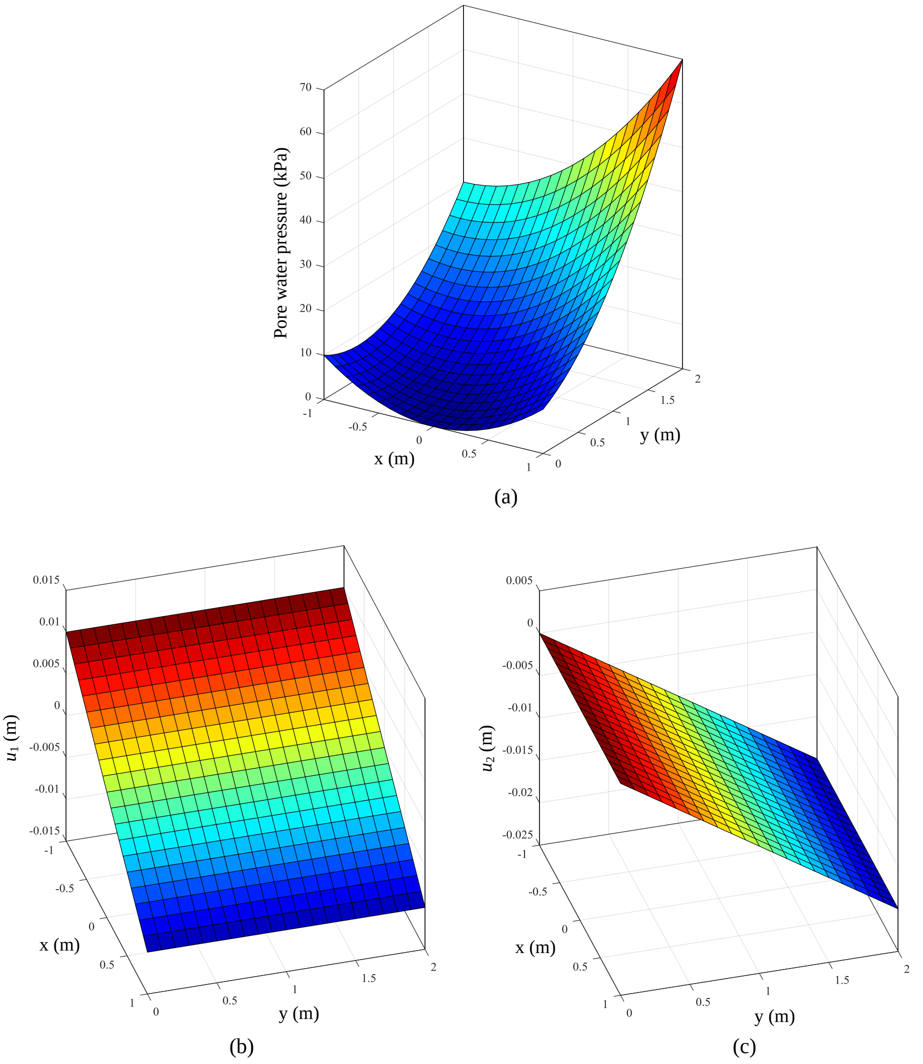

Figure 4-2- Distribution of the field variables in example 1 over the problem domain at $t = 10\,\mathrm{s}$. (a) Pore fluid pressure, (b) Displacement in x direction, (c) Displacement in y direction.

Having calculated the displacements, the components of the body force vector (**F**) required to satisfy the governing equation (3.2) at any time anywhere in the problem domain are calculated as

$$F_1 = -\frac{a_f Etx}{2(1+\nu)} - t\left(2x+y\right)\left[1+\frac{a_f}{4}\frac{E(3-2\nu)}{(1+\nu)(1-2\nu)}\right] \tag{4.11}$$

$$F_2 = -\frac{a_f Ety}{2(1+\nu)} - t\left(2y+x\right)\left[1+\frac{a_f}{4}\frac{E(3-2\nu)}{(1+\nu)(1-2\nu)}\right] \tag{4.12}$$

No source term for the second governing equation is needed in this case, because the MSs are chosen in such a way that they satisfy equation (3.18).

Substituting equations (4.11) and (4.12) in equation (3.71) to obtain the vector of nodal forces, the analysis can be carried out through time to obtain the numerical solutions. The analytical solutions of equations (4.8) to (4.10) can then be used to assess the convergence and accuracy of the numerical solutions.

Figure 4-3 illustrates the summary of the spatial order of accuracy study for this example. In this figure, the error norms of the numerical solutions are plotted for state variables p_f, u_1 and u_2 at $t = 10\,\mathrm{s}$. The second order line is also depicted on the graphs for comparison purposes. The results presented are obtained with double precision computations. There were also no iterations involved in the numerical algorithms. Therefore, the spatial discretisation error is the dominant error in all the calculations.

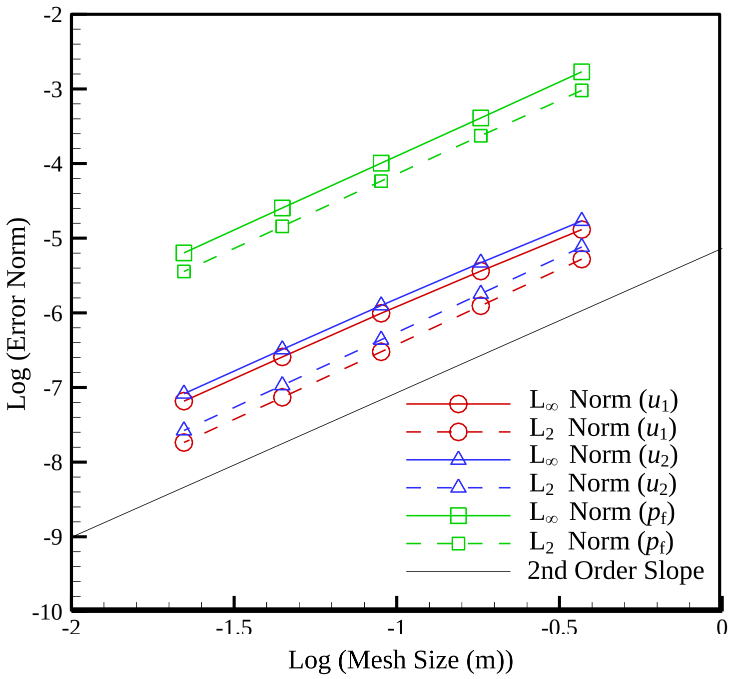

Figure 4-3- Order of accuracy study for example 1 at $t = 10\,\mathrm{s}$ for obtaining the observed spatial orders of accuracy.

Figure 4-4 summarises the observed spatial convergence rates as a function of mesh size. Note the horizontal axes show the average of the three consecutive refinements between which the spatial convergence rate is obtained. As can be clearly seen in Figure 4-4, the numerical method shows second order accuracy in L_2 and L_∞ norms. Due to the simplicity of the adopted state variables in this example, the numerical method is capable of predicting the state variables inside the problem domain very accurately even using a coarse discretisation, and this capability does not seem to be threatened severely as coarser discretisations are adopted. Therefore, the observed convergence rates rarely deviate from 2.0 for different discretisations.

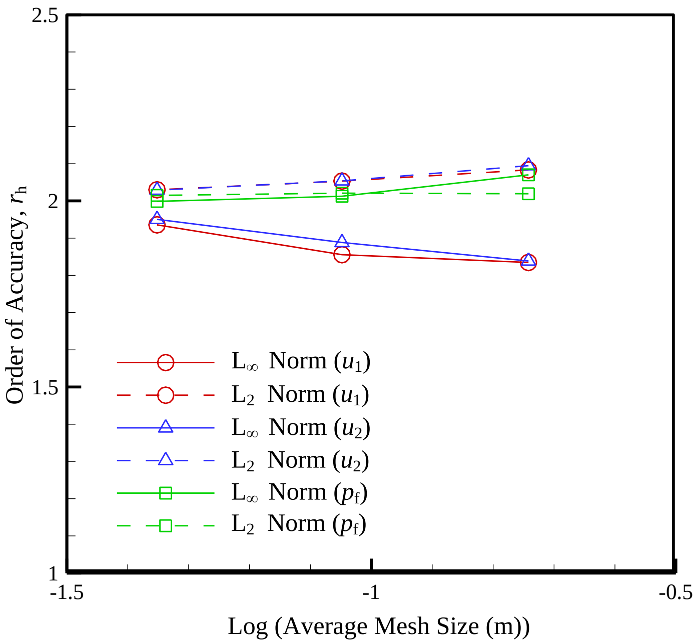

Figure 4-4- Observed spatial order of accuracies at $t = 10\,\mathrm{s}$ for example 1.

To evaluate the observed convergence rates, the formal spatial orders of accuracy are obtained through the procedure elaborated in section 4.3.2. Figure 4-5 illustrates the results of the studies performed for obtaining the formal orders of accuracy for different state variables at $t = 10\,\mathrm{s}$. The observed formal spatial orders of accuracy are also reported in Figure 4-6.

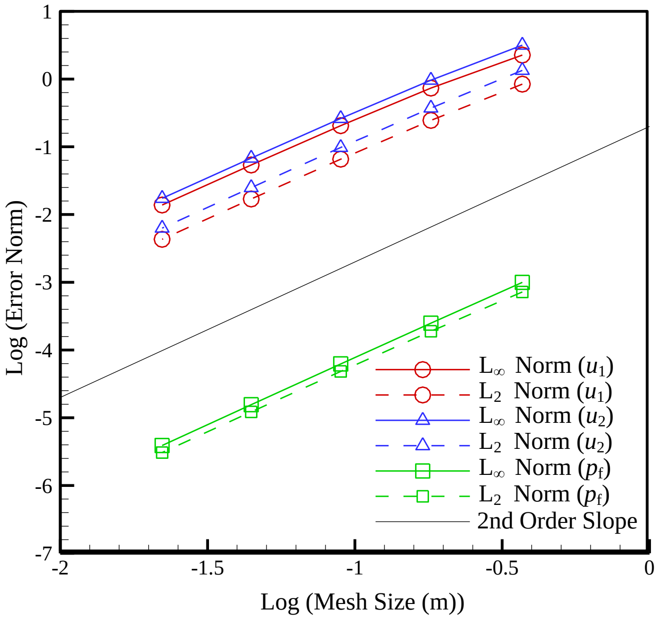

Figure 4-5- Order of accuracy study for example 1 at $t = 10\,\text{s}$ for obtaining the formal spatial orders of accuracy.

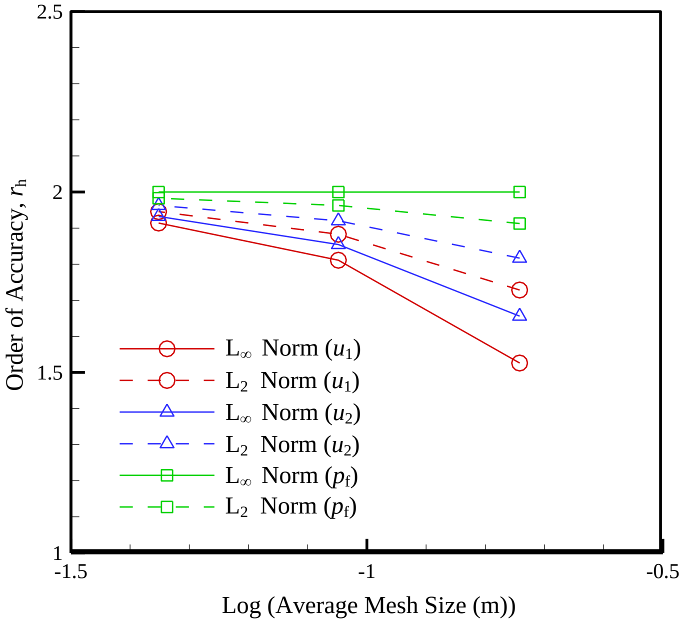

Figure 4-6- Formal spatial orders of accuracy at $t = 10\,\text{s}$ for example 1.

In linear analyses, the study of the accuracy and convergence of the numerical solution are often performed in terms of the energy error norm, E_e, defined as,

$$E_e = \sqrt{\frac{1}{2}\sum_{k=1}^{n_{\mathrm{SD}}}\int_{\Omega_k^{\mathrm{SD}}}\left(\boldsymbol{\varepsilon}_k^{\mathrm{a}} - \boldsymbol{\varepsilon}_k^{\mathrm{n}}\right)^{\mathrm{T}}\mathbf{D}^{\mathrm{e}}\left(\boldsymbol{\varepsilon}_k^{\mathrm{a}} - \boldsymbol{\varepsilon}_k^{\mathrm{n}}\right)\mathrm{d}\Omega_k^{\mathrm{SD}}} \Bigg/ \sqrt{\sum_{k=1}^{n_{\mathrm{SD}}} A_k^{\mathrm{SD}}} \tag{4.13}$$

where $\boldsymbol{\varepsilon}_k^{\mathrm{a}}$ and $\boldsymbol{\varepsilon}_k^{\mathrm{n}}$ are the analytical and numerical strain vectors corresponding to the kth smoothing domain. Figure 4-7 shows the formal and numerically observed spatial convergence rates of energy norm for different nodal discretisations at $t = 10\,\mathrm{s}$.

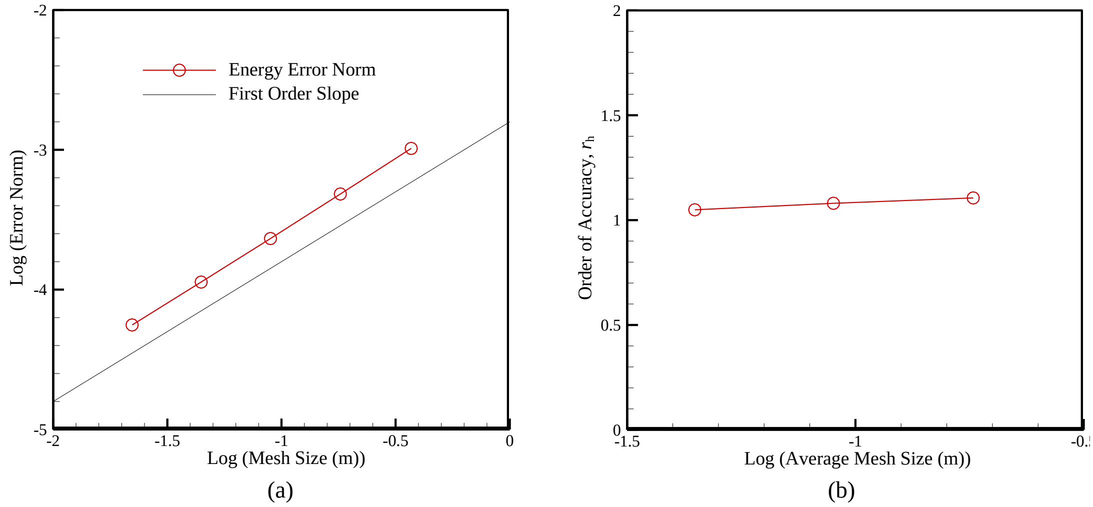

Figure 4-7- (a) Energy error norm at $t = 10\,\mathrm{s}$, (b) Observed spatial order of accuracy in terms of energy error norm, for example 1.

Comparing Figure 4-3 and Figure 4-4 to Figure 4-5 and Figure 4-6, it can be seen that the formal spatial order of accuracies are recovered. The second order of accuracy was expected as the problem is linear and moreover, linear interpolants are used in the ESPIM-Tr3 model. Furthermore, it is known that for smooth solutions like the adopted manufacture solution in this example, the order of accuracy for strain results is one order lower than that of displacements (Belytschko et al., 2000). Noting Figure 4-7, it can be seen that the expected first order accuracy in strain energy is also recovered using the adopted meshfree model and the code is therefore verified, spatially, for the selected MS. It is worth mentioning that for simplicity, the current example was examined using a suit of simple nodal discretisations; however, nodal discretisations with severer irregularities are needed for a more general code verification analysis.

4.4.2. Example 2

The second set of MSs are selected according to the general recommendation by Oberkampf and Roy (2010), as follow

$$u_1 = 0.02 + 0.01(x^2 - 1)^2 (y^2 - 2y)^2 \cos(\frac{\pi t}{9}) \left[3\sin(\frac{5\pi x}{4}) - 2\sin(\frac{3\pi y}{4}) + \cos(\pi xy) \right] \qquad (4.14)$$

$$u_2 = -0.01 + 0.01(x^2 - 1)^2 (y^2 - 2y)^2 \sin(\frac{\pi t}{15}) \left[\sin(\frac{3\pi x}{4}) + 2\cos(\pi y) - \sin(\frac{5\pi xy}{4}) \right] \qquad (4.15)$$

$$p_{\mathrm{f}} = 200 + 5(x^2 - 1)^2 (y^2 - 2y)^2 \cos(\frac{\pi t}{12}) \left[3\sin(\pi x) - \cos(\frac{5\pi xy}{4}) - \cos(\frac{3\pi xy}{4}) \right] \qquad (4.16)$$

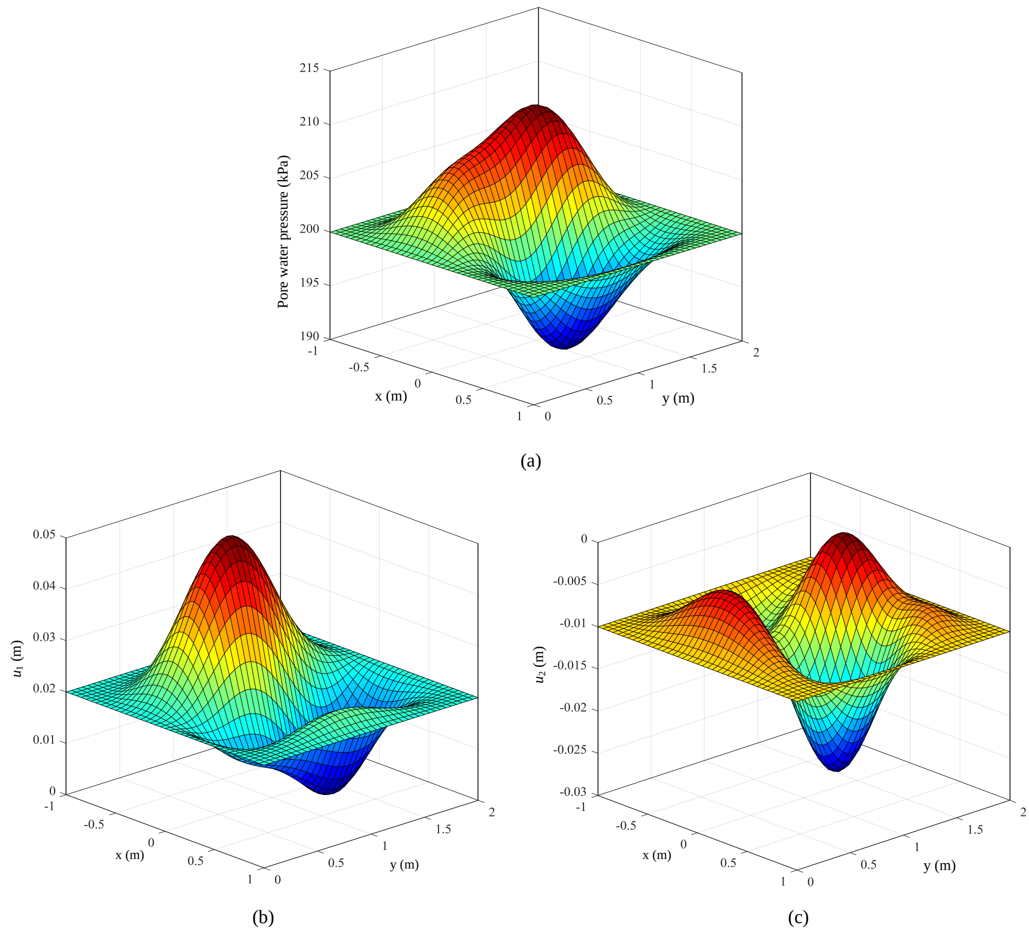

Figure 4-8- Distribution of the field variables in example 2 over the problem domain at $t = 10\,\mathrm{s}$. (a) Pore fluid pressure, (b) Displacement in x direction, (c) Displacement in y direction.

Following recommendations by Bond et al. (2007), the sinusoidal parts of the MSs are multiplied by $(x^2-1)^2(y^2-2y)^2$ to ensure that the boundary conditions for the MSs are simple, similar to the boundary conditions relevant in real applications of the code. A trigonometric function of time is also multiplied to the MSs to induce time dependency of the solution. Due to independent determination of the MSs for pore fluid pressure and displacements, special care must be taken in generating the MS for each state variable fulfilling consistency between the order of magnitude of the variable of interest and the order of magnitude of the coefficients applied in the relevant PDE, as improper solution determination can result in ill-conditioned matrix equations and incorrect results consequently. Note that this condition was automatically satisfied in the first example as the MSs for displacement fields were directly obtained from equation (3.18). Substitution of these MSs into the governing equations (3.2) and (3.18) results in the analytical determination of the source terms. It is worth noting that the second governing equation (equation (3.18)) would also include a source term for this set of MSs. This source term, which can be seen as the required adjustment to the fluid flux at each point of interest, has to be also included in the formulation at the right-hand side of equation (3.75). The variations of the discretisation error norms of the numerical solutions are depicted in a logarithmic scale in Figure 4-9 as a function of the mesh size for this example. Presented in Figure 4-10 are the observed orders of accuracy for the three state variables using L_2 and L_∞ norms of the discretisation error. It is observed that these orders of accuracy are in agreement with those obtained in example 1, especially when finer discretisations are used.

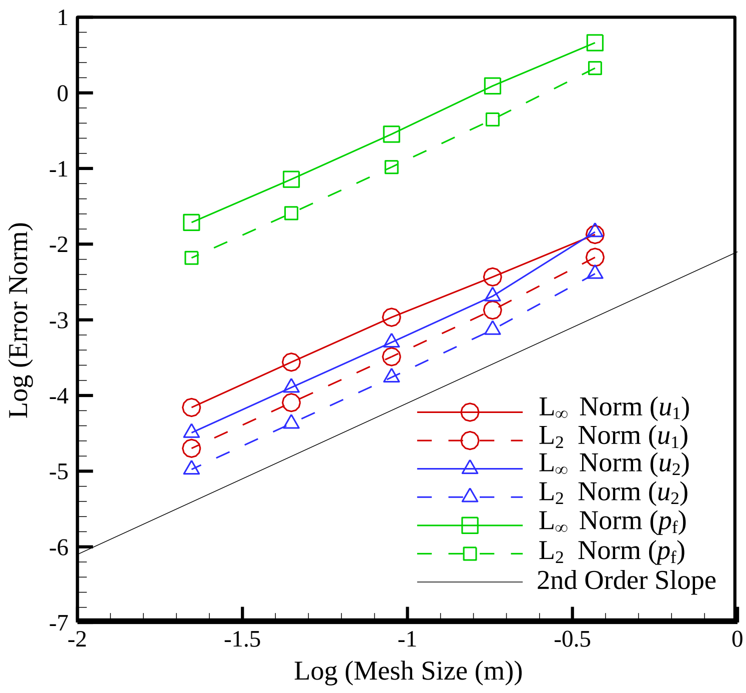

Figure 4-9- Mesh convergence study for example 2 at $t = 10\,\text{s}$ for obtaining the observed spatial orders of accuracy.

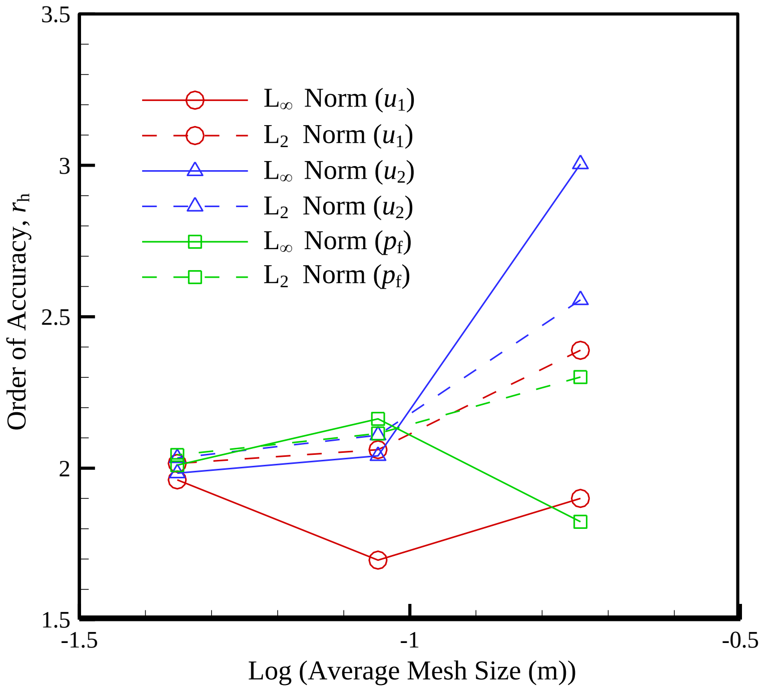

Figure 4-10- Observed spatial orders of accuracy at $t = 10\,\text{s}$ for example 2.

The formal orders of accuracy for the state variables, obtained again using the procedure explained earlier in section 4.3.2, are illustrated in Figure 4-11 and Figure 4-12. It is observed that the formal order of accuracy approaches 2.0 for both L_2 and L_∞ norms as the element size decreases, which is in excellent agreement with the numerically observed convergence rates and also the results of the first example. The formal orders of accuracy, however, slightly deviates from the above values as coarser discretisations are used. This problem is due to inability of coarse background meshes in accurate prediction of the complicated MSs adopted in equations (4.14) to (4.16). This issue was less detectable in example 1 in which the orders of accuracy were not sensitive to mesh size due to simplicity and lack of abrupt variations in the assumed MSs.

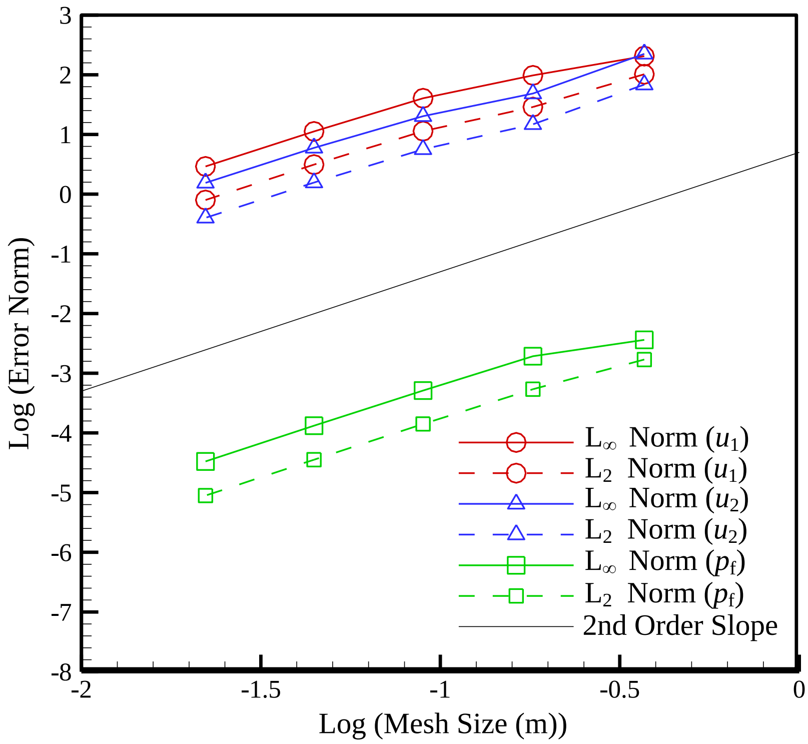

Figure 4-11- Order of accuracy study for example 2 at $t = 10\,\mathrm{s}$ for obtaining the formal spatial orders of accuracy.

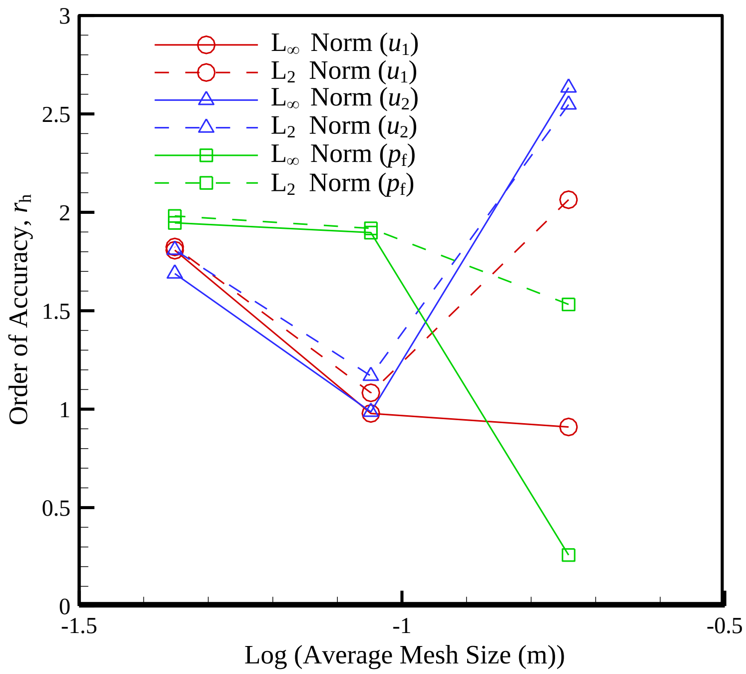

Figure 4-12- Formal spatial orders of accuracy at $t = 10\,\mathrm{s}$ for example 2.

Figure 4-13 shows the numerical order of accuracy in terms of energy error norm for this example. The mesh dependency of the solutions is again evident from this figure, although it is observed in Figure 4-13(a) that the convergence curve approaches the first order accuracy for finer discretisations.

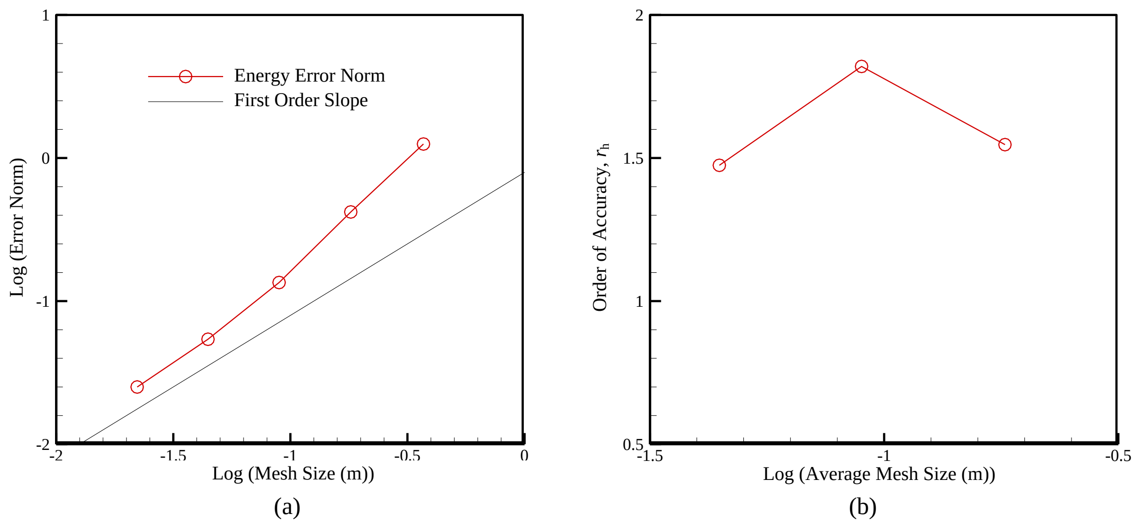

Figure 4-13- (a) Energy error norm at $t = 10\,\mathrm{s}$, (b) Observed spatial order of accuracy in terms of energy error norm, for example 2.

4.5. Conclusion

This chapter presented the application of MMS combined with order of accuracy study for code verification in geomechanics. The procedure for code verification was described in details for an ESPIM in-house code for coupled flow and deformation analysis of poro-elastic media developed in Fortran. Verification of the code was performed through an order of accuracy study in space domain with two MSs for displacement and pore pressure fields that are constructed as functions of both space and time. The results showed that the code successfully passes the spatial order of accuracy test.

Chapter 5

5. Elasto-plastic flow and deformation analysis of saturated porous media

5.1. Introduction

The majority of the problems in geotechnical engineering involve nonlinear behaviour of soils. In this chapter, the edge-based smoothed point interpolation method (ESPIM) discussed in earlier chapters is extended for fully coupled hydro-mechanical analysis of saturated porous media considering material nonlinearity. The ESPIM numerical framework developed in Chapter 3 is employed, utilising the Tr3 and Tr2L node selection schemes resulting in ESPIM-Tr3 and ESRPIM-Tr2L models respectively, due to their great performance in linear analyses which was discussed in Chapter 3. A non-associative Mohr-Coulomb yield criterion is assumed for the behaviour of the solid phase; however, the formulation is developed in a general form so that any other constitutive model can be readily adopted. A substepping scheme (Sloan, 1987) assuming known strain increments is utilised for stress integration, and an iterative modified Newton-Raphson approach is adopted to deal with the nonlinearities arisen from the elastoplastic constitutive model. Finally, the accuracy and efficiency of the numerical model is examined through different numerical examples.

5.2. Governing equation

As presented in Chapter 3, the Biot’s equations governing the coupled hydro-mechanical behaviour of saturated porous media are expressed as

$$\mathbf{L}_{\mathrm{d}}^{\mathrm{T}}\left(\boldsymbol{\sigma}'-\eta p_{\mathrm{f}}\boldsymbol{\delta}\right)+\rho\mathbf{B}=\mathbf{0} \tag{5.1}$$

$$\frac{1}{\rho_{\mathrm{f}}}\mathrm{div}\left[\rho_{\mathrm{f}}\frac{\mathbf{k}}{\mu_{\mathrm{f}}}\left(\nabla p_{\mathrm{f}}+\rho_{\mathrm{f}}\mathbf{g}\right)\right]=a_{\mathrm{f}}\dot{p}_{\mathrm{f}}+\eta\,\mathrm{div}(\dot{\mathbf{u}}) \tag{5.2}$$

In nonlinear problems, it is necessary to solve equations (5.1) and (5.2) incrementally. Therefore, introducing a nonlinear constitutive model to the equations, the effective stress rate $\dot{\boldsymbol{\sigma}}'$ is stated proportional to the strain rate $\dot{\boldsymbol{\varepsilon}}$ through the tangent elastoplastic constitutive matrix $\mathbf{D}^{\mathrm{ep}}$ as

$$\dot{\boldsymbol{\sigma}}'=\mathbf{D}^{\mathrm{ep}}\dot{\boldsymbol{\varepsilon}} \tag{5.3}$$

5.3. Numerical algorithm

5.3.1. Spatial discretisation of the governing equations

Using the GS-Galerkin approach (Liu and Zhang, 2013a), the discretised system of equations are obtained as follows

$$\int_{\Omega}\widehat{\mathbf{B}}_{1}^{\mathrm{T}}\boldsymbol{\sigma}'\mathrm{d}\Omega-\eta\mathbf{Q}\mathbf{P}_{\mathrm{f}}=\mathbf{F}_{\mathrm{u}} \tag{5.4}$$

$$-\eta\mathbf{Q}^{\mathrm{T}}\dot{\mathbf{U}}-\mathbf{H}\mathbf{P}_{\mathrm{f}}-a_{\mathrm{f}}\mathbf{S}\dot{\mathbf{P}}_{\mathrm{f}}=\mathbf{F}_{\mathrm{f}} \tag{5.5}$$

where all the vectors and matrices are the same as those previously defined in Chapter 3 (section 3.5.1).

Utilising the smoothing operation, the tangent stiffness matrix is evaluated as

$$\mathbf{K}_{\mathrm{T}} = \sum_{k=1}^{n_{\mathrm{SD}}} \left(\mathbf{K}_k^{\mathrm{SD}}\right)_{\mathrm{T}} = \sum_{k=1}^{n_{\mathrm{SD}}} \left(\int_{\Omega_k^{\mathrm{SD}}} \widehat{\mathbf{B}}_1^{\mathrm{T}} \mathbf{D}^{\mathrm{ep}} \widehat{\mathbf{B}}_1 \mathrm{d}\Omega \right) \tag{5.6}$$

where the summation shows the assembly process and $\left(\mathbf{K}_k^{\mathrm{SD}}\right)_{\mathrm{T}}$ is the local tangent stiffness matrix of the k th smoothing domain. In ESPIM, $\widehat{\mathbf{B}}_1$ and $\mathbf{D}^{\mathrm{ep}}$ are constant over each smoothing domain, and therefore equation (5.6) can be written as

$$\mathbf{K}_{\mathrm{T}} = \sum_{k=1}^{n_{\mathrm{SD}}} A_k^{\mathrm{SD}} \widehat{\mathbf{B}}_1^{\mathrm{T}} \mathbf{D}^{\mathrm{ep}} \widehat{\mathbf{B}}_1 \tag{5.7}$$

5.3.2. Temporal discretisation of the governing equations

The three-point time discretization scheme (Khoshghalb et al., 2011) is again adopted for time discretisation of the governing equations in this chapter. Equations (5.4) and (5.5) can be discretised in time using equations (3.72) and (3.73), resulting in the fully discretised governing equations of the following form,

$$\int_{\Omega} \widehat{\mathbf{B}}_1^{\mathrm{T}} \left(\boldsymbol{\sigma}'\right)^{t+\alpha\Delta t} \mathrm{d}\Omega - \eta \mathbf{Q} \mathbf{P}_{\mathrm{f}}^{t+\alpha\Delta t} = \mathbf{F}_{\mathrm{u}}^{t+\alpha\Delta t} \tag{5.8}$$

$$-\eta \mathbf{Q}^{\mathrm{T}} \left(A\mathbf{U}^{t+\alpha\Delta t} - B\mathbf{U}^{t} + C\mathbf{U}^{t-\Delta t} \right) - \Delta t \mathbf{H} \mathbf{P}_{\mathrm{f}}^{t+\alpha\Delta t} - a_{\mathrm{f}} \mathbf{S} \left(A\mathbf{P}_{\mathrm{f}}^{t+\alpha\Delta t} - B\mathbf{P}_{\mathrm{f}}^{t} + C\mathbf{P}_{\mathrm{f}}^{t-\Delta t} \right) = \Delta t \mathbf{F}_{\mathrm{f}}^{t+\alpha\Delta t} \tag{5.9}$$

5.3.3. Nonlinear algorithm

The discretised system of equations derived in the previous section are nonlinear when a nonlinear behaviour is assumed for geomaterials and therefore, an appropriate solution strategy is required to solve the nonlinear equations. Among all the approaches in the literature, the following methods have been more popular in geotechnical engineering: The tangent stiffness method, the visco-plastic method, and the modified Newton-Raphson method (Potts and Zdravkovic, 2001). The modified Newton-Raphson method, however, yields the most accurate results compared to the other two strategies (Potts and Zdravkovic, 2001). Consequently, it is adopted in this study to solve the nonlinear fully coupled equation system at each time step through an iterative procedure. To this end, the vectors of the nodal displacement and pore fluid pressure at iteration i of the current time step $t+\alpha\Delta t$ ($\mathbf{U}^{i,t+\alpha\Delta t}$ and, $\mathbf{P}_{\mathrm{f}}^{i,t+\alpha\Delta t}$ respectively) are refined at iteration $i+1$ as

$$\begin{Bmatrix} \mathbf{U}^{i+1,t+\alpha\Delta t} \\ \mathbf{P}_{\mathrm{f}}^{i+1,t+\alpha\Delta t} \end{Bmatrix} = \begin{Bmatrix} \mathbf{U}^{i,t+\alpha\Delta t} \\ \mathbf{P}_{\mathrm{f}}^{i,t+\alpha\Delta t} \end{Bmatrix} + \begin{Bmatrix} \mathrm{d}\mathbf{U}^{i+1,t+\alpha\Delta t} \\ \mathrm{d}\mathbf{P}_{\mathrm{f}}^{i+1,t+\alpha\Delta t} \end{Bmatrix} \tag{5.10}$$

in which d shows the corrections to the current solution resulting from the Newton-Raphson process. The refinement is performed so that the nodal displacements and pore fluid pressures satisfy the following residual form of nonlinear equations at time $t+\alpha\Delta t$

$$\boldsymbol{\Psi}_{\mathrm{u}}^{i+1,t+\alpha\Delta t} = \int_{\Omega} \widehat{\mathbf{B}}_1^{\mathrm{T}} \left(\boldsymbol{\sigma}'\right)^{i+1,t+\alpha\Delta t} \mathrm{d}\Omega - \eta \mathbf{Q}\mathbf{P}_{\mathrm{f}}^{i+1,t+\alpha\Delta t} - \mathbf{F}_{\mathrm{u}}^{t+\alpha\Delta t} = \mathbf{0} \tag{5.11}$$

$$\begin{aligned} \boldsymbol{\Psi}_{\mathrm{f}}^{i+1,t+\alpha\Delta t} &= -\eta \mathbf{Q}^{\mathrm{T}} \left(A\mathbf{U}^{i+1,t+\alpha\Delta t} - B\mathbf{U}^{t} + C\mathbf{U}^{t-\Delta t} \right) - \Delta t \mathbf{H}\mathbf{P}_{\mathrm{f}}^{i+1,t+\alpha\Delta t} \\ &\quad - a_{\mathrm{f}} \mathbf{S} \left(A\mathbf{P}_{\mathrm{f}}^{i+1,t+\alpha\Delta t} - B\mathbf{P}_{\mathrm{f}}^{t} + C\mathbf{P}_{\mathrm{f}}^{t-\Delta t} \right) - \Delta t \mathbf{F}_{\mathrm{f}}^{t+\alpha\Delta t} = \mathbf{0} \end{aligned} \tag{5.12}$$

To evaluate the incremental vector of the nodal displacements and pore fluid pressures, the following matrix equation is formed by expanding equations (5.11) and (5.12) with the first-order truncated Taylor series

$$\begin{Bmatrix} \boldsymbol{\Psi}_{\mathrm{u}}^{i+1,t+\alpha\Delta t} \\ \boldsymbol{\Psi}_{\mathrm{f}}^{i+1,t+\alpha\Delta t} \end{Bmatrix} = \begin{Bmatrix} \boldsymbol{\Psi}_{\mathrm{u}}^{i,t+\alpha\Delta t} \\ \boldsymbol{\Psi}_{\mathrm{f}}^{i,t+\alpha\Delta t} \end{Bmatrix} + \mathbf{J}^{i,t+\alpha\Delta t} \begin{Bmatrix} \mathrm{d}\mathbf{U}^{i+1,t+\alpha\Delta t} \\ \mathrm{d}\mathbf{P}_{\mathrm{f}}^{i+1,t+\alpha\Delta t} \end{Bmatrix} = \mathbf{0} \tag{5.13}$$

in which $\mathbf{J}$ is the Jacobian matrix, defined as

$$\mathbf{J}=\begin{bmatrix} \dfrac{\partial \boldsymbol{\Psi}_{\mathrm{u}}}{\partial \mathbf{U}} & \dfrac{\partial \boldsymbol{\Psi}_{\mathrm{u}}}{\partial \mathbf{P}_{\mathrm{f}}} \\ \dfrac{\partial \boldsymbol{\Psi}_{\mathrm{f}}}{\partial \mathbf{U}} & \dfrac{\partial \boldsymbol{\Psi}_{\mathrm{f}}}{\partial \mathbf{P}_{\mathrm{f}}} \end{bmatrix} \tag{5.14}$$

The term $\int_{\Omega} \widehat{\mathbf{B}}_1^{\mathrm{T}} \left(\boldsymbol{\sigma}'\right)^{i+1,t+\alpha\Delta t} \mathrm{d}\Omega$ in equation (5.11) is the vector of internal nodal forces at iteration $i+1$ of time step $t+\alpha\Delta t$. In problems involving a nonlinear response for the solid phase, the tangent stiffness matrix at each time step is defined as the derivative of the internal force vector with respect to the displacement vector at that time step. Hence, the Jacobian matrix at iteration i of time step $t+\alpha\Delta t$ takes the following form:

$$\mathbf{J}^{i,t+\alpha\Delta t}=\begin{bmatrix} A\mathbf{K}_{\mathrm{T}}^{i,t+\alpha\Delta t} & -A\eta\mathbf{Q} \\ -A\eta\mathbf{Q}^{\mathrm{T}} & -(Aa_{\mathrm{f}}\mathbf{S}+\Delta t\mathbf{H}) \end{bmatrix} \tag{5.15}$$

In derivation of equation (5.15), equation (5.11) is multiplied by A to produce a symmetrical Jacobian matrix to ease the computations when associative plasticity is assumed. Finally, from equation (5.13), the incremental vector of the nodal displacements and pore fluid pressures is obtained at iteration $i+1$ as

$$\begin{Bmatrix} \mathrm{d}\mathbf{U}^{i+1,t+\alpha\Delta t} \\ \mathrm{d}\mathbf{P}_{\mathrm{f}}^{i+1,t+\alpha\Delta t} \end{Bmatrix} = \left(\mathbf{J}^{i,t+\alpha\Delta t}\right)^{-1} \begin{Bmatrix} \boldsymbol{\Psi}_{\mathrm{u}}^{i,t+\alpha\Delta t} \\ \boldsymbol{\Psi}_{\mathrm{f}}^{i,t+\alpha\Delta t} \end{Bmatrix} \tag{5.16}$$

A proper stress integration method has to be used in each iteration to obtain the unknown stresses. The stresses obtained are then used to form the residual vector for the next iteration or as the final stresses for the current time step if the convergence is reached in the current iteration. Convergence is assumed when the following criterion is fulfilled in an iteration,

$$ERROR = \frac{\left\| \mathrm{d}\mathbf{X}^{i+1,t+\alpha\Delta t} \right\|_2}{\left\| \sum_{j=1}^{i+1} \mathrm{d}\mathbf{X}^{j,t+\alpha\Delta t} \right\|_2} < eps \tag{5.17}$$

where $\mathrm{d}\mathbf{X}^{i+1,t+\alpha\Delta t} = \left[\mathrm{d}\mathbf{U}^{i+1,t+\alpha\Delta t} \quad \mathrm{d}\mathbf{P}_{\mathrm{f}}^{i+1,t+\alpha\Delta t} \right]^{\mathrm{T}}$ is the vector of the nodal displacements and pore fluid pressure increments in the ith iteration, $\| . \|_2$ is the Euclidean 2-norm, and eps is a small positive number for controlling the error. $eps = 10^{-6}$ is used in this study to obtain the numerical solutions.

5.3.4. Mohr-Coulomb model

The simple elastic perfectly plastic Mohr-Coulomb model which is extensively utilised in elastoplastic analysis of geotechnical problems is adopted in this chapter. Isotropic elastic behaviour similar to the one presented in Chapter 3 is assumed inside the yield surface. In this work, a simple hyperbolic yield surface is used based on the Mohr-Coulomb yield criterion proposed by Abbo and Sloan (1995), which eliminates the singular tips from the Mohr-Coulomb yield surface at the edge intersections in the π-plane, as seen in Figure 5-1.

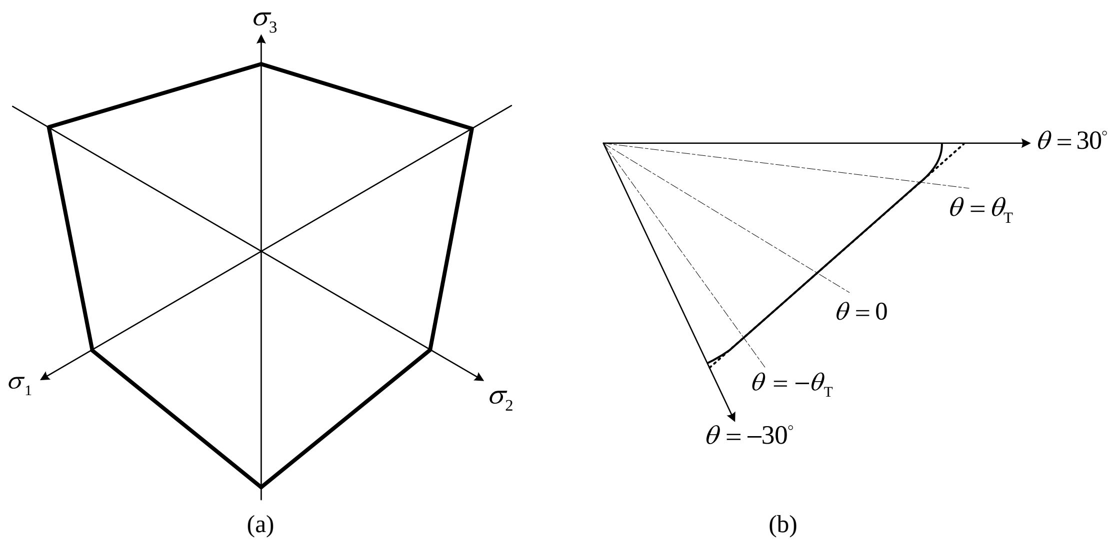

Figure 5-1- (a) Original Mohr-Coulomb yield surface in π-plane, (b) Mohr-Coulomb yield surface with rounded vertices.

The three dimensional Mohr-Coulomb yield surface can be expressed in terms of three stress invariants: the mean effective stress p', the deviatoric stress q, and the Lode angle θ, expressed as follows,

$$p' = \frac{1}{3}(\sigma'_{\mathrm{x}} + \sigma'_{\mathrm{y}} + \sigma'_{\mathrm{z}}) \tag{5.18}$$

$$q = \sqrt{\frac{3}{2}(s_{\mathrm{x}}^2 + s_{\mathrm{y}}^2 + s_{\mathrm{z}}^2) + 3(\tau_{\mathrm{xy}}^2 + \tau_{\mathrm{yz}}^2 + \tau_{\mathrm{zx}}^2)} \tag{5.19}$$

$$\theta = \frac{1}{3}\sin^{-1}\left(-\frac{27}{2}\frac{J_3}{q^3}\right), \quad -30^\circ \le \theta \le 30^\circ \tag{5.20}$$

where

$$J_3 = s_{\mathrm{x}} s_{\mathrm{y}} s_{\mathrm{z}} + 2\tau_{\mathrm{xy}}\tau_{\mathrm{yz}}\tau_{\mathrm{zx}} - s_{\mathrm{x}}\tau_{\mathrm{yz}}^2 - s_{\mathrm{y}}\tau_{\mathrm{xz}}^2 - s_{\mathrm{z}}\tau_{\mathrm{xy}}^2 \quad , \tag{5.21}$$

$$s_{\mathrm{x}} = \sigma'_{\mathrm{x}} - p', \;\; s_{\mathrm{y}} = \sigma'_{\mathrm{y}} - p', \;\; s_{\mathrm{z}} = \sigma'_{\mathrm{z}} - p' \tag{5.22}$$

Having the stress invariants, the Mohr-Coulomb yield criterion is expressed as

$$F(p', q, \theta) = p' \sin\phi' + qK(\theta) - c'\cos\phi' = 0 \tag{5.23}$$

where ϕ' and c' represent the drained friction angle and cohesion of the soil.

The Mohr-Coulomb yield surface becomes singular at Lode angles of $\theta = \pm 30^\circ$, posing difficulties in numerical implementation of the model. Sloan and Booker (1986) proposed the following trigonometric definition for $K(\theta)$ so that the ensuing octahedral cross-section in the π-plane is similar to the Mohr-Coulomb cross section, but smoothed at the vicinity of the singularities where $|\theta| > \theta_{\mathrm{T}}$, with θ_{T} being a transition angle between 0 and 30° defined by the user (see Figure 5-1(b)),

$$K(\theta)=\begin{cases} a-b\sin 3\theta & |\theta|>\theta_{\mathrm{T}} \\ \cos\theta-\dfrac{\sqrt{3}}{3}\sin\phi'\sin\theta & |\theta|\le\theta_{\mathrm{T}} \end{cases} \tag{5.24}$$

The coefficients a and b in equation (5.24) are obtained through the following formulas,

$$a=\frac{\cos\theta_{\mathrm{T}}}{3}\left(3+\tan\theta_{\mathrm{T}}\tan 3\theta_{\mathrm{T}}+\frac{\sqrt{3}}{3}\mathrm{sign}(\theta)(\tan 3\theta_{\mathrm{T}}-3\tan\theta_{\mathrm{T}})\sin\phi'\right) \tag{5.25}$$

$$b=\frac{1}{3\cos 3\theta_{\mathrm{T}}}\left(\mathrm{sign}(\theta)\sin\theta_{\mathrm{T}}+\frac{\sqrt{3}}{3}\sin\phi'\cos\theta_{\mathrm{T}}\right) \tag{5.26}$$

where

$$\mathrm{sign}(\theta)=\begin{cases} +1 & \theta\ge 0^{\circ} \\ -1 & \theta<0^{\circ} \end{cases} \tag{5.27}$$

In this study a transition angle of $\theta_{\mathrm{T}}=25^{\circ}$ is adopted.

In the non-associative Mohr-Coulomb model, the plastic potential function is expressed as

$$G=p'\sin\psi'+qH(\theta)-c'\cos\psi'=0 \tag{5.28}$$

in which ψ' is the dilation angle. The model is associative if the dilation angle is assumed equal to the friction angle, and is non-associative if different values are assumed for the friction and dilation angles. $H(\theta)$ has the same definition as $K(\theta)$ in equation (5.24) except for ψ' replacing ϕ' in the definition of $H(\theta)$.

In the modified Newton-Raphson procedure, the tangent constitutive matrix is required in each iteration for calculation of the Jacobian matrix and convergence check. In general, the elastoplastic tangent constitutive matrix is defined as (Potts and Zdravkovic, 2001),

$$\mathbf{D}^{\mathrm{ep}} = \mathbf{D}^{\mathrm{e}} - \frac{\mathbf{D}^{\mathrm{e}}\mathbf{m}\mathbf{n}^{\mathrm{T}}\mathbf{D}^{\mathrm{e}}}{\mathbf{n}^{\mathrm{T}}\mathbf{D}^{\mathrm{e}}\mathbf{m} + h} \tag{5.29}$$

where $\mathbf{D}^{\mathrm{e}}$ is the elastic constitutive matrix, h is the hardening parameter (not to be confused with the average mesh size defined in Chapter 4) which is zero in elastic perfectly plastic models like the Mohr-Coulomb model, and $\mathbf{n}$ and $\mathbf{m}$ are the unit vectors normal to the yield surface and the plastic potential, respectively, defined as,

$$\mathbf{n} = \frac{\partial F / \partial \boldsymbol{\sigma}'}{\left\| \partial F / \partial \boldsymbol{\sigma}' \right\|} \tag{5.30}$$

$$\mathbf{m} = \frac{\partial G / \partial \boldsymbol{\sigma}'}{\left\| \partial G / \partial \boldsymbol{\sigma}' \right\|} \tag{5.31}$$

The gradients of the yield surface and plastic potential are of importance in elastoplastic numerical analyses. These values are used to obtain $\mathbf{D}^{\mathrm{ep}}$ and also for stress integration purposes explained in the following section. The yield surface gradient can be calculated as follows,

$$\frac{\partial F}{\partial \boldsymbol{\sigma}'} = c_1 \frac{\partial p'}{\partial \boldsymbol{\sigma}'} + c_2 \frac{\partial q}{\partial \boldsymbol{\sigma}'} + c_3 \frac{\partial J_3}{\partial \boldsymbol{\sigma}'} \tag{5.32}$$

where

$$c_1 = \frac{\partial F}{\partial p'} = \sin \varphi' \tag{5.33}$$

$$c_2 = \frac{\partial F}{\partial q} - \frac{\tan 3\theta}{q}\frac{\partial F}{\partial \theta} = K(\theta) - \tan 3\theta \frac{\mathrm{d}K(\theta)}{\mathrm{d}\theta} \tag{5.34}$$

$$c_3 = -\frac{9}{2\cos 3\theta q^3}\frac{\partial F}{\partial \theta} = -\frac{9}{2\cos 3\theta q^2}\frac{\mathrm{d}K(\theta)}{\mathrm{d}\theta} \tag{5.35}$$

and

$$\frac{\partial p'}{\partial \boldsymbol{\sigma}'} = \frac{1}{3}\begin{bmatrix}1 & 1 & 1 & 0 & 0 & 0\end{bmatrix}^{\mathrm{T}} \tag{5.36}$$

$$\frac{\partial q}{\partial \boldsymbol{\sigma}'} = \frac{\sqrt{3}}{2q}\begin{bmatrix}s_{\mathrm{x}} & s_{\mathrm{y}} & s_{\mathrm{z}} & 2\tau_{\mathrm{xy}} & 2\tau_{\mathrm{yz}} & 2\tau_{\mathrm{zx}}\end{bmatrix}^{\mathrm{T}} \tag{5.37}$$

$$\frac{\partial J_3}{\partial \boldsymbol{\sigma}'} = \begin{Bmatrix} s_{\mathrm{y}}s_{\mathrm{z}} - \tau_{\mathrm{yz}}{}^2 - q^2/9 \\ s_{\mathrm{x}}s_{\mathrm{z}} - \tau_{\mathrm{zx}}{}^2 - q^2/9 \\ s_{\mathrm{x}}s_{\mathrm{y}} - \tau_{\mathrm{xy}}{}^2 - q^2/9 \\ 2(\tau_{\mathrm{yz}}\tau_{\mathrm{zx}} - s_{\mathrm{z}}\tau_{\mathrm{xy}}) \\ 2(\tau_{\mathrm{zx}}\tau_{\mathrm{xy}} - s_{\mathrm{x}}\tau_{\mathrm{yz}}) \\ 2(\tau_{\mathrm{xy}}\tau_{\mathrm{yz}} - s_{\mathrm{y}}\tau_{\mathrm{zx}}) \end{Bmatrix} \tag{5.38}$$

It should be noted that for a plane strain setting, which is considered in this work, shear stresses τ_{zx} and τ_{zy} are set to zero. Different entries of $\partial G / \partial \boldsymbol{\sigma}'$ can also be derived in a similar fashion.

5.3.5. Stress integration

The elastoplastic stress-strain relation of equation (5.3) should be integrated using a proper stress integration method in each iteration. There are generally two common classes of stress integration algorithms: The explicit, and the implicit. Potts and Ganendra (1994) evaluated the performance of the two approaches and showed that the explicit algorithm is more accurate considering a particular increment. As a result, a sub-stepping explicit scheme by Sloan (1987) is used in this work. This method is based on the well-known modified Euler method, assumes known strain increments and controls the error of the numerical integrations by adjusting the size of each sub-step automatically. The details of the sub-stepping method can be found in the research paper by Sloan (1987) and is not repeated here.

5.4. Numerical examples

Three numerical examples are examined to show the applicability, accuracy and stability of the proposed nonlinear meshfree model: a bearing capacity problem in a drained medium, a thick-walled cylinder problem and a consolidation problem. In all the examples, the results are compared with those obtained from analytical/reference solutions or the standard linear FEM using the same background mesh.

5.4.1. Bearing capacity of a rigid strip footing

A smooth, rigid strip footing placed on a drained Mohr-Coulomb material in a plane-strain setting is first examined. The permeability of the material is assumed to be sufficiently high to prevent build-up of excess pore fluid pressure during loading. Due to symmetry, only half of the domain is modelled. The thickness of the soil layer is taken as $H = 5\,\mathrm{m}$, the width of the domain is $W = 10\,\mathrm{m}$, and the half width of the footing is considered as $B/2 = 2\,\mathrm{m}$. A surcharge of $Q = 20\,\mathrm{kPa}$ is assumed to be applied on the ground surface. The rigid footing is modelled by imposing controlled vertical displacement increments of $\Delta u_2 = 0.001\,\mathrm{m}$. Associativity is assumed for the material behaviour, with the dilation angle ψ taken equal to the friction angle ϕ of the soil. The details of the model as well as the properties of the soil layer are illustrated in Figure 5-2 (E, ν, c, and γ denote the elastic modulus, Poisson's ratio, cohesion, and unit weight of soil, respectively, with the superscript dash indicating that the corresponding parameter is for a drained condition). Also presented in this figure is the background mesh used in the analyses consisting of 315 nodes and 576 elements. For time marching, $\alpha = 1$ was adopted.

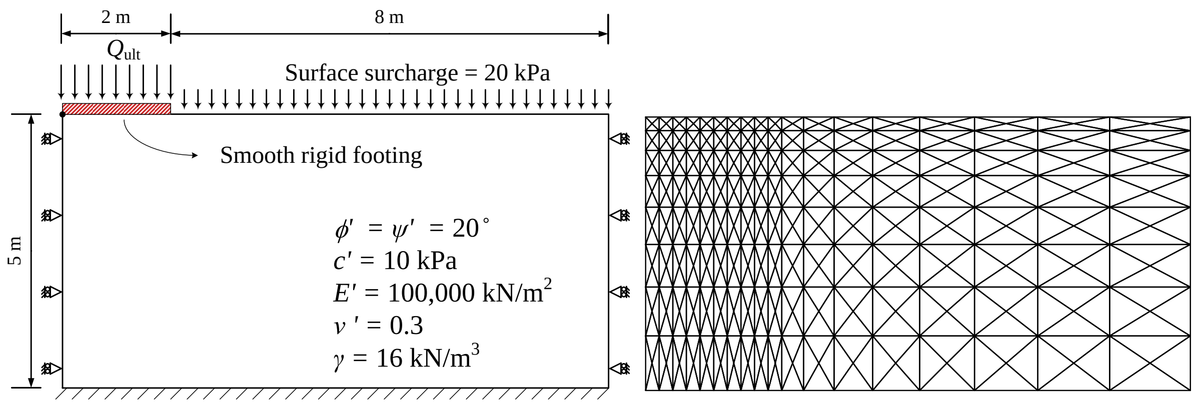

Figure 5-2- Illustration of the problem domain for the bearing capacity problem, and the background mesh used.

In Figure 5-3, the footing pressure, calculated from the sum of the nodal reaction forces under the footing, is plotted versus the vertical footing displacement. The numerical results of ESPIM-Tr3 and ESRPIM-Tr2L are compared to the FEM solution with the same mesh (FEM-Tr3), the numerical solution of Smith et al. (2013) using FEM with 800 regularly distributed FEM-Q8 elements and visco-plastic strain approach, and finally the ultimate bearing capacity obtained using the method of characteristics (Martin, 2004). It is clear from this figure that ESPIM-Tr3 yields more accurate results than does FEM-Tr3. However, ESRPIM-Tr2L yields less accurate results mainly due to the large number of supporting nodes selected in the construction of nodal shape functions, which limits its ability to capture precisely sharp changes in the displacement field normally associated with elastic-perfectly plastic materials.

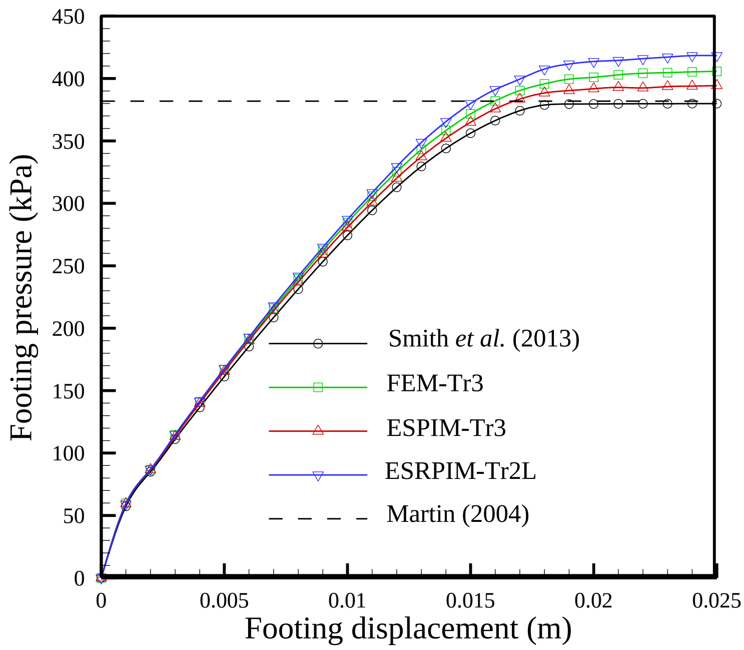

Figure 5-3- Footing pressure versus footing displacement for the bearing capacity problem.

To compare the efficiency of the proposed models to that of FEM-Tr3, the total number of Newton-Raphson iterations, the average time of each iteration, and the total time of the analysis for the proposed methods are normalised with respect to those of FEM-Tr3 and presented in Table 5-1 for the first 25 displacement increments of the analyses. As seen from this table, although each iteration takes slightly longer for ESPIM-Tr3 compared to the linear FEM, adopting ESPIM-Tr3 has not only yielded more accurate results compared to FEM-Tr3, but also reduced the total analysis time by reducing the number of iterations required. ESRPIM-Tr2L on the other hand seems to be less efficient than both ESPIM-Tr3 and FEM-Tr3, as it yielded less accurate results while requiring more computational time.

Table 5-1- Comparison of the computational time required by different numerical procedures adopted in example 5.4.1.

Method	Total number of iterations	Average time of each iteration with respect to that of FEM-Tr3	Total time of the analysis with respect to that of FEM-Tr3
FEM-Tr3	234	1	1
ESPIM-Tr3	226	1.026	0.992
ESRPIM-Tr2L	269	1.102	1.261

5.4.2. Thick-walled cylinder

In the second example, pressurisation of the thick-walled cylinder illustrated in Figure 5-4 is considered in both drained and undrained conditions, as analytical solutions are available for this problem (Small et al., 1976). The cylinder is subjected to an internal pressure Q with no external pressure, as illustrated in Figure 5-4. Only one quarter of the cylinder is simulated due to symmetry. The background mesh used in the numerical analyses is also shown in Figure 5-4.

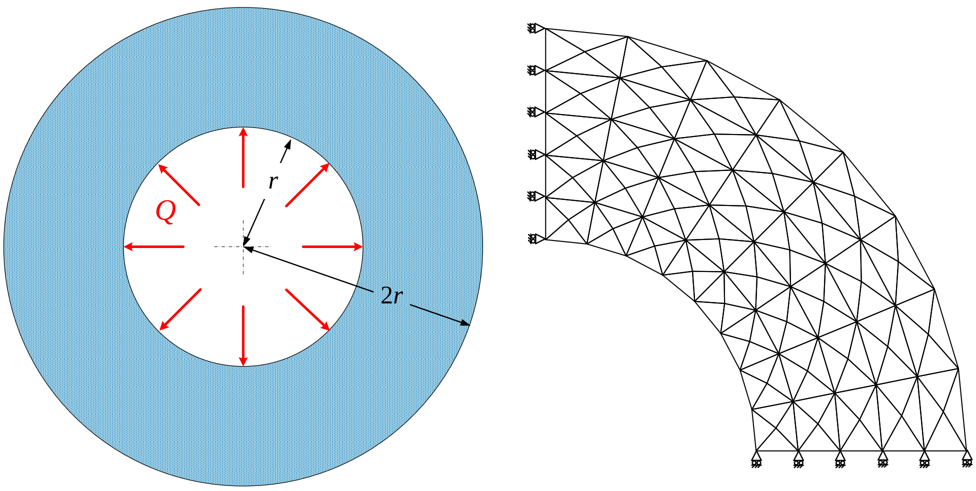

Figure 5-4- Cross section of the thick-walled cylinder and the background mesh assumed for numerical simulations.

The cylinder is initially at a zero stress state, and the drained properties of the solid skeleton, which obeys a non-associative Mohr-Coulomb constitutive law, are as follows: $E'/c' = 200$, $\nu' = 0$, $\phi' = 30$ and $\psi' = 0$. The undrained (indicated with a subscript u) properties of the material used in the analyses are $E_{\mathrm{u}} = 1.5E'/(1+\nu')$, $\nu_{\mathrm{u}} = 0.49$, $\phi_{\mathrm{u}} = 0$ and $c_{\mathrm{u}} = 2c'\sqrt{N_\phi}/(1+N_\phi)$, where $N_\phi = (1+\sin\phi')/(1-\sin\phi')$.

For the drained and undrained responses of the material, two types of analyses are performed. First, a single-phase analysis is conducted considering the drained or undrained properties of the material. Then, a coupled flow and deformation analysis is performed using two extreme loading conditions: a fast loading rate to simulate the undrained behaviour of the material and a slow loading rate to account for the drained response. The loading rate in the problem is defined using the parameter $\omega = \mathrm{d}(Q/c')/\mathrm{d}t_{\mathrm{D}}$ in which t_{D} is the dimensionless time for the one-dimensional consolidation problem, defined as $t_{\mathrm{D}} = E'k_{\mathrm{f}}(1-\nu')t/\left(\gamma_{\mathrm{f}}(1+\nu')(1-2\nu')r^2\right)$, where $\gamma_{\mathrm{f}} = 9.81\,\mathrm{kN/m^3}$ is the unit weight of water and k is the coefficient of permeability. The drained behaviour is captured considering a loading rate of $\omega = 0.09$, as suggested by Small et al. (1976). For simulation of the problem in an undrained condition, a loading rate of $\omega = 900$ is used. This rate is 100 times higher than the rate $\omega = 9$ used by Small *et al.* (Small et al., 1976) because $\omega = 9$ is not sufficiently fast to simulate undrained conditions (Small et al., 1976). The time step growth factor of $\alpha = 1.0$ was adopted in the coupled analyses.

The numerical results from ESPIM-Tr3 for both single-phase and coupled analyses are compared with the analytical solutions in Figure 5-5. In this figure, the vertical axis shows the dimensionless pressure defined as Q/c', and the horizontal axis represents the dimensionless deflection of the cylinder inner radius as $E'u_{\mathrm{r}}/\left((1+\nu')c'r\right)$, where u_{r} is the deflection of the inner radius. As seen from this figure, in both drained and undrained analyses, the numerical results of the proposed method show excellent agreement with the analytical solutions.

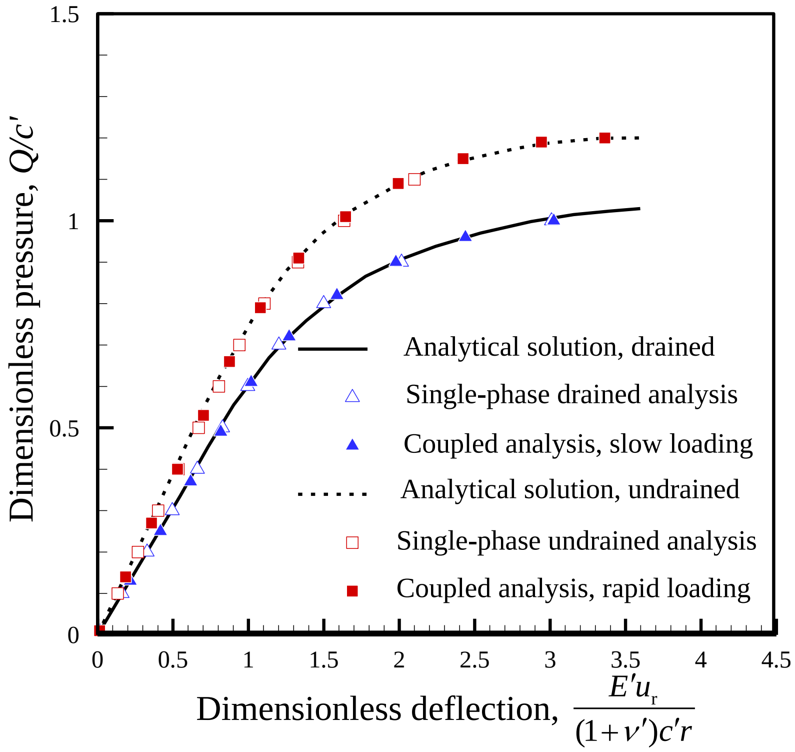

Figure 5-5- Dimensionless pressure versus dimensionless deflection of inner radius of the thick-walled cylinder.

5.4.3. Consolidation analysis of a flexible strip footing

This example involves a flexible, smooth, and impervious strip footing of half width a, placed on a saturated weightless clay layer of thickness $8a$ that extends laterally $16a$ from the centre of the footing. The soil layer is sitting on impervious non-deformable bedrock. Associative Mohr-Coulomb behaviour is assumed for the saturated soil layer. The ground surface is assumed to be free draining. Similar to the example 5.4.1, only half of the model is considered due to symmetry. The geometry of the problem, the background mesh used in the analyses, and the material properties are shown in Figure 5-6 (k_f denotes the coefficient of permeability of the soil). $a = 3\,\text{m}$ is used in the numerical simulations.

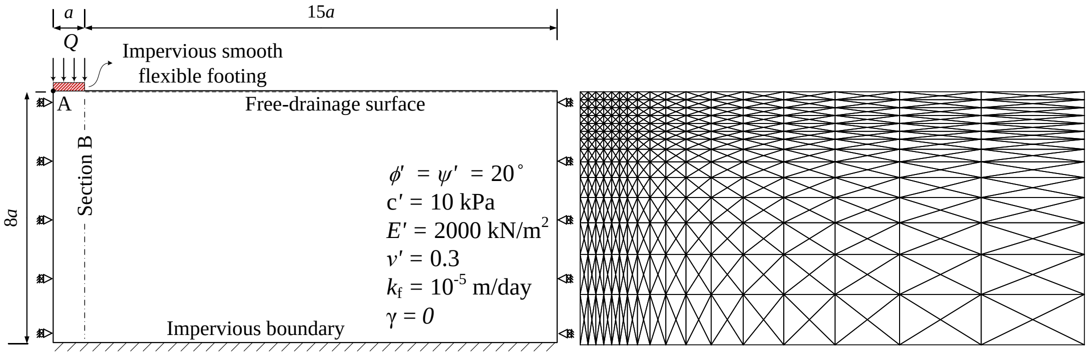

Figure 5-6- Geometry, background mesh, and material parameters for the consolidation problem.

The dimensionless time for plain-strain two-dimensional consolidation problems proposed by Manoharan and Dasgupta (1995) is adopted here: $t_{\mathrm{D}} = E' k_{\mathrm{f}} t \big/ \left(2\gamma_{\mathrm{f}}\left(1+\nu'\right)\left(1-2\nu'\right)a^2\right)$. $\gamma_{\mathrm{f}} = 10\,\mathrm{kN/m^3}$ is assumed in this example to ensure consistency with Manoharan and Dasgupta (1995) and Sabetamal et al. (2016), as their solution to this problem is used here for comparison with the results of the proposed methods. As shown in Figure 5-7, the footing is subjected to a linearly increasing vertical pressure that reaches $Q_0 = 100\,\mathrm{kPa}$ at the dimensionless time $t_{\mathrm{D}} = 0.01$ (t_{L} in Figure 5-7), corresponding to $t = 46.8\,\mathrm{days}$, and is kept constant afterwards. The linear loading is simulated in the analyses through 10 steps of $\Delta Q = 10\,\mathrm{kPa}$. For these ten loading steps, the time increment is assumed to be $\Delta t_{\mathrm{D}} = 0.001$ ($\Delta t = 4.68\,\mathrm{days}$), and the time step growth factor is taken as $\alpha = 1.0$. Then, from the eleventh step onwards, the time step growth factor is increased to $\alpha = 1.1$ to reduce the duration of the analysis.

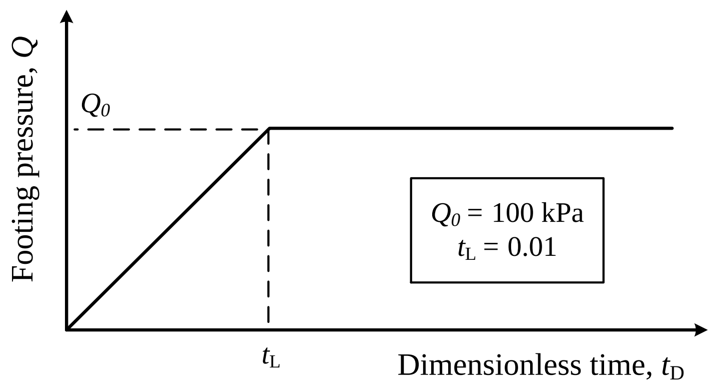

Figure 5-7- Loading regime of the flexible footing (example 5.5.3)

Figure 5-8 illustrates the variations in the dimensionless settlement, $100u_2/a$ at the centre of the footing (point A in Figure 5-6) with time. As seen from Figure 5-8(a), the results from ESPIM-Tr3 and ESRPIM-Tr2L excellently match those obtained by Manoharan and Dasgupta (1995) and Sabetamal et al. (2016). As expected, the footing settles more rapidly as the footing pressure increases to the point corresponding to $t_{\mathrm{D}} = 0.01$ (i.e., end of loading), and then, the settlement continues due to consolidation of the clay layer. Figure 5-8(b) presents a comparison of the predicted settlements at time $t_{\mathrm{D}} = 0.01$ obtained from the proposed MMs, the conventional FEM with the same triangular background mesh (FEM-Tr3), and the reference solution (obtained from the FEM model with a very fine background mesh). As can be clearly observed from this figure, the ESPIM-Tr3 produces the most accurate results, matching almost perfectly the reference solution. ESRPIM-Tr2L is again the least accurate method, most likely because of possible sudden changes in displacement fields of neighbouring smoothing domains when an elastic-perfectly plastic model is used, as explained previously. The softening effect of the smoothing operation is also clear from the results presented in Figure 5-8(b), especially for ESRPIM-Tr2L, compared to the FEM-Tr3 model as also reported by Liu and Zhang (Liu and Zhang, 2008).

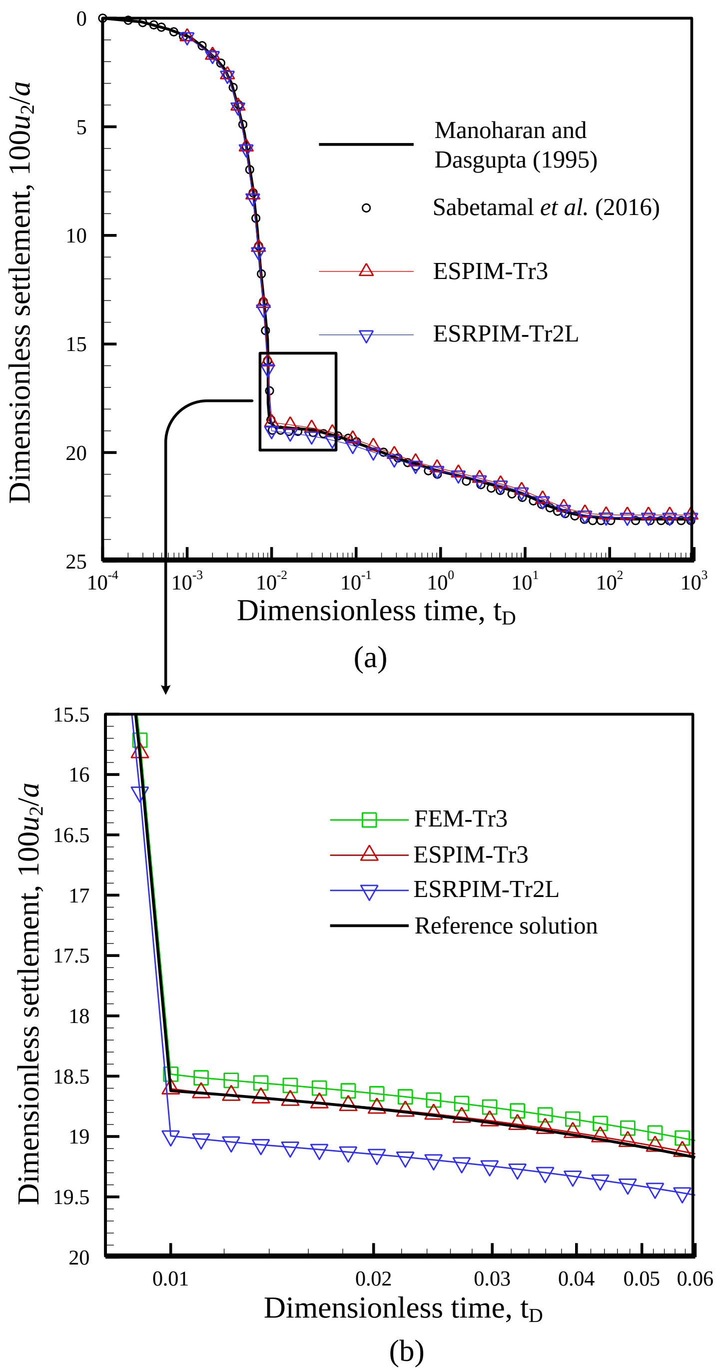

Figure 5-8- Dimensionless settlement at the centre of the footing versus the dimensionless time.

Variations of the dimensionless pore fluid pressure, p_{f}/Q_0, at point A with respect to the dimensionless time, t_{D}, are depicted in Figure 5-9. Again, the agreement between the results of the presented models and the results reported by Manoharan and Dasgupta (1995) and Sabetamal et al. (2016) is acceptable. Figure 5-9(b) shows the pore fluid pressure variations in the vicinity of the peak of the graph. In this case, both edge-based smoothed MMs render a better solution compared to the FEM with the same background mesh, with ESPIM-Tr3 again being the most accurate method.

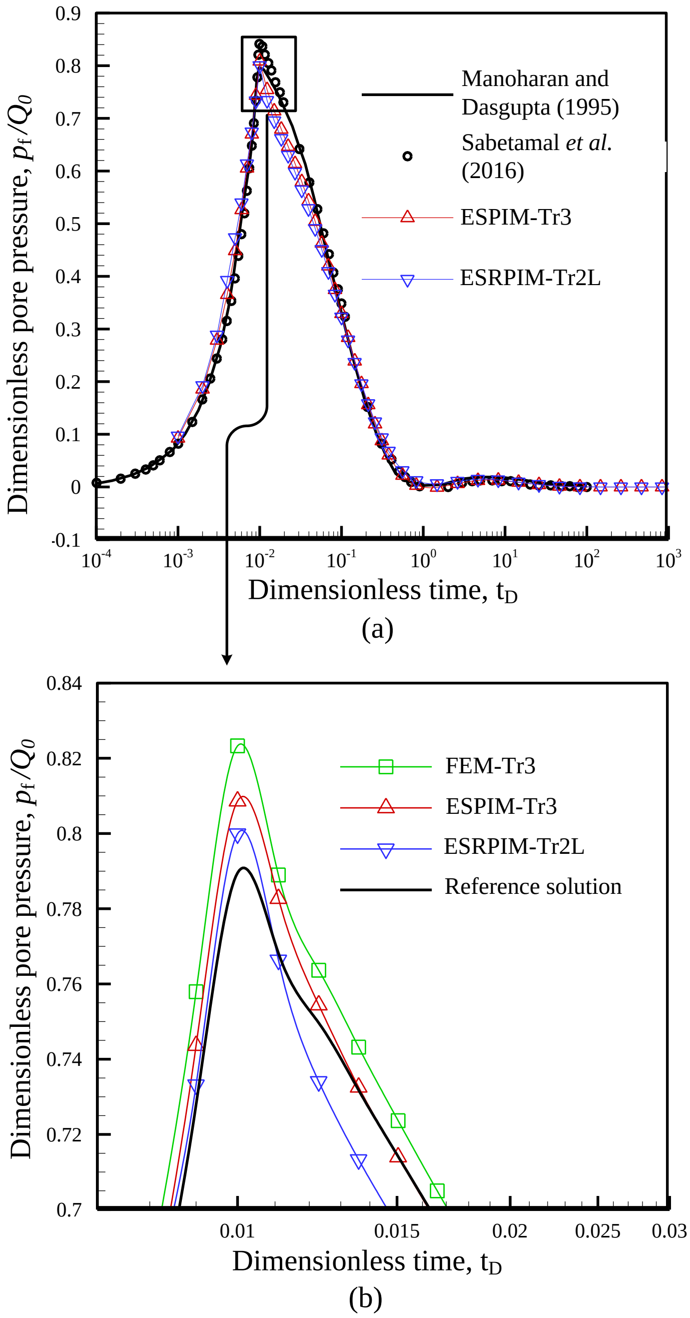

Figure 5-9- Dimensionless pore fluid pressure versus dimensionless time at the point immediately below the centre of the footing.

The dimensionless horizontal displacement of the soil through depth on section B (see Figure 5-6) obtained using different numerical methods at dimensionless time $t_D = 100$

(assumed end of the consolidation process) is given in Figure 5-10. As observed from this figure, once again, ESPIM-Tr3 provides better results compared to FEM-Tr3 and ESRPIM-Tr2L.

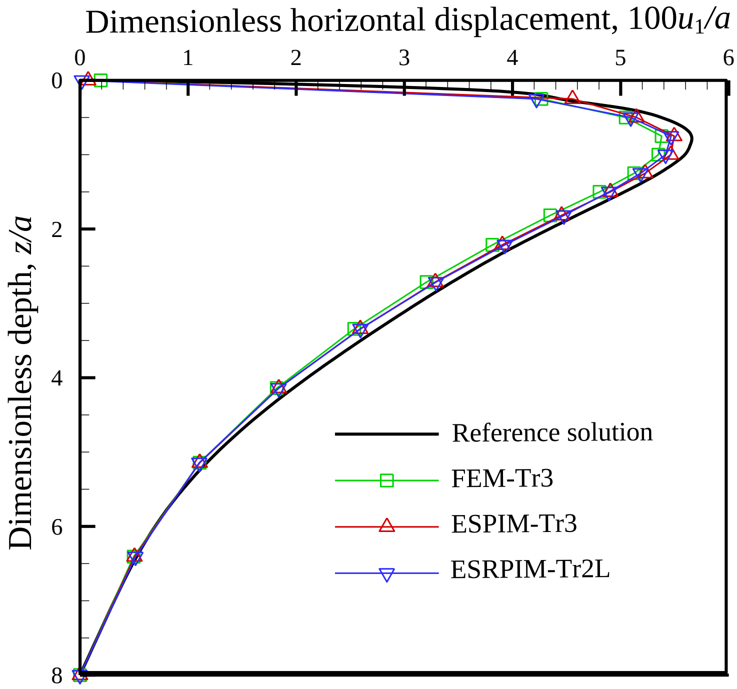

Figure 5-10- Dimensionless horizontal displacement versus dimensionless depth along section B at dimensionless time .

Finally, efficiency analyses were performed for different methods by recording the time required for the analyses up to $t_D = 100$. The results of the analysis are reported in Table 5-2 in a format similar to the format previously presented for example 5.5.1. It can be seen from this table that, once again ESPIM-Tr3 has performed better than FEM-Tr3 in terms of the total analysis time, and its superior accuracy in displacements and pore water pressure calculations is also evident from Figure 5-8 to Figure 5-10. ESRPIM-Tr2L, however, was slightly slower than ESPIM-Tr3 and linear FEM due to the more complicated computational procedure and larger number of selected supporting nodes.

Table 5-2- Comparison of the computational time required by different numerical procedures adopted in example 5.4.3.

Method	Total number of iterations	Average time of each iteration with respect to that of FEM-Tr3	Total time of the analysis with respect to that of FEM-Tr3
FEM-Tr3	572	1	1
ESPIM-Tr3	552	1.033	0.997
ESRPIM-Tr2L	546	1.059	1.011

5.5. Conclusion

Application of the ESPIM to the solution of coupled flow-deformation problems in porous media was presented. Two different node selection schemes for defining the support domains along with employment of polynomial and radial PIMs for construction of nodal shape functions were adopted resulting in two smoothed meshfree algorithms: ESPIM-Tr3 and ESRPIM-Tr2L. Temporal discretisation of the governing equations were performed using a three-point time discretisation technique. Sub-stepping method was adopted for stress integration, and the modified Newton-Raphson method was utilized to solve the nonlinear system of equations. The capability of the developed algorithms in capturing the coupled behaviour of elasto-plastic materials was investigated through three numerical examples with analytical or reference solutions. In all cases, very good agreement between the numerical results of the proposed methods and the analytical or reference solutions was observed. From the comparison between the numerical results of different methods and the analytical or reference solutions, it can be concluded that for flow-deformation problems in elastic-perfectly plastic materials, ESPIM-Tr3 offers very accurate solutions, clearly superior to ESRPIM-Tr2L and linear FEM using the same background mesh in terms of both displacement and pore fluid pressure calculations.

Chapter **6**

6. Coupled flow and deformation analysis of unsaturated porous media

6.1. Introduction

In spite of the focus of the classical soil mechanics on behaviour of saturated porous media and a huge number of numerical investigations in this area based on Biot's theory, the geo-materials routinely encountered in engineering practice belong to a different category, namely unsaturated porous media. The mechanical and hydraulic behaviour of unsaturated porous media are rather complex and proper models should be developed to meticulously address different aspects of engineering problems involving them.

In this chapter, a fully coupled ESPIM algorithm is introduced for hydro-mechanical analysis of unsaturated porous media considering hydraulic hysteresis. The simple Tr3 node selection scheme is adopted which ensures the non-singularity of the moment matrix in constructing the PPIM shape functions. An effective stress based framework based on the work of Khalili et al. (2008) is followed in this work, and a hysteretic water retention model is taken into account which enables the evolution of water retention curve (WRC) with volumetric changes (Pasha et al., 2017; Khoshghalb and Khalili, 2013). An elastoplastic constitutive model is employed within the context of bounding surface plasticity theory for predicting the nonlinear behaviour of soil skeleton in unsaturated porous media. The applicability of the presented model is verified through several numerical examples.

6.2. Governing equations

The theory of mixtures (Fillunger, 1936) is adopted for developing the relevant mathematical framework. According to this theory, a medium is assumed to comprise different overlapping constituents distributed continuously throughout the medium. An unsaturated porous medium is made up of three constituents: Solid skeleton, liquid phase, and gas phase. In geotechnical engineering applications, the liquid and gas phases are often water and air, respectively, and that is assumed in this study too, except for in one of the worked examples in which hypothetical liquid and gas phases are assumed. The framework in this study is presented based on three separate, yet coupled models: a deformation model which takes account of the interaction between the internal stresses and the external applied forces, and two flow models considering the flow of the fluid phases through the porous medium. The coupling between the deformation and the two flow models is established utilising the effective stress concept for unsaturated porous media (Khalili et al., 2000; Khalili et al., 2008), together with the volumetric compatibility relationships for the different phases. The coupling between the two flow models is stablished through the soil WRC. Further coupling among all the phases were accounted for through volume change dependency of the WRC.

6.2.1. Deformation model

As explained in Chapter 3, the deformation model is expressed based on the momentum balance of the solid-fluid mixture. For quasi-static processes, the momentum balance equation is expressed in the following form,

$$\mathbf{L}_{\mathrm{d}}^{\mathrm{T}}\boldsymbol{\sigma} + \rho\mathbf{B} = \mathbf{0} \tag{6.1}$$

in which ρ is the average density of the mixture defined as

$$\rho = n_{\mathrm{w}}\rho_{\mathrm{w}} + n_{\mathrm{a}}\rho_{\mathrm{a}} + (1-n)\rho_{\mathrm{s}} \tag{6.2}$$

where $n_{\mathrm{w}} = nS_{\mathrm{r}}$ and $n_{\mathrm{a}} = n(1-S_{\mathrm{r}})$ are porosity of the water and air phases, respectively, with S_{r} being the degree of saturation, and ρ_{w} and ρ_{a} are density of water and air, respectively.

The only unified approach to deal with equation (6.1) for either saturated or unsaturated porous materials is the effective stress approach (Khalili et al., 2004). The effective stress for unsaturated porous media is expressed in the total and incremental forms in equations (6.3) and (6.4), respectively, as follows

$$\boldsymbol{\sigma}' = \boldsymbol{\sigma}_{\mathrm{net}} - \chi s\boldsymbol{\delta} \tag{6.3}$$

$$\dot{\boldsymbol{\sigma}}' = \dot{\boldsymbol{\sigma}}_{\mathrm{net}} - \psi\dot{s}\boldsymbol{\delta} \tag{6.4}$$

where $\boldsymbol{\sigma}_{\mathrm{net}} = \boldsymbol{\sigma} + p_{\mathrm{a}}\boldsymbol{\delta}$ is the net stress vector. $\psi = \mathrm{d}(\chi s)/\mathrm{d}s$ is the incremental effective stress parameter, with χ being the effective stress parameter, and $s = p_{\mathrm{a}} - p_{\mathrm{w}}$ is the matric suction, which will be simply referred to as suction in this work assuming the osmotic suction is negligible. Adopting an incremental constitutive equation and the relationship for small strains of the solid skeleton (equations (5.3) and (5.4), respectively), equation (6.1) can be rewritten in the following incremental form

$$\mathbf{L}_{\mathrm{d}}^{\mathrm{T}}(\mathbf{D}^{\mathrm{ep}}\dot{\boldsymbol{\varepsilon}}-\psi\,\dot{p}_{\mathrm{w}}\boldsymbol{\delta}+(1-\psi)\,\dot{p}_{\mathrm{a}}\boldsymbol{\delta})+\rho\,\dot{\mathbf{B}}=\mathbf{0} \tag{6.5}$$

The effective stress parameter χ which specifies the relative contribution of the pore air and pore water pressures to the effective stress, can be obtained through various models, many of which are focused in relating this parameter to the degree of saturation S_{r}. In this study, an extension of the widely used effective stress parameter proposed by Khalili and Khabbaz (1998) is adopted. The original model proposed by Khalili and Khabbaz (1998) does not include the hydraulic hysteresis effects, and expresses χ as a function of the suction and air entry/expulsion value of the soil, as follows

$$\chi=\begin{cases}1 & s\le s_{\mathrm{e}}\\ \left(\dfrac{s_{\mathrm{e}}}{s}\right)^{\Omega} & s>s_{\mathrm{e}}\end{cases} \tag{6.6}$$

where Ω is a material parameter, with the best fit of 0.55. For the cases in which suction is increasing on the main drying path, s_{e} is equal to the air entry value (s_{ae}), while when suction is decreasing on the main wetting path, s_{e} is equal to the air expulsion value (s_{ex}). Khalili and Zargarbashi (2010) expanded the model to consider the effect of hydraulic hysteresis on the changes in χ when suction reversal occurs:

$$\chi=\begin{cases}\left(\dfrac{s_{\mathrm{ae}}}{s_{\mathrm{rd}}}\right)^{\Omega}\left(\dfrac{s_{\mathrm{rd}}}{s}\right)^{\zeta} & \text{for drying path reversal} \quad \left(\dfrac{s_{\mathrm{ex}}}{s_{\mathrm{ae}}}\right)^{\frac{\Omega}{\Omega-\zeta}}s_{\mathrm{rd}}\le s\le s_{\mathrm{rd}}\\[2ex] \left(\dfrac{s_{\mathrm{ex}}}{s_{\mathrm{rw}}}\right)^{\Omega}\left(\dfrac{s_{\mathrm{rw}}}{s}\right)^{\zeta} & \text{for wetting path reversal} \quad s_{\mathrm{rw}}\le s\le \left(\dfrac{s_{\mathrm{ae}}}{s_{\mathrm{ex}}}\right)^{\frac{\Omega}{\Omega-\zeta}}s_{\mathrm{rw}}\end{cases} \tag{6.7}$$

where ζ is the slope of the scanning curve, and s_{rd} and s_{rw} are the points of suction reversal on the main drying and main wetting curves, respectively. The evolution of effective stress parameter based on equations (6.6) and (6.7) is presented in Figure 6-1.

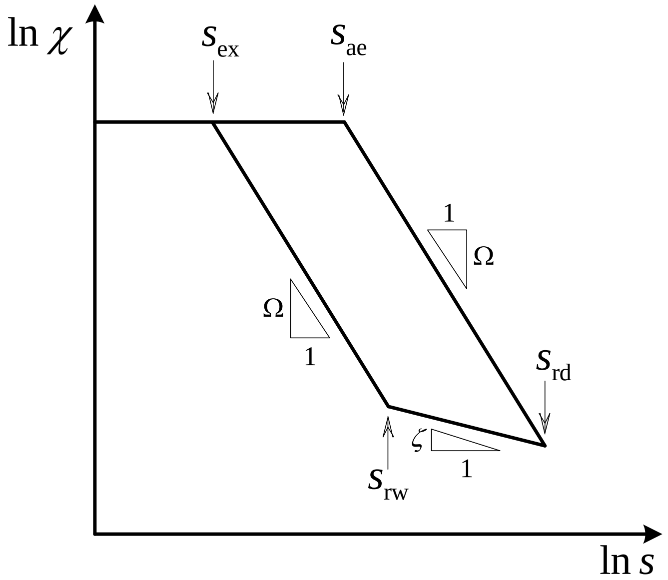

Figure 6-1- Evolution of the effective stress parameter with suction.

6.2.2. Flow models

The flow model which describes the flow of water and air through the unsaturated porous media is stated by combining the equation of linear momentum balance ignoring the inertia and viscous effects (equation (6.8)), with the mass balance equation for each fluid phase (equation (6.9)), as follows

$$\mathbf{v}_{\pi\mathrm{s}} = -\frac{k_{\mathrm{r}\pi}\mathbf{k}}{\mu_\pi}(\nabla p_\pi + \rho_\pi \mathbf{g}) \tag{6.8}$$

$$\frac{\partial}{\partial t}(\rho_\pi n_\pi) + \mathrm{div}(\rho_\pi n_\pi \mathbf{v}_\pi) = 0 \tag{6.9}$$

where $\pi = \mathrm{w,a}$ represents water and air phases; $k_{\mathrm{r}\pi}$ is the relative permeability of phase π; μ_π is the dynamic viscosity of phase π; ρ_π is the density of phase π; n_π is the volumetric content of phase π, and $\mathbf{v}_{\pi\mathrm{s}}$ is the relative velocity vector for phase π with respect to a moving solid, i.e.,

$$\mathbf{v}_{\pi\mathrm{s}} = n_\pi(\mathbf{v}_\pi - \mathbf{v}_s) \tag{6.10}$$

where $\mathbf{v}_\pi = \dot{\mathbf{u}}_\pi$ and $\mathbf{v}_\mathrm{s} = \dot{\mathbf{u}}$ are absolute velocities of fluid phase π and the solid phase, respectively, with $\mathbf{u}_\pi$ indicating the displacement vector of fluid phase π.

Introducing the Lagrangian total derivatives concept with respect to a moving solid, $\mathrm{d}(\cdot)/\mathrm{d}t = \partial(\cdot)/\partial t + \nabla(\cdot)\cdot\mathbf{v}_\mathrm{s}$, and noting $\mathrm{div}\left[(\cdot)\mathbf{v}_\alpha\right] = (\cdot)\,\mathrm{div}(\mathbf{v}_\alpha) + \nabla(\cdot)\cdot\mathbf{v}_\alpha$, equation (6.9) is rearranged to

$$-\mathrm{div}(\rho_\pi \mathbf{v}_{\pi\mathrm{s}}) = n_\pi\dot{\rho}_\pi + \rho_\pi\dot{n}_\pi + n_\pi\rho_\mathrm{f}\,\mathrm{div}(\mathbf{v}_\mathrm{s}) \tag{6.11}$$

Considering the definition of compressibility of barometric fluids, we have

$$\dot{\rho}_\pi = \rho_\pi \mathrm{c}_\pi \dot{p}_\pi \tag{6.12}$$

in which c_π is the coefficient of compressibility for phase π.

In case $\pi = \mathrm{a}$, the density of air is obtained from the ideal gas law as a function of pressure and temperature as follows

$$\rho_\mathrm{a} = \frac{P_\mathrm{a}M}{RT} \tag{6.13}$$

where P_a is the absolute air pressure ($P_\mathrm{a} = p_\mathrm{a} + p_\mathrm{atm}$, where p_atm is the atmospheric air pressure), M is the average molecular mass of air, R is the universal air constant, and T is the absolute temperature.

From the definition of n_π ($n_\pi = V_\pi / V$), the rate of change in porosity of phase π can be derived as

$$\dot{n}_\pi = \frac{1}{V}\left(\dot{V}_\pi - n_\pi \dot{V}\right) \tag{6.14}$$

Substituting equations (3.7), (3.12) and (3.13) into equation (6.11), and noting that $\left(\mathrm{d}V/\mathrm{d}t\right)/V = \mathrm{div}(\mathbf{v}_\mathrm{s})$, the following equation for the flow of fluid phase π through porous media is obtained,

$$\frac{1}{\rho_\pi}\mathrm{div}\left(\rho_\pi \frac{k_{r\pi}\mathbf{k}}{\mu_\pi}\left(\nabla p_\pi + \rho_\pi \mathbf{g}\right)\right) - n_\pi c_\pi \dot{p}_\pi - \frac{\dot{V}_\pi}{V} = 0 \tag{6.15}$$

6.2.3. Constitutive coefficients

To capture the dependency of the model parameters on suction and volume change, the constitutive relationships can be expressed relating the pore water and pore air volumetric deformations to changes in volumetric strain and suction (Khalili et al., 2008),

$$-\frac{\dot{V}_\mathrm{w}}{V} = \psi \dot{\varepsilon}_\mathrm{v} + a_{12}\dot{s} \tag{6.16}$$

$$-\frac{\dot{V}_\mathrm{a}}{V} = (1-\psi)\dot{\varepsilon}_\mathrm{v} - a_{21}\dot{s} \tag{6.17}$$

where $a_{21} = a_{12}$ are the constitutive coefficients relating the changes in pore water and pore air volumetric deformations to changes in pore water and pore air pressures, V_w is the volume of water phase and V_a is the volume of air phase.

The constitutive coefficients and the incremental effective stress parameter can be obtained by exposing an element of unsaturated porous medium to perturbations of pore water and pore air pressure and measuring the volume changes associated with each phase. An alternative approach, according to (Khalili et al., 2008), is followed here. From the definition of degree of saturation $S_\mathrm{r} = V_\mathrm{w}/V_\mathrm{v}$, where V_w is the volume of the water phase and V_v is the void volume, we have

$$\frac{\dot{V}_\mathrm{w}}{V} = n\dot{S}_\mathrm{r} - S_\mathrm{r}\dot{\varepsilon}_\mathrm{v} \tag{6.18}$$

$$\frac{\dot{V}_\mathrm{a}}{V} = -n\dot{S}_\mathrm{r} - (1 - S_\mathrm{r})\dot{\varepsilon}_\mathrm{v} \tag{6.19}$$

The degree of saturation is a function of both suction and volume change of the soil skeleton. Therefore, its rate can be expressed in the differential form of

$$\dot{S}_\mathrm{r} = \frac{\partial S_\mathrm{r}}{\partial s}\dot{s} + \frac{\partial S_\mathrm{r}}{\partial \varepsilon_\mathrm{v}}\dot{\varepsilon}_\mathrm{v} \tag{6.20}$$

Now, from equations (6.18) to (6.20) we have

$$\frac{\dot{V}_\mathrm{w}}{V} = n\frac{\partial S_\mathrm{r}}{\partial s}\dot{s} - (S_\mathrm{r} - n\frac{\partial S_\mathrm{r}}{\partial \varepsilon_\mathrm{v}})\dot{\varepsilon}_\mathrm{v} \tag{6.21}$$

$$\frac{\dot{V}_\mathrm{a}}{V} = -n\frac{\partial S_\mathrm{r}}{\partial s}\dot{s} - (1 - S_\mathrm{r} + n\frac{\partial S_\mathrm{r}}{\partial \varepsilon_\mathrm{v}})\dot{\varepsilon}_\mathrm{v} \tag{6.22}$$

Comparing equations (6.21) and (6.22) with equations (6.16) and (6.17), constitutive parameters ψ and a_{12} are obtained as

$$\psi = S_\mathrm{r} - n\frac{\partial S_\mathrm{r}}{\partial \varepsilon_\mathrm{v}} \tag{6.23}$$

$$a_{12} = -n\frac{\partial S_{\mathrm{r}}}{\partial s} \tag{6.24}$$

Noting that $\varepsilon_{\mathrm{v}} = -tr(\boldsymbol{\varepsilon}) = -\mathrm{div}(\mathbf{u})$ and considering zero compressibility for the solid skeleton $\left(c_{\mathrm{s}} = 0\right)$ the fully coupled flow equations can be obtained employing equations (6.23) and (6.24) in conjunction with equation (6.15) as

$$\frac{1}{\rho_{\mathrm{w}}}\mathrm{div}\left(\rho_{\mathrm{w}}\frac{k_{\mathrm{rw}}\mathbf{k}}{\mu_{\mathrm{w}}}\left(\nabla\dot{p}_{\mathrm{w}} + \rho_{\mathrm{w}}\mathbf{g}\right)\right) - \psi\,\mathrm{div}(\dot{\mathbf{u}}) - a_{11}\dot{p}_{\mathrm{w}} + a_{12}\dot{p}_{\mathrm{a}} = \mathbf{0} \tag{6.25}$$

$$\frac{1}{\rho_{\mathrm{a}}}\mathrm{div}\left(\rho_{\mathrm{a}}\frac{k_{\mathrm{ra}}\mathbf{k}}{\mu_{\mathrm{a}}}\left(\nabla p_{\mathrm{a}} + \rho_{\mathrm{a}}\mathbf{g}\right)\right) - (1-\psi)\mathrm{div}(\dot{\mathbf{u}}) + a_{21}\dot{p}_{\mathrm{w}} - a_{22}\dot{p}_{\mathrm{a}} = \mathbf{0} \tag{6.26}$$

where

$$a_{11} = c_{\mathrm{w}}n_{\mathrm{w}} + a_{12}\,,\; a_{22} = c_{\mathrm{a}}n_{\mathrm{a}} + a_{21} \tag{6.27}$$

and the compressibility of air is obtained as

$$c_{\mathrm{a}} = P_{\mathrm{a}}^{-1} = \left(p_{\mathrm{a}} + p_{\mathrm{atm}}\right)^{-1} \tag{6.28}$$

6.2.4. Void ratio dependent water retention model

A critical step in modelling the behaviour of unsaturated soils is determining the water retention capacity at various suctions and hydraulic loading conditions, i.e. drying, wetting, or suction reversals, at a given density state. Numerous models have been so far proposed for this purpose (Van Genuchten, 1980; Brooks and Corey, 1964; Fredlund and Xing, 1994). Soil WRC is an *a priori* function of the volume change of the solid skeleton; however, the majority of the current WRC models overlook the influence of soil density on the soil water retention capacity. A number of models are proposed to take account of volume change dependency of the WRC (Tarantino, 2009; Mašín, 2010;

Salager et al., 2013; Tsiampousi et al., 2013a; Khoshghalb et al., 2015; Pasha et al., 2017). According to equations (6.23) and (6.24), the constitutive coefficients have to be evaluated considering the evolution of the degree of saturation with changes in volumetric strain and suction. In this study, a void ratio dependent WRC similar to that presented in Pasha et al. (2017) is adopted. This model is briefly explained in the remainder of this section.

Based on the model originally proposed by Brooks and Corey (1964) and later extended by Khalili and Zargarbashi (2010) to include the effect of hydraulic hysteresis, the variation of the effective degree of saturation S_{eff} with suction can be evaluated at a given void ratio as

$$S_{\mathrm{eff}} = \begin{cases} 1 & s \le s_{\mathrm{e}} \\ \left(\dfrac{s_{\mathrm{e}}}{s}\right)^{\lambda_{\mathrm{p}}} & s > s_{\mathrm{e}} \end{cases} \tag{6.29}$$

$$S_{\mathrm{eff}} = \begin{cases} \left(\dfrac{s_{\mathrm{ae}}}{s_{\mathrm{rd}}}\right)^{\lambda_{\mathrm{pd}}} \left(\dfrac{s_{\mathrm{rd}}}{s}\right)^{\xi} & \text{for drying path reversal} \quad \dfrac{s_{\mathrm{ex}}^{\frac{\lambda_{\mathrm{pw}}}{\lambda_{\mathrm{pw}}-\xi}}}{s_{\mathrm{ae}}^{\frac{\lambda_{\mathrm{pd}}}{\lambda_{\mathrm{pw}}-\xi}}} s_{\mathrm{rd}}^{\frac{\lambda_{\mathrm{pd}}-\xi}{\lambda_{\mathrm{pw}}-\xi}} \le s \le s_{\mathrm{rd}} \\ \left(\dfrac{s_{\mathrm{ex}}}{s_{\mathrm{rw}}}\right)^{\lambda_{\mathrm{pw}}} \left(\dfrac{s_{\mathrm{rw}}}{s}\right)^{\xi} & \text{for wetting path reversal} \quad s_{\mathrm{rw}} \le s \le \dfrac{s_{\mathrm{ae}}^{\frac{\lambda_{\mathrm{pd}}}{\lambda_{\mathrm{pd}}-\xi}}}{s_{\mathrm{ae}}^{\frac{\lambda_{\mathrm{pw}}}{\lambda_{\mathrm{pd}}-\xi}}} s_{\mathrm{rw}}^{\frac{\lambda_{\mathrm{pw}}-\xi}{\lambda_{\mathrm{pd}}-\xi}} \end{cases} \tag{6.30}$$

where $S_{\mathrm{eff}} = \left(S_{\mathrm{r}} - S_{\mathrm{res}}\right)/\left(1 - S_{\mathrm{res}}\right)$ and S_{res} is the residual degree of saturation. In equation (6.29), s_{e} is the air entry value (s_{ae}) on the main drying path, and the air expulsion value (s_{ex}) on the main wetting path. Similarly, for the pore size distribution index, λ_{p}, we have $\lambda_{\mathrm{p}} = \lambda_{\mathrm{pd}}$ on the main drying path and $\lambda_{\mathrm{p}} = \lambda_{\mathrm{pw}}$ on the main wetting path. The adopted WRC is shown schematically in Figure 6-2. It is noteworthy that the suction reversal values s_{rd} and s_{rw} in the WRC should be consistent with those stated in equation (6.7) and shown in Figure 6-2.

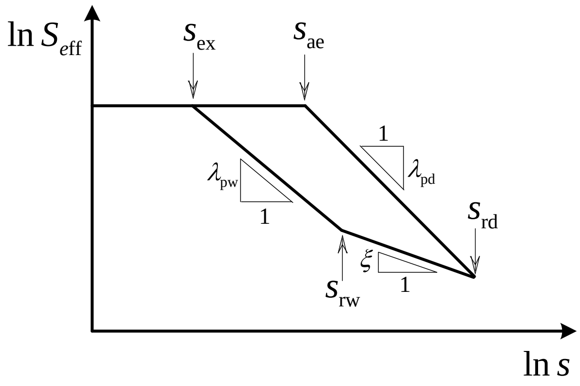

Figure 6-2- WRC model adopted in this study.

The volume change dependency of the WRC model is accounted for assuming s_{e}, λ_{p} and ξ are functions of void ratio (e). For capturing the evolution of s_{e} with void ratio, equation (6.23) can be rearranged as

$$\mathrm{d}S_{\mathrm{r}} = (\psi - S_{\mathrm{r}})\frac{\mathrm{d}e}{e} \tag{6.31}$$

Combining equations (6.6), (6.29) and (6.31) for the main drying and wetting paths, the updated effective degree of saturation, S^{*}_{eff}, due to a small change in the void ratio, $\mathrm{d}e$, can be expressed as (Pasha et al., 2017)

$$S^{*}_{\mathrm{eff}} = S_{\mathrm{eff}} + \mathrm{d}S_{\mathrm{eff}} = (\frac{s_{\mathrm{e}}}{s})^{\lambda_{\mathrm{p}}} + \frac{(1-\Omega)(\frac{s_{\mathrm{e}}}{s})^{\Omega} - (1-S_{\mathrm{res}})(\frac{s_{\mathrm{e}}}{s})^{\lambda_{\mathrm{p}}} - S_{\mathrm{res}}}{1-S_{\mathrm{res}}}\frac{\mathrm{d}e}{e} \tag{6.32}$$

Now, considering the point of transition from saturation to unsaturation ($S^{*}_{\mathrm{eff}} = 1$ and $s = s^{*}_{\mathrm{e}}$) and employing Taylor's series expansion, the following expression can be obtained for the void ratio dependency of s_{e}

$$s_{\mathrm{e}}^{*} = s_{\mathrm{e}}(1+\frac{\Omega}{1-S_{\mathrm{res}}}\frac{\mathrm{d}e}{e})^{-1/\lambda_{\mathrm{psu}}} \tag{6.33}$$

where λ_{psu} is the pore size distribution index at the transition point from saturated to unsaturated state. For small increments of void ratio, equation (6.33) can be further simplified to the incremental form of

$$\frac{\mathrm{d}s_{\mathrm{e}}}{\mathrm{d}e} = -\frac{\Omega\, s_{\mathrm{e}}}{e(1-S_{\mathrm{res}})\lambda_{\mathrm{psu}}} \tag{6.34}$$

which can be expressed in the following form after integration

$$s_{\mathrm{e}}^{*} = s_{\mathrm{e}}(\frac{e^{*}}{e})^{\frac{-\Omega}{(1-S_{\mathrm{res}})\lambda_{\mathrm{psu}}}} \tag{6.35}$$

where $e^{*} = e + \mathrm{d}e$ is the updated void ratio.

Variations of the degree of saturation with void ratio on the main drying and wetting paths can be expressed in terms of the variations of the WRC model parameters, s_{e} and λ_{p}, with void ratio as follows

$$\frac{\partial S_{\mathrm{r}}}{\partial e} = \frac{\partial S_{\mathrm{r}}}{\partial s_{\mathrm{e}}}\frac{\partial s_{\mathrm{e}}}{\partial e} + \frac{\partial S_{\mathrm{r}}}{\partial \lambda_{\mathrm{p}}}\frac{\partial \lambda_{\mathrm{p}}}{\partial e} \tag{6.36}$$

Calculating the partial derivatives of S_{r} with respect to s_{e} and λ_{p}, and making use of equation (6.34), the void ratio dependency of λ_{p} is expressed through the following equation

$$\frac{\partial \lambda_{\mathrm{p}}}{\partial e} = \frac{\psi - S_{\mathrm{r}} + \Omega S_{\mathrm{eff}}\dfrac{\lambda_{\mathrm{p}}}{\lambda_{\mathrm{psu}}}}{(1-S_{\mathrm{res}})S_{\mathrm{eff}}\ln S_{\mathrm{eff}}}\frac{\lambda_{\mathrm{p}}}{e} \tag{6.37}$$

Equation (6.37) indicates that λ_{p} is a function of both void ratio and suction. However, Pasha et al. (2017) showed that the suction dependency of λ_{p} is negligible, and therefore $\lambda_{\mathrm{psu}} = \lambda_{\mathrm{p}}$ is adopted in this study. Through linearisation of equation (6.37) between two points with the effective degrees of saturation of 1.0 and 0.5, the following relationship can be obtained for evaluation of the updated pore size distribution index due to small change in void ratio,

$$\lambda_{\mathrm{p}}^{*} = \lambda_{\mathrm{p}}\left[1 - \frac{3\left[(1-\Omega)\left(2^{1-\Omega/\lambda_{\mathrm{p}}}-1\right)-S_{\mathrm{res}}\right]}{2(1-S_{\mathrm{res}})}\frac{\mathrm{d}e}{e}\right] \tag{6.38}$$

Now, expressing the updated S_{eff} in a similar manner as in equation (6.32), we can obtain the updated slope of the WRC along the scanning path, ξ^{*}, as follows

$$\xi^{*} = \xi\left[1 + \frac{(1-\zeta)(\xi-\zeta)\chi}{\xi S_{\mathrm{eff}}}\frac{\mathrm{d}e}{e}\right] \tag{6.39}$$

Ensuring consistency between the effective stress parameter model and the WRC in suction reversal paths, the slope of the transition line in $\ln\chi - \ln s$ plane can be expressed as follows,

$$\zeta = \Omega\xi\left[\frac{\ln\left(\dfrac{s_{\mathrm{ex}}s_{\mathrm{rd}}}{s_{\mathrm{ae}}s_{\mathrm{rw}}}\right)}{\ln\left(\left(\dfrac{s_{\mathrm{rd}}}{s_{\mathrm{ae}}}\right)^{\lambda_{\mathrm{pd}}}\left(\dfrac{s_{\mathrm{ex}}}{s_{\mathrm{rw}}}\right)^{\lambda_{\mathrm{pw}}}\right)}\right] \tag{6.40}$$

and therefore the updated slope of the scanning line in $\ln\chi - \ln s$ plane (ζ^{*}) can be obtained from equation (6.40) once s_{e}^{*}, λ_{p}^{*} and ξ^{*} are calculated. If $\lambda_{\mathrm{pd}} = \lambda_{\mathrm{pw}} = \lambda_{\mathrm{p}}$, equation (6.41) is simplified to the following form

$$\zeta = \frac{\Omega \xi}{\lambda_{\mathrm{p}}} \tag{6.41}$$

6.2.5. Coefficient of permeability

The coefficients of permeability of both water and air phases are functions of void ratio and the degree of saturation of the porous medium. The variations of the void ratio directly affect the intrinsic permeability of the medium. Various models have been proposed for capturing this void ratio dependency of the intrinsic permeability (Poiseuille, 1838; Kozeny, 1927; Carman, 1937; Taylor, 1948) . In this study, the widely used model by Kozeny-Carman (Scheidegger, 1958) for isotropic porous media is adopted, which is as follows

$$k = k_0 \left(\frac{e}{e_0} \right) \left(\frac{1+e_0}{1+e} \right) \tag{6.42}$$

where $\mathbf{k}_0 = k_0 \mathbf{I}$ is the reference intrinsic permeability matrix and e_0 is the reference void ratio.

The dependency of the air and water coefficients of permeability on the degree of saturation of the porous media is accounted for using the model proposed by Brooks and Corey (1964), which expresses the relative permeability coefficients as functions of the effective degree of saturation and the pore size distribution of the porous media as follows

$$k_{\mathrm{rw}} = S_{\mathrm{eff}}{}^{\delta_1} \tag{6.43}$$

$$k_{\mathrm{ra}} = \left(1 - S_{\mathrm{eff}}\right)^2 \left(1 - S_{\mathrm{eff}}{}^{\delta_2}\right) \tag{6.44}$$

where $\delta_1 = (2+3\lambda_{\mathrm{p}})/\lambda_{\mathrm{p}}$ and $\delta_2 = (2+\lambda_{\mathrm{p}})/\lambda_{\mathrm{p}}$, according to recommendations by Brooks and Corey (1966).

6.2.6. Initial and boundary conditions

The solid skeleton displacement $\mathbf{u}(\mathbf{x},t)$ and the pore pressures $p_\pi(\mathbf{x},t)$ where $\pi = \mathrm{w},\mathrm{a}$, are the main variables in the governing equations (6.5), (6.25) and (6.26). The required initial conditions for solving these equations are exactly the same as those elaborated in Chapter 3, through equation (3.20) to (3.25). It should only be noted that the boundary conditions for the fluid phase now apply to both air and water phases.

6.3. Numerical solution of the governing equations

The edge-based smoothed point interpolation method (ESPIM), based on the polynomial point interpolation shape functions in conjunction with Tr3 node selection scheme for defining the support domain at each point of interest is adopted for numerical solution of the governing equations. The details of the method can be found in Chapter 3, section 3.4.

6.3.1. Spatial discretisation

Introducing the GS-Galerkin approach to equations (6.5), (6.25) and (6.26), the following system of fully coupled algebraic equations is derived in matrix form

$$\int_\Omega \widehat{\mathbf{B}}_1^{\mathrm{T}} \boldsymbol{\sigma}' \mathrm{d}\Omega - \chi \mathbf{Q}\mathbf{P}_{\mathrm{w}} - (1-\chi)\mathbf{Q}\mathbf{P}_{\mathrm{a}} = \mathbf{F}_{\mathrm{u}} \tag{6.45}$$

$$-\psi \mathbf{Q}^{\mathrm{T}}\dot{\mathbf{U}} - \mathbf{H}_{\mathrm{w}}\mathbf{P}_{\mathrm{w}} - a_{11}\mathbf{S}\dot{\mathbf{P}}_{\mathrm{w}} + a_{12}\mathbf{S}\dot{\mathbf{P}}_{\mathrm{a}} = \mathbf{F}_{\mathrm{w}} \tag{6.46}$$

$$-(1-\psi)\mathbf{Q}^{\mathrm{T}}\dot{\mathbf{U}} - \mathbf{H}_{\mathrm{a}}\mathbf{P}_{\mathrm{a}} + a_{21}\mathbf{S}\dot{\mathbf{P}}_{\mathrm{w}} + a_{22}\mathbf{S}\dot{\mathbf{P}}_{\mathrm{a}} = \mathbf{F}_{\mathrm{a}} \tag{6.47}$$

where $\mathbf{P}_{\mathrm{w}}$ and $\mathbf{P}_{\mathrm{a}}$ are the vectors of the nodal pore water and air pressures, respectively; $\mathbf{F}_{\mathrm{w}}$ and $\mathbf{F}_{\mathrm{a}}$ are the vector of nodal water and air fluxes, respectively; and $\mathbf{H}_{\mathrm{w}}$ and $\mathbf{H}_{\mathrm{a}}$ are the global water permeability and air permeability matrices, respectively. The global tangent stiffness matrix $\mathbf{K}_{\mathrm{T}}$, the global property matrices $\mathbf{Q}$, $\mathbf{S}$, and $\mathbf{F}_{\mathrm{u}}$ are evaluated through assembly procedures over the smoothing (integration) domains as expressed in Chapters 3 and 5. The permeability matrices and the vectors of nodal fluid fluxes are evaluated as follows,

$$\mathbf{H}_{\pi} = \sum_{k=1}^{n_{\mathrm{SD}}} (\mathbf{H}_{\pi})_k^{\mathrm{SD}} = \sum_{k=1}^{n_{\mathrm{SD}}} \left(\int_{\Omega_k^{\mathrm{SD}}} \widehat{\mathbf{B}}_2^{\mathrm{T}} \frac{\mathbf{k}}{\mu_{\pi}} \widehat{\mathbf{B}}_2 \mathrm{d}\Omega \right) = \sum_{k=1}^{n_{\mathrm{SD}}} \frac{A_k^{\mathrm{SD}}}{\mu_{\pi}} \widehat{\mathbf{B}}_2^{\mathrm{T}} \mathbf{k} \widehat{\mathbf{B}}_2, \quad \pi = \mathrm{w}, \mathrm{a} \tag{6.48}$$

$$\mathbf{F}_{\pi} = \sum_{k=1}^{n_{\mathrm{SD}}} (\mathbf{F}_{\pi})_k^{\mathrm{SD}} = \sum_{k=1}^{n_{\mathrm{SD}}} \int_{\Gamma_k^{\mathrm{SD}}} \mathbf{\Phi}^{\mathrm{pqT}} q_{\pi} \mathrm{d}\Omega, \quad \pi = \mathrm{w}, \mathrm{a} \tag{6.49}$$

6.3.2. Time discretisation

Using the three-point time discretisation scheme with variable time steps as detailed in section 3.5.2, the fully coupled discretised governing equations can now be obtained by applying equation (3.72) and (3.73) to equations (6.45) to (6.47) as follows,

$$\begin{aligned}
&\int_{\Omega} \widehat{\mathbf{B}}_1^{\mathrm{T}} (\boldsymbol{\sigma}')^t \mathrm{d}\Omega - \chi^t \mathbf{Q} \mathbf{P}_{\mathrm{w}}^t - \left(1 - \chi^t\right) \mathbf{Q} \mathbf{P}_{\mathrm{a}}^t \\
&+ \int_{\Omega} \widehat{\mathbf{B}}_1^{\mathrm{T}} \left[(\boldsymbol{\sigma}')^{t+\alpha\Delta t} - (\boldsymbol{\sigma}')^t \right] \mathrm{d}\Omega - \psi^{t+\alpha\Delta t} \mathbf{Q} \left(\mathbf{P}_{\mathrm{w}}^{t+\alpha\Delta t} - \mathbf{P}_{\mathrm{w}}^t \right) - \left(1 - \psi^{t+\alpha\Delta t}\right) \mathbf{Q} \left(\mathbf{P}_{\mathrm{a}}^{t+\alpha\Delta t} - \mathbf{P}_{\mathrm{a}}^t \right) \\
&= \mathbf{F}_{\mathrm{u}}^{t+\alpha\Delta t}
\end{aligned} \tag{6.50}$$

$$\begin{aligned}
&-\psi^{t+\alpha\Delta t} \mathbf{Q}^{\mathrm{T}} \left(A\mathbf{U}^{t+\alpha\Delta t} - B\mathbf{U}^t + C\mathbf{U}^{t-\Delta t} \right) - \Delta t \mathbf{H}_{\mathrm{w}} \mathbf{P}_{\mathrm{w}}^{t+\alpha\Delta t} \\
&- a_{11}^{t+\alpha\Delta t} \mathbf{S} \left(A\mathbf{P}_{\mathrm{w}}^{t+\alpha\Delta t} - B\mathbf{P}_{\mathrm{w}}^t + C\mathbf{P}_{\mathrm{w}}^{t-\Delta t} \right) + a_{12}^{t+\alpha\Delta t} \mathbf{S} \left(A\mathbf{P}_{\mathrm{a}}^{t+\alpha\Delta t} - B\mathbf{P}_{\mathrm{a}}^t + C\mathbf{P}_{\mathrm{a}}^{t-\Delta t} \right) = \Delta t \mathbf{F}_{\mathrm{w}}^{t+\alpha\Delta t}
\end{aligned} \tag{6.51}$$

$$\begin{aligned}
&-(1 - \psi^{t+\alpha\Delta t}) \mathbf{Q}^{\mathrm{T}} \left(A\mathbf{U}^{t+\alpha\Delta t} - B\mathbf{U}^t + C\mathbf{U}^{t-\Delta t} \right) - \Delta t \mathbf{H}_{\mathrm{a}} \mathbf{P}_{\mathrm{a}}^{t+\alpha\Delta t} \\
&+ a_{21}^{t+\alpha\Delta t} \mathbf{S} \left(A\mathbf{P}_{\mathrm{w}}^{t+\alpha\Delta t} - B\mathbf{P}_{\mathrm{w}}^t + C\mathbf{P}_{\mathrm{w}}^{t-\Delta t} \right) - a_{22}^{t+\alpha\Delta t} \mathbf{S} \left(A\mathbf{P}_{\mathrm{a}}^{t+\alpha\Delta t} - B\mathbf{P}_{\mathrm{a}}^t + C\mathbf{P}_{\mathrm{a}}^{t-\Delta t} \right) = \Delta t \mathbf{F}_{\mathrm{a}}^{t+\alpha\Delta t}
\end{aligned} \tag{6.52}$$

It is worth noting that equation (6.50) is obtained by decomposing the left-hand side of equation (6.45) into the contributions at time t, and the time increment $\alpha\Delta t$.

6.3.3. Solution algorithm

Following the line of the modified Newton-Raphson iterative process, the vector of the nodal displacement and pore fluid pressures at iteration i of the current time step $(t+\alpha\Delta t)$, are improved at iteration $i+1$ as

$$\begin{Bmatrix} \mathbf{U}^{i+1,t+\alpha\Delta t} \\ \mathbf{P}_{\mathrm{w}}^{i+1,t+\alpha\Delta t} \\ \mathbf{P}_{\mathrm{a}}^{i+1,t+\alpha\Delta t} \end{Bmatrix} = \begin{Bmatrix} \mathbf{U}^{i,t+\alpha\Delta t} \\ \mathbf{P}_{\mathrm{w}}^{i,t+\alpha\Delta t} \\ \mathbf{P}_{\mathrm{a}}^{i,t+\alpha\Delta t} \end{Bmatrix} + \begin{Bmatrix} \mathrm{d}\mathbf{U}^{i+1,t+\alpha\Delta t} \\ \mathrm{d}\mathbf{P}_{\mathrm{w}}^{i+1,t+\alpha\Delta t} \\ \mathrm{d}\mathbf{P}_{\mathrm{a}}^{i+1,t+\alpha\Delta t} \end{Bmatrix} \tag{6.53}$$

where $\square^{i,t}$ indicates the value of $\square = (\mathbf{U}, \mathbf{P}_{\mathrm{w}} \text{ or } \mathbf{P}_{\mathrm{a}})$ at the *i*th iteration at time *t*. The improvements are obtained so that the nodal displacements and pore fluid pressures satisfy the following residual form of the nonlinear equations at time $t+\alpha\Delta t$

$$\begin{aligned} \mathbf{\Psi}_{\mathrm{u}}^{i+1,t+\alpha\Delta t} &= \int_\Omega \widehat{\mathbf{B}}_1^{\mathrm{T}} (\boldsymbol{\sigma}')^t \,\mathrm{d}\Omega - \chi^{i,t+\alpha\Delta t}\mathbf{Q}\mathbf{P}_{\mathrm{w}}^t - \left(1-\chi^{i,t+\alpha\Delta t}\right)\mathbf{Q}\mathbf{P}_{\mathrm{a}}^t \\ &+ \int_\Omega \widehat{\mathbf{B}}_1^{\mathrm{T}} (\mathrm{d}\boldsymbol{\sigma}')^{i+1,t+\alpha\Delta t} d\Omega - \psi^{i,t+\alpha\Delta t}\mathbf{Q}\mathrm{d}\mathbf{P}_{\mathrm{w}}^{i+1,t+\alpha\Delta t} - \left(1-\psi^{i,t+\alpha\Delta t}\right)\mathbf{Q}\mathrm{d}\mathbf{P}_{\mathrm{a}}^{i+1,t+\alpha\Delta t} \\ &- \mathbf{F}_{\mathrm{u}}^{i+1,t+\alpha\Delta t} = \mathbf{0} \end{aligned} \tag{6.54}$$

$$\begin{aligned} \mathbf{\Psi}_{\mathrm{w}}^{i+1,t+\alpha\Delta t} &= -\psi^{i,t+\alpha\Delta t}\mathbf{Q}^{\mathrm{T}}\left(A\mathbf{U}^{i+1,t+\alpha\Delta t} - B\mathbf{U}^t + C\mathbf{U}^{t-\Delta t}\right) \\ &- \Delta t\mathbf{H}_{\mathrm{w}}\mathbf{P}_{\mathrm{w}}^{i+1,t+\alpha\Delta t} - a_{11}^{i,t+\alpha\Delta t}\mathbf{S}\left(A\mathbf{P}_{\mathrm{w}}^{i+1,t+\alpha\Delta t} - B\mathbf{P}_{\mathrm{w}}^t + C\mathbf{P}_{\mathrm{w}}^{t-\Delta t}\right) \\ &+ a_{12}^{i,t+\alpha\Delta t}\mathbf{S}\left(A\mathbf{P}_{\mathrm{a}}^{i+1,t+\alpha\Delta t} - B\mathbf{P}_{\mathrm{a}}^t + C\mathbf{P}_{\mathrm{a}}^{t-\Delta t}\right) - \Delta t\mathbf{F}_{\mathrm{w}}^{t+\alpha\Delta t} = \mathbf{0} \end{aligned} \tag{6.55}$$

$$\begin{aligned} \mathbf{\Psi}_{\mathrm{a}}^{i+1,t+\alpha\Delta t} &= -\left(1-\psi^{i,t+\alpha\Delta t}\right)\mathbf{Q}^{\mathrm{T}}\left(A\mathbf{U}^{i+1,t+\alpha\Delta t} - B\mathbf{U}^t + C\mathbf{U}^{t-\Delta t}\right) \\ &- \Delta t\mathbf{H}_{\mathrm{a}}\mathbf{P}_{\mathrm{a}}^{i+1,t+\alpha\Delta t} + a_{21}^{i,t+\alpha\Delta t}\mathbf{S}\left(A\mathbf{P}_{\mathrm{w}}^{i+1,t+\alpha\Delta t} - B\mathbf{P}_{\mathrm{w}}^t + C\mathbf{P}_{\mathrm{w}}^{t-\Delta t}\right) \\ &- a_{22}^{i,t+\alpha\Delta t}\mathbf{S}\left(A\mathbf{P}_{\mathrm{a}}^{i+1,t+\alpha\Delta t} - B\mathbf{P}_{\mathrm{a}}^t + C\mathbf{P}_{\mathrm{a}}^{t-\Delta t}\right) - \Delta t\mathbf{F}_{\mathrm{a}}^{t+\alpha\Delta t} = \mathbf{0} \end{aligned} \tag{6.56}$$

Now, to evaluate the incremental vector of the nodal displacements and pore fluid pressures, the following matrix equation is formed by expanding equations (6.54) to (6.56) with the first-order truncated Taylor series

$$\begin{Bmatrix} \boldsymbol{\Psi}_{\mathrm{u}}^{i+1,t+\alpha\Delta t} \\ \boldsymbol{\Psi}_{\mathrm{w}}^{i+1,t+\alpha\Delta t} \\ \boldsymbol{\Psi}_{\mathrm{a}}^{i+1,t+\alpha\Delta t} \end{Bmatrix} = \begin{Bmatrix} \boldsymbol{\Psi}_{\mathrm{u}}^{i,t+\alpha\Delta t} \\ \boldsymbol{\Psi}_{\mathrm{w}}^{i,t+\alpha\Delta t} \\ \boldsymbol{\Psi}_{\mathrm{a}}^{i,t+\alpha\Delta t} \end{Bmatrix} + \mathbf{J}^{i,t+\alpha\Delta t} \begin{Bmatrix} \mathrm{d}\mathbf{U}^{i+1,t+\alpha\Delta t} \\ \mathrm{d}\mathbf{P}_{\mathrm{w}}^{i+1,t+\alpha\Delta t} \\ \mathrm{d}\mathbf{P}_{\mathrm{a}}^{i+1,t+\alpha\Delta t} \end{Bmatrix} = \mathbf{0} \tag{6.57}$$

in which $\mathbf{J}$ is the Jacobian matrix, defined as

$$\mathbf{J} = \begin{bmatrix} \dfrac{\partial \boldsymbol{\Psi}_{\mathrm{u}}}{\partial \mathbf{U}} & \dfrac{\partial \boldsymbol{\Psi}_{\mathrm{u}}}{\partial \mathbf{P}_{\mathrm{w}}} & \dfrac{\partial \boldsymbol{\Psi}_{\mathrm{u}}}{\partial \mathbf{P}_{\mathrm{a}}} \\ \dfrac{\partial \boldsymbol{\Psi}_{\mathrm{w}}}{\partial \mathbf{U}} & \dfrac{\partial \boldsymbol{\Psi}_{\mathrm{w}}}{\partial \mathbf{P}_{\mathrm{w}}} & \dfrac{\partial \boldsymbol{\Psi}_{\mathrm{w}}}{\partial \mathbf{P}_{\mathrm{a}}} \\ \dfrac{\partial \boldsymbol{\Psi}_{\mathrm{a}}}{\partial \mathbf{U}} & \dfrac{\partial \boldsymbol{\Psi}_{\mathrm{a}}}{\partial \mathbf{P}_{\mathrm{w}}} & \dfrac{\partial \boldsymbol{\Psi}_{\mathrm{a}}}{\partial \mathbf{P}_{\mathrm{a}}} \end{bmatrix} \tag{6.58}$$

The Jacobian matrix at iteration *i* of the time $t+\alpha\Delta t$ can be expressed in the following explicit form

$$\mathbf{J}^{i,t+\alpha\Delta t} = \begin{bmatrix} A\mathbf{K}_{\mathrm{T}}^{i,t+\alpha\Delta t} & A\psi^{i,t+\alpha\Delta t}\mathbf{Q} & A\left(1-\psi^{i,t+\alpha\Delta t}\right)\mathbf{Q} \\ A\psi^{i,t+\alpha\Delta t}\mathbf{Q}^{\mathrm{T}} & -\left(Aa_{11}^{i,t+\alpha\Delta t}\mathbf{S}+\Delta t\mathbf{H}_{\mathrm{w}}\right) & Aa_{12}^{i,t+\alpha\Delta t}\mathbf{S} \\ A\left(1-\psi^{i,t+\alpha\Delta t}\right)\mathbf{Q}^{\mathrm{T}} & Aa_{12}^{i,t+\alpha\Delta t}\mathbf{S} & -\left(Aa_{22}^{i,t+\alpha\Delta t}\mathbf{S}+\Delta t\mathbf{H}_{\mathrm{a}}\right) \end{bmatrix} \tag{6.59}$$

It should be noted that equation (6.54) is multiplied by A so that the Jacobian matrix is symmetric when elasticity or associative plasticity assumptions are made. Finally, from equation (6.57), the incremental vector of the nodal displacements and pore fluid pressures is obtained at iteration $i+1$ as

$$\begin{Bmatrix} \mathrm{d}\mathbf{U}^{i+1,t+\alpha\Delta t} \\ \mathrm{d}\mathbf{P}_{\mathrm{w}}^{i+1,t+\alpha\Delta t} \\ \mathrm{d}\mathbf{P}_{\mathrm{a}}^{i+1,t+\alpha\Delta t} \end{Bmatrix} = \left(\mathbf{J}^{i,t+\alpha\Delta t}\right)^{-1} \begin{Bmatrix} \boldsymbol{\Psi}_{\mathrm{u}}^{i,t+\alpha\Delta t} \\ \boldsymbol{\Psi}_{\mathrm{w}}^{i,t+\alpha\Delta t} \\ \boldsymbol{\Psi}_{\mathrm{a}}^{i,t+\alpha\Delta t} \end{Bmatrix} \tag{6.60}$$

A proper stress integration method has to be used in each iteration to obtain the unknown stresses. The stresses obtained are then used to form the residual vector for the next iteration or as the final stresses for the current time step if the convergence is reached in the current iteration. The convergence criterion adopted in this chapter is similar to equation (5.17) presented in Chapter 5.

6.4. Bounding surface plasticity model

The UNSW bounding surface plasticity model (BSM) is adopted in this study to simulate the behaviour of the soil. The model was originally developed by Russell and Khalili (2004), within the framework of critical-state soil mechanics, to simulate the stress-strain behaviour of sands. It was later extended to model cyclic response of saturated and unsaturated sands by Khalili et al. (2005) and Khalili et al. (2008). Kan et al. (2013) introduced a new mapping rule to the model which uses only the last stress reversal state to locate the image point on the bounding surface, and is less complex compared to the mapping rule originally proposed. In the following, the essential elements of the UNSW BSM are described. These elements, in conjunction with the elastoplastic stress-strain relationship (see equation (5.29)) can be used to predict the elastoplastic response of the solid skeleton in unsaturated soils.

6.4.1. Bounding and loading surfaces

In the model adopted, a bounding surface is defined which encompasses all the admissible stress states in the stress space. In each stress plane hosting the hydrostatic axis, the bounding surface for each soil conforms to the boundaries of undrained response of the soil in its loosest state (Khalili et al., 2005). In UNSW model, the shape of the bounding surface is expressed in terms of p', q and θ (which were defined in section 5.3.4 in Chapter 5), as follows

$$F(\bar{p}',\bar{q},\bar{\theta},\bar{p}_c') = \left(\frac{\bar{q}}{M_{cs}(\bar{\theta}).\bar{p}'}\right)^N - \frac{\ln(\bar{p}_c'/\bar{p}')}{\ln R} = 0 \tag{6.61}$$

where the over-bar denotes stress condition on the bounding surface. R and N are material parameters, respectively indicating the ratio of $\bar{p}_c'$ to $\bar{p}'$ where F intercepts the critical state line (CSL), and the curvature of the bounding surface. $\bar{p}_c'$ controls the size of the bounding surface, and M_{cs} is the slope of the CSL in the $q-p'$ plane defined as a function of the Lode angle θ as follows (Sheng et al., 2000),

$$M_{cs}(\theta) = M_{max}\left(\frac{2\alpha^4}{1+\alpha^4-(1-\alpha^4)\sin 3\theta}\right)^{\frac{1}{4}} \tag{6.62}$$

where α (not to be confused with the time step growth factor defined in the three point time discretisation scheme explained in section 3.5.2) is given by

$$\alpha = \frac{M_{min}}{M_{max}} = \frac{3-\sin\phi_{cs}'}{3+\sin\phi_{cs}'} \tag{6.63}$$

with ϕ_{cs}' being the constant volume effective friction angle. M_{max} is the slope of the CSL line for triaxial compression and M_{min} is the slope of the CSL for triaxial extension.

A loading surface is also defined on which the current stress point always lies. This surface is homologous to the bounding surface about the centre of homology. The centre of homology is the origin of the $q-p'$ plane during the first time loading; however, it moves to the last point of stress reversal for unloading and reloading. The cross sections of the bounding and loading surfaces in $q-p'$ plane are shown in Figure 6-3.

The direction of loading is determined using the unit normal to the loading surface at the current stress state $(\mathbf{n})$, which can be obtained through the same expression as in equation (5.30) in Chapter 5, assuming F as the loading surface. Alternatively, $\mathbf{n}$ can be obtained by calculating the normal vector on an image point located on the bounding surface. The image point can be located through a simple radial mapping rule where the bounding surface intersects a straight line connecting the new centre of homology to the current stress state, as shown in Figure 6-3.

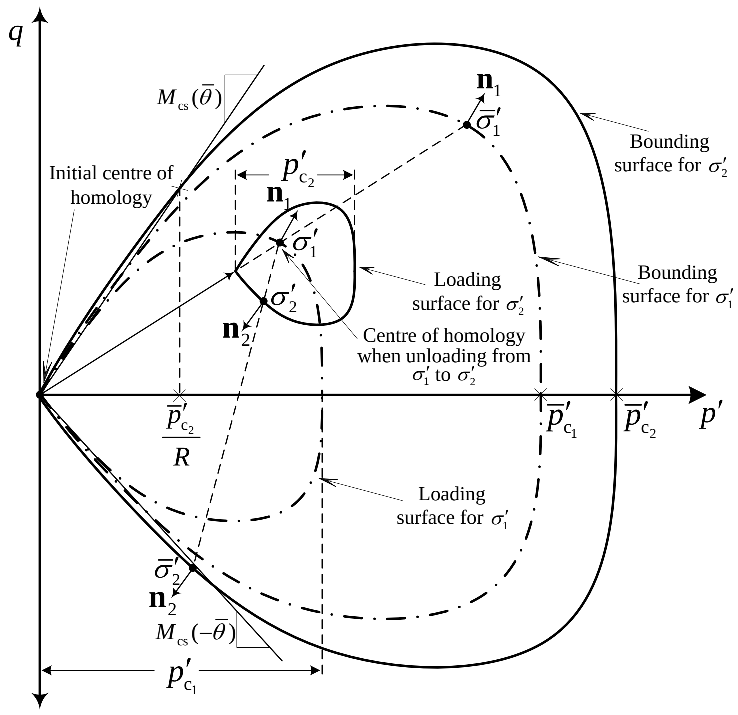

Figure 6-3- Schematic representation of the bounding surface, and the loading surface for the first time loading (from the origin to σ'_1) and unloading (from σ'_1 to σ'_2), and the mapping rule in each case (dashed lines).

6.4.2. Plastic potential

A plastic potential is defined to determine the direction and magnitude of plastic strains. The plastic potential is expressed using a plastic flow rule relating the plastic dilatancy, $d = \dot{\varepsilon}_v^p / \dot{\varepsilon}_q^p$, to the stress ratio q / p', where $\dot{\varepsilon}_v^p$ and $\dot{\varepsilon}_q^p$ are the volumetric and deviatoric plastic strain rates, respectively. The expression for the plastic potential is as follows (Kan et al., 2013)

$$G\left(p',q,\theta,p_0\right)=\begin{cases}\tilde{t}\,q+\dfrac{AM_{\mathrm{cs}}\left(\theta\right)p'}{A-1}\left(\left(p'/p_0\right)^{A-1}-1\right) & for\ A\neq 1\\ \tilde{t}\,q+M_{\mathrm{cs}}\left(\theta\right)p'\ln\left(p'/p_0\right) & for\ A=1\end{cases}\tag{6.64}$$

where p_0 controls the size of the plastic potential, and A is a material constant dependent on the mechanism and amount of energy dissipation. The direction of the plastic flow is then determined using the unit normal to the plastic potential surface at the current stress state $(\mathbf{m})$, as expressed in equation (5.31) in Chapter 5.

Two vectors of plastic flow are identified at any stress state, one corresponding to compressive loading ($\mathbf{m}^{+}$) and the other to extensive ($\mathbf{m}^{-}$) as shown in Figure 6-4. The sign of $\tilde{t}$ in equation (6.64) determines the direction of plastic flow in the deviatoric plane. More details in this regard can be found in Khalili et al. (2008).

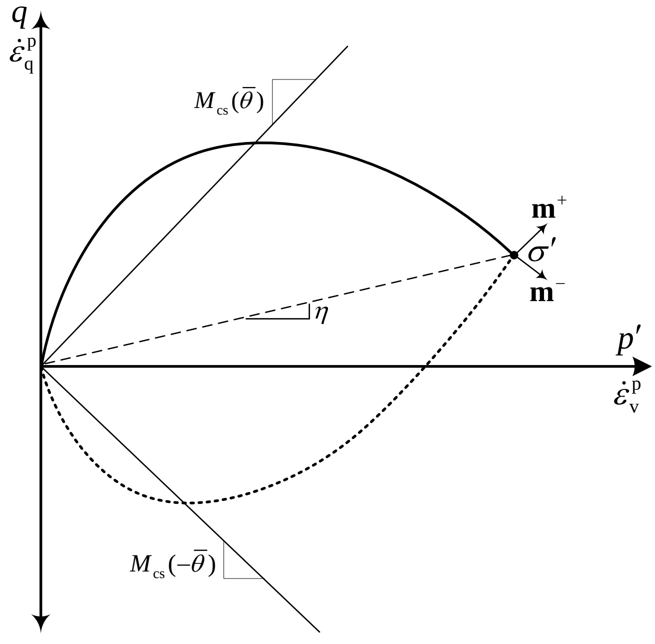

Figure 6-4- Schematic representation of the plastic potential surface in compression and extension.

6.4.3. Hardening modulus

A hardening modulus comprising two components is defined for the current model as

$$h = h_{\mathrm{b}} + h_{\mathrm{f}} \tag{6.65}$$

where h_{b} is the hardening modulus at $\bar{\boldsymbol{\sigma}}'$ on the bounding surface, and h_{f} is the hardening modulus at the current stress state $\boldsymbol{\sigma}'$ defined as a function of the distance between $\bar{\boldsymbol{\sigma}}'$ and $\boldsymbol{\sigma}'$. Imposing the consistency condition at the bounding surface and assuming isotropic hardening of the bounding surface with plastic volumetric compression, h_{b} for unsaturated soils is obtained as

$$h_{\mathrm{b}} = -\frac{\partial F}{\partial \bar{p}'_{\mathrm{c}}}\left(\frac{\partial \bar{p}'}{\partial \varepsilon_{\mathrm{v}}^{\mathrm{p}}} + \frac{\partial \bar{p}'}{\partial s}\frac{\dot{s}}{\dot{\varepsilon}_{\mathrm{v}}^{\mathrm{p}}}\right)\frac{m_{\mathrm{p}}}{\left\|\partial F/\partial \bar{\boldsymbol{\sigma}}'\right\|} \tag{6.66}$$

with $m_{\mathrm{p}} = \dfrac{\partial G/\partial \bar{p}'}{\left\|\partial G/\partial \boldsymbol{\sigma}'\right\|}$.

The modulus h_{f} is defined based on the distance between the current stress point and the image point such that it is zero on the bounding surface and infinity at the point of stress reversal. In the UNSW model, h_{f} is defined as

$$h_{\mathrm{f}} = \tilde{t}\left(\frac{\partial \bar{p}'_{\mathrm{c}}}{\partial \varepsilon_{\mathrm{v}}^{\mathrm{p}}} + \frac{\partial \bar{p}'_{\mathrm{c}}}{\partial s}\frac{\dot{s}}{\dot{\varepsilon}_{\mathrm{v}}^{\mathrm{p}}}\right)\frac{p'}{\bar{p}'_{\mathrm{c}}}\left(\frac{\bar{p}'}{\hat{p}'_{\mathrm{c}}} - 1\right)\left(\eta_{\mathrm{p}} - \frac{q}{p'}\right)k_{\mathrm{m}} \tag{6.67}$$

where $\bar{p}'_{\mathrm{c}}$ and $\hat{p}'_{\mathrm{c}}$ are the sizes of the bounding and loading surfaces, respectively; $\eta_{\mathrm{p}} = \left(1 - 2(\upsilon - \upsilon_{\mathrm{cs}})\right)M_{\mathrm{cs}}$ is the slope of the peak strength line in the $q - p'$ plane; k_{m} is a material parameter; $\upsilon = 1 + e$ is the specific volume and υ_{cs} is the critical state specific volume.

6.4.4. Suction hardening

The effect of suction variations on the critical state of unsaturated soils is referred to as suction hardening. For unsaturated soils, the slope of the CSL in $q - p'$ plane is assumed to be suction independent (Loret and Khalili, 2002). However, the CSL in $\upsilon - p'$ space is prone to suction hardening and is defined as

$$\upsilon_{\mathrm{cs}} = \Gamma(s) - \lambda(\mathrm{s})\ln(p'_{\mathrm{cs}}) \tag{6.68}$$

in which $\Gamma(s)$ is the intercept of the CSL at the reference mean effective stress of $p' = 1\mathrm{kPa}$, $\lambda(s)$ is the slope of the CSL in the $\upsilon - p'$ plane, and p'_{cs} is the mean effective stress at the critical state ($\square(s)$ indicates that $\square$ is a function of suction).

Parallel to the CSL, a limiting isotropic compression line (LICL) also exists for unsaturated soils whose equation is given by

$$\upsilon_{\mathrm{LICL}} = N(s) - \lambda(s)\ln(p'_{\mathrm{c}}) \tag{6.69}$$

where υ_{LICL} is the specific volume on the LICL and $N(s)$ is the specific volume at the reference mean effective stress of $p' = 1\mathrm{kPa}$.

Any suction increase leads to an increase in soil stiffness and consequently, both the intercept and the slope of the isotropic compression line increase. In the bounding surface model employed in this study, a coupled suction hardening approach is adopted according to Loret and Khalili (2002) in which the hardening rule is expressed as

$$\bar{p}'_{\mathrm{c}}(\varepsilon_{\mathrm{v}}^{\mathrm{p}}, s) = \bar{p}'_{\mathrm{c0}}\Psi(s)\exp\left(\frac{\upsilon_0 \Delta\varepsilon_{\mathrm{v}}^{\mathrm{p}}}{\lambda(s) - \kappa}\right) \tag{6.70}$$

In the above equation, υ_0 is the initial specific volume, $\bar{p}'_{\mathrm{c0}}$ is the initial value of the hardening parameter, κ is the slope of the unloading-reloading line in the $\upsilon - p'$ plane, $\Delta\varepsilon_{\mathrm{v}}^{\mathrm{p}}$ is the volumetric plastic strain increment, and $\Psi(s)$ is a function expressed as

$$\Psi(s)=\exp\left(\frac{N(s)-N(s_0)}{\lambda(s)-\kappa}-\frac{\lambda(s)-\lambda(s_0)}{\lambda(s)-\kappa}\ln(\bar{p}'_{c0})\right) \tag{6.71}$$

where $N(s_0)$ and $\lambda(s_0)$ are the intercept and slope of the LICL at the initial suction s_0. $\Gamma(s)$ and $\lambda(s)$ for the CSL are obtained from the required consistency of the CSL with the LICL through a parallel transition of the LICL along the effective stress axis (Loret and Khalili (2002)).

6.5. Numerical examples

Several examples are investigated in this section to examine the proposed model. One-dimensional consolidation of elastic unsaturated porous media is studied first. Then, two examples are studied to examine the effect of hydraulic hysteresis on hydro-mechanical response of porous media and the results are compared to those of an FEM solution. The next example involves a series of plane strain compression (PSC) tests incorporating the BSM detailed in section 6.4 and the numerical results are compared to the results from another study. $g = 9.8\,\text{m/s}^2$ is assumed in all examples.

6.5.1. One-dimensional consolidation problem

One-dimensional consolidation of elastic unsaturated porous media is studied in this section. First, a simplified consolidation problem with constant parameters, whose analytical solution is available in the literature, is studied for verification of the proposed formulation. The effect of the void ratio dependency of the WRC on the results is discussed next. Finally, a one-dimensional consolidation problem is investigated to highlight the effect of hydraulic hysteresis on the behaviour of unsaturated geomaterials during consolidation. The results of a series of FE simulations are used for code-to-code verification of the proposed ESPIM model in the latter example.

6.5.1.1. 1D consolidation assuming constant parameters

The first example considers one-dimensional consolidation of an elastic unsaturated weightless soil column under a uniform distributed load. A $10\,\mathrm{m}$ thick soil column is considered with a porosity of $n = 0.45$ and a degree of saturation of $S_{\mathrm{r}} = 0.8$. The residual degree of saturation is assumed zero, the elastic properties of the material are considered $E = 10,000\,\mathrm{kPa}$ and $\nu = 0.25$, solid grains and water are assumed incompressible $(c_{\mathrm{s}} = c_{\mathrm{w}} = 0)$, and the dynamic viscosity of water is taken $\mu_{\mathrm{w}} = 10^{-6}\,\mathrm{kPa.s}$. The problem domain is illustrated in Figure 6-5, together with the background mesh used in the numerical analyses which consists of 185 nodes and 320 triangular elements.

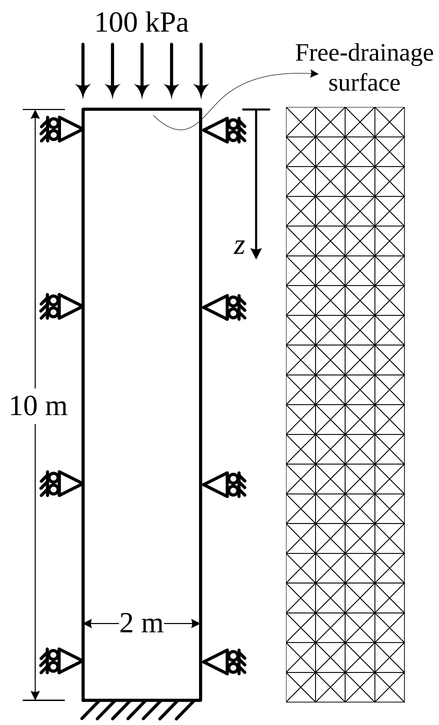

Figure 6-5- Mesh representation along with boundary conditions for 1D consolidation problem.

Qin et al. (2008) and Ho et al. (2014) presented analytical solutions to this problem making a number of simplifying assumptions. Similar simplifications are assumed in this section and the numerical results are compared to those presented by Ho et al. (2014). The coefficient of permeability of water in saturated state and the constitutive coefficient a_{12} are set to $k_{\mathrm{w_{sat}}} = 10^{-10}$ m/s and $a_{12} = 0.001$, and are kept constant throughout the numerical simulations. No hysteresis effect is considered, and an initial value of $\psi = 0.33$ is assumed.

To determine the WRC for the soil of interest, $\lambda_{\mathrm{p}} = 0.396$ is obtained based on the definition of ψ ($\psi = \mathrm{d}(\chi s)/\mathrm{d}s$) and using equations (6.6) and (6.29). Equation (6.24) then yields $s_{\mathrm{e}} = 81\,\mathrm{kPa}$. Having assumed $S_{\mathrm{r}} = 0.8$, it is obtained that the soil is initially in equilibrium condition under an initial suction of $s = 142\,\mathrm{kPa}$. The initial pore air pressure is assumed zero attributing the initial suction to the initial negative pore water pressure.

The problem is analysed using five different permeability ratios, $k_{\mathrm{a}}/k_{\mathrm{w}}$, varying from 0.01 to 100. k_{a} and k_{w} are the coefficients of permeability of air and water phases, respectively, defined as $k_{\mathrm{a}} = k_{\mathrm{ra}} \times k_{\mathrm{a_{dry}}}$ and $k_{\mathrm{w}} = k_{\mathrm{rw}} \times k_{\mathrm{w_{sat}}}$, where $k_{\mathrm{a_{dry}}}$ is the coefficient of permeability of the air phase at dry condition. In this example, it is assumed that $k_{\mathrm{a_{dry}}} = k_{\mathrm{w_{sat}}}$ and k_{rw} is always taken as 1, allowing the value of k_{ra} to control the changes in $k_{\mathrm{a}}/k_{\mathrm{w}}$.

The soil column is loaded initially with a $100\,\mathrm{kPa}$ surcharge. In the numerical model, the application of this surcharge load results in uniformly distributed initial excess pore water and pore air pressures generation of $(\Delta p_{\mathrm{w}})_0 = 11.9\,\mathrm{kPa}$ and $(\Delta p_{\mathrm{a}})_0 = 9.4\,\mathrm{kPa}$ in the soil column, respectively. To make a meaningful comparison with the results of Ho et al. (2014), these initial excess pore pressures are then used as inputs to generate the analytical solutions presented by Ho et al. (2014). It is also worth noting that according to the equations for one consolidation of unsaturated porous media by Fredlund and Hasan (1979), the application of a $100\,\mathrm{kPa}$ surcharge generates uniformly distributed initial excess pore water and pore air pressures of $(\Delta p_{\mathrm{w}})_0 = 11.0\,\mathrm{kPa}$ and $(\Delta p_{\mathrm{a}})_0 = 8.4\,\mathrm{kPa}$ which are in good agreement with the proposed numerical model. The minor differences observed are due to the slight deviation of ψ and S_{r} from the initial value of 0.33 and 0.8, respectively, right after the surcharge application, which occurs in the current model according to the adopted WRC model. Adopting constant ψ and S_{r} in the numerical formulation would lead to the generation of initial pore pressures which are exactly identical to those obtained through the approach by Fredlund and Hasan (1979). The WRC, however, is kept in effect in this example to maintain the structure of the proposed model.

Figure 6-6 illustrates the numerical and analytical solutions for the surface settlement through time for different values of $k_{\mathrm{a}}/k_{\mathrm{w}}$. It is worth noting that the whole surface surcharge is applied in the first time step where $\Delta t_0 = 1\,\mathrm{s}$, which results in an instantaneous initial settlement of $\Delta u_0 = 0.0749\,\mathrm{m}$ in the soil column, due to the low compressibility of the air phase. To be able to compare the numerical results with the analytical solution of Ho et al. (2014), this initial settlement is subtracted from all the numerical results for settlements, and the time origin is set to be at $t = 1\,\mathrm{s}$, i.e. the end of the loading stage. A time step growth factor of $\alpha = 1.1$ is adopted in the analyses. A similar example was also studied by Tang et al. (2017) using an effective stress based

FE model for unsaturated porous media. However, they related the difference in the initial volume changes obtained from the analytical and numerical results to different air compressibility coefficients adopted in the analytical and numerical models. They then back calculated the soil elastic properties to end up with the same final surface settlement values in their numerical solution as those observed in the analytical solutions. This approach is, however, erroneous as similar assumptions are made for air compressibility in the two approaches. As a result, the elastic properties back calculated by Tang et al are vastly different from those reported in the reference solution.

It should be again emphasized that although ψ is not enforced to be constant in the analyses, it shows negligible deviations from its initial value due to assuming a volume change independent WRC in the analyses. This is essentially in accord with the assumption of constant model parameters made for comparing the numerical results to the analytical results of Ho et al. (2014).

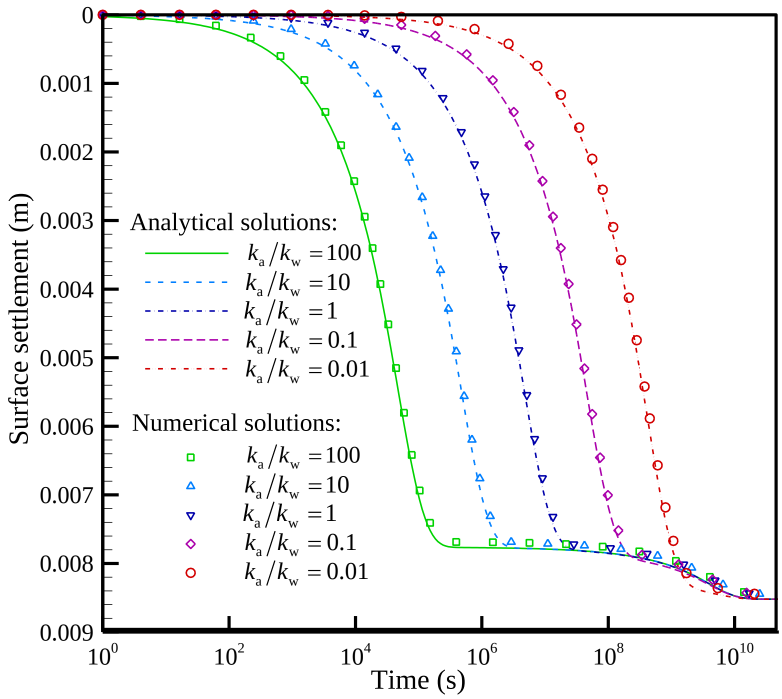

Figure 6-6- Surface settlement versus time for different permeability ratios.

Figure 6-7 and Figure 6-8 show the dissipation rates of pore air and pore water pressures at a point in the middle of the column ($z = 5\,\mathrm{m}$) for both numerical and analytical solutions. Again, different values of k_a/k_w are considered according to Ho et al. (2014). It can be observed that the numerical pore pressure results are in perfect agreement with those from the analytical solutions.

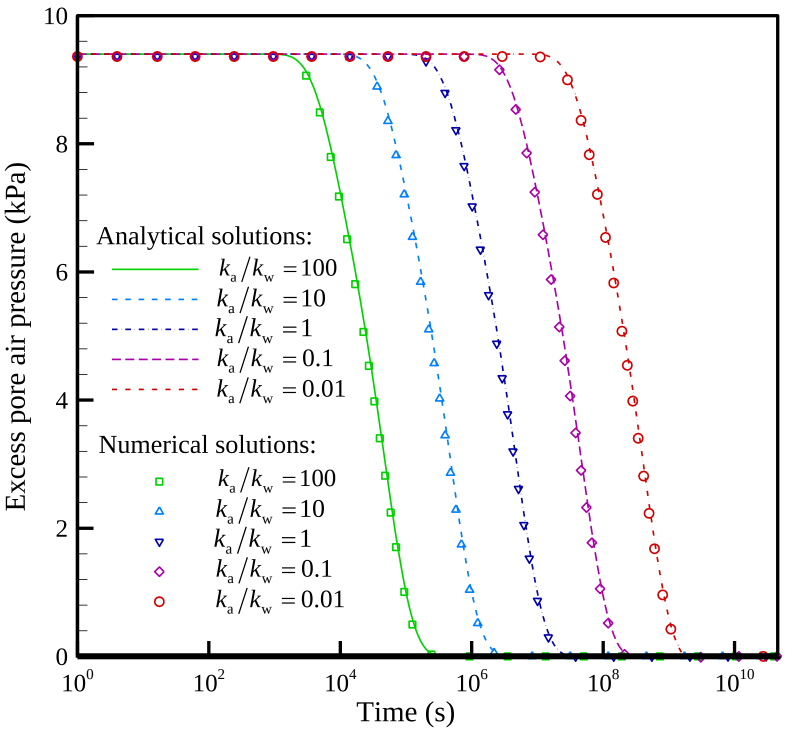

Figure 6-7- Change of excess pore air pressure at $z = 5\,\mathrm{m}$ with time for different permeability ratios.

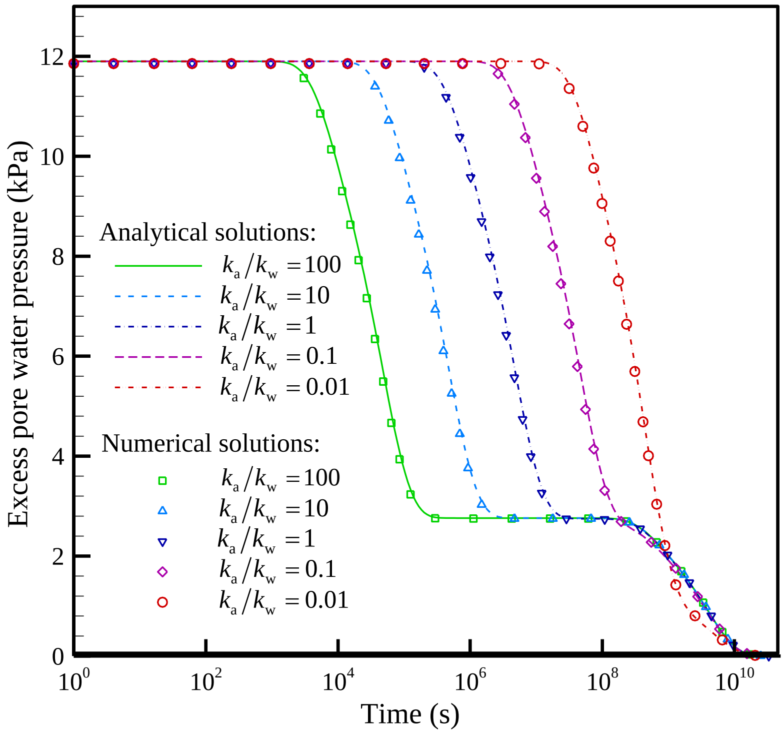

Figure 6-8- Change of excess pore water pressure at $z = 5\,\text{m}$ with time for different permeability ratios.

6.5.1.2. Effect of the void ratio dependent WRC model in 1D consolidation

The effect of the void ratio dependent WRC is studied in this example. The WRC is considered as a function of the void ratio according to the model detailed in section 6.2.4. a_{12} is also not constant throughout the analyses and is obtained from equation (6.24) at each node. The geometry, boundary conditions and material parameters are all the same as those in the previous example with the exception of adopting a smaller Young's Modulus of $E = 2{,}000\,\text{kPa}$ in this example to highlight the effect of volume change on the hydraulic response of the material. $k_a/k_w = 1$ is used for all the analyses in this example.

The results of the model are compared with those obtained from the model with constant parameters, as depicted in Figure 6-9. It can be observed from Figure 6-9(a) that the initial increase in the degree of saturation is more pronounced when the WRC is updated as the void ratio changes. This is basically due to the rise in the air entry value s_e and the drop in the pore size distribution index λ_p due to the instantaneous settlement after the application of the load. The updated WRC necessitates hydraulic equilibrium at a higher degree of saturation considering the fact that the initial suction change in the two models are almost identical (see Figure 6-9(c)). This higher initial degree of saturation also results in a smaller instantaneous settlement as seen in Figure 6-9(b). Furthermore, updating the WRC with void ratio causes a greater final settlement as observed in Figure 6-9(b). This is because when the WRC is updated with the void ratio change, higher degrees of saturation and higher χ values are obtained, resulting in higher effective stresses throughout the analysis compared to the cases where the WRC is assumed stationary. This implies that ignoring the volume change dependency of the WRC in one-dimensional consolidation of unsaturated porous media results in under predication of the settlements. The variations of excess pore water and air pressures with time are also depicted in Figure 6-9(d) and (e), respectively. As can be seen from these figures, a volume change independent WRC model also leads to underprediction of the initial pore water and air pressures generated due to loading in one-dimensional consolidation problems.

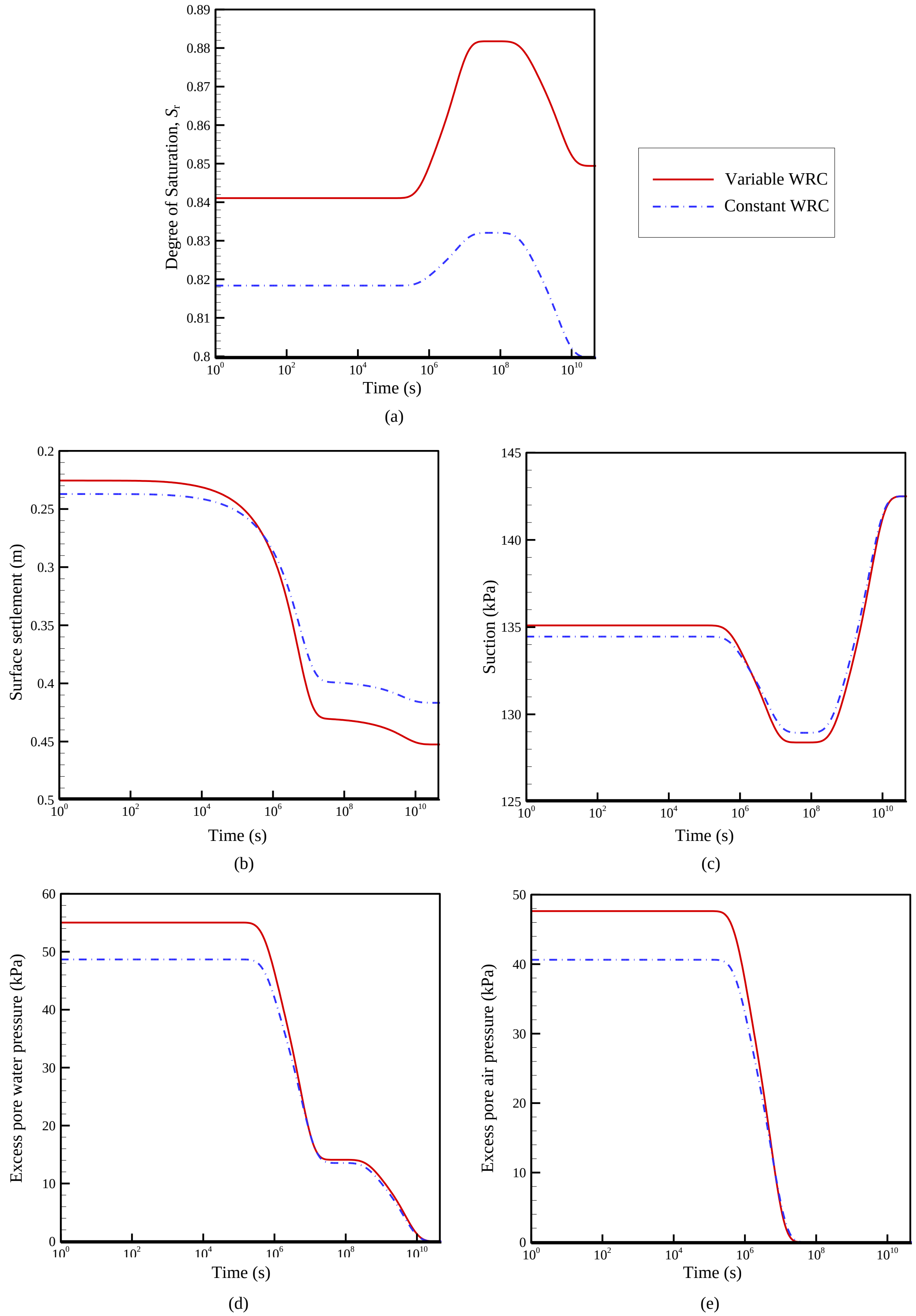

Figure 6-9- Effect of updating the WRC with changes in void ratio on temporal variations of: (a) Surface settlement, (b) degree of saturation at $z = 5\,\mathrm{m}$, (c) excess pore water pressure at $z = 5\,\mathrm{m}$, (d) excess air water pressure at $z = 5\,\mathrm{m}$, in one dimensional consolidation problem.

The importance of updating the WRC for volume change during the analyses can also be highlighted by studying the surface settlement versus time for four consolidation problems similar to the one shown in Figure 6-5, but with different initial degrees of saturation. All other assumptions and parameters are the same among the four examples, and are similar to those used in the previous section. The results of the analyses of these four consolidation problems are shown in Figure 6-10. It can be observed from this figure that the four examples manifest different final settlements. Such a behaviour can only be captured when the WRC is updated as a function of the void ratio of the soil. As the soil's initial degree of saturation decreases, a larger initial settlement is obtained due to loading, resulting in a larger shift of the WRC towards higher suctions, and therefore higher values of χ, which in turn results in higher effective stresses and therefore higher final settlements.

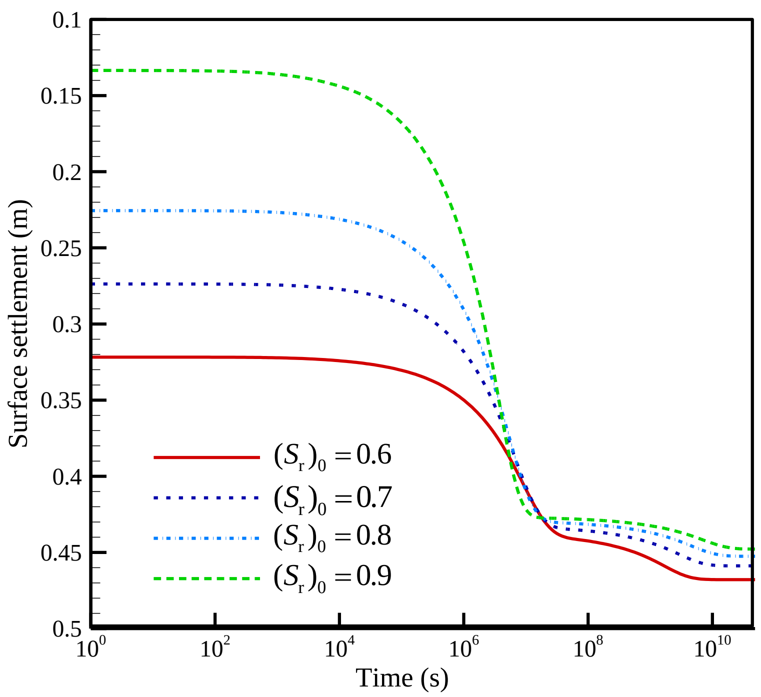

Figure 6-10- Surface settlement of the soil column versus time for different initial degrees of saturation.

6.5.1.3. Effect of hydraulic hysteresis in 1D consolidation

The effect of considering the hydraulic hysteresis on the results of one dimensional consolidation of elastic unsaturated porous media is studied in this section. A one-dimensional consolidation problem whose FEM solution is available (Shahbodagh-Khan et al., 2015) is adopted for this purpose. The problem involves a $100\,\mathrm{m}$ long unsaturated soil column as illustrated in Figure 6-11. Drainage is only allowed on the upper boundary of the soil, and other boundaries are considered impervious. The displacement boundary conditions are also shown in Figure 6-11, along with the triangular background mesh with 302 nodes and 400 elements used for the simulations.

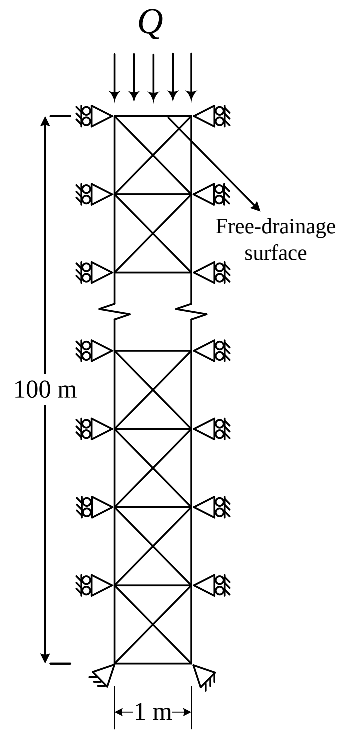

Figure 6-11- Schematic representation of the soil column and its associated mesh and boundary conditions.

The material properties adopted are summarised in Table 6-1. It should be noted that according to Shahbodagh-Khan et al. (2015), a fluid phase with hypothetical mechanical properties is considered in this example. Also, in order to be consistent with the reference FEM solution, equation (6.42) is replaced by an empirical equation proposed by Taylor (1948) for updating the intrinsic permeability of the medium with void ratio, as follows

$$k = k_0 \exp\left(\frac{e - e_0}{C_k}\right) \tag{6.72}$$

where C_k is a material parameter taken as 1.0 in this example.

Table 6-1- Material properties considered for the numerical analyses.

Parameter	Symbol	Value	Unit
Young's Modulus	E	3,000	kPa
Poisson's Ratio	ν	0.2	
Initial porosity	n_0	0.33	
Initial permeability of the liquid phase when $S_{\mathrm{r}} = 1$	k_{f_0}	1.425×10^{-2}	m/s
Initial permeability of the air phase when $S_{\mathrm{r}} = S_{\mathrm{res}}$	k_{a_0}	5×10^{-2}	m/s
Density of the liquid phase	ρ_{f}	0.2977	$\mathrm{gr/cm^3}$
Compressibility coefficient of the liquid phase	c_{f}	2.5×10^{-5}	$\mathrm{kPa^{-1}}$
Air entry value	s_{ae}	10	kPa
Air expulsion value	s_{ex}	10 or 5	kPa
Pore size distribution index	$\lambda_{\mathrm{pd}} = \lambda_{\mathrm{pw}}$	0.15	
Slope of the transition line in WRC	ξ	0.04	
Residual degree of saturation	S_{res}	0.2	

A linearly increasing distributed surcharge, as shown in Figure 6-12, is applied on the soil surface which reaches a maximum value of $\sigma_{\max} = 100\,\mathrm{kPa}$ at $t = 100\,\mathrm{s}$ (t_{L} in Figure 6-12).

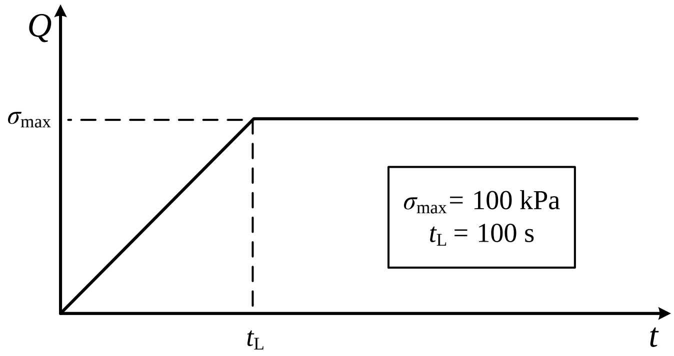

Figure 6-12- Surface loading regime applied on the soil column.

A series of simulations are carried out considering different initial degrees of saturation. In the first set of the analyses, the hydraulic hysteresis is ignored, i.e., $s_{\mathrm{ae}} = s_{\mathrm{ex}} = 10\,\mathrm{kPa}$. The WRC is also assumed void ratio independent throughout the analyses, in accordance with Shahbodagh-Khan et al. (2015). An initial time step of $\Delta t_0 = 10\,\mathrm{s}$ is employed and remained unchanged during the analyses (i.e., $\alpha = 1$). This means that the linear surcharge is applied gradually over the first ten time steps through 10 kPa surcharge increments. Figure 6-13 shows the surface settlement of the soil column versus time for dry, saturated, and three unsaturated cases with different initial states of initial suction to air entry value ratios of 1.5, 2.0, and 4.0. Also shown in Figure 6-13 are the results of the simulations by Shahbodagh-Khan et al. (2015) using a FEM model. The model by Shahbodagh-Khan et al. (2015) includes large deformation effects. For the sake of consistency, in this study the nodal coordinates are updated in each time step which is adequate due to the small strains observed (maximum vertical strain is 3%), and lack of any rotation in the domain. As seen in Figure 6-13, the ESPIM results in terms of vertical settlement are in excellent accordance with the results of the FEM simulations in all cases studied.

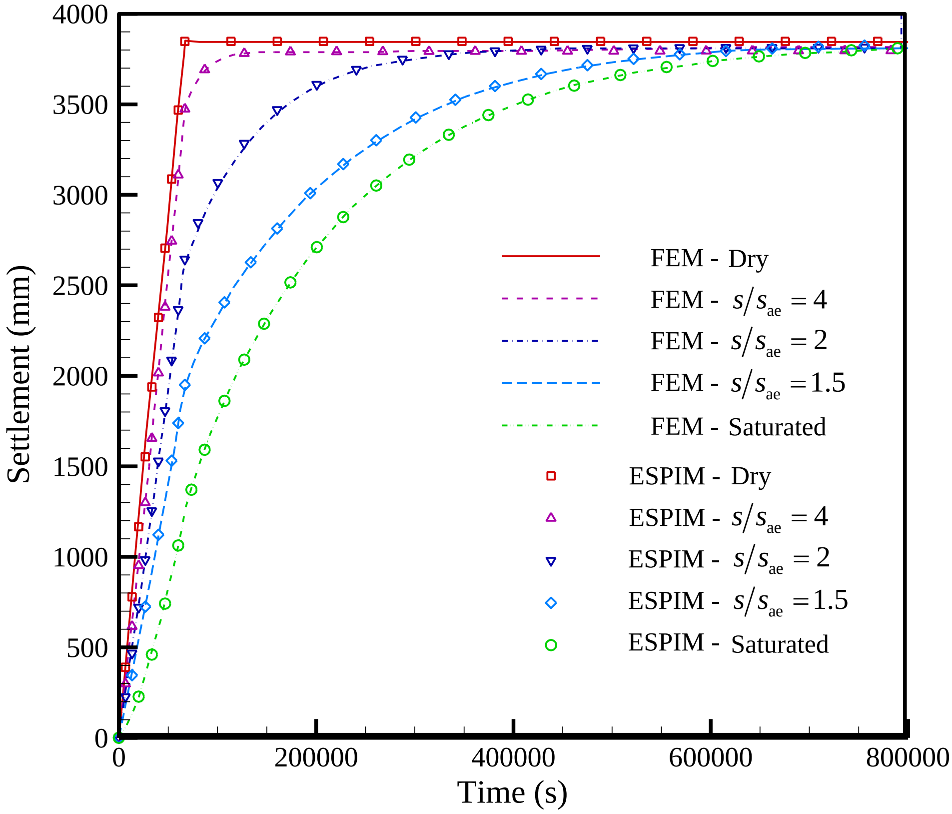

Figure 6-13- Settlement of the soil column with time for different initial suction ratios.

Figure 6-14 to Figure 6-16 show the vertical distribution of suction, pore water pressure, and pore air pressure along the length of the column for the case with the initial condition of $s/s_{ae} = 2$, for both ESPIM and FEM models. Again, the results are in perfect agreement implying that the validity of the computational scheme developed for the analysis of elastic unsaturated porous media.

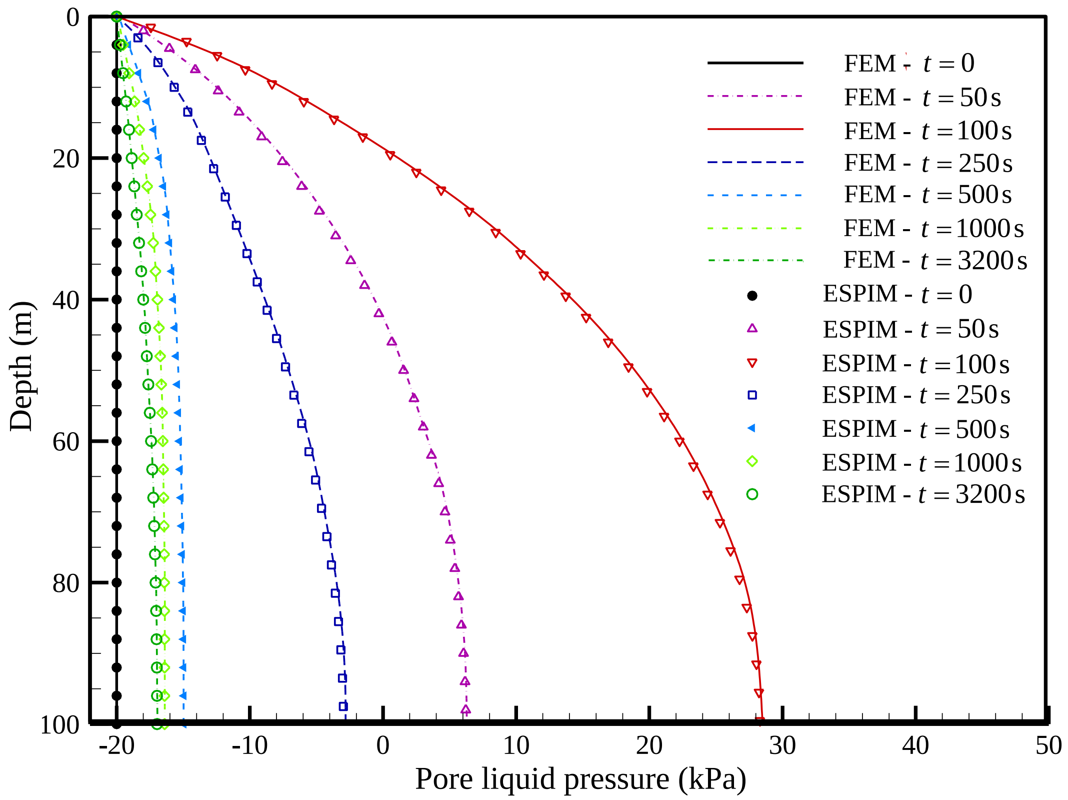

Figure 6-14- Distribution of pore fluid pressure in depth at different times for an initial suction of 20 kPa.

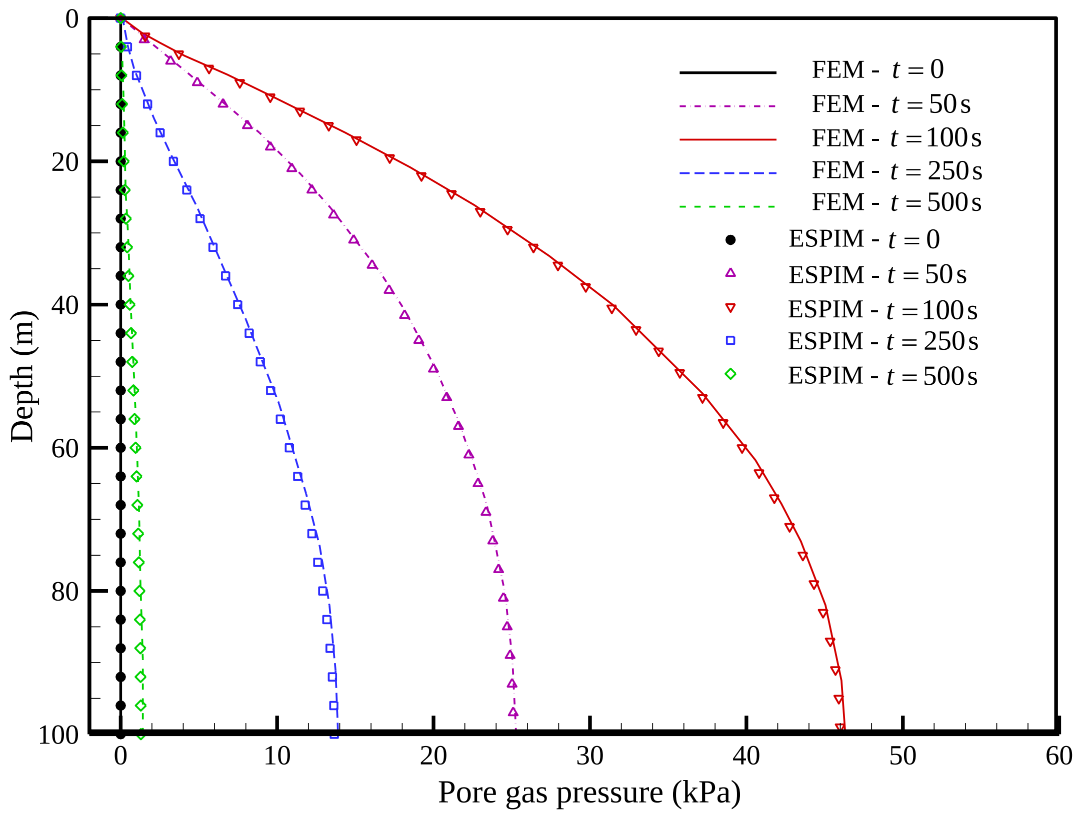

Figure 6-15- Distribution of pore air pressure in depth at different times for an initial suction of 20 kPa.

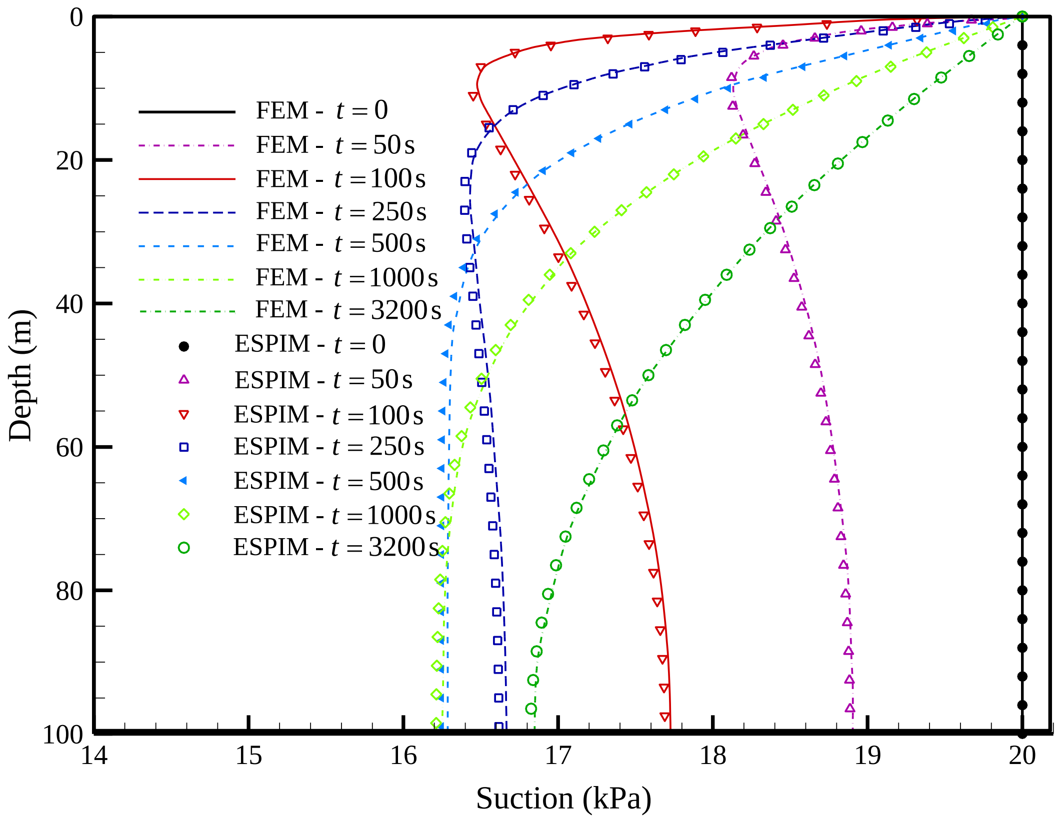

Figure 6-16- Suction distribution in depth at different times for an initial suction of 20 kPa.

To verify the implementation of the hydraulic hysteresis model included in the ESPIM, and also to highlight the effect of hydraulic hysteresis on the results of one dimensional consolidation of unsaturated soils, another simulation is carried out assuming and initial suction of $s_0 = 20\,\text{kPa}$, an air entry value of $s_{ae} = 10\,\text{kPa}$, an air expulsion value of $s_{ex} = 5\,\text{kPa}$, implying the existence of hydraulic hysteresis in this case. To meticulously simulate the hydraulic route of the material at each point and possible transitions from the main paths to the scanning paths and vice versa, a smaller time step of $\Delta t = 0.1\text{s}$ is considered in the analysis when hydraulic hysteresis is in effect. The results in terms of the surface settlement versus time obtained from the ESPIM model are shown in Figure 6-17. Also included in this figure are the results obtained using a FE model by Shahbodagh-Khan (Shahbodagh-Khan, 2 July 2018, personal communication). It is worth mentioning that due to a modification applied to the hydraulic hysteresis implementation in the FEM code by Shahbodagh-Khan, the FEM results for the case with hydraulic hysteresis reported in this work are slightly different from those reported in Shahbodagh-Khan et al. (2015). As can be seen from Figure 6-17, the numerical results of this study are in perfect agreement with the benchmark solution. Figure 6-17 shows that taking account of hydraulic hysteresis markedly reduces the rate of consolidation. This essentially happens due to the change in the hydraulic path from the main path in the non-hysteretic model to the scanning path in the hysteretic model, which leads to larger pore pressure generations and lower suctions during the analysis when hydraulic hysteresis is included in the model (Shahbodagh-Khan et al., 2015).

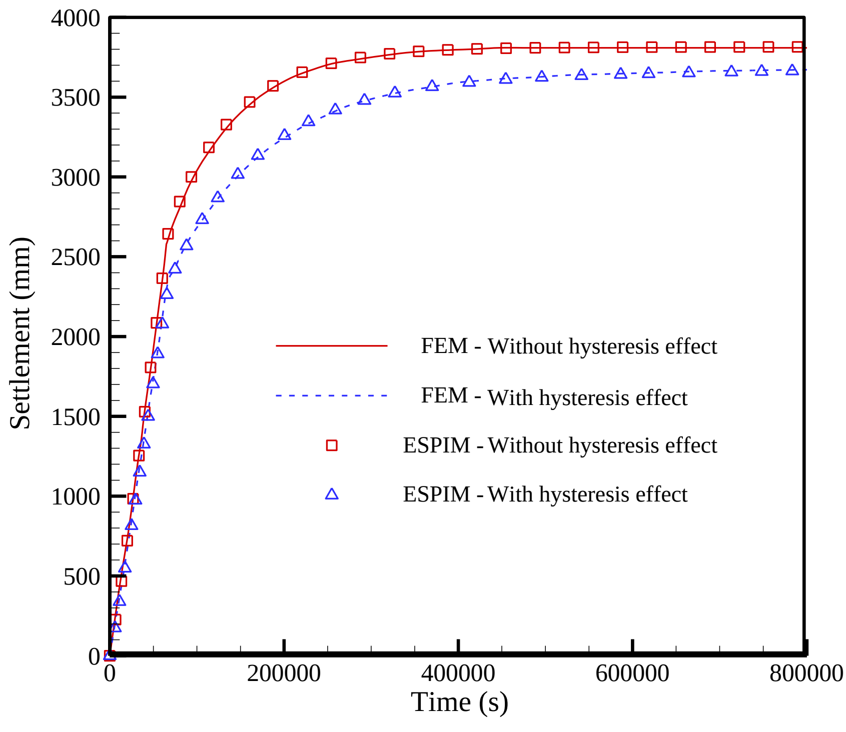

Figure 6-17- Effect of hydraulic hysteresis on the surface settlement of the soil column with time.

6.5.2. Two-dimensional consolidation problem

This example concerns a flexible, smooth, and pervious strip footing placed on an unsaturated weightless porous layer with an initial suction of $s_0 = 20\,\mathrm{kPa}$, which can drain freely on the top surface. The soil layer is located on an impervious rigid bedrock.

The geometry of the problem, the displacement boundary conditions and the adopted triangular background mesh are depicted in Figure 6-18. The same materials as the those assumed in the previous example are considered here, except for the liquid phase which is water in this example with a density of $\rho_{\mathrm{w}} = 1\,\mathrm{gr/cm^3}$ and compressibility coefficient of $c_{\mathrm{w}} = 4.5\times10^{-7}\,\mathrm{kPa}^{-1}$. A step load which linearly increases from zero at time $t = 0$ to $\sigma_{\max} = 400\,\mathrm{kPa}$ at $t = t_{\mathrm{L}} = 20\,\mathrm{s}$ is gradually applied on the strip footing, as shown in Figure 6-19. Similar to the previous example, two analyses are performed: one assuming that there is no hydraulic hysteresis, and one including the hydraulic hysteresis. The time increment adopted for the non-hysteretic simulation is $\Delta t = 1\mathrm{s}$ while for the hysteretic simulations a small time increment of $\Delta t = 0.1\mathrm{s}$ is used due to the highly nonlinear WRC. For the both cases, Δt is kept constant throughout the analyses.

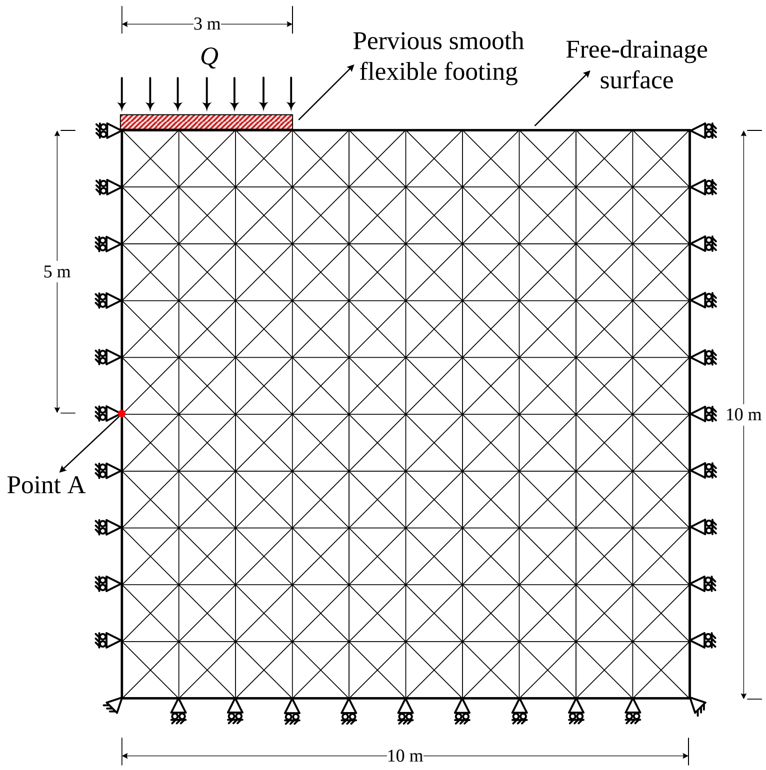

Figure 6-18- Problem geometry, boundary conditions, and background mesh for the 2D consolidation problem.

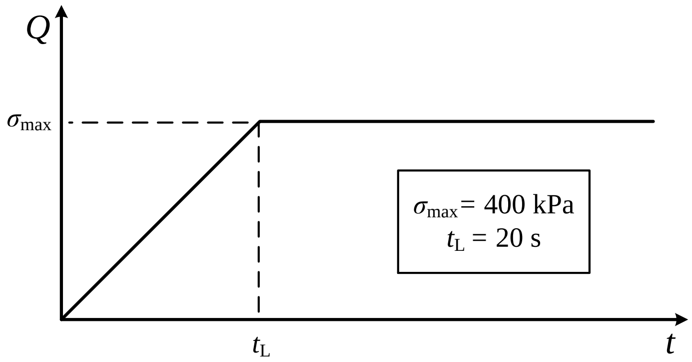

Figure 6-19- Loading regime applied on the footing in the 2D consolidation problem.

Comparisons are made in Figure 6-20 and Figure 6-21 between the results of the hysteretic model and non-hysteretic model, obtained by the ESPIM of this study and FE model by Shahbodagh-khan (Shahbodagh-Khan, 25 July 2018, personal communication). Due to the same reason as the previous example, the results of the hysteretic model for the FEM solution are slightly different from those in Shahbodagh-Khan et al. (2015). Figure 6-20 depicts the vertical displacement of a point of interest (Point A shown in Figure 6-18) versus time. It can be seen that taking account of hydraulic hysteresis does not show a significant effect on the consolidation rate in this example. This is mainly because the instantaneous settlement due to the application of the load accounts for a significant fraction of the total settlement, in comparison to the consolidation settlement. Figure 6-21 shows the variations of suction through time at the same point of interest. It can be seen that more severe suction reduction occurs in the hysteretic model compared to the non-hysteretic model, which agrees with the observations of the 1D consolidation example. Again, Figure 6-20 and Figure 6-21 show that the ESPIM and FEM results are in perfect agreement.

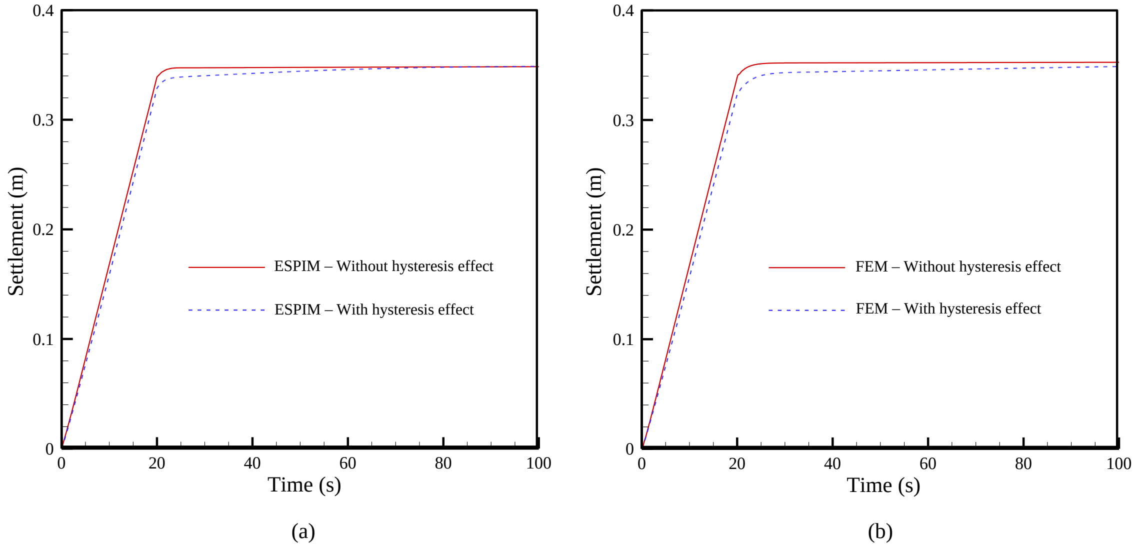

Figure 6-20- Vertical displacement of point A for the hysteretic and non-hysteretic models, (a) ESPIM results, (b) FEM results.

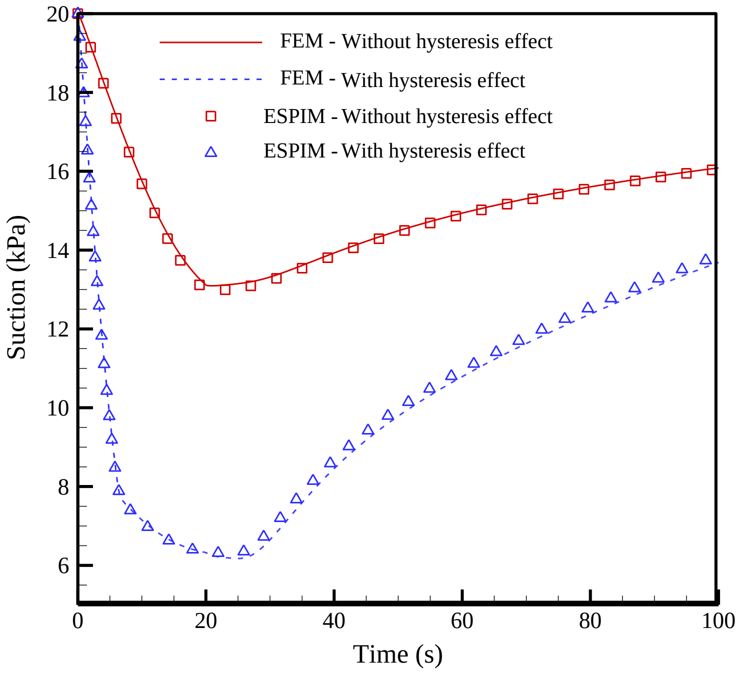

Figure 6-21- Suction variations at point A for the hysteretic and non-hysteretic models, obtained using ESPIM and FEM.

6.5.3. Plane strain compression problem

The bounding surface plasticity model implemented in the ESPIM developed in this study is examined in this example which concerns a series of PSC tests conducted on unsaturated Bourke silt from the Bourke region of New South Wales, Australia as reported in Perić et al. (2014). The elastoplastic behaviour of the material is captured using the BSM presented in this chapter. The model parameters are selected the same as those presented by Perić et al. (2014), listed in Table 6-2. Suction dependency of the LICL parameters (λ and N) are also summarised in Table 6-3. The background mesh adopted in the numerical analyses along with the displacement boundary conditions are illustrated in Figure 6-22. The tests involve application of a vertical compressive strain to the top of the medium at the constant rate of $10^{-6}\,\mathrm{s}^{-1}$. In the numerical simulations, a stationary WRC with no hydraulic hysteresis is considered in accordance with the assumptions of Perić et al. (2014). A constant time step of $\Delta t = 1\mathrm{s}$ is assumed throughout the analyses.

Two sets of drained simulations, with initial net stresses of 30 and 100 kPa are carried out. No pore pressure change is allowed in the drained analyses. For each simulation set, initial suctions of 50, 150, and 250 kPa are assumed. Another simulation is performed assuming a constant water content condition in which only the pore water pressure is allowed to change while the pore air pressure is assumed constant all over the problem domain. An initial net stresses of 100 kPa and an initial suction of 50 kPa are considered in the latter analysis.

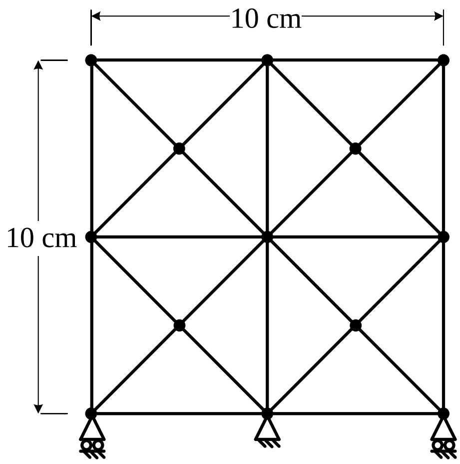

Figure 6-22- Background mesh and displacement boundary conditions for the PSC problem.

Table 6-2- Suction-independent parameters of the Bourke silt for the BSM.

Parameter	Value
M_{cs}	1.17
ν	0.25
κ	0.006
A	2.0
N	3.0
R	2.0
k_m	200
λ_p	0.41
s_{ae} (kPa)	18

Table 6-3- Parameters defining the isotropic compression line as a function of suction for the Bourke silt.

	suction, s (kPa)		
	$s \leq 18$	100	300
$\lambda(s)$	0.090	0.090	0.090
$N(s)$	2.049	2.058	2.068

The results of the drained analyses are summarised in Figure 6-23 to Figure 6-25. The variations of the deviatoric stress versus the axial strain are illustrated for the initial net stress of 30 kPa in Figure 6-23 and for the initial net stress of 100 kPa in Figure 6-24. Figure 6-25 shows how the volumetric strain is generated with loading. Presented in Figure 6-26 are the variations of the deviatoric stress, volumetric strain and suction versus the axial strain for the constant water content analysis. In all cases, the ESPIM results are compared to the numerical results presented by Perić et al. (2014) which were already verified using a series of conventional triaxial compression tests performed on Bourke silt by Uchaipichat and Khalili (2009). In all cases, perfect agreements are observed between the results of this study and the reference solutions of Perić et al. (2014).

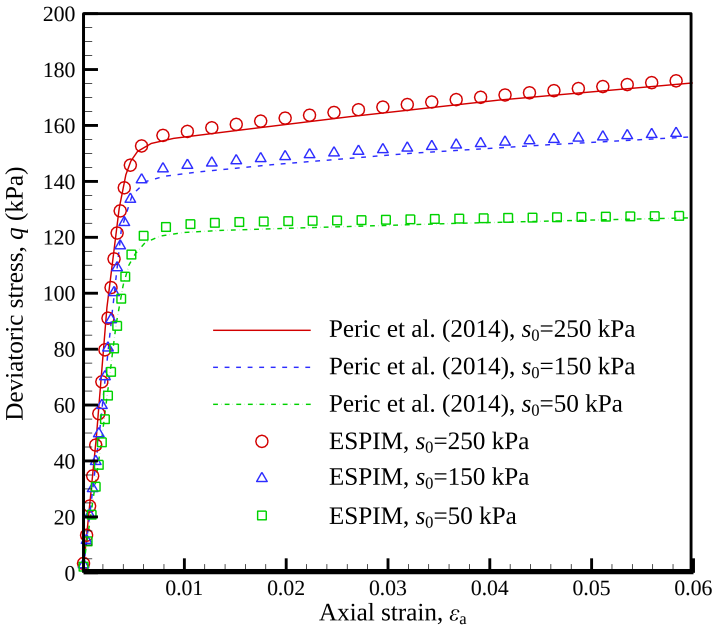

Figure 6-23- Variations of the deviatoric stress versus axial strain in the drained PSC analyses for different initial suctions with the initial net stress of 30 kPa.

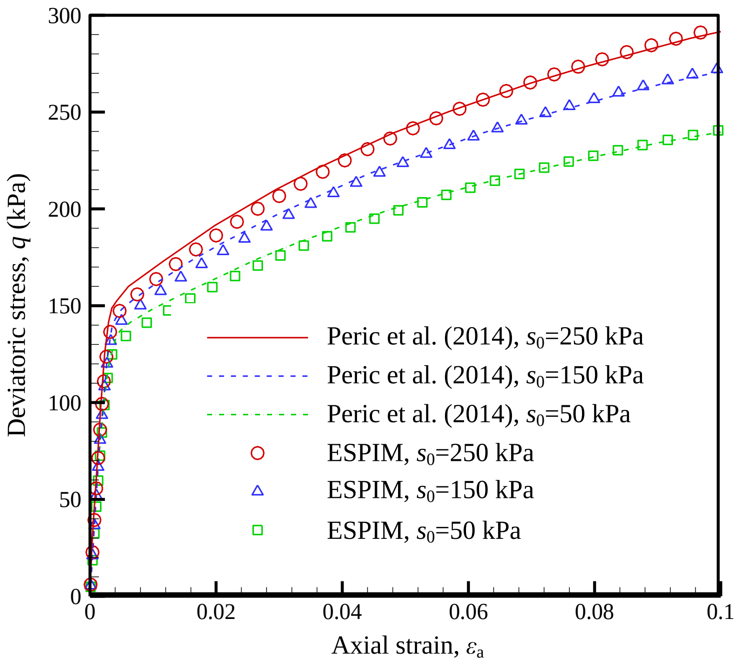

Figure 6-24- Variations of the deviatoric stress versus axial strain in the drained PSC analyses for different initial suctions with the initial net stress of 100 kPa.

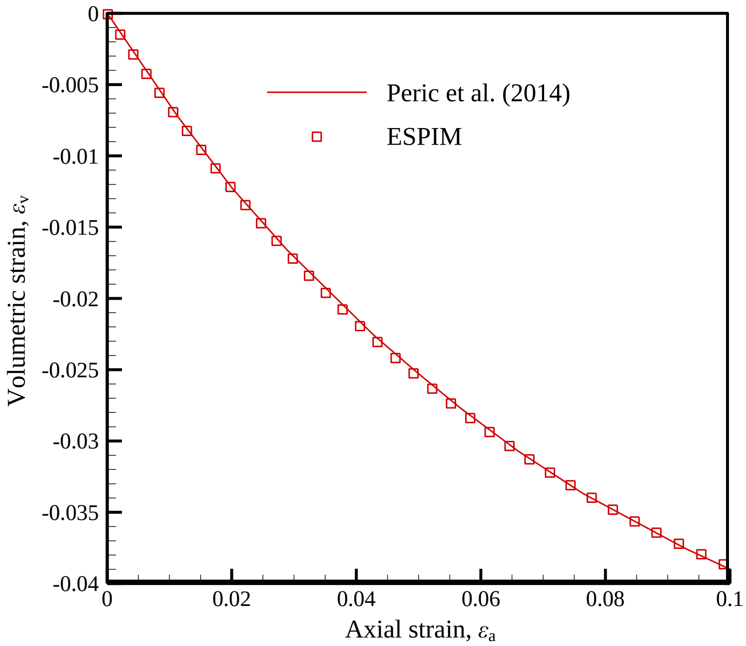

Figure 6-25- Volumetric strain versus axial strain in the drained analysis for an initial suction of 50 kPa and initial net stress of 100 kPa.

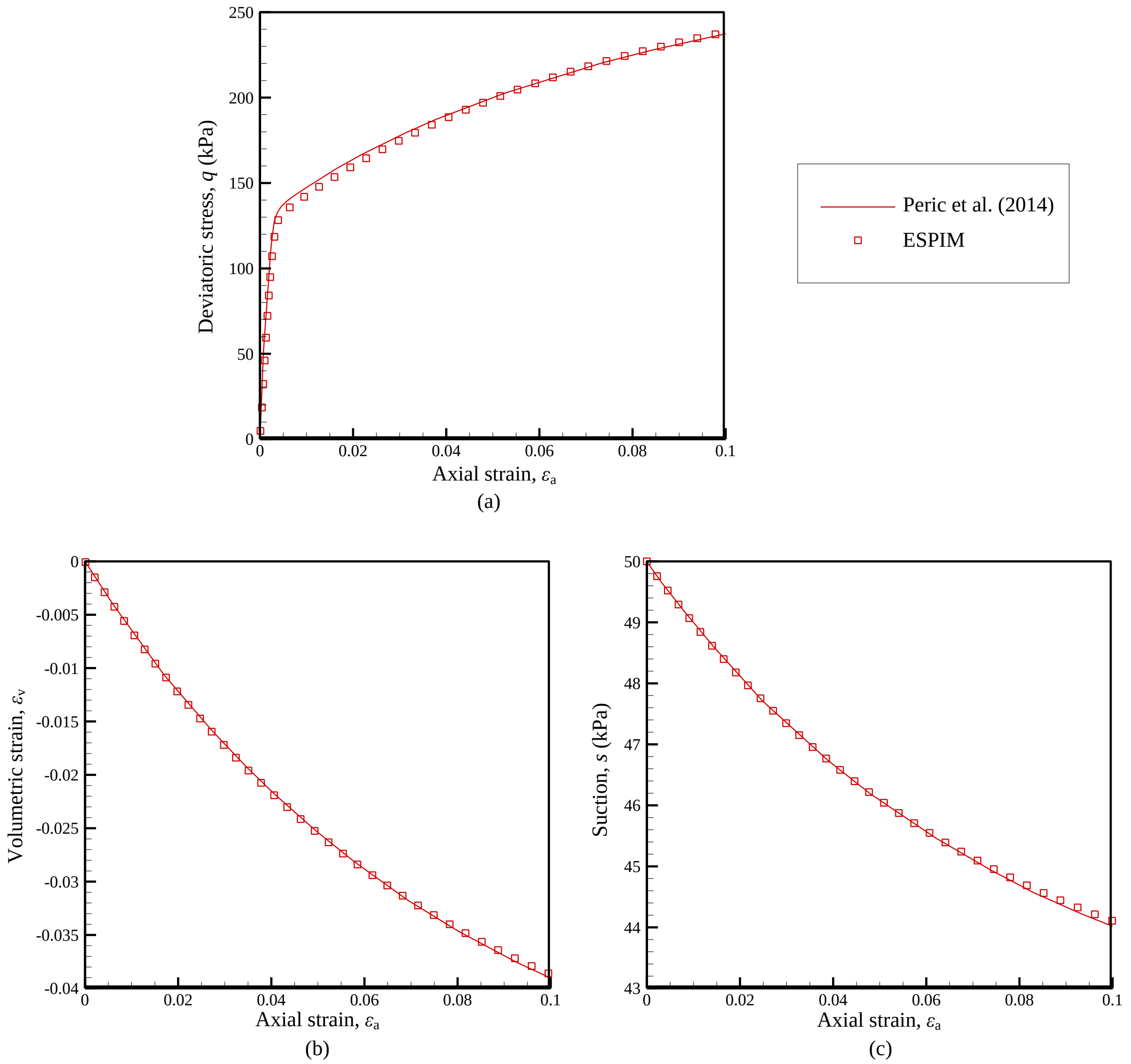

Figure 6-26- Constant water PSC simulation with an initial suction of 50 kPa and initial net stress of 100 kPa, variations of (a) deviatoric stress, (b) Volumetric strain, and (c) Suction, versus axial strain.

6.6. Conclusion

An ESPIM formulation was introduced for flow and deformation analysis of unsaturated porous media. The deformation and flow models were developed based on the principle of effective stress, and momentum and mass conservation of the phases. A hysteretic water retention model was implemented which takes into account the evolution of the WRC with changes in void ratio. An elastoplastic constitutive model was adopted within the context of the bounding surface plasticity theory for predicting the nonlinear behaviour of soil skeleton in unsaturated porous media. The proposed

ESPIM was thoroughly verified against several reference solutions from the literature. The importance of inclusion of hydraulic hysteresis and volume change dependency of WRC model was highlighted through the numerical investigations. In particular, it was shown that a volume change independent WRC model may result in incorrect prediction of the settlements and initial pore water and air pressures generated due to loading in unsaturated porous media.

Chapter 7

7. Conclusion

7.1. General

Fully coupled flow and deformation analysis of porous media requires robust and efficient numerical schemes for well-grounded simulation of problems in geotechnical engineering. Advances in computing power and computational mechanics have made it possible to develop a variety of numerical techniques for the solution of geotechnical engineering problems. Among them, FEM has attracted the attention of many engineers and researchers and is routinely used in the geotechnical engineering community. However, FEM has some inherent deficiencies which make it improper in certain applications. Various MMs have been so far developed to overcome the shortcomings attributed to the classical FEM. Despite their distinct advantages, every of the proposed MMs has its own disadvantages. SPIMs are a recently introduced category of MMs which possess excellent properties such as ultra-accuracy and super convergence, and no mapping is required in their formulation, circumventing many of the problems involved with other MMs. Despite their excellent features, SPIMs have been vastly overlooked by geotechnical engineering community. To date, only a few basic studies have been performed on the application of these methods for coupled flow and deformation analysis of porous media, and even those studies suffer from inconsistencies and mathematical inaccuracies.

The main objective of this study has been to develop SPIM formulations for the flow and deformation analysis of porous media to exploit their full potentials in improving the currently available numerical schemes. The main tasks accomplished in this study are:

1- Development of a coupled SPIM formulation for flow and deformation analysis of saturated elastic porous media which performs more accurately compared to the previous formulation proposed for the same porpuse;
2- Introduction of a new verification procedure, the method of manufactured solutions (MMS), to the geomechanics community,
3- Development of a nonlinear SPIM framework for modelling coupled flow and deformation in nonlinear saturated porous media,
4- Development of an effective stress based SPIM formulation for coupled flow and deformation analysis in unsaturated elasto-plastic porous media.

Each of the abovementioned accomplishments are explained in more details in the following.

7.2. Coupled SPIM formulation for flow and deformation analysis of saturated elastic porous media

SPIMs were originally introduced for applications in solid mechanics and they therefore need to be overhauled for multiphase problems. The main challenge in this regard was to come up with a mathematically well-founded procedure to evaluate the coupling matrix where the shape functions and their derivatives are involved in the integrations over each smoothing domain. Such an integration cannot be carried out solely using the Gauss points on the boundary of the smoothing domains normally adopted in SPIMs. A new group of interior Gauss points were exploited for this purpose, and the coupling matrix was calculated by decomposition into the integration of the derivatives of the shape functions over the boundary of the smoothing domains (using the smoothing operation), and the integration of the shape functions over the smoothing domains. Through three numerical examples it was shown that the proposed formulation perfectly captures different aspects of the hydro-mechanical behaviour of saturated elastic porous media. The performance of four different ESPIMs employing four different approaches for selecting supporting nodes were also evaluated in the numerical examples.

7.3. ESPIM code verification using the method of manufactured solutions

There are different criteria for scientific code verification ranging from professional evaluation of the outputs of the code under study by an expert, to making a comparison between the outputs of the code of interest and an already verified computational code, and to the robust order of accuracy study which requires the exact solutions to the PDEs of interest as a reference. For the first time within the geomechanics community, the method of manufactured solutions (MMS) was adopted in this study for verification of a code developed for coupled flow and deformation analysis of porous media. The MMS basically involves assuming exact solutions for the equations governing the problem and computing the source terms by substituting the assumed solutions into the equations. The computed source terms are then used in the code for obtaining the numerical solutions which are compared to the assumed exact solutions through an order of accuracy study. The applicability of the method was shown using two numerical examples in which different exact solutions were considered for problem variables, i.e. displacements and pore fluid pressure. Five sets of spatial domain discretisations were adopted to obtain the numerical orders of accuracy which were then compared to the formal orders of accuracy.

7.4. Hydro-mechanical analysis of saturated porous media considering material nonlinearity

The majority of the geotechnical engineering problems are involved with material nonlinearity. A nonlinear ESPIM framework based on the modified Newton-Raphson technique and an elastic-perfectly plastic Mohr Coulomb constitutive model was developed for simulation of saturated porous media. A sub-stepping technique assuming known strain increments was used for stress integration. Two different node selection schemes for obtaining the support domains at each point of interest along with employment of polynomial and radial PIM for construction of nodal shape functions were discussed resulting in two smoothed meshfree algorithms: ESPIM-Tr3 and ESRPIM-Tr2L. It was shown that not only the ESPIM-Tr3 provides the most accurate results compared to the ESRPIM-Tr2L and the conventional FEM-Tr3 in terms of displacement and pore pressure calculations for the same background mesh, but also it performs the best in terms of computational efficiency.

7.5. Hydro-mechanical analysis of unsaturated elasto-plastic porous media

An effective stress based model for capturing the coupled flow and deformation behaviour of unsaturated porous media was developed in this part of the work. The effect of hydraulic hysteresis was included using a hysteretic water retention model which also takes account of volume change and suction dependency of the model parameters. A modified Newton-Raphson framework was designed for dealing with nonlinearities of the problem and an elastoplastic constitutive model was employed within the context of bounding surface plasticity theory for predicting the nonlinear behaviour of soil skeleton in unsaturated porous media. The applicability of the presented model was validated through some numerical examples.

7.6. Recommendations for further research

Based on the findings and results of this study, the following topics are suggested for further investigation:

- A comprehensive comparison of the performance of different SPIMs, i.e. edge-based, cell-based, and node-based, with different node selection schemes and nodal shape functions in fully coupled multiphase problems,
- Extension of the proposed numerical models for dynamic analysis of saturated/unsaturated porous media,
- Extension of the proposed numerical models for problems involving large deformations,
- Developing a coupled thermo-hydro-mechanical model for unsaturated porous media and studying the effect of temperature on the model parameters and behaviour of the porous media,
- Extending the presented models to include weak and strong discontinuities, and contacts for application in problems like hydraulic fracturing or Cone Penetration Test (CPT) modelling,

- Extending the presented models to include automatic adaptivity to enhance the efficiency of the models, particularly in problems involving large strain gradients.

References

Abbo, A. & Sloan, S. 1995. A smooth hyperbolic approximation to the Mohr-Coulomb yield criterion. *Computers and Structures,* 54(3)**,** pp 427-441.

Abe, K., Nakamura, S., Nakamura, H. & Shiomi, K. 2017. Numerical study on dynamic behavior of slope models including weak layers from deformation to failure using material point method. *Soils and Foundations,* 57(2)**,** pp 155-175.

Aitchison, G. Soil properties, shear strength and consolidation. proceeding 6th Interational Conference Soil Mechanic Foundations Engineering, 1965. 318-321.

Alonso, E., Vaunat, J. & Gens, A. 1999. Modelling the mechanical behaviour of expansive clays. *Engineering geology,* 54(1)**,** pp 173-183.

Alonso, E. E., Gens, A. & Josa, A. 1990. A constitutive model for partially saturated soils. *Géotechnique,* 40(3)**,** pp 405-430.

ASME 2009. Standard for verification and validation in computational fluid dynamics and heat transfer. *American Society of Mechanical Engineers, New York*.

Atluri, S. & Zhu, T. 1998. A new meshless local Petrov-Galerkin (MLPG) approach in computational mechanics. *Computational mechanics,* 22(2)**,** pp 117-127.

Babuška, I., Banerjee, U. & Osborn, J. E. 2003. Survey of meshless and generalized finite element methods: a unified approach. *Acta Numerica,* 12(1-125.

Baliga, B. R. & Lokhmanets, I. Y. 2016. Generalized Richardson extrapolation procedures for estimating grid-independent numerical solutions. *International Journal of Numerical Methods for Heat & Fluid Flow,* 26(3/4)**,** pp 1121-1144.

Bandara, S. & Soga, K. 2015. Coupling of soil deformation and pore fluid flow using material point method. *Computers and Geotechnics,* 63(199-214.

Belytschko, T., Krongauz, Y., Organ, D., Fleming, M. & Krysl, P. 1996. Meshless methods: an overview and recent developments. *Computer methods in applied mechanics and engineering,* 139(1)**,** pp 3-47.

Belytschko, T., Liu, W. K. & Moran, B. 2000. Finite elements for nonlinear continua and structures. *J. Wiley*.

Belytschko, T., Lu, Y. Y. & Gu, L. 1994. Element-free Galerkin methods. *International Journal for Numerical Methods in Engineering,* 37(2)**,** pp 229-256.

Bhandari, T., Hamad, F., Moormann, C., Sharma, K. & Westrich, B. 2016. Numerical modelling of seismic slope failure using MPM. *Computers and Geotechnics,* 75(126-134.

Biot, M. A. 1941. General theory of three-dimensional consolidation. *Journal of applied physics,* 12(2)**,** pp 155-164.

Biot, M. A. 1956. Theory of propagation of elastic waves in a fluid-saturated porous solid. II. Higher frequency range. *The Journal of the acoustical Society of america,* 28(2)**,** pp 179-191.

Bishop, A. W. 1959. The principle of effective stress. *Teknisk ukeblad,* 39(859-863.

Bishop, A. W., Alpan, I., Blight, G. & Donald, I. 1960. Factors controlling the strength of partly saturated cohesive soils.

Bishop, A. W. & Blight, G. 1963. Some aspects of effective stress in saturated and partly saturated soils. *Geotechnique,* 13(3)**,** pp 177-197.

Blanc, T. & Pastor, M. Numerical simulation of debris flows with the 2D-SPH depth integrated model. EGU General Assembly Conference Abstracts, 2009. 1978.

Blottner, F. G. 1990. Accurate Navier-Stokes results for the hypersonic flow over a spherical nosetip. *Journal of spacecraft and Rockets,* 27(2)**,** pp 113-122.

Bolzon, G., Schrefler, B. & Zienkiewicz, O. 1996. Elastoplastic soil constitutive laws generalized to partially saturated states. *Géotechnique,* 46(2)**,** pp 279-289.

Bond, R. B., Ober, C. C., Knupp, P. M. & Bova, S. W. 2007. Manufactured solution for computational fluid dynamics boundary condition verification. *AIAA journal,* 45(9)**,** pp 2224-2236.

Brackley, I. Partial collapse in unsaturated expansive clay. Proceedings of the 5th Regional Conference for Africa on Soil Mechanics and Foundation Engineering,[Luanda], 1971. 23-30.

Brooks, R. & Corey, T. 1964. Hydraulic Properties Of Porous Media. *Hydrology Papers, Colorado State University*.

Brooks, R. H. & Corey, A. T. 1966. Properties of porous media affecting fluid flow. *Journal of the Irrigation and Drainage Division,* 92(2)**,** pp 61-90.

Bui, H., Fukagawa, R., Sako, K. & Wells, J. 2011. Slope stability analysis and discontinuous slope failure simulation by elasto-plastic smoothed particle hydrodynamics (SPH). *Géotechnique,* 61(7)**,** pp 565-574.

Bui, H., Fukagawa, R. & Sato, K. 2006. Smoothed particle hydrodynamics for soil mechanics. *proceedings of Numerical Methods in Geotechnical Engineering, Graz,* 275-281.

Bui, H., Kodikara, J., Pathegama, R., Bouazza, A. & Haque, A. 2015. Large deformation and post-failure simulations of segmental retaining walls using mesh-free method (SPH). *arXiv preprint arXiv:1501.04000*.

Bui, H. H. & Fukagawa, R. 2013. An improved SPH method for saturated soils and its application to investigate the mechanisms of embankment failure: Case of hydrostatic pore-water pressure. *International Journal for Numerical and Analytical Methods in Geomechanics,* 37(1)**,** pp 31-50.

Burg, C. & Murali, V. 2006. The residual formulation of the method of manufactured solutions for computationally efficient solution verification. *International Journal of Computational Fluid Dynamics,* 20(7)**,** pp 521-532.

Carbonell, J. M., Oñate, E. & Suárez, B. 2009. Modeling of ground excavation with the particle finite-element method. *Journal of engineering mechanics,* 136(4)**,** pp 455-463.

Carbonell, J. M., Oñate, E. & Suárez, B. 2013. Modelling of tunnelling processes and rock cutting tool wear with the particle finite element method. *Computational Mechanics,* 52(3)**,** pp 607-629.

Carman, P. C. 1937. Fluid flow through granular beds. *Trans. Inst. Chem. Eng.,* 15(150-166.

Carter, J., Booker, J. & Small, J. 1979. The analysis of finite elasto-plastic consolidation. *International Journal for Numerical and Analytical Methods in Geomechanics,* 3(2)**,** pp 107-129.

Ceccato, F., Beuth, L. & Simonini, P. 2016. Analysis of piezocone penetration under different drainage conditions with the two-phase material point method. *Journal of Geotechnical and Geoenvironmental Engineering,* 142(12)**,** pp 04016066.

Chen, C.-H. 2015. *Development of Soft Particle Code (SPARC)*: Logos Verlag Berlin GmbH.

Chen, J. S., Wu, C. T., Yoon, S. & You, Y. 2001. A stabilized conforming nodal integration for Galerkin mesh-free methods. *International journal for numerical methods in engineering,* 50(2)**,** pp 435-466.

Chiu, C. & Ng, C. W. 2003. A state-dependent elasto-plastic model for saturated and unsaturated soils. *Géotechnique,* 53(9)**,** pp 809-830.

Choudhary, A., Roy, C. J., Dietiker, J.-F., Shahnam, M., Garg, R. & Musser, J. 2016. Code verification for multiphase flows using the method of manufactured solutions. *International Journal of Multiphase Flow,* 80(150-163.

Coetzee, C., Vermeer, P. & Basson, A. 2005. The modelling of anchors using the material point method. *International journal for numerical and analytical methods in geomechanics,* 29(9)**,** pp 879-895.

Coombs, W. M., Charlton, T. J., Cortis, M. & Augarde, C. E. 2018. Overcoming volumetric locking in material point methods. *Computer Methods in Applied Mechanics and Engineering,* 333(1-21.

Cortis, M., Coombs, W., Augarde, C., Brown, M., Brennan, A. & Robinson, S. 2018. Imposition of essential boundary conditions in the material point method. *International Journal for Numerical Methods in Engineering,* 113(1)**,** pp 130-152.

Cui, X., Liu, G., Li, G., Zhao, X., Nguyen-Thoi, T. & Sun, G. 2008. A smoothed finite element method (SFEM) for linear and geometrically nonlinear analysis of plates and shells. *Comput Model Eng Sci,* 28(2)**,** pp 109-125.

Cundall, P. A. & Strack, O. D. 1979. A discrete numerical model for granular assemblies. *geotechnique,* 29(1)**,** pp 47-65.

Das, B. M. 2013. *Advanced soil mechanics*: Crc Press.

Das, R., Zhang, Y., Schaubs, P. & Cleary, P. 2014. Modelling rock fracturing caused by magma intrusion using the smoothed particle hydrodynamics method. *Computational Geosciences,* 18(6)**,** pp 927-947.

Dolbow, J. & Belytschko, T. 1999a. Numerical integration of the Galerkin weak form in meshfree methods. *Computational mechanics,* 23(3)**,** pp 219-230.

Dolbow, J. & Belytschko, T. 1999b. Volumetric locking in the element free Galerkin method. *International Journal for numerical methods in engineering,* 46(6)**,** pp 925-942.

Eça, L. & Hoekstra, M. 2009. Evaluation of numerical error estimation based on grid refinement studies with the method of the manufactured solutions. *Computers & Fluids,* 38(8)**,** pp 1580-1591.

Eça, L., Hoekstra, M., Hay, A. & Pelletier, D. 2007a. A manufactured solution for a two-dimensional steady wall-bounded incompressible turbulent flow. *International Journal of Computational Fluid Dynamics,* 21(3-4)**,** pp 175-188.

Eça, L., Hoekstra, M., Hay, A. & Pelletier, D. 2007b. On the construction of manufactured solutions for one and two-equation eddy-viscosity models. *International journal for numerical methods in fluids,* 54(2)**,** pp 119-154.

Étienne, S., Garon, A. & Pelletier, D. 2012. Some manufactured solutions for verification of fluid-structure interaction codes. *Computers & Structures,* 106(56-67.

Fillunger, P. 1936. *Erdbaumechanik?*: Selbstverl. d. Verf.

Franke, C. & Schaback, R. 1998. Solving partial differential equations by collocation using radial basis functions. *Applied Mathematics and Computation,* 93(1)**,** pp 73-82.

Fredlund, D. G. & Hasan, J. U. 1979. One-dimensional consolidation theory: unsaturated soils. *Canadian Geotechnical Journal,* 16(3)**,** pp 521-531.

Fredlund, D. G. & Morgenstern, N. R. 1977. Stress state variables for unsaturated soils. *Journal of Geotechnical and Geoenvironmental Engineering,* 103(ASCE 12919)**,** pp.

Fredlund, D. G. & Xing, A. 1994. Equations for the soil-water characteristic curve. *Canadian geotechnical journal,* 31(4)**,** pp 521-532.

Gabrieli, F., Cola, S. & Calvetti, F. 2009. Use of an up-scaled DEM model for analysing the behaviour of a shallow foundation on a model slope. *Geomechanics and Geoengineering: An International Journal,* 4(2)**,** pp 109-122.

Gallipoli, D., Gens, A., Sharma, R. & Vaunat, J. 2003. An elasto-plastic model for unsaturated soil incorporating the effects of suction and degree of saturation on mechanical behaviour. *Géotechnique.,* 53(1)**,** pp 123-136.

Gens, A., Jouanna, P. & Schrefler, B. 1995. *Modern issues in non-saturated soils*: Springer.

Georgiadis, K., Potts, D. M. & Zdravkovic, L. 2005. Three-dimensional constitutive model for partially and fully saturated soils. *International Journal of Geomechanics,* 5(3)**,** pp 244-255.

Ghaffaripour, O., Khoshghalb, A. & Khalili, N. 2017. An edge-based smoothed point interpolation method for elasto-plastic coupled hydro-mechanical analysis of saturated porous media. *Computers and Geotechnics,* 82(99-109.

Ghorbani, J., Airey, D. W. & El-Zein, A. 2018a. Numerical framework for considering the dependency of SWCCs on volume changes and their hysteretic responses in modelling elasto-plastic response of unsaturated soils. *Computer Methods in Applied Mechanics and Engineering,* 336(80-110.

Ghorbani, J., Nazem, M. & Carter, J. 2016. Numerical modelling of multiphase flow in unsaturated deforming porous media. *Computers and Geotechnics,* 71(195-206.

Ghorbani, J., Nazem, M., Carter, J. P. & Sloan, S. W. 2018b. A stress integration scheme for elasto-plastic response of unsaturated soils subjected to large deformations. *Computers and Geotechnics,* 94(231-246.

Gingold, R. A. & Monaghan, J. J. 1977. Smoothed particle hydrodynamics: theory and application to non-spherical stars. *Monthly Notices of the Royal Astronomical Society,* 181(3)**,** pp 375-389.

Goudarzi, M. & Mohammadi, S. 2014. Weak discontinuity in porous media: an enriched EFG method for fully coupled layered porous media. *International Journal for Numerical and Analytical Methods in Geomechanics*.

Goudarzi, M. & Mohammadi, S. 2015. Analysis of cohesive cracking in saturated porous media using an extrinsically enriched EFG method. *Computers and Geotechnics,* 63(183-198.

Gu, Y. 2008. An elasto-plastic analysis of solids by the local meshless method based on MLS. *International Journal of Modern Physics B,* 22(31n32)**,** pp 5780-5786.

Ho, L., Fatahi, B. & Khabbaz, H. 2014. Analytical solution for one-dimensional consolidation of unsaturated soils using eigenfunction expansion method. *International Journal for Numerical and Analytical Methods in Geomechanics,* 38(10)**,** pp 1058-1077.

Holmes, D. W., Williams, J. R., Tilke, P. & Leonardi, C. R. 2016. Characterizing flow in oil reservoir rock using SPH: absolute permeability. *Computational Particle Mechanics,* 3(2)**,** pp 141-154.

Hu, D. a., Sun, Z., Liang, C. & Han, X. 2013. A mesh-free algorithm for dynamic impact analysis of hyperelasticity. *Acta Mechanica Solida Sinica,* 26(4)**,** pp 362-372.

Hu, M., Liu, M., Xie, M. & Liu, G. 2015. Three-dimensional run-out analysis and prediction of flow-like landslides using smoothed particle hydrodynamics. *Environmental Earth Sciences,* 73(4)**,** pp 1629-1640.

Idelsohn, S. R., Oñate, E. & Becker, P. 2018. Particle methods in computational fluid dynamics. *Encyclopedia of Computational Mechanics Second Edition,* 1-41.

Idelsohn, S. R., Oñate, E., Del Pin, F. & Calvo, N. 2006. Fluid–structure interaction using the particle finite element method. *Computer methods in applied mechanics and engineering,* 195(17-18)**,** pp 2100-2123.

Idelsohn, S. R., Oñate, E. & Pin, F. D. 2004. The particle finite element method: a powerful tool to solve incompressible flows with free-surfaces and breaking waves. *International journal for numerical methods in engineering,* 61(7)**,** pp 964-989.

Jassim, I., Stolle, D. & Vermeer, P. 2013. Two-phase dynamic analysis by material point method. *International journal for numerical and analytical methods in geomechanics,* 37(15)**,** pp 2502-2522.

Jefferies, A., Kuhnert, J., Aschenbrenner, L. & Giffhorn, U. 2015. Finite pointset method for the simulation of a vehicle travelling through a body of water. *Meshfree Methods for Partial Differential Equations VII.* Springer.

Jennings, J. & Burland, J. 1962. Limitations to the use of effective stresses in partly saturated soils. *Géotechnique,* 12(2)**,** pp 125-144.

Jiang, M. & Yin, Z.-Y. 2012. Analysis of stress redistribution in soil and earth pressure on tunnel lining using the discrete element method. *Tunnelling and Underground Space Technology,* 32(251-259.

Kan, M. E., Taiebat, H. A. & Khalili, N. 2013. Simplified mapping rule for bounding surface simulation of complex loading paths in granular materials. *International Journal of Geomechanics,* 14(2)**,** pp 239-253.

Kansa, E. J. 1990. Multiquadrics—A scattered data approximation scheme with applications to computational fluid-dynamics—II solutions to parabolic, hyperbolic and elliptic partial differential equations. *Computers & mathematics with applications,* 19(8)**,** pp 147-161.

Kardani, O., Nazem, M., Kardani, M. & Sloan, S. 2017. On the application of the maximum entropy meshfree method for elastoplastic geotechnical analysis. *Computers and Geotechnics,* 84(68-77.

Khalili, N., Geiser, F. & Blight, G. 2004. Effective stress in unsaturated soils: review with new evidence. *International journal of Geomechanics,* 4(2)**,** pp 115-126.

Khalili, N., Habte, M. & Valliappan, S. 2005. A bounding surface plasticity model for cyclic loading of granular soils. *International journal for numerical methods in engineering,* 63(14)**,** pp 1939-1960.

Khalili, N., Habte, M. & Zargarbashi, S. 2008. A fully coupled flow deformation model for cyclic analysis of unsaturated soils including hydraulic and mechanical hystereses. *Computers and Geotechnics,* 35(6)**,** pp 872-889.

Khalili, N. & Khabbaz, M. 1998. A unique relationship of chi for the determination of the shear strength of unsaturated soils. *Geotechnique,* 48(5)**,** pp.

Khalili, N., Khabbaz, M. & Valliappan, S. 2000. An effective stress based numerical model for hydro-mechanical analysis in unsaturated porous media. *Computational mechanics,* 26(2)**,** pp 174-184.

Khalili, N. & Valliappan, S. 1996. Unified theory of flow and deformation in double porous media. *European Journal of Mechanics, A/Solids,* 15(2)**,** pp 321-336.

Khalili, N., Valliappan, S. & Wan, C. 1999. Consolidation of fissured clays. *Geotechnique,* 49(1)**,** pp 75-89.

Khalili, N. & Zargarbashi, S. 2010. Influence of hydraulic hysteresis on effective stress in unsaturated soils. *Geotechnique,* 60(9)**,** pp 729-734.

Khoei, A. & Mohammadnejad, T. 2011. Numerical modeling of multiphase fluid flow in deforming porous media: a comparison between two-and three-phase models for seismic analysis of earth and rockfill dams. *Computers and Geotechnics,* 38(2)**,** pp 142-166.

Khoshghalb, A. & Khalili, N. 2010. A stable meshfree method for fully coupled flow-deformation analysis of saturated porous media. *Computers and Geotechnics,* 37(6)**,** pp 789-795.

Khoshghalb, A. & Khalili, N. 2013. A meshfree method for fully coupled analysis of flow and deformation in unsaturated porous media. *International Journal for Numerical and Analytical Methods in Geomechanics,* 37(7)**,** pp 716-743.

Khoshghalb, A. & Khalili, N. 2015. An alternative approach for quasi-static large deformation analysis of saturated porous media using meshfree method. *International Journal for Numerical and Analytical Methods in Geomechanics,* 39(9)**,** pp 913-936.

Khoshghalb, A., Khalili, N. & Selvadurai, A. 2011. A three-point time discretization technique for parabolic partial differential equations. *International Journal for Numerical and Analytical Methods in Geomechanics,* 35(3)**,** pp 406-418.

Khoshghalb, A., Pasha, A. & Khalili, N. 2015. A fractal model for volume change dependency of the water retention curve. *Géotechnique,* 65(2)**,** pp 141-146.

Khosrojerdi, M. & Pak, A. 2015. Numerical investigation on the behavior of the gravity waterfront structures under earthquake loading. *Ocean Engineering,* 106(152-160.

Knupp, P. & Salari, K. 2002. *Verification of computer codes in computational science and engineering*: CRC Press.

Komoróczi, A., Abe, S. & Urai, J. L. 2013. Meshless numerical modeling of brittle–viscous deformation: first results on boudinage and hydrofracturing using a coupling of discrete element method (DEM) and smoothed particle hydrodynamics (SPH). *Computational Geosciences,* 17(2)**,** pp 373-390.

Kozeny, J. 1927. Uber kapillare leitung der wasser in boden. *Royal Academy of Science, Vienna, Proc. Class I,* 136(271-306.

Kuhnert, J. & Ostermann, I. 2014. The finite pointset method (FPM) and an application in soil mechanics. *Mathematics of Planet Earth.* Springer.

Kumar, R. P. & Dodagoudar, G. 2008. Two-dimensional modelling of contaminant transport through saturated porous media using the radial point interpolation method (RPIM). *Hydrogeology Journal,* 16(8)**,** pp 1497-1505.

Laloui, L., Klubertanz, G. & Vulliet, L. 2003. Solid–liquid–air coupling in multiphase porous media. *International Journal for Numerical and Analytical Methods in Geomechanics,* 27(3)**,** pp 183-206.

Leng, W., Ju, L., Gunzburger, M. & Price, S. 2013. Manufactured solutions and the verification of three-dimensional Stokes ice-sheet models. *The Cryosphere,* 7(1)**,** pp 19.

Lewis, R. & Schrefler, B. 1982. A finite element simulation of the subsidence of gas reservoirs undergoing a water drive. *Finite Elem. Fluids 4,* 179–199.

Lewis, R. & Schrefler, B. 1999. The finite element method in the static and dynamic deformation and consolidation of porous media. *Meccanica,* 34(3)**,** pp 231-232.

Lewis, R. W., Schrefler, B. A. & Abd Rahman, N. 1998. A finite element analysis of multiphase immiscible flow in deforming porous media for subsurface systems. *Communications in numerical methods in engineering,* 14(2)**,** pp 135-149.

Li, X., Ding, D., Chan, A. H. C. & Zienkiewicz, O. C. 1989. A coupled fnite element method for the soil-pore fluid interaction problems with immiscible two-phase fluid flow. *Proc. 5th Int. Symp. on Numerical Methods in Eng., Lausanne*.

Libersky, L. D., Petschek, A. G., Carney, T. C., Hipp, J. R. & Allahdadi, F. A. 1993. High strain Lagrangian hydrodynamics: a three-dimensional SPH code for dynamic material response. *Journal of computational physics,* 109(1)**,** pp 67-75.

Lim, K. W. & Andrade, J. E. 2014. Granular element method for three-dimensional discrete element calculations. *International Journal for Numerical and Analytical Methods in Geomechanics,* 38(2)**,** pp 167-188.

Liu, G.-R. 2010a. *Meshfree methods: moving beyond the finite element method*: CRC press.

Liu, G.-R. & Gu, Y.-T. 2005. *An introduction to meshfree methods and their programming*: Springer.

Liu, G.-R. & Gu, Y. 2001. A point interpolation method for two-dimensional solids. *International Journal for Numerical Methods in Engineering,* 50(4)**,** pp 937-951.

Liu, G.-R. & Liu, M. B. 2003. *Smoothed particle hydrodynamics: a meshfree particle method*: World Scientific.

Liu, G.-R. & Zhang, G.-Y. 2013a. *Smoothed point interpolation methods: G space theory and weakened weak forms*: World Scientific.

Liu, G.-R. & Zhang, G.-Y. 2013b. *Smoothed point interpolation methods: G space theory and weakened weakforms*.

Liu, G. 2009. On G space theory. *International Journal of Computational Methods,* 6(02)**,** pp 257-289.

Liu, G. 2010b. AG space theory and a weakened weak (W2) form for a unified formulation of compatible and incompatible methods: Part I theory. *International Journal for Numerical Methods in Engineering,* 81(9)**,** pp 1093-1126.

Liu, G., Dai, K. & Nguyen, T. 2007a. A smoothed finite element method for mechanics problems. *Computational Mechanics,* 39(6)**,** pp 859-877.

Liu, G., Gu, Y. & Dai, K. 2004. Assessment and applications of point interpolation methods for computational mechanics. *International Journal for Numerical Methods in Engineering,* 59(10)**,** pp 1373-1397.

Liu, G., Nguyen-Thoi, T. & Lam, K. 2009a. An edge-based smoothed finite element method (ES-FEM) for static, free and forced vibration analyses of solids. *Journal of Sound and Vibration*, 320(4)**,** pp 1100-1130.

Liu, G., Nguyen-Thoi, T., Nguyen-Xuan, H. & Lam, K. 2009b. A node-based smoothed finite element method (NS-FEM) for upper bound solutions to solid mechanics problems. *Computers & structures,* 87(1)**,** pp 14-26.

Liu, G., Nguyen, T., Dai, K. & Lam, K. 2007b. Theoretical aspects of the smoothed finite element method (SFEM). *International journal for numerical methods in Engineering,* 71(8)**,** pp 902-930.

Liu, G. & Zhang, G. 2008. Edge-based smoothed point interpolation methods. *International Journal of Computational Methods,* 5(04)**,** pp 621-646.

Liu, G. & Zhang, G. 2009. A normed G space and weakened weak (W2) formulation of a cell-based smoothed point interpolation method. *International Journal of Computational Methods,* 6(01)**,** pp 147-179.

Liu, G., Zhang, G., Dai, K., Wang, Y., Zhong, Z., Li, G. & Han, X. 2005. A linearly conforming point interpolation method (LC-PIM) for 2D solid mechanics problems. *International Journal of Computational Methods,* 2(04)**,** pp 645-665.

Liu, W. K., Jun, S. & Zhang, Y. F. 1995. Reproducing kernel particle methods. *International Journal for Numerical Methods in Fluids,* 20(8-9)**,** pp 1081-1106.

Loret, B. & Khalili, N. 2000. A three-phase model for unsaturated soils. *International Journal for Numerical and Analytical Methods in Geomechanics,* 24(11)**,** pp 893-927.

Loret, B. & Khalili, N. 2002. An effective stress elastic–plastic model for unsaturated porous media. *Mechanics of Materials,* 34(2)**,** pp 97-116.

Lucy, L. B. 1977. A numerical approach to the testing of the fission hypothesis. *The Astronomical Journal,* 82(1013-1024.

Manoharan, N. & Dasgupta, S. 1995. Consolidation analysis of elasto-plastic soil. *Computers & structures,* 54(6)**,** pp 1005-1021.

Martin, C. 2004. User guide for ABC: Analysis of bearing capacity. *Technical Report OUEL 2261/03, University of Oxford, Department of Engineering Science.*

Mašín, D. 2010. Predicting the dependency of a degree of saturation on void ratio and suction using effective stress principle for unsaturated soils. *International*

Journal for Numerical and Analytical Methods in Geomechanics, 34(1)**,** pp 73-90.

Matyas, E. L. & Radhakrishna, H. 1968. Volume change characteristics of partially saturated soils. *Géotechnique,* 18(4)**,** pp 432-448.

Michel, I., Kuhnert, J. & Kolymbas, D. Meshfree simulation of avalanches with the Finite Pointset Method (FPM). EGU General Assembly Conference Abstracts, 2017. 13203.

Modaressi, H. & Aubert, P. 1995. Coupled FEM-EFGM for consolidation modelling. *Numerical Models in Geomechanics,* 417-422.

Modaressi, H. & Aubert, P. 1998. Element-free Galerkin method for deforming multiphase porous media. *International Journal for Numerical Methods in Engineering,* 42(2)**,** pp 313-340.

Morel-Seytoux, H. J. & Billica, J. A. 1985. A two-phase numerical model for prediction of infiltration: Applications to a semi-infinite soil column. *Water Resources Research,* 21(4)**,** pp 607-615.

Murakami, A., Kawabata, H. & Aoyama, S. 2000. EFGM analysis for saturated soil. *Computer methods and advances in geomechanics,* 1(153-156.

Muraleetharan, K. K., Liu, C., Wei, C., Kibbey, T. C. & Chen, L. 2009. An elastoplatic framework for coupling hydraulic and mechanical behavior of unsaturated soils. *International Journal of Plasticity,* 25(3)**,** pp 473-490.

Narasimhan, T. N. & Witherspoon, P. 1978. Numerical model for saturated-unsaturated flow in deformable porous media: 3. Applications. *Water Resources Research,* 14(6)**,** pp 1017-1034.

Nayroles, B., Touzot, G. & Villon, P. 1992. Generalizing the finite element method: diffuse approximation and diffuse elements. *Computational Mechanics,* 10(5)**,** pp 307-318.

Nazem, M., Kardani, M., Bienen, B. & Cassidy, M. 2016. A stable Maximum-Entropy Meshless method for analysis of porous media. *Computers and Geotechnics,* 80(248-260.

Nguyen-Xuan, H., Rabczuk, T., Bordas, S. & Debongnie, J.-F. 2008. A smoothed finite element method for plate analysis. *Computer Methods in Applied Mechanics and Engineering,* 197(13)**,** pp 1184-1203.

Nguyen-Thoi, T., Liu, G., Lam, K. & Zhang, G. 2009. A face-based smoothed finite element method (FS-FEM) for 3D linear and geometrically non-linear solid mechanics problems using 4-node tetrahedral elements. *International Journal for Numerical Methods in Engineering,* 78(3)**,** pp 324-353.

Nguyen-Xuan, H., Bordas, S. & Nguyen-Dang, H. 2008. Smooth finite element methods: convergence, accuracy and properties. *International Journal for Numerical Methods in Engineering,* 74(2)**,** pp 175-208.

Nguyen-Xuan, H. & Nguyen-Thoi, T. 2009. A stabilized smoothed finite element method for free vibration analysis of Mindlin–Reissner plates. *Communications in Numerical Methods in Engineering,* 25(8)**,** pp 882-906.

Oberkampf, W. L. & Blottner, F. G. 1998. Issues in computational fluid dynamics code verification and validation. *AIAA journal,* 36(5)**,** pp 687-695.

Oberkampf, W. L. & Roy, C. J. 2010. *Verification and validation in scientific computing*: Cambridge University Press.

Oberkampf, W. L., Trucano, T. G. & Hirsch, C. 2004. Verification, validation, and predictive capability in computational engineering and physics. *Applied Mechanics Reviews,* 57(5)**,** pp 345-384.

Oberkampf, W. L., Trucano, T. G. & Pilch, M. M. 2003. On the role of code comparisons in verification and validation,

Obermayr, M., Dressler, K., Vrettos, C. & Eberhard, P. 2013. A bonded-particle model for cemented sand. *Computers and Geotechnics,* 49(299-313.

Oliaei, M. & Pak, A. 2009. Element Free Galerkin Mesh-Less Method for Fully Coupled Analysis of a Consolidation Process. *Scientia Iranica, Transaction A,* 16(1)**,** pp 65-77.

Oliaei, M. N., Pak, A. & Soga, K. 2014. A coupled hydro-mechanical analysis for prediction of hydraulic fracture propagation in saturated porous media using EFG mesh-less method. *Computers and Geotechnics,* 55(254-266.

Oliaei, M. N., Soga, K. & Pak, A. 2009. Some numerical issues using element-free Galerkin mesh-less method for coupled hydro-mechanical problems. *International journal for numerical and analytical methods in geomechanics,* 33(7)**,** pp 915-938.

Oñate, E., Idelsohn, S. R., Celigueta, M. A., Rossi, R., Marti, J., Carbonell, J., Ryzhakov, P. & Suárez, B. 2011. Advances in the particle finite element method (PFEM) for solving coupled problems in engineering. *Particle-Based Methods.* Springer.

Oñate, E., Idelsohn, S. R., Del Pin, F. & Aubry, R. 2004. The particle finite element method—an overview. *International Journal of Computational Methods,* 1(02)**,** pp 267-307.

Ortiz, A., Puso, M. & Sukumar, N. 2010. Maximum-entropy meshfree method for compressible and near-incompressible elasticity. *Computer Methods in Applied Mechanics and Engineering,* 199(25-28)**,** pp 1859-1871.

Ortiz, A., Puso, M. & Sukumar, N. 2011. Maximum-entropy meshfree method for incompressible media problems. *Finite Elements in Analysis and Design,* 47(6)**,** pp 572-585.

Pamin, J., Askes, H. & de Borst, R. 2003. Two gradient plasticity theories discretized with the element-free Galerkin method. *Computer Methods in Applied Mechanics and Engineering,* 192(20)**,** pp 2377-2403.

Pasha, A. Y., Khoshghalb, A. & Khalili, N. 2017. Hysteretic Model for the Evolution of Water Retention Curve with Void Ratio. *Journal of Engineering Mechanics,* 143(7)**,** pp 04017030.

Pelletier, D. 2010. Verification, validation, and uncertainty in Computational Fluids Dynamics. *Canadian Journal of Civil Engineering,* 37(7)**,** pp 1003-1013.

Pelletier, D. & Roache, P. J. 2000. Verification and validation of computational heat transfer. *Handbook of Numerical Heat Transfer, Second Edition,* 417-442.

Peng, C., Wu, W., Yu, H.-s. & Wang, C. 2015. A SPH approach for large deformation analysis with hypoplastic constitutive model. *Acta Geotechnica,* 10(6)**,** pp 703-717.

Perić, D., Zhao, G. & Khalili, N. 2014. Strain localization in unsaturated elastic-plastic materials subjected to plane strain compression. *Journal of Engineering Mechanics,* 140(7)**,** pp 04014050.

Petersson, N. A. & Sjögreen, B. 2018. High order accurate finite difference modeling of seismo-acoustic wave propagation in a moving atmosphere and a heterogeneous earth model coupled across a realistic topography. *Journal of Scientific Computing,* 74(1)**,** pp 290-323.

Poiseuille, J. 1838. Ecoulement des Liquides: Societe Philomatique de Paris. *Extraits des Proces-Verbaux des Seances Pendant I'Annee,* 3(77-81.

Potts, D. & Ganendra, D. 1994. An evaluation of substepping and implicit stress point algorithms. *Computer Methods in Applied Mechanics and Engineering,* 119(3-4)**,** pp 341-354.

Potts, D. M. & Zdravkovic, L. 2001. *Finite element analysis in geotechnical engineering: application*: Thomas Telford.

Qin, A.-f., Chen, G.-j., Tan, Y.-w. & Sun, D.-a. 2008. Analytical solution to one-dimensional consolidation in unsaturated soils. *Applied mathematics and mechanics,* 29(10)**,** pp 1329-1340.

Rethore, J., Borst, R. d. & Abellan, M. A. 2007. A two-scale approach for fluid flow in fractured porous media. *International Journal for Numerical Methods in Engineering,* 71(7)**,** pp 780-800.

Roache, P., Knupp, P., Steinberg, S. & Blaine, R. Experience with benchmark test cases for groundwater flow. 1990 Spring Meeting of the Fluids Engineering Division, Toronto, Ont, Can, 06/04-07/90, 1990. 49-56.

Roache, P. J. 2002. Code verification by the method of manufactured solutions. *Journal of Fluids Engineering,* 124(1)**,** pp 4-10.

Roache, P. J. 2004. Building PDE codes to be verifiable and validatable. *Computing in science & engineering,* 6(5)**,** pp 30-38.

Roache, P. J. & Knupp, P. M. 1993. Completed richardson extrapolation. *International Journal for Numerical Methods in Biomedical Engineering,* 9(5)**,** pp 365-374.

Roy, C. J. 2005. Review of code and solution verification procedures for computational simulation. *Journal of Computational Physics,* 205(1)**,** pp 131-156.

Roy, C. J. & Blottner, F. G. 2003. Methodology for turbulence model validation: application to hypersonic flows. *Journal of Spacecraft and Rockets,* 40(3)**,** pp 313-325.

Roy, C. J., Nelson, C., Smith, T. & Ober, C. 2004. Verification of Euler/Navier–Stokes codes using the method of manufactured solutions. *International Journal for Numerical Methods in Fluids,* 44(6)**,** pp 599-620.

Russell, A. R. & Khalili, N. 2004. A bounding surface plasticity model for sands exhibiting particle crushing. *Canadian Geotechnical Journal,* 41(6)**,** pp 1179-1192.

Sabetamal, H., Nazem, M., Sloan, S. W. & Carter, J. P. 2016. Frictionless contact formulation for dynamic analysis of nonlinear saturated porous media based on the mortar method. *International Journal for Numerical and Analytical Methods in Geomechanics*, 40(1)**,** pp 25-61.

Salager, S., Nuth, M., Ferrari, A. & Laloui, L. 2013. Investigation into water retention behaviour of deformable soils. *Canadian Geotechnical Journal,* 50(2)**,** pp 200-208.

Salari, K. & Knupp, P. 2000. Code verification by the method of manufactured solutions,

Salazar, F., Irazábal, J., Larese, A. & Oñate, E. 2016. Numerical modelling of landslide-generated waves with the particle finite element method (PFEM) and a non-Newtonian flow model. *International Journal for Numerical and Analytical Methods in Geomechanics,* 40(6)**,** pp 809-826.

Samimi, S. & Pak, A. 2012. Three-dimensional simulation of fully coupled hydro-mechanical behavior of saturated porous media using Element Free Galerkin (EFG) method. *Computers and Geotechnics,* 46(75-83.

Samimi, S. & Pak, A. 2014. A novel three-dimensional element free Galerkin (EFG) code for simulating two-phase fluid flow in porous materials. *Engineering Analysis with Boundary Elements,* 39(53-63.

Samimi, S. & Pak, A. 2016. A fully coupled element-free Galerkin model for hydro-mechanical analysis of advancement of fluid-driven fractures in porous media. *International Journal for Numerical and Analytical Methods in Geomechanics,* 40(16)**,** pp 2178-2206.

Santagiuliana, R. & Schrefler, B. 2006. Enhancing the Bolzon–Schrefler–Zienkiewicz constitutive model for partially saturated soil. *Transport in porous media,* 65(1)**,** pp 1-30.

Scheidegger, A. 1958. *The physics of flow through porous media*: University Of Toronto Press: London.

Schenkengel, K.-U. & Vrettos, C. „Modelling of liquefactioninduced lateral spreading using the Lattice Boltzmann Method ". 5th International Conference on Earthquake Geotechnical Engineering, 2011.

Schiffman, R. L., Chen, A. & Jordan, J. C. 1969. An analysis of consolidation theories. *Journal of Soil Mechanics & Foundations Div*.

Schneider-Muntau, B., Chen, C.-H. & Bathaeian, S. I. 2017. Simulation of shear bands with Soft PARticle Code (SPARC) and FE. *GEM-International Journal on Geomathematics,* 8(1)**,** pp 135-151.

Schönewald, A., Soares, D. & von Estorff, O. 2012. A smoothed radial point interpolation method for application in porodynamics. *Computational Mechanics,* 50(4)**,** pp 433-443.

Selvadurai, A. 2009. Influence of residual hydraulic gradients on decay curves for one-dimensional hydraulic pulse tests. *Geophysical Journal International,* 177(3)**,** pp 1357-1365.

Selvadurai, A. & Carnaffan, P. 1997. A transient pressure pulse method for the mesurement of permeability of a cement grout. *Canadian Journal of Civil Engineering,* 24(3)**,** pp 489-502.

Shahbodagh-Khan, B., Khalili, N. & Esgandani, G. A. 2015. A numerical model for nonlinear large deformation dynamic analysis of unsaturated porous media including hydraulic hysteresis. *Computers and Geotechnics,* 69(411-423.

Sharan, M., Kansa, E. & Gupta, S. 1997. Application of the multiquadric method for numerical solution of elliptic partial differential equations. *Applied Mathematics and Computation,* 84(2-3)**,** pp 275-302.

Sheng, D., Fredlund, D. G. & Gens, A. 2008a. A new modelling approach for unsaturated soils using independent stress variables. *Canadian Geotechnical Journal,* 45(4)**,** pp 511-534.

Sheng, D., Gens, A., Fredlund, D. G. & Sloan, S. W. 2008b. Unsaturated soils: from constitutive modelling to numerical algorithms. *Computers and Geotechnics,* 35(6)**,** pp 810-824.

Sheng, D., Sloan, S. & Yu, H. 2000. Aspects of finite element implementation of critical state models. *Computational mechanics,* 26(2)**,** pp 185-196.

Sheng, D., Sloan, S. W., Gens, A. & Smith, D. W. 2003a. Finite element formulation and algorithms for unsaturated soils. Part I: Theory. *International Journal for Numerical and Analytical Methods in Geomechanics,* 27(9)**,** pp 745-765.

Sheng, D., Smith, D. W., W Sloan, S. & Gens, A. 2003b. Finite element formulation and algorithms for unsaturated soils. Part II: Verification and application. *International Journal for Numerical and Analytical Methods in Geomechanics,* 27(9)**,** pp 767-790.

Sheu, G. 2007. Characterizing soil properties by the meshless local Petrov-Galerkin method. *Geotechnical and Geological Engineering,* 25(4)**,** pp 473-486.

Shih, T. 1985. A procedure to debug computer programs. *International Journal for Numerical Methods in Engineering,* 21(6)**,** pp 1027-1037.

Sloan, S. & Booker, J. 1986. Removal of singularities in Tresca and Mohr–Coulomb yield functions. *International Journal for Numerical Methods in Biomedical Engineering,* 2(2)**,** pp 173-179.

Sloan, S. W. 1987. Substepping schemes for the numerical integration of elastoplastic stress–strain relations. *International Journal for Numerical Methods in Engineering,* 24(5)**,** pp 893-911.

Small, J. C., Booker, J. & Davis, E. H. 1976. Elasto-plastic consolidation of soil. *International Journal of Solids and Structures,* 12(6)**,** pp 431-448.

Smith, I., Griffiths, D. & Margetts, L. 2013. *Programming the Finite Element Method*: John Wiley & Sons.

Soares, D., Sladek, V. & Sladek, J. 2012. Modified meshless local Petrov–Galerkin formulations for elastodynamics. *International Journal for Numerical Methods in Engineering,* 90(12)**,** pp 1508-1828.

Soares Jr, D. 2010. Dynamic Analysis of Porous Media Considering Unequal Phase Discretization by Meshless Local Petrov-Galerkin Formulations. *Computer Modeling in Engineering & Sciences(CMES),* 61(2)**,** pp 177-200.

Soares Jr, D. 2013a. Dynamic elastoplastic analyses by smoothed point interpolation methods. *International Journal of Computational Methods,* 10(05)**,** pp 1350030.

Soares Jr, D. 2013b. Iterative dynamic analysis of linear and nonlinear fully saturated porous media considering edge-based smoothed meshfree techniques. *Computer Methods in Applied Mechanics and Engineering,* 253(73-88.

Soares Jr, D., Großeholz, G. & von Estorff, O. 2014. A more flexible and effective analysis of porous media considering edge-based smoothed meshfree techniques. *Computational Mechanics,* 53(6)**,** pp 1265-1277.

Soga, K., Alonso, E., Yerro, A., Kumar, K. & Bandara, S. 2015. Trends in large-deformation analysis of landslide mass movements with particular emphasis on the material point method. *Géotechnique,* 66(3)**,** pp 248-273.

Steinberg, S. & Roache, P. J. 1985. Symbolic manipulation and computational fluid dynamics. *Journal of Computational Physics,* 57(2)**,** pp 251-284.

Sukumar, N. 2004. Construction of polygonal interpolants: a maximum entropy approach. *International journal for numerical methods in engineering,* 61(12)**,** pp 2159-2181.

Sulsky, D., Chen, Z. & Schreyer, H. L. 1994. A particle method for history-dependent materials. *Computer methods in applied mechanics and engineering,* 118(1-2)**,** pp 179-196.

Sun, D., Matsuoka, H., Cui, H. & Xu, Y. 2003. Three-dimensional elasto-plastic model for unsaturated compacted soils with different initial densities. *International Journal for Numerical and Analytical Methods in Geomechanics,* 27(12)**,** pp 1079-1098.

Sun, D., Sheng, D., Cui, H. & Sloan, S. 2007a. A density-dependent elastoplastic hydro-mechanical model for unsaturated compacted soils. *International journal for numerical and analytical methods in geomechanics,* 31(11)**,** pp 1257-1279.

Sun, D. a., Sheng, D. & Sloan, S. W. 2007b. Elastoplastic modelling of hydraulic and stress–strain behaviour of unsaturated soils. *Mechanics of Materials*, 39(3)**,** pp 212-221.

Tamagnini, R. 2004. An extended Cam-clay model for unsaturated soils with hydraulic hysteresis. *Géotechnique,* 54(3)**,** pp 223-228.

Tang, Q., Zhang, G., Liu, G., Zhong, Z. & He, Z. 2012. An efficient adaptive analysis procedure using the edge-based smoothed point interpolation method (ES-PIM) for 2D and 3D problems. *Engineering Analysis with Boundary Elements,* 36(9)**,** pp 1424-1443.

Tang, Y., Taiebat, H. A. & Russell, A. R. 2016. Bearing capacity of shallow foundations in unsaturated soil considering hydraulic hysteresis and three drainage conditions. *International Journal of Geomechanics,* 17(6)**,** pp 04016142.

Tang, Y., Taiebat, H. A. & Russell, A. R. 2017. Numerical Modeling of Consolidation of Unsaturated Soils Considering Hydraulic Hysteresis. *International Journal of Geomechanics,* 18(2)**,** pp 04017136.

Tarantino, A. 2009. A water retention model for deformable soils. *Géotechnique,* 59(9)**,** pp 751-762.

Taylor, D. 1948. *Fundamentals of soil mechanics*: Chapman And Hall, Limited.; New York.

Terzaghi, K. 1925. *Erdbaumechanik auf bodenphysikalischer grundlage*, Leipzig u. Wien: F. Deuticke.

Tootoonchi, A., Khoshghalb, A. & Liu, G. 2018. A novel approach for application of smoothed point interpolation methods to axisymmetric problems in poroelasticity. *Computers and Geotechnics,* 102(39-52.

Tootoonchi, A., Khoshghalb, A., Liu, G. & Khalili, N. 2016. A cell-based smoothed point interpolation method for flow-deformation analysis of saturated porous media. *Computers and Geotechnics,* 75(159-173.

Tsiampousi, A., Zdravkovic, L. & Potts, D. 2013a. A 3-Dimensional hysteretic soil-water retention curve.

Tsiampousi, A., Zdravković, L. & Potts, D. M. 2013b. A new Hvorslev surface for critical state type unsaturated and saturated constitutive models. *Computers and Geotechnics,* 48(156-166.

Turner, M., J 1959. The direct stiffness method of structural analysis. *Structural and Materials Panel Paper, AGARD Meeting, Aachen.*

Uchaipichat, A. & Khalili, N. 2009. Experimental investigation of thermo-hydro-mechanical behaviour of an unsaturated silt. *Géotechnique,* 59(4)**,** pp 339-353.

Ullah, Z., Coombs, W. & Augarde, C. 2013. An adaptive finite element/meshless coupled method based on local maximum entropy shape functions for linear and nonlinear problems. *Computer methods in applied mechanics and engineering,* 267(111-132.

Van Genuchten, M. T. 1980. A closed-form equation for predicting the hydraulic conductivity of unsaturated soils. *Soil science society of America journal,* 44(5)**,** pp 892-898.

Veeraragavan, A., Beri, J. & Gollan, R. 2016. Use of the method of manufactured solutions for the verification of conjugate heat transfer solvers. *Journal of Computational Physics,* 307(308-320.

Wang, D. & Sun, Y. 2011. A Galerkin meshfree method with stabilized conforming nodal integration for geometrically nonlinear analysis of shear deformable plates. *International Journal of Computational Methods,* 8(04)**,** pp 685-703.

Wang, J. & Liu, G. 2002a. On the optimal shape parameters of radial basis functions used for 2-D meshless methods. *Computer Methods in Applied Mechanics and Engineering,* 191(23)**,** pp 2611-2630.

Wang, J. & Liu, G. 2002b. A point interpolation meshless method based on radial basis functions. *International Journal for Numerical Methods in Engineering,* 54(11)**,** pp 1623-1648.

Wang, J., Liu, G. & Lin, P. 2002. Numerical analysis of Biot's consolidation process by radial point interpolation method. *International Journal of Solids and Structures,* 39(6)**,** pp 1557-1573.

Wang, J., Liu, G. & Wu, Y. 2001. A point interpolation method for simulating dissipation process of consolidation. *Computer Methods in Applied Mechanics and Engineering,* 190(45)**,** pp 5907-5922.

Wang, W., Wang, J., Wang, Z. & Nogami, T. 2007. An unequal-order radial interpolation meshless method for Biot’s consolidation theory. *Computers and Geotechnics,* 34(2)**,** pp 61-70.

Wheeler, S. 1996. Inclusion of specific water volume within an elasto-plastic model for unsaturated soil. *Canadian Geotechnical Journal,* 33(1)**,** pp 42-57.

Wheeler, S., Gallipoli, D. & Karstunen, M. 2002. Comments on use of the Barcelona Basic Model for unsaturated soils. *International journal for numerical and analytical methods in Geomechanics,* 26(15)**,** pp 1561-1571.

Wheeler, S., Sharma, R. & Buisson, M. 2003. Coupling of hydraulic hysteresis and stress–strain behaviour in unsaturated soils. *Géotechnique,* 53(1)**,** pp 41-54.

Wu, C.-T., Chen, J.-S., Chi, L. & Huck, F. 2001. Lagrangian meshfree formulation for analysis of geotechnical materials. *Journal of engineering mechanics,* 127(5)**,** pp 440-449.

Wu, S., Liu, G., Cui, X., Nguyen, T. & Zhang, G. 2010. An edge-based smoothed point interpolation method (ES-PIM) for heat transfer analysis of rapid manufacturing system. *International Journal of Heat and Mass Transfer,* 53(9)**,** pp 1938-1950.

Wu, Y.-S. & Forsyth, P. A. 2001. On the selection of primary variables in numerical formulation for modeling multiphase flow in porous media. *Journal of contaminant hydrology,* 48(3-4)**,** pp 277-304.

Xikui, L. & Zienkiewicz, O. 1992. Multiphase flow in deforming porous media and finite element solutions. *Computers & structures,* 45(2)**,** pp 211-227.

Zakrzewski, N., Nazem, M., Sloan, S. & Cassidy, M. On application of the maximum entropy meshless method for large deformation analysis of geotechnical problems. Applied Mechanics and Materials, 2016. Trans Tech Publications, 331-335.

Zeng, W. & Liu, G. 2016. Smoothed finite element methods (S-FEM): An overview and recent developments. *Archives of Computational Methods in Engineering,* 1-39.

Zhang, G., Li, Y., Gao, X., Hui, D., Wang, S. & Zong, Z. 2015. Smoothed Point Interpolation Method for Elastoplastic Analysis. *International Journal of Computational Methods,* 12(04)**,** pp 1540013.

Zhang, G., Liu, G., Nguyen, T., Song, C., Han, X., Zhong, Z. & Li, G. 2007. The upper bound property for solid mechanics of the linearly conforming radial point interpolation method (LC-RPIM). *International Journal of Computational Methods,* 4(03)**,** pp 521-541.

Zhang, Y. 2007. Solving partial differential equations by meshless methods using radial basis functions. *Applied Mathematics and Computation,* 185(1)**,** pp 614-627.

Zhu, H., Miao, Y. & Cai, Y. 2006. Meshless natural neighbour method and its application in elasto-plastic problems. *Computational Methods.* Springer.

Zhuang, X., Augarde, C. & Mathisen, K. 2012. Fracture modeling using meshless methods and level sets in 3D: framework and modeling. *International Journal for Numerical Methods in Engineering,* 92(11)**,** pp 969-998.

Zienkiewicz, O. C., Xie, Y., Schrefler, B., Ledesma, A. & Biĉaniĉ, N. 1990. Static and dynamic behaviour of soils: a rational approach to quantitative solutions. II. Semi-saturated problems. *Proc. R. Soc. Lond. A,* 429(1877)**,** pp 311-321.